University of Southampton

Faculty of Engineering and Physical Sciences

School of Engineering

Non-invasive Method of Measuring Resonance Properties of Fish Swim Bladders

by

Luocheng Wu

BEng, MSc

Thesis for the degree of Doctor of Philosophy

January 2025

University of Southampton

Abstract

Faculty of Engineering and Physical Sciences

School of Engineering

Doctor of Philosophy

Non-invasive Method of Measuring Resonance Properties of Fish Swim Bladders

by

Luocheng Wu

Fish face elevated mortality risks at hydraulic structures such as dams and hydropower turbines. In response, this thesis proposes a novel, non-invasive technique for measuring swim bladder resonance in live, free-swimming fish and evaluates whether resonance-specific acoustic stimuli can alter their behaviour. The research begins by establishing experimental protocols using surrogate bubbles, whereby inflated latex balloons mimic fish swim bladders. Laboratory tests confirm the ability to detect resonance peaks in these surrogates. Subsequently, recently euthanised fish serve to extend these measurements in a more biologically representative context, allowing factors such as swim bladder shape, volume, wall thickness, and damping factors to be included. Finite element modelling then helps validate measured resonance properties, matching theoretical expectations when realistic morphological parameters are applied. Building on these foundations, a custom cylindrical test tank was created for non-invasive *in vivo* measurements and behavioural studies. Acoustic tests in this facility confirmed that fish could swim freely and remain unanaesthetised throughout the measurement process, preserving natural buoyancy and movement. Resonance peaks were successfully measured and observed in individual fish, revealing notable inter-individual variation. In several cases, morphological factors such as body length, height, and weight were correlated with resonance frequency shifts, indicating that fish with larger body size or swim bladder volume often showed lower resonance frequencies. With the support of computed tomography, comprehensive finite element simulations of swim bladder resonance behaviours coupled with the frequency response of the test tank were performed to validate the results of the experimental measurements and achieved satisfying alignment. The final experiments explored whether fish, upon exposure to tonal signals tuned near their measured swim bladder resonance, would exhibit stronger startle reactions than under off-resonance conditions. Behavioural observations, supplemented by statistical modelling, demonstrated that fish responses were more pronounced when the stimulus frequency tuned closely to the measured swim bladder resonance. While not all individuals displayed equally robust reactions, a clear trend emerged, suggesting that resonance-driven oscillations of the swim bladder can heighten the perceptual or physiological response of the test fish. Collectively, these findings lay the groundwork for a more focused and potentially species-specific deterrent strategy. By enabling precise non-invasive *in vivo* resonance measurements, the method permits greater insight into the interplay of acoustic excitation, swim bladder oscillations, and fish behaviour. This approach also shows the potential for practical applications in endangered species conservation and fisheries management, where minimising fish mortalities and improving passage efficiency remain pressing concerns.

Table of Contents

Table of Tables

Table of Figures

Research Thesis: Declaration of Authorship

Print name: Luocheng Wu

Title of thesis: Non-invasive method of measuring resonance properties of fish swim bladders

I declare that this thesis and the work presented in it are my own and has been generated by me as the result of my own original research.

I confirm that:

1. This work was done wholly or mainly while in candidature for a research degree at this University;
2. Where any part of this thesis has previously been submitted for a degree or any other qualification at this University or any other institution, this has been clearly stated;
3. Where I have consulted the published work of others, this is always clearly attributed;
4. Where I have quoted from the work of others, the source is always given. With the exception of such quotations, this thesis is entirely my own work;
5. I have acknowledged all main sources of help;
6. Where the thesis is based on work done by myself jointly with others, I have made clear exactly what was done by others and what I have contributed myself;
7. Parts of this work have been published as:

Wu, L., White, P.R., Kemp, P. (2024). Measurements of the Resonance Properties of Dummy Fish Swim Bladders. In: Kalinowska, M.B., Mrokowska, M.M., Rowiński, P.M. (eds) Advances in Hydraulic Research. ISH 2023. GeoPlanet: Earth and Planetary Sciences. Springer, Cham. https://doi.org/10.1007/978-3-031-56093-4_32

Signature: .... Date:........................

Acknowledgements

"The heights yield to endeavour | strenuis ardua cedunt"

This journey of PhD has had some ups and downs, but luckily, I have received support, help, and guidance from many people. First and foremost, thank you to my main supervisor Prof. Paul White for his tireless guidance and close supervision from conceptualisation to experimental measurements, and then the thesis writing. This interdisciplinary project could never have been without his expertise and kind support. Secondly, to my second supervisor Prof. Paul Kemp. Thank you for your inspiration and reassurance throughout the project, and your valuable feedback from the perspective of freshwater ecology and fish biology.

Thank you to all the Marie Curie RIBES group for the company on this journey and all the fun presentations and conversations we shared, among whom I would love to thank Philip and James the most for your friendship and our cooperation on fish bioacoustics. I am also grateful to all the members (especially Lewis, Matt, and Amelia) of ICER for your assistance on fish-related experiments, and particularly to Andy who covered every detail regarding fish throughout the six months of the final experiment. Thank you to colleagues and friends in ISVR, Muvis X-ray Centre, EDMC, NOC, and ORC.

Lastly, thank you to my wife Yishan for your endless love and never-absent support from day one. For countless days and nights, you have been by my side no matter what I do or where I go. I will never stop loving you until the last breath of my life.

I value the motto of University of Southampton, and will carry it with me for the years to come.

This project has received funding from the European Union Horizon 2020 Research and Innovation Programme under the Marie Sklodowska-Curie Actions, Grant Agreement No. 860800: River flow regulation, fish Behaviour and Status.

Definitions and Abbreviations

General Terms

Acoustic Deterrent	An underwater sound-based intervention designed to repel or guide fish away from potentially harmful areas (*e.g.*, turbine intakes, dam spillways) by exploiting auditory or physical responses to noise or vibration.
Behavioural Response	A measurable change in fish activity (*e.g.*, startle, avoidance, movement pattern) triggered by an external stimulus such as an acoustic signal.
Buoyancy Control	The process by which fish adjust their depth in the water column, often via regulating gas volume in the swim bladder, thereby minimising energy expenditure.
Encapsulated Bubble	A bubble (or gas pocket) enclosed by an elastic boundary (*e.g.*, the swim bladder wall in a fish), which can resonate at certain frequencies and exhibits damping due to surrounding tissue and fluid interactions.
Finite Element Modelling	A numerical method used to approximate solutions to complex physical phenomena by dividing a domain into smaller elements and systematically solving for variables such as acoustic pressure or boundary displacement.
In vivo Measurement	The process of recording a biological or physiological property (like resonance frequency) in live organisms under realistic conditions, rather than using extracted tissues or euthanised specimens.

Latex Balloon Surrogate	An inflated latex sphere used as an experimental stand-in for the swim bladder, enabling preliminary resonance measurement and validation of acoustic protocols.
Morphological Attribute	Any anatomical characteristic of a fish, such as total length, body mass, or swim bladder volume examined for its relationship to acoustic or behavioural properties.
Non-invasive Method	A technique that does not require surgery, anaesthesia, or lethal sampling, ensuring minimal stress or harm to the study organisms.
Quality Factor	A dimensionless parameter indicating how underdamped a resonant system is; a higher quality factor implies a narrower peak and less energy loss per oscillation cycle.
Resonance Frequency	The specific frequency at which a system (*e.g.*, a swim bladder) naturally oscillates with the largest amplitude, given a driving sound wave of matching frequency.
Startle (Reflex) Response	A rapid, involuntary movement or change in orientation by fish in reaction to sudden or intense stimuli (*e.g.*, a pulse of sound at near-resonant frequency).
Swim Bladder	A gas-filled organ in many bony fish used primarily for buoyancy regulation. In the context of acoustics, it may also enhance hearing or produce/scatter sound due to its bubble resonance properties.
Weberian Ossicles	A chain of small bones in certain fishes (otophysans) that mechanically couple the swim bladder to the inner ear, thereby improving auditory sensitivity.

Young’s modulus	A measure of a material’s stiffness, defined as the ratio of stress (force per unit area) to strain (relative deformation). Higher values indicate that the material deforms less under a given load.
Poisson’s ratio	A dimensionless property describing how a material in tension or compression expands or contracts perpendicular to the direction of load. When a sample is stretched longitudinally, it tends to contract in the transverse directions, with Poisson’s ratio quantifying the extent of that lateral contraction.
Isotropic structural loss factor	A parameter indicating the degree of internal damping or energy dissipation in a uniformly structured material. In isotropic materials (the same properties in all directions), this factor affects how vibration energy is lost, influencing resonance and wave propagation.
Viscosity	The measure of a fluid or soft material’s resistance to flow or shear deformation. Higher viscosity means greater internal friction, playing a role in acoustic damping—particularly for motions in or around fluids and tissues.
Damping	The broad concept of energy dissipation within an oscillatory system, reducing the amplitude of vibrations over time. It can arise from mechanisms such as friction, heat conduction, or radiation of energy into the environment.
Inner ear	An anatomical structure in fish (and other vertebrates) responsible for detecting sound and maintaining balance. In fish, the otolith organs within the inner ear transduce particle motion; in some species, the swim bladder helps enhance pressure detection.
Impedance tube	A cylindrical apparatus designed for acoustic testing, allowing accurate measurement of sound propagation, reflection, or absorption in materials or small samples. By controlling boundary conditions, it helps determine acoustic properties under relatively simple wave conditions.
Inertial shaker	A device or assembly that imparts controlled vibrational energy to a test specimen or structure. It applies oscillatory force, often used to

	induce resonance in surrogates or to excite sample responses for measurement and analysis.
Structural modes	The characteristic vibration patterns of a solid body or assembly, each associated with a natural (resonant) frequency. When excited, a structure deforms in a specific mode shape, with energy concentrated at that frequency.

Symbols

a	Radius of a sphere.
β	Void fraction, the proportion of the fish's swim bladder gas volume to a larger container or tube water volume.
β_0	In logistic regression analyses, it is the slope coefficient that quantifies the influence of a predictor variable (*e.g.*, resonant frequency offset, amplitude) on the log-odds of a response outcome (*e.g.*, fish startle = 1 vs. no startle = 0). A positive β_0 implies an increasing probability of the event with rising predictor values.
c	Speed of sound in water ($\mathrm{m \cdot s^{-1}}$), dependent on temperature, salinity, and pressure.
c_m	The phase speed of sound in a mixture containing bubbles. When bubbles (or the swim bladder) are present, they lower the overall sound speed due to compressibility effects.
D	Thermal diffusivity, a measure of how quickly heat is conducted within the bubble gas. Larger diffusivity means the gas can more rapidly exchange heat with the environment, influencing damping and resonance width.
δ	Damping ratio or damping coefficient, indicating how quickly oscillations decay.
δ_{rad}	Radiation damping loss due to re-radiation of sound from the vibrating bubble boundary back into the surrounding fluid.

δ_{vis}	Viscous damping from viscous shear and friction in the medium adjacent to the bubble or swim bladder surface.
δ_{therm}	Thermal damping for heat exchange between the oscillating gas inside the bubble and the fluid outside, as the bubble expands and contracts.
ε	Eccentricity parameter is an aspect ratio capturing how elongated or flattened the swim bladder is.
f	Generic notation for frequency (Hz). In context, it may refer to the driving or stimulus frequency in an experiment.
f_R	Resonance frequency (Hz) of the swim bladder (or latex balloon). This is the principal frequency at which maximum amplitude oscillation occurs.
k	Wave number of the driving sound field, defined by ω / c, where c is the speed of sound in the fluid or tissue. The assumption $ka \ll 1$ means the bubble with the radius a is much smaller than the acoustic wavelength, so the wave sees the bubble as a sub-wavelength scatterer.
L	Characteristic length scale (fish fork length) relevant to acoustic or morphological measurements.
λ	The spatial period of a propagating wave, defined as the distance over which one full cycle of the wave repeats.

μ	viscosity of the material surrounding the swim bladder (in some analyses, the fish's internal tissues). Higher viscosity leads to stronger viscous damping.
ω	Angular frequency, the frequency parameter in radians per second. It is related to the ordinary frequency f by $\omega = 2\pi f$.
p	Sound pressure (Pa) or amplitude of an acoustic signal, which may be varied to gauge fish responses.
$\wp(a)$	Bubble size distribution function of how bubbles are distributed by radius a . In simpler contexts, one deals with a single bubble radius, but more complex analyses integrate over a distribution of radii.
Q	Quality factor denoting how sharply peaked the resonance is. A higher Q implies lower damping and narrower bandwidth.
R^2	A statistical measure (coefficient of determination) indicating how well a regression or model fit explains the variance in the data. In acoustic or logistic models, higher R^2 suggests a better fit.
σ	The liquid's surface tension. In bubble resonance, it modifies the restoring force at the bubble boundary, shifting the natural frequency.
t	Time (s), used in the context of signal duration or wave-phase measurements during resonance detection.
V	Characteristic volumetric scale.

Φ	A complex function capturing thermal effects and diffusivity D of the bubble gas, which in turn affects the bubble's resonant behaviour.
γ	Ratio of specific heats is the ratio of a gas's specific heat at constant pressure to its specific heat at constant volume. It appears in bubble oscillation theory because the gas inside the bubble undergoes thermodynamic processes (compression/expansion) during acoustic drive.
W	Characteristic weight scale (total fish weight) relevant to acoustic or morphological measurements.

Abbreviations

AEBR	Acoustically Evoked Behavioural Response. An approach for determining fish hearing or response thresholds by observing startle or avoidance reactions to acoustic stimuli, rather than relying solely on electrophysiological or conditioned methods.
AEP	Auditory Evoked Potential. An electrophysiological technique sometimes used to measure hearing thresholds in fish but not employed in detail here due to the thesis emphasis on behavioural and resonance-based methods.
CFD	Computational Fluid Dynamics. Although not the primary focus of this thesis, CFD principles can be relevant for understanding flow fields around fish or within test tanks.
CP model	Commander and Prosperetti model. A theoretical model formulated by Commander and Prosperetti for describing the behaviour of bubbles in an acoustic field. It includes both the dynamics of bubble oscillations and the scattering of sound.
CT	Computed Tomography. A scanning method that can produce detailed 3D images of fish morphology (including swim bladder shape), assisting in resonance modelling.
DAQ	Data acquisition card. The system (hardware and software) for collecting and digitising physical signals (*e.g.*, pressure, displacement, voltage) to enable monitoring, analysis, or control in experiments.
dB	Decibel. A logarithmic unit measuring relative acoustic pressures or signal intensities.

FEM	Finite Element Modelling (or Method). The numerical simulation approach used extensively to predict resonance phenomena in surrogate and biological systems, as well as tank acoustic fields.
Hz	Hertz. Unit of frequency, specifying the number of cycles per second for a sound wave or oscillation.
LDV	Laser Doppler vibrometer. A non-contact instrument using laser interferometry to measure the velocity with high sensitivity and resolution.
NACWO	Named Animal Care and Welfare Officer. An individual officially responsible for overseeing and ensuring compliance with animal welfare regulations and ethical standards in a research institution or facility.
NI	National Instruments. A manufacturer specialising in automated test equipment and virtual instrumentation software (*e.g.*, LabVIEW). Their hardware products (*e.g.*, data acquisition boards) are often used in laboratory measurement setups.
PA	Particle acceleration. A vector quantity describing how fluid or tissue particles accelerate in an acoustic field, often measured in meters per second squared (m/s^2). In the context of fish hearing, it represents the vibrational component directly perceived by inner ear structures (or enhanced by a swim bladder).
PML	Perfectly matched layer. A computational boundary condition in finite element or finite difference simulations that absorbs outgoing

	waves with minimal reflection, simulating an unbounded domain or free-field environment.
PSD	Power spectrum density. A representation of a signal’s power across different frequencies, typically expressed in units such as dB/Hz. It shows how signal energy or amplitude is distributed as a function of frequency.
Q	Quality Factor. An abbreviation repeated from the Symbols section; kept in Abbreviations for quick reference.
RMSE	Root Mean Square Error. A statistical measure assessing the average magnitude of error between predicted values and observed values. Lower RMSE values indicate closer agreement between model and experiment.
ROI	Region of interest. A specified subset of an image, volume, or dataset on which measurements, analyses, or further processing (*e.g.*, segmentation, acoustic interrogation) are focused.
SNR	Signal-to-noise ratio. A dimensionless measure comparing the level of a desired signal (*e.g.*, acoustic wave amplitude) to the background noise level. Higher SNR indicates a cleaner, more distinguishable signal relative to noise.
SPLrms	Root-mean-squared Sound Pressure Level. An expression of acoustic pressure, typically measured in decibels relative to a reference pressure (1 μPa in water, 20 μPa in air).
TF	Transfer Function. A ratio of output to input signal characterising how amplitude and phase vary with frequency.

Chapter 1 Research Introduction

Anthropogenic activities have profoundly altered freshwater and marine ecosystems, impacting fish populations and the broader ecological balance. Dams, weirs, and hydropower structures, while beneficial for energy supply, have fragmented habitats and introduced physical hazards to fish passing through turbines (Northcote, 1978; Jordan and Wortley, 1985; Brown *et al.*, 2009). Migratory species, in particular, may face significant mortality or suffer sublethal injuries that compromise their ability to navigate, reproduce, or maintain buoyancy (Radinger *et al.*, 2021; Carr, 2000). Given the increasing demand for water resources in energy production and agriculture, there is a growing call to develop new strategies that can guide fish away from dangerous sites, such as turbine intakes, while preserving free passage for critical lifecycle movements (Popper and Carlson, 1998).

Recent research suggests that acoustic-based deterrent systems might offer a viable alternative or complement to physical barriers (Putland and Mensinger, 2019). Underwater sound can propagate efficiently and be tuned to target fish sensory mechanisms, potentially persuading them to avoid acoustically uncomfortable zones. Broadband acoustic methods often require high-intensity noise to be broadcast continuously, raising concerns about energetic costs, noise pollution, and variable effectiveness (Putland and Mensinger, 2019).The concept of using acoustics for fish guidance, however, also accounts for the swim bladder, a gas-filled organ that many bony fish use for buoyancy control. This swim bladder also interacts with the fish's auditory system, particularly in species known as hearing specialists that possess structural coupling between the swim bladder and the inner ear, thereby enhancing sensitivity to certain sound frequencies (Popper and Hawkins, 2021). It is hypothesised that if the swim bladder resonates in response to sound waves at a given frequency, moderate acoustic signals at that frequency will cause the swim bladder to oscillate more strongly, potentially inducing a noticeable or aversive sensation (Li *et al.* 2024). By intentionally driving the fish's swim bladder resonance, one might encourage fish to move away from hazardous regions, thus reducing the risk of injury or mortality from turbines or similar hazards.

Despite the theoretical appeal of resonance-based acoustic deterrence, practical implementation is challenging. In order to use the swim bladder resonance to better understand fish hearing and enhance acoustic deterrents, the crucial part is the successful measurement of the swim bladder resonance. Traditional measurements of swim bladder resonance were often conducted in large bodies of water or under free-field conditions (McCartney and Stubbs, 1971; Sand and Hawkins, 1973), with complicated experimental settings, limited control over acoustic parameters or restricted to saltwater species. Some laboratory attempts used anaesthetised or euthanised fish (Cox and Rogers, 1987), which precluded real-time observation of swim bladder resonance behaviour using high-accuracy ultrasound-based systems. A missing element in many prior studies has been an effective way to non-invasively measure swim bladder resonance in freely swimming fish, l*et al*one simultaneously monitor whether the swim bladder resonance itself elicits any significant behavioural response. Achieving these targets requires controlled tank experiments on live, unstressed, freely swimming specimens, bringing a task that demands a well-defined acoustic environment, efficient measurement protocols, and reliable validations.

1.1 Research Aims and Objectives

This thesis seeks to develop, implement, and validate a non-invasive methodology to measure swim bladder resonance in live, free-swimming fish and to observe how resonance-tuned acoustic signals influence fish behaviour. By linking controlled experiments, numerical simulations, and ecological considerations, the project aspires to advance knowledge on the role of swim bladder resonance in fish hearing and behavioural response, while informing future designs of acoustic deterrent systems. The study is structured around the following key research objectives:

1. Examine and consolidate existing knowledge on fish auditory mechanisms, underwater bubble acoustics, and swim bladder resonance.

2. Develop experimental protocols to measure encapsulated bubble resonance using surrogate objects and recently euthanised fish, validating the approach with theoretical and numerical models.

3. Design and construct a specialised tank setup that enables non-invasive testing of resonance frequencies and quality factors in free-swimming fish.

4. Measure and analyse *in vivo* swim bladder resonance for free-swimming fish without anaesthesia or euthanasia, correlating morphological attributes to measured swim bladder resonance properties.

5. Evaluate how fish behaviour changes under acoustic stimuli at their swim bladder resonance frequencies, especially relative to off-resonance noise conditions.

1.2 Thesis Overview

To fulfil the above objectives, the thesis is structured as follows:

Chapter 1 outlines the motivations, overarching goals, and key research objectives of the study, situating them within current challenges in underwater acoustics, fisheries management, and aquatic ecology.

Chapter 2 provides a comprehensive literature review, detailing fish hearing mechanisms, the roles of the swim bladder and Weberian ossicles, and existing acoustic deterrent methods. It also discusses previous approaches to the measurement of the resonance properties of free bubbles, encapsulated bubbles, and fish swim bladders under various experimental settings.

Chapter 3 introduces the experimental protocols used to measure resonance in dummy swim bladders (latex balloons) and in recently euthanised fish. Emphasis is placed on validating these measurements through theoretical analyses and finite element modelling (FEM) simulations, demonstrating robust alignment between practical testing and numerical predictions.

Chapter 4 describes the design and characterisation of a newly built cylindrical tank, guided by FEM to produce a controlled acoustic environment. Ethical considerations for housing live fish are addressed, and successful measurements confirm that the tank supports consistent, repeatable, non-invasive acoustical measurements on the free-swimming test fish. Experimentally measured resonance properties were later validated by fine scale FEM that was based on the 3D-reconstruction of computed tomography (CT) scanned swim bladders in combination with the test tank.

Chapter 5 presents results from behavioural experiments with live fish. Data are collected while exposing specimens to tonal stimuli at, or near, their measured resonance frequencies, allowing the identification of any enhanced startle responses. Statistical analyses link resonance proximity and stimulus amplitude to observed behaviour.

Chapter 6 draws together the main findings, reflecting on how the new measurement methods and tank environment can inform practical acoustic deterrent strategies as well as fundamental fish bioacoustics. It proposes future directions for refining *in vivo* swim bladder resonance measurements and investigates how these techniques may extend to diagnosing swim bladder pathologies like parasitic infection, with potential benefits for conservation programmes targeting critically endangered species.

Through this integrated approach of combining tank-based experiments, modelling via FEM, and direct behavioural observations, this thesis develops a truly non-invasive experimental method of measuring swim bladder resonance properties on free-swimming fish and advances the concept that deliberate exploitation of fish swim bladder resonance offers a possible approach to guide or deter fish more selectively and effectively. The findings promise to shed new light on how fish perceive and respond to acoustically induced swim bladder oscillations, bridging ecological objectives with innovative underwater acoustical engineering solutions.

Chapter 2 Literature Review

2.1 The Sense of Hearing in Fish

The underwater environment includes a complex composition of fluid motions and pressure perturbations, some of which result in the propagation of sound waves. Fish, that have evolved underwater, have specialised receptor organs to detect water particle motion and pressure disturbances. There are, however, no clear lines separating the detection of acoustic particle motion and acoustic pressure from the other mechanical disturbances and there is no definite delineation of which organs are responsive to which stimuli (Popper and Hawkins, 2021).

Historically, the first question for researchers to answer was whether or not fish could hear. Bigelow (1904) was the first to show that goldfish (*Carassius auratus*), respond in a definite manner to sound in water, disputing an earlier assertion that the fish could not hear. In his experiments, Bigelow observed the response of goldfish to sound in an aquarium. Then he surgically severed the fifth and seventh nerves, the lateral line nerves and the spinal cord close to the medulla, effectively desensitizing the skin and the lateral line. These fishes responded to sound the same as untreated fish. In other fishes, only the eighth nerve (leading to the ear) was cut, and they didn't respond to sound at all. Therefore, he concluded that goldfish could hear and that the inner ear was probably responsible.

Apart from the inner ear, sound detection in fishes is thought to also involve the lateral line. The lateral line detects the spatial and temporal patterns of relative motion between the water environment and the surface of the fish (Platt *et al.*, 1989). Its bandwidth approximately spans from 1 Hz to 250 Hz (Popper, 1983). The lateral line is responsive to hydrodynamic water motion as well as those caused by an acoustic source. However, since its threshold for motion detection is much higher than the inner ear's, the lateral line's contribution to hearing is thought to be relatively unimportant (Thomas, 1994).

2.1.1 The Fish Ear

In teleost fishes, each ear is embedded in the cranial cavity, roughly at the level of the medulla, though specific orientation may vary by species (Popper *et al.*, 2003). Like other vertebrates, fish ears contain a vestibular component: three semicircular canals and associated ampullary regions that process angular acceleration. In addition, there are three otolith organs: the saccule, lagena, and utricle. These otolith organs carry dense calcium carbonate structures (the otoliths: sagitta, asteriscus, and lapillus correspondingly) that rest upon sensory epithelia (maculae), as is shown in Figure 2.1. Fishes differ from terrestrial vertebrates insofar as they generally do not require external or middle-ear structures, given that water has a density close to that of fish bodies. Thus, the acoustic impedance mismatch that terrestrial vertebrates must overcome in air does not exist in the same form underwater (Popper and Hawkins, 2021).

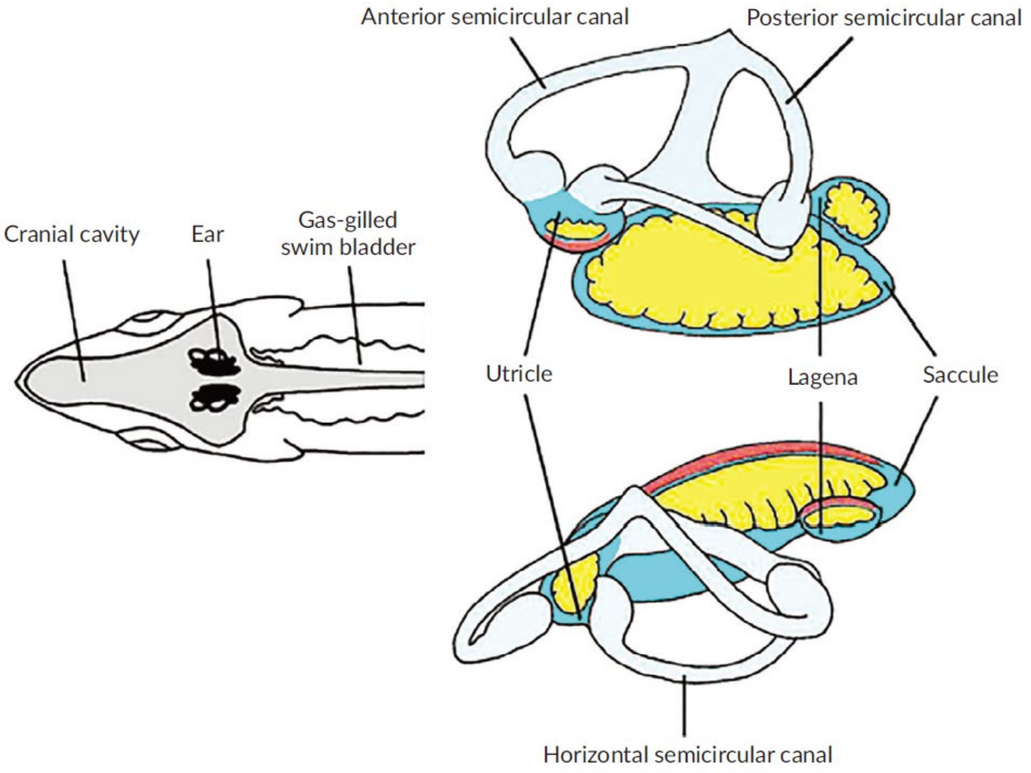

Figure 2.1 Schematic drawing of the ear of Atlantic cod (*Gadus morhua*) (anterior is to the left): (a)top view of the body showing the location of the ears in the cranial cavity as well as the proximity of the rostral end of the swim bladder to the ear; (b) lateral and (c) top view of the same ear. Each ear is set at an angle relative to the midline of the fish. The dark blue part is the otolith organs, the light blue part is the semi-circular canals (enlarged areas are the ampullae regions that contain the sensory cells); The yellow part is the dense calcareous otolith lying in close proximity to the sensory epithelium (the red part) (Popper and Hawkins, 2018).

Although all three otolith organs may contribute to sound detection (Popper *et al*., 1988; Popper *et al*., 2003), the saccule is frequently cited as the principal auditory end-organ in many species, notably goldfish and other otophysans that have a series of bones, the Weberian ossicles, which acoustically couple the swim bladder to the inner ear. (Popper and Fay, 1999). However, the saccule’s prominence as a hearing sensor can vary. The utricle is sometimes implicated in equilibrium and detection of linear acceleration, whereas the lagena plays a dual role in both hearing and potential positional orientation. This morphological variety extends across teleost lineages, leading to significant interspecies differences in hearing ranges and thresholds. For example, clupeids, like Atlantic herring (*Clupea harengus*), and otophysans, like goldfish and catfish (*Siluriformes*), can perceive relatively high frequencies (above 1 kHz in some cases), whereas many "non-hearing-specialist" fishes can only detect lower frequencies in the range of tens to a few hundred Hz (Ladich, 2012; Mann *et al.*, 2001; Popper and Hawkins, 2019).

The operation of the otolith organ at its most fundamental involves relative motion between the otolith and the fish's body, including the sensory hair cells. When a sound wave passes through the fish, the body vibrates in phase with the water, but the otolith, being denser, vibrates out of phase. This differential movement bends the stereocilia of the hair cells, releasing neurotransmitters and generating signals in the auditory nerve (Popper and Hawkins, 2021). Such direct stimulation by particle motion is universal among fishes, giving them at least a basic capacity for detecting sound waves below about 200 to 400 Hz (Popper *et al.*, 2003; Radford *et al.*, 2012; Nedelec *et al.*, 2016). Other enhancements to hearing, particularly for higher frequencies or better sensitivity to pressure, derive from accessory structures that couple ambient pressure changes to the otolith. Chief among these structures is the swim bladder, though some families employ other gas-filled vesicles. Otophysans, for instance, have Weberian ossicles that link the swim bladder to the ear, drastically increasing pressure detection range (Popper *et al.*, 1982; Ladich, 2000).

2.1.2 The Swim Bladder

Von Frisch (1938) was among the first to propose that the swim bladder in many fish acts as an accessory hearing organ by scattering or reflecting incident acoustic energy, producing augmented localised particle motion that the inner ear can register. As Figure 2.2 shows, swim bladders are typically gas-filled sacs in the dorsal portion of the body cavity, though morphological details and positioning differ among species (Alexander, 1966; Popper and Hawkins, 2019). Two main categories are acknowledged: physostomes (open or physostomatous species) and physoclists (closed or physoclistous species) (Jones and Marshall, 1953).

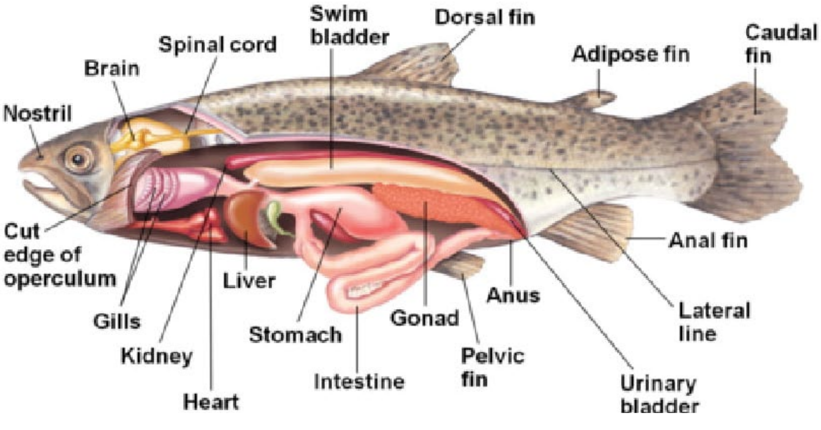

Figure 2.2 The anatomy of a brown trout showing the swim bladder (Brinza, 2016).

In physostomatous fish such as cyprinids and salmonids, a pneumatic duct connects the swim bladder to the foregut, enabling rapid release of gas and re-ingestion of air at the surface. In many cyprinids, including goldfish, the swim bladder divides into an anterior and a posterior chamber, joined by a ductus communicans. By contrast, physoclistous fish lack a functional pneumatic duct and regulate swim bladder volume through a gas gland and resorptive area called the oval (Alexander, 1959; Jones and Marshall, 1953). Structurally, the swim bladder wall is composed of an inner tunica interna (smooth muscle and pavement epithelium) and an outer tunica externa (collagenous and elastic fibres). Between them lies connective tissue, sometimes described as oily or lacy, that allows the layers to move against each other freely (Alexander, 1966). Gas exchange typically concentrates in the anterior portion in many species, especially where hearing specialisations exist.

Because gas density is markedly less than that of water or fish tissues, the swim bladder can resonate at specific frequencies like a bubble in water, thus scattering and re-radiating incident acoustic waves (Minnaert, 1933; Alexander, 1966; Popper and Hawkins, 2019). At resonance, even a relatively small amplitude wave might produce significant swim bladder vibration. Many fishes that possess robust bladder-ear couplings can detect these re-radiated motions as they modulate the relative motion of otoliths in the inner ear. Otophysan fish, such as goldfish, exemplify this arrangement through their Weberian apparatus.

2.1.3 The Weberian Ossicles

Dijkgraaf (1960) considered the Otophysi, like the goldfish, catfish, minnows (*Phoxinus phoxinus*), and relatives, hearing specialists due to the presence of their Weberian ossicles. The Weberian ossicles (tripus, intercalarium, and scaphium) are derived from the anterior vertebrae (Alexander, 1966). The tripus is the most posterior, attaching to the edge of the slit of the tunica externa. Next is the intercalarium and then the scaphium, all connected by a series of ligaments. When the swim bladder expands during the rarefaction phase of an acoustic wave (negative acoustic pressure), the tunica interna stretches, but the tunica externa does not, because of the slit in between. The edges of the slit move apart and the ossicles rotate forward due to the tension in the connections from the ossicles to the vertebrae (Popper, 1971b). This action is illustrated in Figure 2.3. As the swim bladder contracts, the ossicles rotate back as the edges of the slit are moved together by the elastic recoil of ligaments which connect the tripodes to processes of the fourth vertebra.

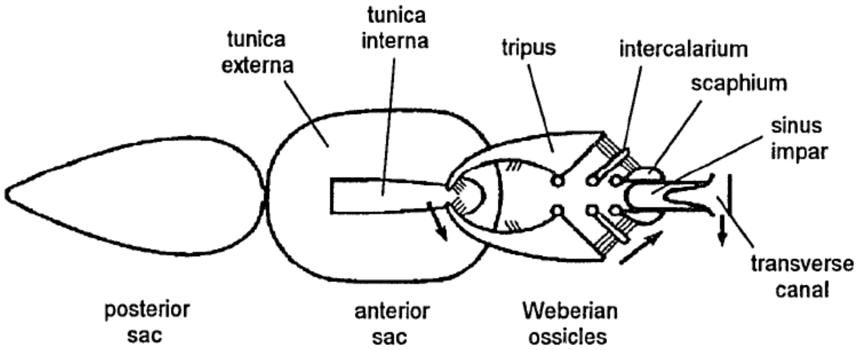

Figure 2.3 Diagram showing the function of the swim bladder and Weberian ossicles of the goldfish. Arrows indicate the direction of motion due to the rarefaction phase of an acoustic wave (Alexander, 1966).

The scaphia are incorporated in the walls of the central fluid-filled cavity, the sinus impar (Alexander, 1966). The sacculi of the two ears are connected by a transverse canal. A posterior diverticulum of this canal, the sinus endolymphaticus, projects into the cavity of the sinus impar. It has a very thin wall. When the ossicles move forward, the scaphia press on the sinus impar, driving the fluid in it forward, compressing the sinus endolymphaticus and displacing fluid from it into the sacculi. This is possible because there is a flexible region in the saccular wall. The saccular otoliths bear wing-like projections which lie in the path of the endolymph movements caused by the Weberian ossicles. Therefore, motion of the ossicles due to the passage of sound waves causes movements of the saccular otoliths and thus stimulates the saccular hair cells.

Weberian ossicles effectively amplify and extend the fish's hearing range to higher frequencies, often surpassing 1 kHz in some species (Ladich, 2012). By turning the swim bladder's resonance-induced fluctuations into direct mechanical pressure upon the inner ear's fluids, these fish gain a unique advantage in detecting acoustic pressure. Indeed, removal of the tripus alone in some catfish can raise the fish's hearing threshold by 30–40 dB, though the overall shape of the audiogram remains intact (Poggendorf, 1952). In other words, the swim-bladder-ossicle connection primarily boosts sensitivity rather than creating entirely new hearing ranges, consistent with the notion that the fish's fundamental ear structure (*i.e.*, the otolith organ) is the ultimate sensor.

2.1.4 Sound Stimulation and Perception

Current understanding, synthesised by Popper and Hawkins (2019, 2021), holds that fish can directly sense the particle motion component of sound via the otolith organs. In species equipped with large or resonant swim bladders and mechanical couplings like the Weberian apparatus, sound pressure fluctuating in the environment is converted into local particle motion, thereby intensifying the stimulus that arrives at the otolith hair cells. This enhancement is often frequency-dependent and culminates in an improvement in sensitivity at particular frequencies, frequently near the resonance of the swim bladder. Van Bergeijk (1967) referred to the swim bladder as a “secondary source of sound,” implying that the swim bladder vibrates and radiates motion when exposed to an external acoustic field. While the fish’s ear is inherently sensitive to particle motion, the swim bladder reintroduces energy near its resonant band in a manner the otolith organs can more easily detect (Fay, 1984; Popper *et al.*, 2014).

Because fish are immersed in water and has a similar body density to water, there is no strong impedance mismatch between water and fish body, like the air–fluid interface in terrestrial ears, where the pressure wave must pass from one medium to another. The critical difference is that gas pockets in the swim bladder, with a drastically different acoustic impedance from the fish’s body, can vibrate at amplitude and phase different from that of the tissues. This phenomenon underlies not just hearing specialisation but also accounts for variation in hearing among fish families without swim bladders or with reduced swim bladders (Popper *et al.*, 2003). Furthermore, it explains why certain families (*e.g.*, Clupeidae), which have novel connections between their auditory bullae and the external environment, can detect ultrasonic frequencies beyond the range typical of many teleosts (Mann *et al.*, 2001).

The lateral line may play some role, especially in low-frequency or near-field contexts, but under typical conditions of propagating far-field sound, it is the ear—potentially aided by the swim bladder or other vesicle—that confers the primary acoustic acuity (Higgs and Radford, 2012). In some sculpin species, for example, the lateral line can detect biologically meaningful flows and vibrations (Braun and Coombs, 2000), though these detections often represent local flow or hydrodynamic events rather than distant acoustic signals. Consequently, while the lateral line is an essential sense for navigation, schooling, or predator–prey interactions at close range, the ear generally dominates hearing tasks involving more typical acoustic stimuli.

2.1.5 Fish Hearing Thresholds

Having established that fishes can hear through the direct stimulation of otoliths by particle motion and, in many cases, via indirect coupling of pressure through the swim bladder, researchers have long sought to measure the sensitivity and range of fish hearing. One of the central concepts here is the audiogram, a curve that charts the minimum detectable threshold across different frequencies (Popper and Schilt, 2008; Popper *et al.*, 1982). Audiograms can be expressed either in terms of root-mean-squared sound pressure level (SPLrms) in dB re 1 µPa or in terms of particle motion (*e.g.*, acceleration, velocity). The choice depends on the species in question and the experimental approach.

Studies of fish hearing thresholds typically employ one of several major methods. One approach is behavioural conditioning, where fish learn to associate an auditory signal with a reward or punishment. For instance, avoidance conditioning involves a mild electric shock paired with a tone. If the fish “hears” the tone, it eventually learns to change its behaviour in anticipation of the shock, and the experimenter can record the lowest amplitude at which the fish reliably responds (Weiss, 1966). However, historical discrepancies arose: older experiments sometimes used in-air loudspeakers, ignoring the mismatch at the air-water boundary and introducing uncertain calibrations. Therefore, thresholds determined in that manner could vary widely, sometimes by tens of decibels for the same species (Enger, 1966; Offutt, 1968; Ladich and Fay, 2013).

Another technique is Auditory Evoked Potential (AEP), where electrodes placed near the fish’s head record electrophysiological responses to tone bursts (Ladich and Fay, 2013; Sliwinska-Kowalska, 2015). AEP is relatively fast and minimally invasive, so it has been used on over a hundred fish species (Ladich and Fay, 2013). Yet differences in tone-burst duration or tank acoustics across labs can yield somewhat divergent thresholds (Radford *et al.*, 2012). AEP thresholds also may not fully reflect behavioural responses, especially if extremely short stimuli are used, or if the fish’s lateral line inputs under 400 Hz are inadvertently included in the signal measured (Enger, 1967). Thus, while AEP is invaluable, it must be interpreted with some caution in cross-species comparisons (Fay and Coombs, 1983).

Moreover, the Acoustically Evoked Behavioural Response (AEBR), zeroes in on a startle or Mauthner-mediated reflex. Unlike conditioning protocols, the AEBR paradigm triggers an unlearned avoidance or “panic” reflex when the stimulus surpasses a certain threshold (Zeddies and Fay, 2005; Alderks and Sisneros, 2013). By systematically lowering the stimulus amplitude and frequency, one can pinpoint the onset of a consistent startle reaction. This threshold is often higher than the absolute hearing threshold, because the fish must detect and then respond with an overt reflex. However, AEBR results can be especially relevant for management or conservation scenarios in which fish avoidance is the interest (Kastelein *et al.*, 2008).

Because fish hearing relies on detecting particle motion in at least some portion of the frequency band, investigators increasingly measure particle acceleration (PA) thresholds as an alternative or complement to SPL-based audiograms (Horodysky *et al.*, 2008; Radford *et al.*, 2012). Enger (1966) and others showed that some fish, such as red drum (*Sciaenops ocellatus*), demonstrate thresholds more consistent with the direct PA stimulus near the fish’s body. These thresholds may diverge significantly from pressure-based thresholds in species lacking close ear–bladder coupling (Radford *et al.*, 2012). Yet it is not trivial to relate particle acceleration with sound pressure in a small tank environment, because the acoustic near-field can become inhomogeneous, with multiple reflections. Variation in measured PA hearing sensitivity results between research groups can exceed 40 dB for certain species (Radford *et al.*, 2012), underscoring the complexities of replicating near-field conditions in a tank.

Despite these methodological discrepancies, some broad patterns emerge. Otophysans with well-developed bladder–ear couplings often display pressure thresholds substantially lower than fish without such coupling, in some cases extending hearing range up to several kHz (Popper and Fay, 1999; Ladich and Fay, 2013). Non-hearing-specialist fishes typically detect frequencies below 1 kHz and are less sensitive to acoustic pressure (Popper *et al.*, 2014; Nedelec *et al.*, 2016). Meanwhile, fish wholly reliant on particle motion, or with minimal accessory structures, generally possess narrower hearing ranges that cluster around 100–300 Hz (Popper *et al.*, 2019). This diversity in hearing thresholds is reflective not only of morphological differences but also of ecological and behavioural niches: species that communicate or survive in noisy habitats might develop or maintain refined hearing specialisations, whereas those that rely less on acoustic signals show more modest sensitivity.

Audiograms are often depicted as a U-shaped curve, with minimal thresholds at some middle frequency band. In otophysans such as goldfish, the best sensitivity may lie between about 200 and 800 Hz, whereas additional lobes or expansions can appear at higher frequencies, approaching 2 kHz or more (Ladich and Fay, 2013). Clupeids can detect still higher frequencies, including ultrasonic ranges in some shad and herring species (Mann *et al.*, 2001). Many demersal fish, lacking a functional swim bladder or similar structure, show maximum sensitivity only up to about 300–400 Hz. In all cases, the shape and depth of an audiogram may change with fish size, swim bladder volume, or gas tension within the swim bladder, introducing further dynamic variation (Popper *et al.*, 2003).

Given the growing interest in underwater noise pollution, fish deterrent systems, and acoustic ecology, understanding fish auditory mechanisms is increasingly pressing. The synergy between the physiology of the ear, the swim bladder, and, in some species, Weberian ossicles, stands as a testament to the evolutionary adaptations fishes have undergone to interpret, exploit, and respond to the bustling soundscape of aquatic environments (Slabbekoorn *et al.*, 2010; Popper and Hawkins, 2019). By combining morphological, behavioural, and electrophysiological research, scientists continue to refine our knowledge of the fish ear's complexity, revealing not just how fish "hear", but also how they use sound to navigate the challenges and opportunities under the surface.

2.2 Fish Guidance and Deterrence Barriers

2.2.1 Physical and Behavioural Barriers

For the purpose to mitigate the effect of man-made facilities on fish, efforts have been devoted to the development of guidance technologies for fisheries management to direct fish movement (Noatch and Suski, 2012). Physical and mechanical methods like fish ladders, runs, lifts and screens are designed to make structures like dams and hydropower plants more fish-friendly (Odeh, 2000; Hocutt, 1981).

The successful design of the fish passage for a particular species in a specific life-cycle stage does not guarantee the same efficiency for all fish, due to the biodiversity, complexities in life cycles and geographical variation. Historically, special focus had been given to the preservation of commercially important species (*e.g.*, adult salmonids) without considering the entire ecosystem, which consequently resulted in an imbalance in species abundance and a reduction in biodiversity (Lucas and Baras, 2001; Dudgeon, 1992). Hence, one of the important factors for developing successful fish-friendly structures in order to help migrants and repelling invasive species lies in the knowledge of matters like the behavioural response of various species to flow, sound and other stimuli (Enders *et al*., 2009). Therefore, the interest in studying the behavioural response and developing non-physical guidance methods to improve the efficiency of physical methods has been gaining more and more attention (Kemp *et al*., 2012).

A behavioural deterrent (or guidance system) can be defined as "*any stimulus or non-solid obstruction that discourages or prevents a selected species from passing through a target region*" (Noatch and Suski, 2012). Fish deterrence systems could either be used as preventing commercially or biologically valuable species from moving into facilities that would threaten their survival or employed for repelling invasive or exotic species away from natural or human-mediated intake pathways of ecosystems (Taft, 2000; Noatch and Suski, 2012). Hocutt (1981) conducted the first major review about fish guidance systems deployed at power facilities and case studies on *in situ* response of fish being attracted or driven away from certain facilities with mainly temperature and level of dissolved oxygen recorded.

Multiple kinds of stimuli, separately or jointly, have been used to attract, repel, and guide fish (Turnpenny *et al*., 1998). Electrical barriers (*e.g.*, Reynolds, 1996; Katopodis *et al*., 1994), illumination (*e.g.*, Volwes and Kemp, 2012), air bubble curtains (*e.g.*, Zielinski *et al*., 2016), acoustics (*e.g.*, Deleau *et al*., 2020; Piper *et al*., 2019), changes in flow (*e.g.*, Enders *et al*., 2009), and combinations of the above (*e.g.*, air bubbles and sound, Taylor *et al.,* 2005; air bubbles and strobe lights, Patrick *et al.,* 1985) have been attempted and discussed in recent decades.

2.2.2 Acoustical Fish Deterrence

Acoustical fish deterrents (AFD) project broadband or pure tone sound stimuli in regions to drive migrating fish from dangerous regions like turbines to desirable areas like the fish passage or prevent invasive species from entering habitats while visual or other stimulus is not efficient enough in some site conditions.

Putland and Mensinger (2019) has reviewed several early attempts of AFDs, most of which were considered less successful (Popper *et al.*, 2020). This article collectively revisited aspects like the designing of different AFD systems, experimental set-ups and results with respect to several commercially popular target species. Maes *et al.* (2004) had limited success with an acoustic repellent system tested at a nuclear power station in Belgium. They found that sounds between 20 and 600 Hz repelled some species (*e.g.*, salmon, sea trout, herring) from the water intake of a power plant with generally less than 50% efficiency, but neither lampreys nor eels appeared to respond to the acoustic deflector system used. The European eel (*Anguilla anguilla*) has also gained growing research interest for its endangered biological status and the socio-economic importance. Recent research carried out by Deleau *et al.* (2019, 2020) used acoustics to enhance the efficiency of physical barriers like screen and maze designed to protect downstream moving eels, as is shown in Figure 2.4. 100 Hz pulse and continuous 60-1000Hz broadband noise were chosen to test the fish response to the acoustic stimuli. Around 15% of rejection rate was achieved long with the physical structures, the lack of connection from swim bladders to inner ears was suggested to be one of the reasons that the efficiency of the AFD on the European eel was poor (Deleau *et al.*, 2020).

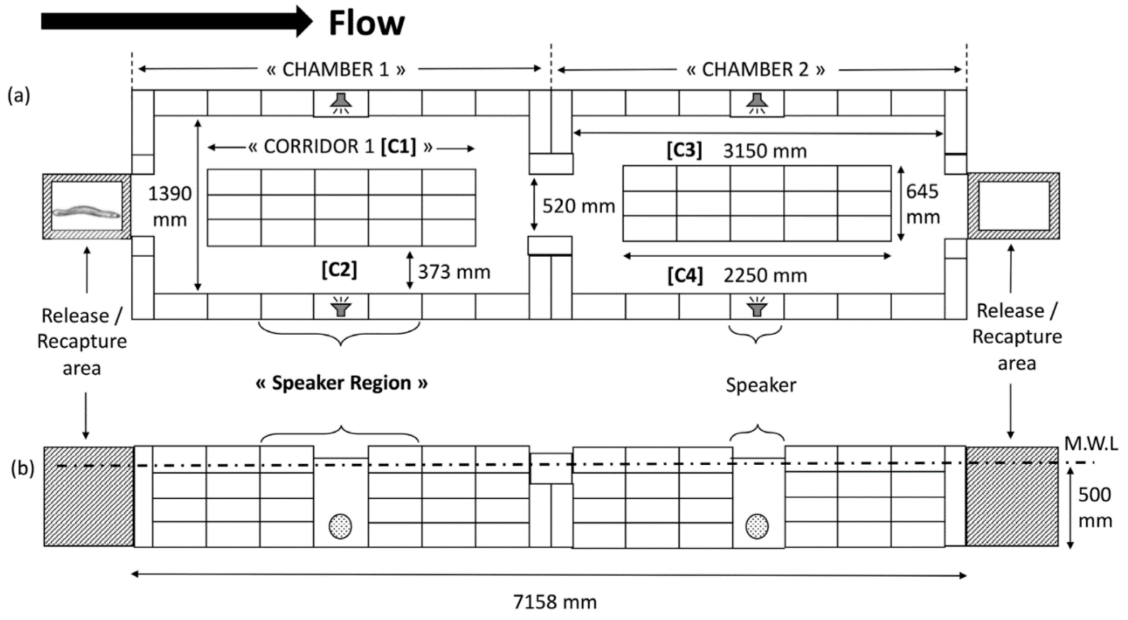

Figure 2.4 The acoustic maze installed in an outdoor flume to study the behavioural response of eels when exposed to acoustic stimuli (Deleau *et al.*, 2020).

Not only in the applications of guiding endangered species, AFD has been thought out as a key factor in the history of combating invasive fish species and fisheries management. Attempts have been made to use sound to deter several invasive Asian carp species from moving into new bodies of water (Popper *et al.*, 2020). A series of experiments was organised to use acoustic deterrents to repel invasive species like silver carp (*Hypophthalmichthys molitrix*) and bighead carp (*Hypophthalmichthys nobilis*) (Vetter *et al.,* 2015). Four underwater speakers were used in an experimental pond that was equipped with gridlines to help with video fish tracking. Pure tones (500, 1000, 1500, 2000Hz) and broadband sound recorded from a boat engine noise were projected by the speakers separately at approximately 150 dB re 1μPa @ 1m directly in front of the speakers, which was approximately 30 dB re 1 μPa @ 1 m above the minimum ambient noise (Vetter *et al.,* 2015). Here, the unit 'dB re 1 μPa @ 1 m', typically associated with Source Levels, is interpreted as referring to Received Levels measured at 1 m from the speaker, with the 30 dB difference representing the signal-to-noise ratio above the minimum ambient noise. Trials were completed on five groups of fish; 30 s of sound stimuli were projected when the fish school reached one end of the pond, in order to deter fish away from that end using the sound stimuli. The results in Figure 2.5 showed that very limited responses were observed when playing pure tones (black solid bars at each end) at different frequencies to fishes reaching one end of the pond, while the use of complex sounds (red solid bars at each end) showed a higher rate of rejection response and a faster average swim speed (Vetter *et al.*, 2015).

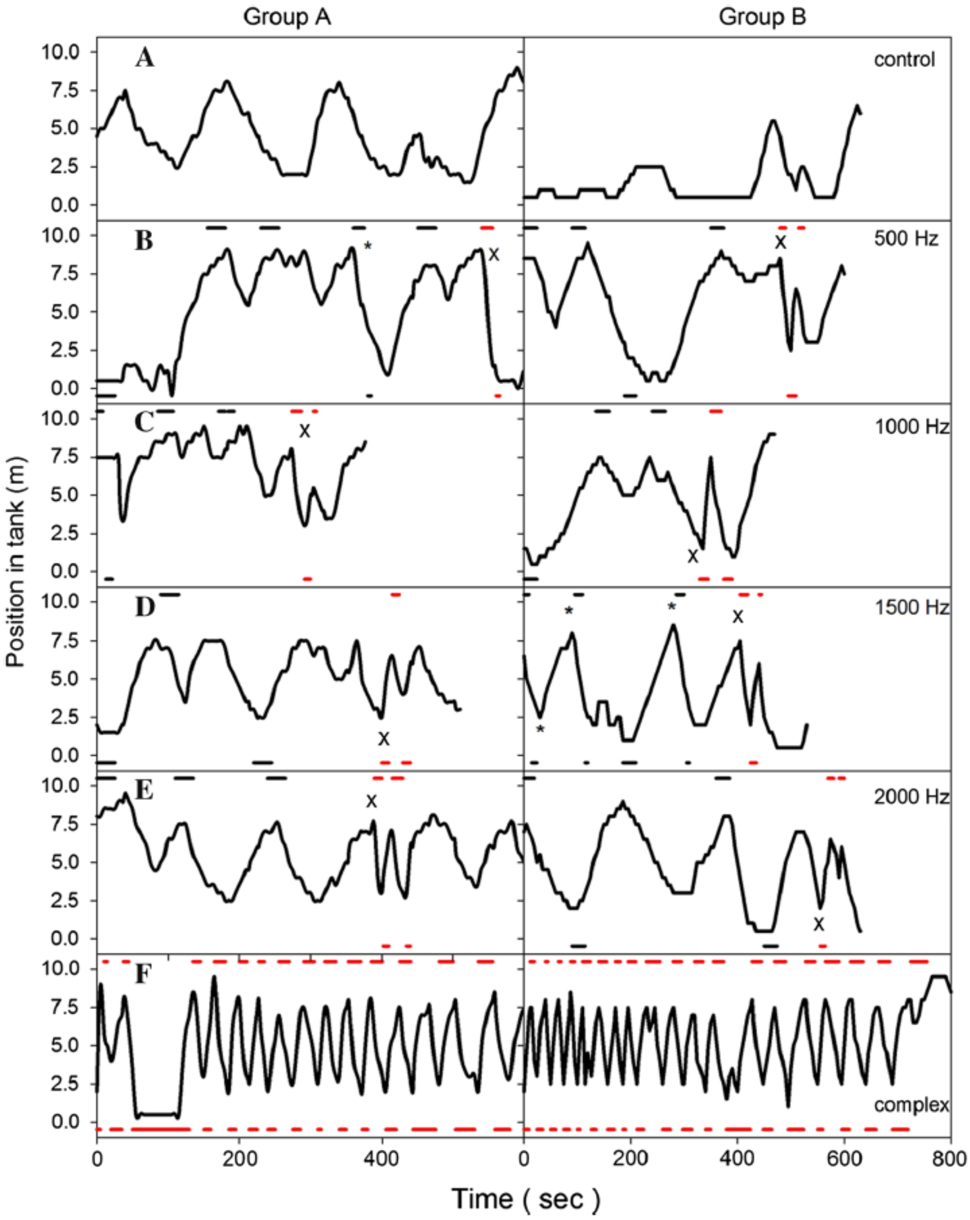

Figure 2.5 Representative silver carp behavioural response to acoustic stimulation for two groups of fish (Group A and Group B) (Vetter *et al.*, 2015). Black solid bars at each end of the pond shown above indicated pure tones and the red ones indicated complex motor sounds.

Following these trials, Wamboldt *et al.* (2019) carried out an evaluation experiment in shallow water using the conclusion of Vetter *et al.* (2015). The movement and rate of entrance of Passive Integrated Transponders (PIT) tagged fish were analysed and 29% of tagged silver carp were detected to enter the intake through an underwater speaker array. Though the acoustic stimuli did not significantly reduce the passage of silver carp, numerous jumping responses were observed at the acoustically active region. The low-frequency stimulus (<2000 Hz) that silver carp was sensitive to suffered rapid attenuation in shallow water structures, depth-related attenuations affected the efficacy of this AFD system at this location (Vetter *et al.*, 2015).

The low rejection response to pure tones and high rejection response to broadband noise potentially indicated that the test carp were sensitive to harmonics at certain frequencies that were present in the broadband noise, which could hypothetically be the resonance frequencies of their swim bladders. To better understand the relationship between swim bladder resonance and fish behavioural response, the crucial part is to estimate or directly measure the resonance properties of the swim bladder.

2.3 Acoustical Properties of Swim Bladders

2.3.1 Previous Efforts on Measuring Acoustical Properties of Swim Bladders

The gas-filled swim bladder typically occupies about 5% of the total volume for saltwater species and 8% for freshwater species (Jones and Marshall, 1953; Alexander, 1959). When present, it dominates the acoustic scattering properties of the fish at low frequencies (Weston, 1967). The reason is that the acoustic parameters for the ordinary fish tissue are very close to those for water, but the acoustic impedance mismatch to the contained gas is very great at all frequencies. However, as a damped air bubble, the swim bladder resonates at a characteristic frequency based on its size, its shape, and the characteristics of the surrounding tissue, normally below 1 kHz for most of the fish when placed near the water surface at atmospheric pressure (Weston, 1967; Cox and Rogers, 1987).

Due to the important role of swim bladders in fish swimming, hearing, and communication, investigations about the biological and acoustical properties have been widely conducted and discussed. In order to study the relationship between swim bladders and fish hearing, Fay and Popper measured the microphonic potentials from the ears of some species like catfish and goldfish in response to underwater sound stimulation and direct head vibration and compared the sensitivities to stimuli before and after the deflation of swim bladders (Fay and Popper, 1974a; Fay and Popper, 1974b). It was concluded that the direct vibration response was not affected by the deflation whilst the hearing sensitivities to sound pressure declined significantly for both catfish and goldfish but not for African mouthbreeder (*Tilapia macrocephala*).

Another measurement performed by Popper (1974) recorded the frequency response of the swim bladder of a euthanised goldfish. After the fish was killed, a 0.5 mm probe (no. 25-gauge steel hypodermic needle) held in a Bruel & Kjaer probe adapter was inserted into the swim bladder. Another hydrophone was held at the side of the fish body as a reference, control groups of inserting the probe into muscle were also conducted. The result indicated that the frequency response of the swim bladder was essentially flat, which meant that the swim bladder was highly damped due to the presence of surrounding tissue, as is shown in Figure 2.6 (Popper, 1974). A small loss of sound energy between the outside and the inside of the swim bladder was observed.

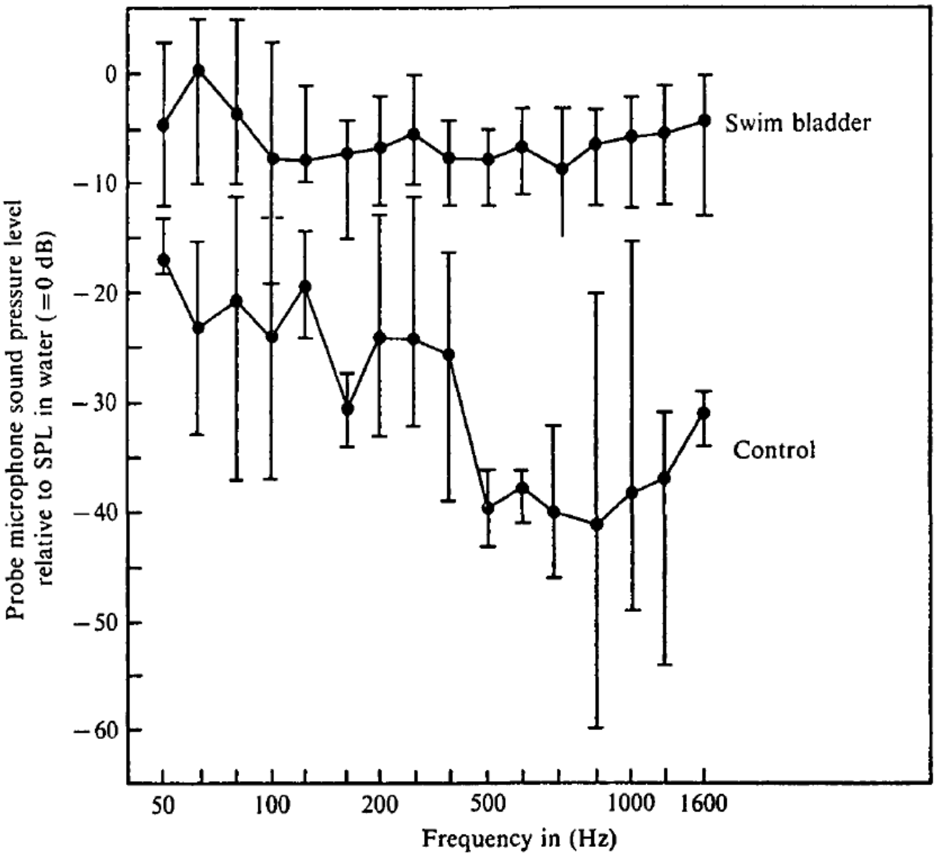

Figure 2.6 The averaged relative level of the measured frequency response in the swim bladder and control group to the reference hydrophone (0 dB) (Popper, 1974).

However, the act of inserting a needle probe through the swim bladder wall would compromise the swim bladder as a complete gas-filled chamber and change the interior pressure, in which case the swim bladder might no longer function as an encapsulated bubble and the measurement of the frequency response was no longer accurate.

From the perspective of acoustical engineering, the frequency response of swim bladders was expressed by the measurement of sound scattering properties and target strength. While fish biologists were focusing on the role of swim bladders in fish hearing, oceanographers also putting more effort into measuring the acoustic properties and estimating the fish size and abundance. To measure the acoustic scattering of a fish, McCartney and Stubbs (1971) took a captive live fish in a controlled condition and used a ring hydrophone and a far-field sound source, as is illustrated by Figure 2.7.

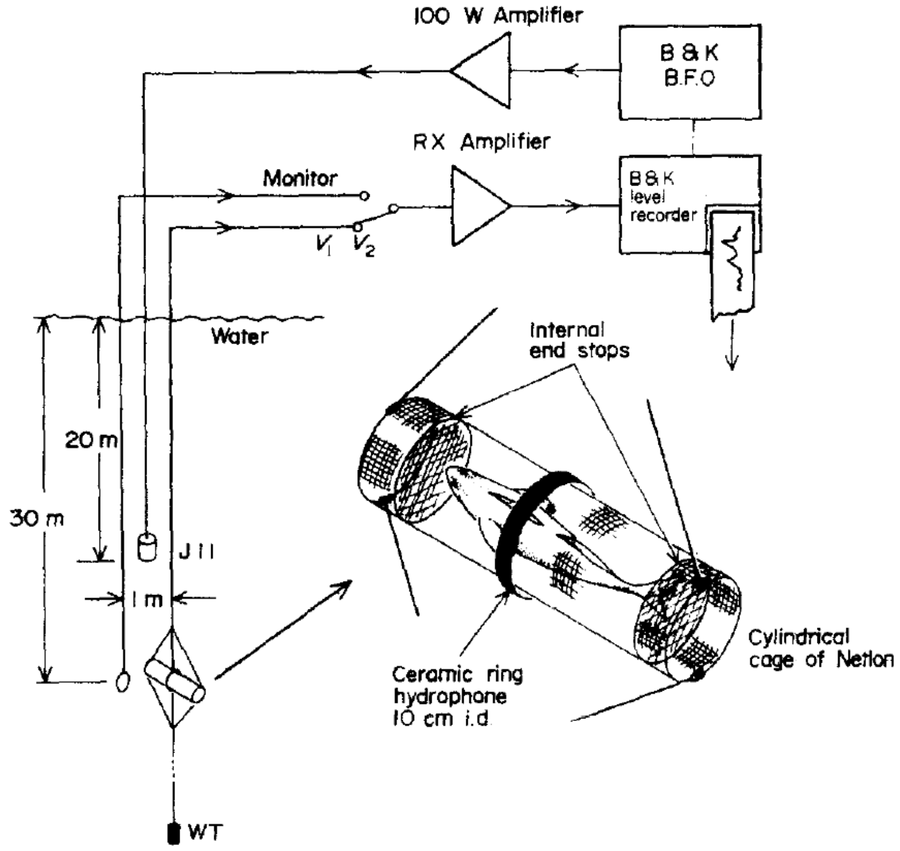

Figure 2.7 The schematic of "Ring method" to measure the swim bladder resonance (McCartney and Stubbs, 1971).

The experiment was performed on *F.R.S Mara* moored in Loch Torridon. A basic principle was to measure the signal v_1 received by the ceramic ring hydrophone and calculate the portion of $|v_1 / v_2|$, where v_2 was the signal from a reference ring hydrophone 1 m away to monitor the transmitted source level. A plastic mesh cage, that the fish could be easily inserted into, was used. The acoustic interference from the cage was negligible below 5 kHz. A range of species including Atlantic cod, common ling (*Molva molva*), Atlantic pollack (*Pollachius pollachius*), and coalfish (*Pollachius virens*) was caught and tested with care (McCartney and Stubbs, 1971). Figure 2.8 shows the results for three cod plotting 20log $|v_1 / v_2|$ versus frequency. The main feature of these results, in which resonance is clearly demonstrated, is that the 35 cm cod (around 500 Hz) has a lower resonance than the 32 cm cod (around 900 Hz), but that the resonance of the 39 cm cod (around 700 Hz with a lower amplitude), which would be expected to be even lower, fell in between the two; this fish was later found to have a ruptured swim bladder, which might be the explanation of lower peak amplitude and higher resonance because of the loss of gas (McCartney and Stubbs, 1971).

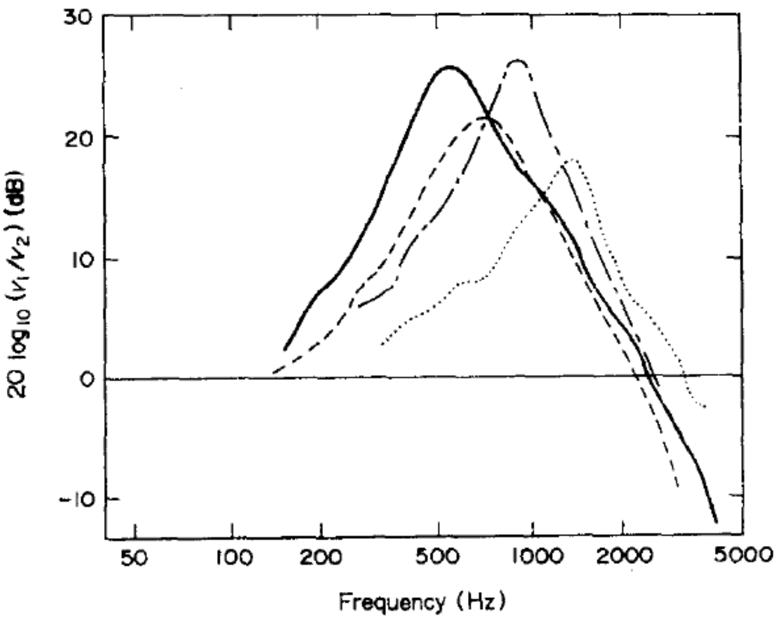

Figure 2.8 Resonance curves for cod (McCartney and Stubbs, 1971). Cod A: 32 cm, - — -, 14:20 26 September ······ 06:50 27 September; cod B, 39 cm, - - -, swim bladder ruptured; cod C, 35 cm, —.

Measurements on various species, at different depths, and how the resonance changes within 24 hours were also conducted. McCartney and Stubbs (1971) suggested that the three major reasons for the higher frequency of resonance are (a) the elongation of the swim bladder, (b) an excess internal pressure due to the stiffness of the swim bladder wall and (c) the fact that apparently the swim bladders of the experimental fish were insufficiently inflated to provide neutral buoyancy. The damping of resonance was high in all cases due to the swim bladder wall tissue and the gut. It was also suggested that the method of *in situ* resonance technique was considered to be a valuable method of monitoring the swim bladder imperfections like rupture, infection, or parasite load.

Following this project, a similar measurement was conducted by Sand and Hawkins (1972) with a focus on studying the relationship between resonance frequency and quality factor of cod swim bladders and the adaptation of depths. In shallow water, the resonance suffers high damping due to the tension of surrounding tissues. The hydrostatic pressure increases as the depth increases, making the volume of swim bladders smaller and easing the tension of fish flesh. Hence, a higher resonance frequency and lower damping of the swim bladder would be expected for a deeper depth. The difference between fish swim bladders and unrestrained gas bubbles were discussed to detail as well, in which were mainly differences in shape and the shear modulus of surrounding tissues. The resonance frequency was concluded to experience an immediate drop as the fish was moved to a new depth, but the elevated values were rapidly restored with time (Sand and Hawkins, 1972).

A comprehensive experimental investigation of swim bladder resonance using the same method was carried out by Lovik and Hovem (1979) to analyse the resonance frequency as a function of depth. The changing tendency of the resonance frequency with respect to how long the fish has stayed on a particular depth was investigated. If a fish was suddenly transferred to a new depth it would take from 12 to 24 h to adapt. Adaptation to a deeper depth, which requires the production of gas to obtain neutral buoyancy, would take significantly longer time than adaptation to a shallower depth. This article also presented an empirical equation of resonance frequency f_0 (Hz) and fish length L(cm): $f_0 = 7232 / L$. Even though there were various kinds of deviation from this relationship, it still provided a reasonably good prediction for saltwater species like coalfish, trout, pollack, and sprat (McCartney and Stubbs, 1971; Lovik and Hovem, 1979). Comparison with earlier published theoretical models showed that the resonance frequencies are higher than should be expected for elongated gas-filled bubbles, and the difference could be due to either tension in the wall and excess pressure in the swim bladder or to the shear modulus of the fish tissue (Andreeva, 1964).

The NIVAMS (Non-Invasive Vibration Amplitude Measurement System) developed by Cox and Rogers (1987) was developed for measuring the scattering of sound by a fish by measuring the frequency response *in vivo* of the swim bladder using ultrasound. As was shown in Figure 2.9, the scatter sound field of a fish with a swim bladder were determined by measuring the radial displacement of the swim bladder wall when excited by low frequency stimulus. The single-chambered swim bladder of the oscar (*Astronotus ocellatus*) acted like a damped air bubble resonating in the low frequency stimulus, scattering significant amounts of acoustic energy in all directions. The response of the two-chambered swim bladder in the goldfish was found to be more complex. However, the act of using ultrasound to detect the radial displacement of swim bladder wall required very high level of accuracy in order to align the focal point of the ultrasound system with the 0.1 mm thick swim bladder wall, resulting in complication and a lack of robustness to the method. The application of anaesthetics on the test fish to hold the swim bladder wall at the focal point also compromised the non-invasiveness of NIMVAS when measuring swim bladder resonance.

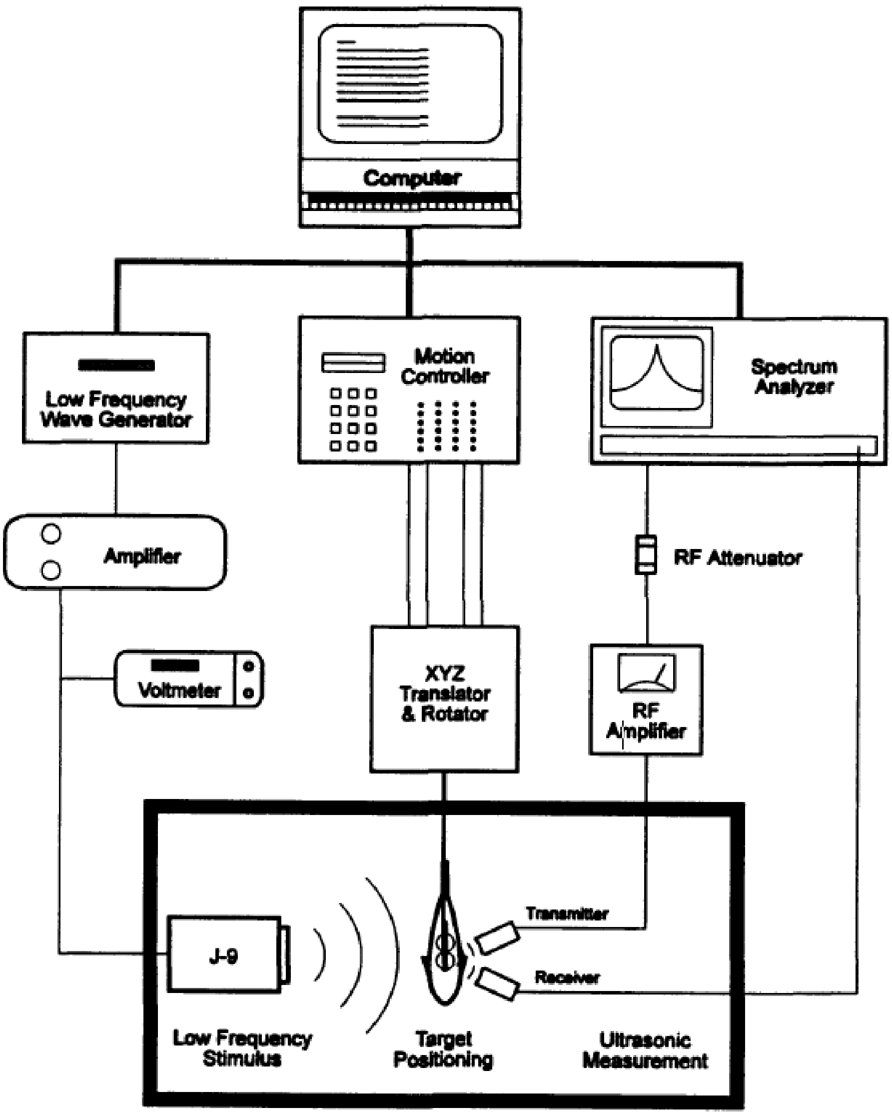

Figure 2.9 Schematic of the NIVAMS tank to measure the radial displacement of the stationary fish swim bladder excited by low frequency stimulus (Roger and Cox, 1987).

2.3.2 Measuring Acoustical Properties of Resonant Bubbles Using a Small Tank

Measurements of the resonance properties of swim bladders based on the ring method (McCartney and Stubbs, 1971) permits researchers to study the sound scattering of swim bladder on different conditions. To some extent, the ring method is still a rather complicated solution for swim bladder resonance measurement. In order to reproduce this method, researchers have to perform experiments in open water like the sea (*e.g.*, McCartney and Stubbs, 1971) or deep quarries (*e.g.*, Sand and Hawkins, 1972). It is much more inconvenient and budget-costing to move all the measuring equipment and fish husbandry rigs onto an experimental ship and then use cranes and long cables to perform the trials in water. Since the swim bladder is well recognised as a model of a small, elongated soft shell enclosing an air cavity in water, it is essentially an encapsulated gas-filled bubble with higher damping (Leighton, 1994). Thus, it is worthwhile to revisit some of the projects about measuring the resonant properties of free or encapsulated bubbles using impedance tube or small tank systems.

Wilson *et al*., (2003) presented the design of a water-filled impedance tube capable of generating plane wanes and measuring the acoustic properties related to free bubble resonance. Later on, another method of measurement of bubble resonance was conducted by Argo and Wilson, (2008) to use a laser Doppler vibrometer (LDV) in a small tank. The result of LDV corresponded with the acoustical measurements and the free bubble model (Leighton *et al*., 2002).

Apart from free bubbles, the properties of encapsulated bubbles have also accumulated attention. Lee *et al*., (2011) started the research about using the resonance properties of large, encapsulated bubble arrays to attenuate undesirable low-frequency noise. For the purpose of measuring the resonance frequency and damping of tethered large encapsulated bubbles, Lee *et al*., (2012) developed a closed water-filled tank using the method of measuring the resonance properties of free bubbles in a tank by Leighton *et al*., (2002), and successfully measured and observed the resonance peak of the latex balloon, though the original tank resonance seemed to be shifted due to the presence of the encapsulated bubble. The schematic of the experimental apparatus is displayed in Figure 2.10.

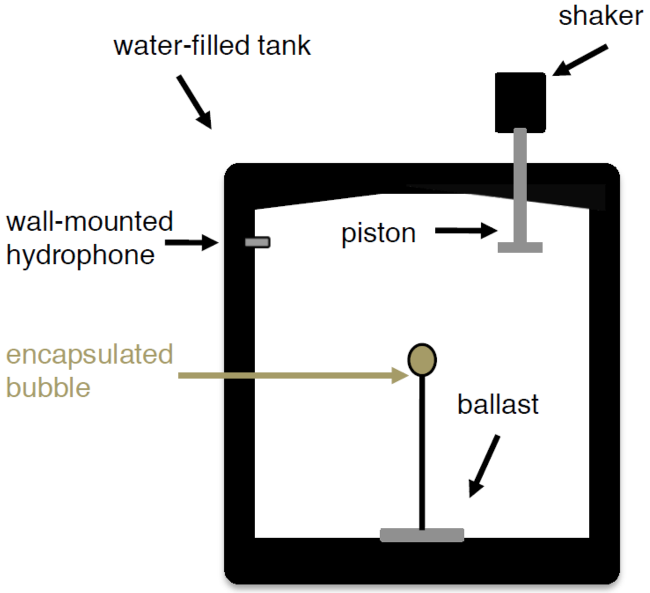

Figure 2.10 Schematic of the tank apparatus to measure the resonance properties of the stationary encapsulated bubble (Lee *et al*., 2012).

Latex balloons were also used as artificial fish swim bladders. Nero *et al.*, (2007) built arrays of artificial swim bladders to simulate the sound scattering of real fish schools. Since the swim bladder contributes most of the sound scattering of individual fish, arrays of artificial swim bladders with different spacing could be considered to be the dummy fish schools with different sparseness (Nero *et al.*, 2007).

2.3.3 Measuring Free Bubble Resonances in Controlled Laboratory Conditions

Apart from tank-based measurements on encapsulated bubbles, efforts on measuring free bubble resonance have also been made towards developments in the design of underwater acoustic metamaterials. While free bubbles in water exhibit well-characterised resonance behaviour, stabilising these bubbles for precise measurement remains a challenge due to buoyancy and gas dissolution effects. To address this, recent advances have explored encapsulated or framed bubbles, allowing for controlled observation of resonance phenomena.

A study by Harazi *et al.* (2019) introduced the concept of cubic bubbles, stabilised within 3D-printed frames. This novel design overcomes the spatial instability and dissolution issues associated with free bubbles by trapping gas within cubic geometries. The study demonstrated that each bubble face behaves as an individual oscillator, coupled to the others through both the gas inside and the surrounding liquid medium. The analytical and numerical models developed provided excellent agreement with experimental data, highlighting the utility of cubic bubbles as stable acoustic resonators. Their monopole-like acoustic emission, despite the non-spherical geometry, further established the potential for using framed bubbles in acoustic sensing and metamaterials.

Boughzala *et al.* (2021) extended this concept by investigating bubbles stabilised within the five Platonic solid frames—tetrahedron, cube, octahedron, dodecahedron, and icosahedron. The resonance frequencies of these polyhedral bubbles were found to closely approximate those predicted by the Minnaert formula (Eq. 1) for spherical bubbles of equivalent volume, with deviations of less than 10% (Minnaert, 1933). This result was unexpected given the non-spherical nature of the bubbles but was consistent across multiple frame geometries. The study also highlighted the scalability of this approach, enabling the creation of larger bubbles by increasing the number of faces while maintaining predictable resonance characteristics.

Further innovation was demonstrated by Alloul *et al.* (2022), who explored toroidal bubble resonance. Toroidal bubbles, constrained by 3D-printed ring-shaped frames, introduced a new degree of freedom in resonance tuning by varying the torus aspect ratio. The resonance frequency of toroidal bubbles increased significantly with larger aspect ratios, deviating by as much as 60% from the resonance frequency observed for spherical bubbles of the same volume

(Minnaert, 1933). This departure from spherical resonance characteristics opens new pathways for designing tuneable acoustic resonators by modifying the geometric parameters of the stabilising frame.

The collective findings from these studies underscore the versatility of encapsulated bubbles as platforms for measuring acoustic resonance properties. By embedding bubbles within geometrically diverse frames, researchers have effectively mitigated the limitations associated with free-floating bubbles, such as positional instability and gas dissolution. This methodology not only enhances the accuracy of acoustic measurements but also broadens the scope for studying resonance phenomena in a controlled and reproducible manner.

In practical terms, the use of small tanks and structured frames simplifies laboratory setups, eliminating the logistical challenges associated with open-water experiments. The ability to design and fabricate tailored frames using 3D printing further accelerates the development of novel resonators, allowing for rapid prototyping and iterative design improvements. Moreover, the results from polyhedral and toroidal bubbles provide a foundation for exploring more complex geometries and multi-bubble interactions, potentially leading to the next generation of acoustic metamaterials. The experimental set-up of measuring bubble resonances in controlled lab conditions also shed light on the better design of swim bladder resonance measurement.

2.3.4 Simulating Swim Bladder Resonance Using Finite Element Modelling

FEM has emerged as a tool for investigating the resonance properties of swim bladders, offering a cost-effective and controlled alternative to field experiments. This approach leverages computational simulations to explore the acoustic behaviour of swim bladders under various environmental conditions and anatomical configurations, reducing the need for complex open-water trials.

The earliest application of FEM in this area was conducted by Salas *et al*. (2018, 2019), who aimed to predict pressure sensitivity and resonance characteristics in larval red drum (*Sciaenops ocellatus*). By using micro-computed tomography (micro-CT) to capture detailed morphological data, they constructed 3D models of swim bladders and otoliths, simulating their response to acoustic plane waves. The study revealed that the air-filled swim bladder amplified otolith motion by a factor ranging from 57 to 3773 times compared to a water-filled bladder at 2000 Hz, underscoring the swim bladder's crucial role in enhancing auditory sensitivity. In a subsequent investigation, Salas *et al*. (2019) explored ontogenetic changes in swim bladder resonance. Their FEM simulations revealed that as the otolith-to-bladder distance increased with growth, the amplification of otolith motion decreased. However, the concurrent enlargement of swim bladder volume partially offset this effect, suggesting that swim bladder development is critical for maintaining auditory sensitivity during early life stages.

Expanding on the application of FEM to larger teleost species, Su *et al*. (2023) modelled the acoustic properties and call directivity of large yellow croaker (*Larimichthys crocea*). CT scans of the fish were used to reconstruct swim bladder geometries, enabling simulations that assessed the influence of bladder size and shape on acoustic radiation patterns. Notably, a 20% reduction in swim bladder size resulted in increased forward-directed sidelobes, emphasizing the structural role of the swim bladder in sound modulation.

Most recently, Li *et al*. (2024) investigated the contribution of swim bladders to hearing in crucian carp (*Carassius carassius*). By integrating AEP tests with numerical FEM simulations, the study provided further evidence of the swim bladder's role in sound reception. Micro-CT scanning and reconstruction of the fish anatomy allowed for the development of detailed models to simulate swim bladder motion in response to sound stimuli. Their findings demonstrated that intact swim bladders of crucian carps of similar sizes produced peak acoustic responses at around 826 Hz, significantly enhancing sound reception compared to deflated bladders. This study highlights the ability of FEM to capture frequency-dependent variations in auditory sensitivity.

In the context of swim bladder resonance, FEM not only provides a novel means to investigate acoustic properties but also facilitates parametric studies to evaluate the effects of bladder morphology, viscosity, and external pressure. This modelling approach continues to advance the understanding of fish bioacoustics, contributing to the broader field of marine mammal studies and underwater acoustics.

Therefore, this project is aiming to achieve truly non-invasive measurements of swim bladder resonance properties on live, free-swimming fish using a method inspired by measurements on free bubbles (Leighton *et al*., 2002) and encapsulated bubbles (Lee *et al*., 2012), with micro-CT aided FEM as the result validation (Salas *et al*., 2019; Li *et al*., 2024).

Chapter 3 Measurements of Swim Bladder Resonance Properties on Recently Euthanised Fish

3.1 Introduction

Efforts towards the measurement and application of the acoustic properties of fish swim bladders have been made in the past decades (McCartney and Stubbs, 1971; Cox and Rogers, 1987; Li *et al.*, 2024). The majority of related research mainly focused on developing the successful measurement of acoustic target strength of swim bladders of fish individuals and fish schools in deep and open water for fisheries biomass estimation. Information like fish size, quantity, and species of fish can be collected by commercial fishermen and marine biologists using broadband echo sounders, fish finders, and other fishery sonar systems. However, these methods and applications were developed to be used in free, far-field conditions, and for the purpose of the utilisation of fish as a natural resource or the better understanding of marine ecosystems.

The measurement and application of the acoustic properties of freshwater fish species are relatively underdeveloped due to the complexity of the acoustic environment of freshwater ecosystems like rivers, ponds, streams, and lakes. The free, far-field conditions of using fisheries sonar systems do not apply because of water depth, river width, and the complexity of the riverbed surface. Due to physical obstacles like shallow water low-frequency cut-off effect, multi-path reflections, and reverberation, it is extremely challenging to directly apply marine fishery sonar systems to detect or classify fish in rivers. However, some narrow beam high-frequency echo sounders and imaging sonars, also known as “acoustic cameras”, are capable of monitoring fish movement in freshwater ecosystems with limited working range (around 30 m) and very narrow beam angle (*e.g.*, 120 kHz and 7° for EK60, 1.8 MHz and 28.8° from 96 beams for DIDSON) (Patrick *et al.*, 2014). These acoustic cameras can only monitor a small area of interest, and do not measure fish swim bladder resonance properties.

The difficulties of achieving target detection and species classification using underwater acoustics in freshwater ecosystems like rivers do not mean that the resonance properties of fish swim bladders are useless in such circumstances. As was mentioned in Chapter 2, biologists and ecological engineers have made direct measurements of the motion of the resonating swim bladder wall to better understand the role of swim bladders in fish hearing. It has shown that the swim bladder has the ability to enhance fish hearing sensitivity to sound pressure, especially in species with the Weberian ossicles, leading to wider auditory bandwidth and a higher hearing sensitivity (Alexander, 1966; Vetter and Sisneros, 2020; Li *et al.*, 2024). For the purpose of better understanding the relationship between fish hearing and behavioural response and their swim bladders, the development of a method to measure the frequency response and resonance properties of fish swim bladders is key.

However, most of the previous methods of measuring the resonance properties of fish swim bladders have some limitations on the experimental set-up and requirements. Studies on the resonance re-radiation by swim bladders in fishes by McCartney and Stubbs (1971), Sand and Hawkins (1973), and Lovik and Hovem (1979) only took measurements on saltwater species far from the water surface (to avoid surface reflection) and require complicated experimental preparation and arrangement. Hence, it was not suitable for researchers to use this method to measure acoustical properties of freshwater fish in the lab, or during a field work. NIVAMS developed by Cox and Rogers (1987) was able to use ultrasound to determine the scattering sound field in a test tank, but the act of anesthetization of the target fish compromised the definition of “non-invasive measurement” due to the fact that the target fish were not in their natural living mode. It also suffered from the limitation of the ultrasonic monitoring as matching the swim bladder wall with the focal point requires a very high level of accuracy, and any accidental movement of the target fish will affect the result of the measurement significantly.

Salas *et al.*, (2019) and Li *et al.*, (2024) proposed the method of using CT scan to acquire an accurate 3D model of fish swim bladders, otoliths, and surrounding soft tissue, which was later used as the input to the numerical model for further FEM analysis. This method simulated the re-radiation field of resonating swim bladders and predicted the amplification of fish hearing when the swim bladder was excited by sound stimuli at the resonance frequency. However, this method could only provide a theoretical approach to simulating swim bladder resonance properties and the scattering fields instead of the ability to directly measure those properties on unanaesthetised, live, free-swimming fish in real life. Meanwhile, the act of CT scanning, on the one hand, increased the complexity of experimental procedures and, on the other hand, compromised the definition of a truly non-invasive method due to the requirement of anaesthesia or euthanasia for the test fish to keep steady during CT scanning. The CT-aided FEM method, however, would be a great validation tool to better support and validate the directly measured results from fish swim bladders.

Therefore, this thesis aimed to develop a novel method for the purpose of non-invasively measuring resonance frequencies and quality factors of naturally inflated swim bladders on live, free-swimming fish using a closed, water-filled test tank. Inspired by Leighton *et al.,* 2002 and Lee *et al.,* 2012, the proposed method only requires a relatively small and portable container that was capable of holding a living fish inside during the period of the measurement, which would also have the potential of being modified and brought to a biological field trip for fish biologists to capture, measure, and then release the fish back into the freshwater ecosystems like rivers, ponds, and lakes without anesthetising or euthanising the test fish.

3.2 Experimental Methodology

As a first approximation, the swim bladder is thought to scatter sound in the form of a resonant encapsulated air bubble. Since the wavelength of sound at the resonance frequency of the swim bladder is much greater (about 100 times) than any characteristic length of the swim bladder, the swim bladder responds to the oscillations of acoustic pressure by uniform volume contraction and expansion, scattering sound energy in all directions regardless of the incident angle of the sound excitation (Weston, 1967; Cox and Rogers, 1987).

3.2.1 Free Bubble Resonance

The resonance of a gas-filled bubble excited by sound waves in water has been a fundamental concept in underwater acoustics for decades (Leighton, 1994). When a sound wave encounters a bubble, the rapid fluctuations in pressure cause the bubble to expand and contract. At a particular frequency, known as the resonance frequency or natural frequency, these radial oscillations of the bubble wall will reach a maximum amplitude, scattering the highest sound energy omnidirectionally. The underlying physics can be approximated by considering the bubble as a simple harmonic oscillator, with the compressible gas acting as a “spring” and the inertia of the surrounding fluid acting as the “mass.”

For a free spherical ideal gas bubble in a liquid, Minnaert (1933) derived an approximate formula, also known as Minnaert Equation, for the resonance frequency. Assuming that the bubble radius is much smaller than the acoustic wavelength and that the oscillations are sufficiently rapid for the gas within to behave adiabatically, the resonance frequency, f_0, of an ideal bubble of the radius, a, is given by:

$$f_0 = \frac{1}{2\pi a}\sqrt{\frac{3\gamma P_{b0}}{\rho_w}} \tag{1}$$

where γ is the specific heat ratio of the gas, ρ_w is the density of the surrounding medium, and $P_{b0} = P_0(z)$ is the static ambient pressure, which is the hydrostatic pressure, $P_0(z)$, at the depth of the bubble, z (Minnaert, 1933). For a single bubble in water at standard pressure (P_{b0} = 100 kPa, ρ_w = 1000 kg/m^3) , this equation reduces to $f_0 \cdot a \approx 3.26$ m / s. This implies smaller bubbles resonate at higher frequencies, while larger bubbles resonate at lower frequencies. The pressure at depth also affects resonance: higher static ambient pressure increases the bubble's stiffness and thus raises the resonance frequency.

Realistic bubble behaviour deviates from the idealized theory due to factors such as non-sphericity, dissolved gases, and surface contamination, but the Minnaert approximation remains a useful first-order estimate. Damping mechanisms, such as viscous losses in the fluid, thermal exchanges at the bubble interface, and acoustic radiation of energy, affect the sharpness of the resonance peak, which could be generally characterised by the quality factor (Q-factor). Lower damping results in a narrower, more pronounced resonance peak in the frequency domain, while a higher damping broadens the peak and reduces its amplitude.

Damping can be characterised through the dimensionless damping constant, δ. For a bubble, this damping coefficient contains three frequency dependent terms,

$$\delta \approx \delta_{\mathrm{rad}} + \delta_{\mathrm{visc}} + \delta_{\mathrm{th}} = ka + \frac{4\mu}{\rho\omega a^2} + \frac{P_{b0}}{\rho\omega a^2}\operatorname{Im}\phi, \tag{2}$$

radiation damping, δ_{rad}, which accounts for energy loss through the re-radiation of sound, viscous damping, δ_{visc}, due to viscous dissipation in the medium surrounding the bubble, and thermal damping, δ_{th}, resulting from the loss of heat to the medium as the bubble expands and contracts (Leighton, 1994). In this treatment, $k = \omega / c$ is the wave number and assumed to satisfy $k \cdot a \ll 1$, while $\omega = 2\pi f$ is the angular frequency. The thermal effects are described by the complex valued function ϕ, whose real part gives the effective polytropic index $\gamma_{eff} = \operatorname{Re}(\phi / 3)$ in terms of the ratio of the specific heats, and the thermal diffusivity D of the bubble gas:

$$\begin{aligned} \phi &= \frac{3\gamma}{1 - 3(\gamma - 1)i\chi[(i/\chi)^{1/2}\coth(i/\chi)^{1/2} - 1]}, \\ \chi &= \frac{D}{\omega a_0^2}. \end{aligned} \tag{3}$$

3.2.2 Experimental Set-up

The main difference between a free air bubble and a swim bladder is that the swim bladder has an isinglass wall and is surrounded by fish soft tissue. The wall and the surrounding tissue have a certain elasticity and viscosity, which will greatly increase the damping of the swim bladder resonance, resulting in a lowering of the quality factor.

The other difference from free resonant bubbles is that swim bladders are usually elongated, meaning the resonance frequency of the swim bladder also depends on the eccentricity parameter ε, which increases the resonance frequency compared to an equivalent spherical bubble (Leighton, 1994). Other than the effect of the surrounding fish tissue and the geometric elongation, the contribution of the swim bladder to the scattering characteristics of an individual fish is assumed to be equivalent to air bubbles.

This method, discussed in detail in Chapter 4 and inspired by the experiments carried out by Leighton *et al.*, (2002) on free bubbles, and Lee *et al.*, (2012) on large, encapsulated bubbles, was developed for the purpose of measuring the resonance frequency and the damping factor of swim bladder on freshwater fish. The goal is to achieve non-invasive measurements on live, free-swimming fish without the need for anesthetisation or physical constraints. Before designing a bespoke system, a series of preliminary experiments were carried out on dummy swim bladders (small, inflated latex balloons) and recently euthanised fish using a pre-existing stainless-steel impedance tube. It is not practical, or ethical to test live fish in this set-up, but it serves to develop understanding and inform later designs.

The closed, water-filled impedance tube had an inner diameter of 0.1 m, a length of 1 m, and a wall thickness of 1 cm. Both ends of the tube were sealed by 2 mm thick stainless-steel plates on which an inertial shaker was mounted and transmitted sound waves into the water. On each end, the steel plates were bolted by eight M10 bolts between the flange of the tube and the 2.5 cm thick removable steel lid. Various ports and attachments were machined onto the tube and the lid to permit the insertion of shakers and hydrophones and allow the tube to be filled with water. Once the tube was completely full of water, all openings could be sealed so that the tube was closed. Special care should be given during the water-filling process: no bubbles or air pockets should be left within the tube and the water body. Since this experiment was performed to detect and measure the frequency response of the target bubble within the water, any unexpected existence of other bubbles or air pockets would compromise the result of the measurement. Therefore, the impedance tube was tilted multiple times during the filling process to expel air through an outlet port prior to every measurement, as is shown in Figure 3.1.

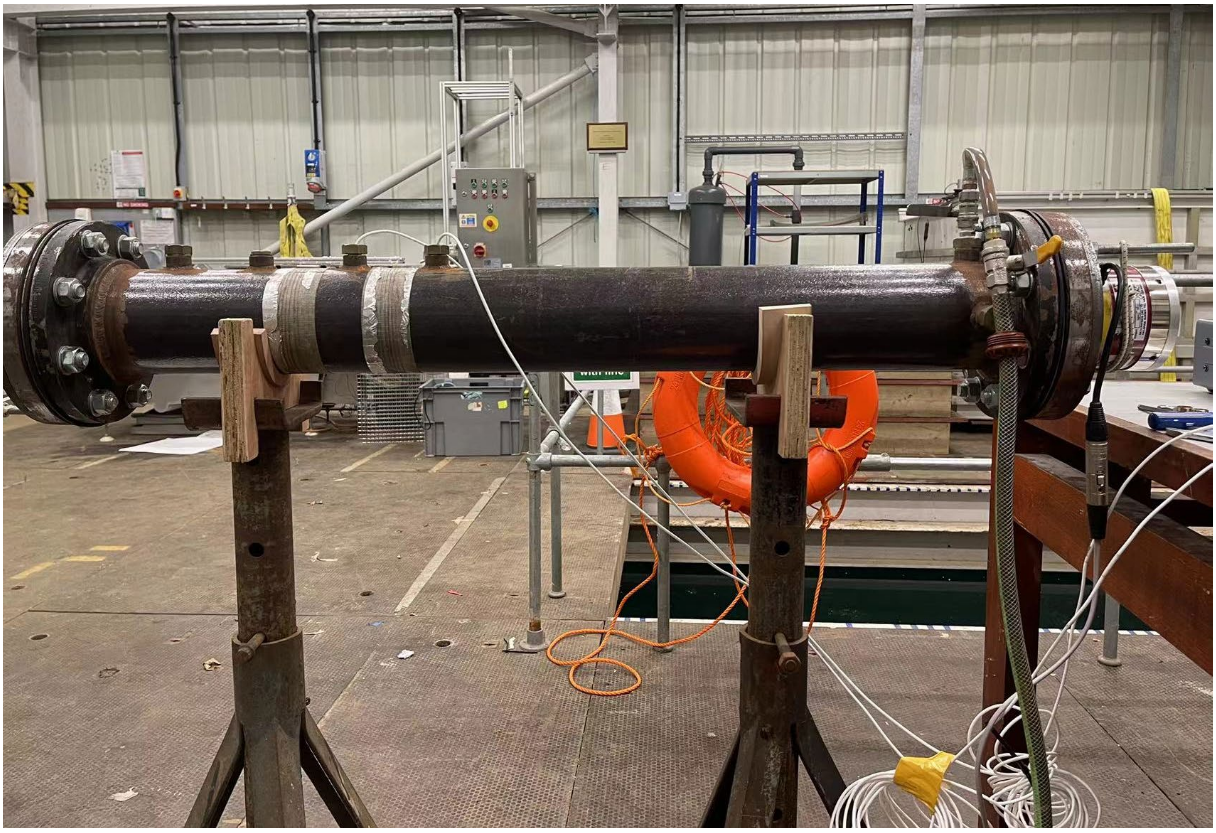

Figure 3.1 Photo of the pre-existing stainless-steel impedance tube.

Apart from the impedance tube, the set-up also consisted of two subsystems linked by computer control: white noise generation and signal collection. The final experimental configuration is shown in Figure 3.2.

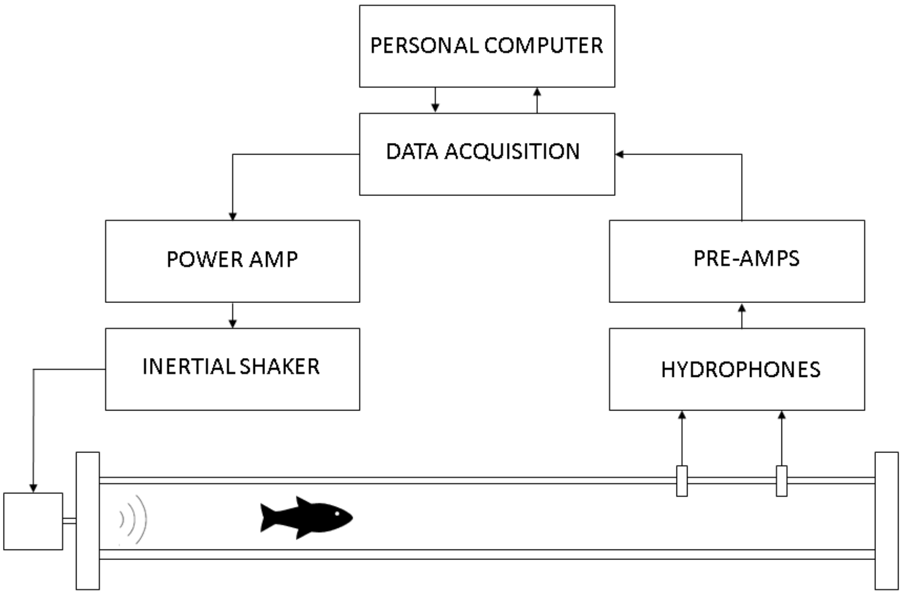

Figure 3.2 A schematic of the experimental apparatus, approximately to scale. The impedance tube had an internal diameter of 10 cm and a total length of 1 m. The target was placed inside the water-filled tube and was excited by the inertial shaker.

A DataPhysics GW-IV45 inertial shaker with a maximum sine force of 50 N and an inertial mass of 4.2 kg was used to as the sound source to excite the system and was mounted on the 2 mm thick steel plate with a specially designed adapter to transmit sound energy into the water body inside the impedance tube. For most of the measurements, a band-limited pseudorandom white noise signal was generated by a DELL PRECISION 7550 running MATLAB R2020a and was sent from a National Instrument (NI) USB-6361 data acquisition (DAQ) to a DataPhysics PA30E power amplifier, which provided the amplified driving signal for the shaker. The pressure signal arising from the acoustic field inside of the tube was then measured using a pair of wall-mounted Bruel & Kjaer 8103 hydrophones with a sensitivity of -211dB re 1V/µPa, and the signal was conditioned by RESON EC 6081 mk2 VP2000 preamplifier. The hydrophones were mounted on the machined ports at the top of the tube (approximately 10 cm and 20 cm from the steel plate furthest from the shaker). As the input signal to the inertial shaker, the excitation signal, $x(t)$, was generated in MATLAB as a 100-second duration white noise sequence, sampled at 4000 Hz, providing a bandwidth up to the Nyquist frequency of 2000 Hz. Based on the size of the encapsulated bubbles and fish swim bladders examined in this chapter, their estimated resonance frequencies were in the range of 90-500 Hz, thus the measurement and analysis of the received signals were set to be below 2000 Hz, and the sampling rate for the DAQ was set to be 4000 Hz.

With the acoustic excitation on, the pressure signals measured by the hydrophone, $y_{total}\left(t\right)$, can be considered as the superposition of two primary contributions: the intrinsic acoustic field inside the tube when no bubble is present (denoted as the empty tube condition), and the acoustic field scattered by the bubble within the tube:

$$y_{total}\left(t\right) = y_{tube}\left(t\right) + \hat{y}_{bubble}\left(t\right) \tag{4}$$

where $y_{tube}\left(t\right)$ is the signal that is recorded in the absence of a bubble but only water filling the impedance tube, which is defined here as the empty tube condition for the convenience of terminology; and $\hat{y}_{bubble}\left(t\right)$ is the estimated signal arising from the acoustic field generated by scattering from the bubble. As the measurement of the hydrophone signal from the empty tube, $y_{tube}\left(t\right)$, and the tube with the bubble inside, $y_{total}\left(t\right)$ is much easier to be achieved than the scattering signal from only the bubble, the field scattered by the bubble can be estimated by the difference of the two measurable quantities:

$$\hat{y}_{bubble}\left(t\right) = y_{total}\left(t\right) - y_{tube}\left(t\right). \tag{5}$$

Initially, it was assumed, following the method described by Leighton *et al.*, (2002), that the scattered acoustic signal from the bubble could be estimated by a straightforward subtraction of the signal measured with the bubble present, $y_{total}(t)$, by the empty tube condition, $y_{tube}(t)$. However, further investigation revealed that the presence of the bubble significantly modified the original frequency response of the tube itself. Consequently, the simple subtraction method yielded a residual signal contaminated by artifacts due to shifts in the resonance modes of the tube induced by bubble presence, necessitating a more robust frequency domain analysis.

To rigorously characterise the tube system's frequency response, the recorded hydrophone signals were processed using Welch's method to compute both the power spectral density (PSD) and the transfer function (TF). Welch's method involves dividing the signal into multiple overlapping segments to reduce variance and enhance spectral reliability. Specifically, the sampled signals, recorded at a rate of 4000 Hz (thus allowing accurate frequency resolution up to 2000 Hz, according to the Nyquist criterion), were segmented into overlapping windows, each containing 1024 samples (corresponding to a duration of 0.256 seconds). A Hann window function was applied to each segment to minimise spectral leakage by smoothly tapering the data at the segment boundaries. The segments overlapped by 50%, equivalent to 512 samples, thus ensuring sufficient frequency resolution and statistical reliability.

In theory, the PSD was calculated by first obtaining the autocorrelation function of the measured signal, *y*(*t*), followed by computing its Fourier transform:

$$S_Y(f) = \mathscr{F}[R_Y(\tau)] = \int_{-\infty}^{\infty} R_Y(\tau) e^{-j2\pi f\tau} d\tau, \qquad (6)$$

where $R_Y(\tau)$ is the autocorrelation function of *y*(*t*), and $\mathscr{F}(x)$ stands for the Fourier transform;

In practice, each windowed segment underwent a Fast Fourier Transform (FFT) of length 2048 points, yielding a spectral resolution of approximately 1.95 Hz per frequency bin. Because each data segment contains only 1024 real samples, the remaining 1024 points supplied to the FFT are zeros—*i.e.*, each segment is zero-padded by a factor of two. Zero padding does not add new information to the spectrum; it simply interpolates between the discrete frequency bins that would otherwise be spaced at 3.91 Hz (4000 Hz / 1024). The denser 1.95 Hz bin spacing improves the legibility of narrow resonance peaks and facilitates a more precise visual comparison of spectra recorded under different conditions. In this study the same padded length was used for the cross- and auto-spectral density calculations, so the transfer-function estimate benefited from the identical interpolated frequency grid. The PSD estimate was then computed by averaging the squared magnitude of the FFT from each segment:

$$\hat{S}_Y(f) = \frac{1}{MU}\sum_{k=1}^{M}\left|Y_k(f)\right|^2 \tag{7}$$

where $Y_k(f)$ is the FFT of the k^{th} windowed segment of the measured signal, M is the total number of segments, and U is a normalisation factor based on window power.

Simultaneously, the transfer function, $\hat{H}(f)$, characterising the system's frequency-dependent behaviour, was computed from the ratio of the cross-power spectral density between the input excitation and hydrophone output signals, $\hat{S}_{xy}(f)$, to the auto-power spectral density of the input excitation signal, $\hat{S}_{xx}(f)$:

$$\hat{H}(f) = \frac{\hat{S}_{xy}(f)}{\hat{S}_{xx}(f)}. \tag{8}$$

The cross-power and auto-power spectral densities, $\hat{S}_{xy}(f)$ and $\hat{S}_{xx}(f)$, respectively, were consistently estimated using Welch's method, employing the same parameters of segmentation, windowing, overlap, and FFT length as used in the PSD calculation. This consistency ensured coherence between PSD results and transfer function estimations.

The PSD method provides valuable insights into how signal power is distributed across the frequency spectrum, making it effective in identifying dominant frequency components and overall noise characteristics of the measured signals, $y(t)$. However, PSD estimates alone cannot explicitly distinguish system behaviour from input excitation characteristics. In contrast, the transfer function method offers a clearer representation of the intrinsic system dynamics by effectively normalising the output signal, $y(t)$, against the input excitation, $x(t)$. Thus, the transfer function method is particularly advantageous for identifying resonance features related specifically to the resonant bubbles or biological objects like swim bladders within the impedance tube. The use of TF enhances the interpretability of resonance data by clearly separating the system response from input signal influences, thereby providing a more accurate and robust method for detecting and analysing the resonance frequencies of encapsulated bubbles or fish swim bladders.

3.3 Experimental Measurements

Three parts of the measurement were performed under different experimental conditions in order to achieve a more comprehensive understanding of the method: the tube filled with water only, the tube with a balloon, and the tube with a recently euthanised fish.

3.3.1 The Empty Tube

The impedance tube was filled with tap water and bubble expelled by tilting the tube. Ball valves of the water inlet and outlet were later closed after the water-filling and air-expelling. 100 s white noise signal generated by MATLAB was used as the input to the DAQ and signals received by hydrophones were recorded and saved as .mat files in the computer. The power spectral density was calculated and plotted in MATLAB. Figure 3.3 shows the power spectral level of the empty tube below 1 kHz.

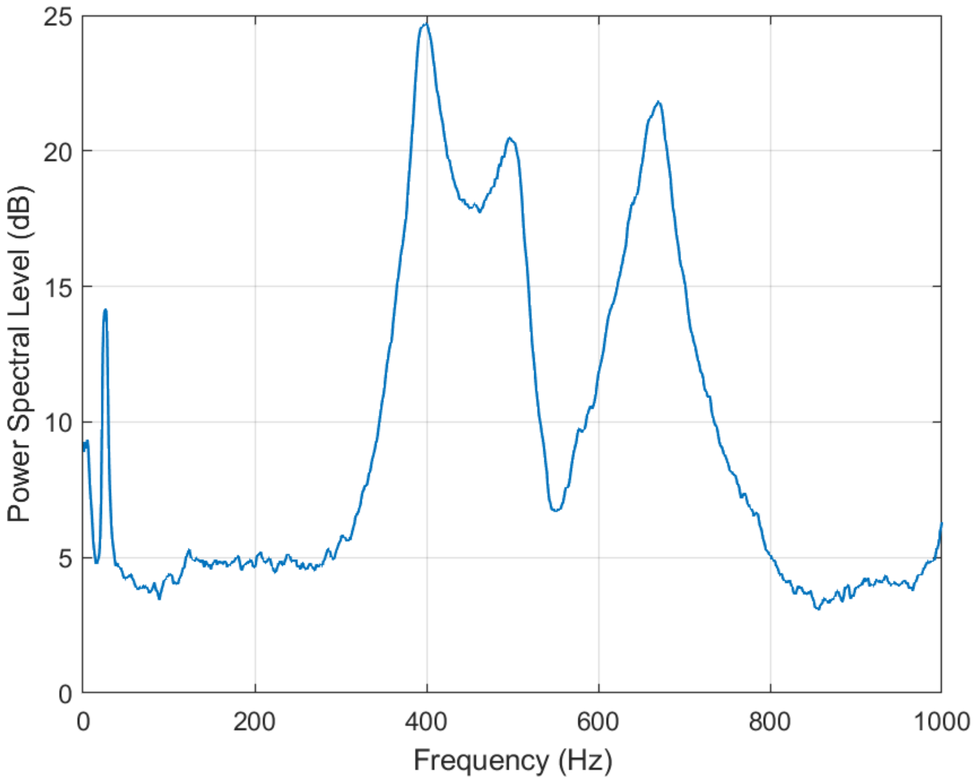

Figure 3.3 Power spectral density of the signal recorded in the empty tube.

Four significant resonance peaks can be observed in Figure 3.3. The first one at 26 Hz is very sharp and is due to the spring-mass resonance of the inertial shaker, and this mechanical resonance would appear in all results. The other three resonance peaks were visible at around 400 Hz, 500 Hz, and 670 Hz. These resonance frequencies were not close to the normal modes that one would expect for a closed rigid tube based on the theory of the propagation of plane sound waves in tubes:

$$f_n = \frac{n}{2}\frac{c}{L} \tag{9}$$

where *n* is the mode number, *c* is the sound speed in water, and *L* is the length of the water column.

For this tube, Eq. (9) predicts resonances at 750 Hz and 1500 Hz, assuming *c* = 1480 m/s. The first measured resonance at 400 Hz had a wavelength of 3.7 m, corresponding to about four times the tube length. In theory, the quarter wavelength resonance would happen in a tube that was closed at one end and open at the other. In this experiment, the tube was closed at both ends with 2 mm thick steel plates that did not sufficiently represent rigid boundaries, and one of them was mounted with an inertial shaker acting as the sound source, resulting in a semi-open resonator with a mode at the quarter wavelength. The other possibility could be because of the change of sound speed in the impedance tube. However, the speed of propagation of pressure waves in elastic tubes might change in certain conditions. Hence, the sound speed in the water-filled stainless-steel impedance tube was recalculated using the Moens-Korteweg formula:

$$c_{Korteweg} = \frac{c}{\sqrt{1+\frac{K}{E}\frac{D_P}{e}}}, \tag{10}$$

where *c* is the sound speed for water at room temperature, D is the pipe diameter, e for pipe wall thickness, E is the Young's modulus of elasticity for steel, K is the bulk modulus of steel (Moens, 1877; Korteweg, 1878).

The sound speed is 1428 m/s, and 3.5% lower than the original sound speed, which was not sufficient enough to explain the longer wavelength associated with the first measured tube resonance.

A possible explanation is that the original modes of the steel plate that served as a steel diaphragm transforming the kinetic energy of the inertial shaker to sound energy into the impedance tube. However, the impedance tube was not designed and manufactured specially for this project, so using the 3D model of the impedance tube to simulate its modal response in FEM was not done for these preliminary tests. However, for a better understanding of the tank frequency response and the original modes, FEM was performed during the designing process of the acrylic test tank before manufacture, which will be further addressed in the next chapter.

The resonance peaks of the empty tube condition stayed at the same frequencies with the same amplitude after multiple repeated measurements throughout the experiments. The empty tube frequency response was measured as part of each experiment and so was seen to be repeatable. The observed tube resonance frequencies were consistent throughout the experiment. Therefore, the tube response shown in Figure 3.3 was used as the baseline frequency response curve for the empty tube condition in further analysis.

3.3.2 Inflated Latex Balloon

A second measurement employed small latex balloons as a proxy for swim bladders demonstrating the estimation of resonance properties. Figure 3.4 is the photo of a test balloon with a 4.8 cm diameter, several balloons of different sizes were tested and got consistent results, but this section only presents the result of a 6.8 cm diameter balloon. A latex balloon was inflated to a diameter of 6.8 cm and placed into the impedance tube before filling the tube completely with water. Initially, the balloon was floating freely in the water and would have been in contact with the upper tube wall due to its buoyancy. Several tests were performed trying to tether the balloon to fix its position, but the results showed no significant difference between the free-floating and tethered conditions.

Figure 3.4 Photo of an inflated balloon with a diameter of 4.8 cm.

The volume of an ideal spherical bubble is given by

$$V_0 = \frac{4\pi}{3} a_0^{\ 3} \tag{11}$$

where a_0 is the radius of the bubble.

As the approximation of an encapsulated air bubble, the shell thickness of the test balloon was 0.2 mm, whose resonance frequency would not be significantly different from the ideal bubble (Church, 1995; Lee *et al.*, 2014). Thus, the resonance frequency of a test balloon with a radius of 3.4 cm was estimated to be f_{balloon} = 96 Hz according to the Minnaert equation.

The power spectral density of the closed impedance tube with an inflated latex balloon inside was calculated from the recorded signal, which was collected following the same experimental procedure as that of the empty tube. Figure 3.5 presents the power spectral density of the tube with a balloon, and together with the power spectral density of the empty tube.

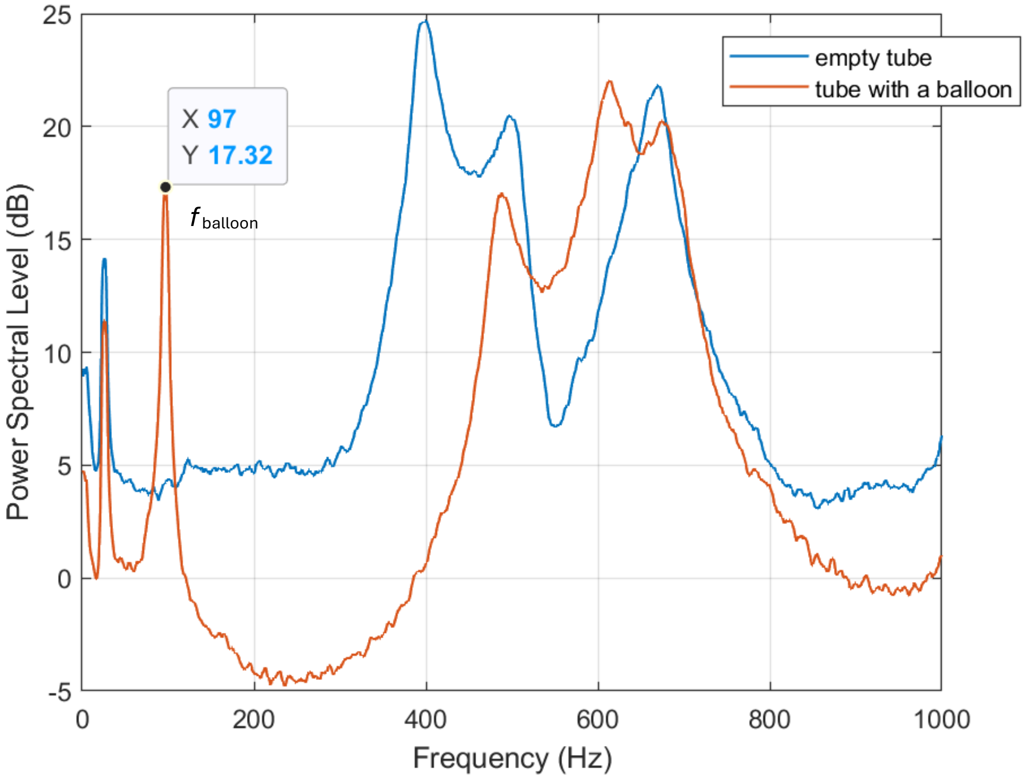

Figure 3.5 Power spectral density level of recorded signals of the water-filled impedance tube with (orange) and without an inflated balloon present (blue).

When the balloon was present in the water-filled impedance tube, a very sharp resonance peak developed in the spectrum near 100 Hz, distinct from the original frequency response curve of the empty tube. The resonance frequency corresponds to the frequency at which the maximum amplitude occurs, which in this case was f_{balloon} = 97 Hz, very close to the predicted value of 96 Hz based on the Minnaert equation (Eq. 1). The quality factor *Q* of the bubble is found by determining the bandwidth of the resonance peak at half-power (also known as the 3dB bandwidth), denoted *Δf*, and dividing the resonance frequency by this amount:

$$Q = \frac{f_0}{\Delta f}. \tag{12}$$

The quality factor is approximately equivalent to the number of cycles required for an oscillator to reach the steady state, and it is proportional to the inverse of the bubble's damping at resonance (Leighton, 2002). For the example shown in Figure 3.5, the quality factor was $Q_{balloon}$ = 22.3, indicating the balloon resonance was lightly damped.

Measurements were typically made at frequencies, *i.e.* below 300 Hz, the lowest impedance tube resonance in a flat region of the acoustic pressure spectrum to minimize tube reverberation effects that are associated with the bubble being in an enclosed space. Reverberation is greatest near the test container resonances and can modify the bubble resonance frequency and damping from their free-field values due to enhanced loading on the bubble by the reverberant field (Leighton *et al.*, 2002; Lee *et al.*, 2012).

Apart from the resonance peak of the balloon, some other changes in the overall power spectral density can be observed in Figure 3.5. The first one is that the original resonance frequencies of the empty tube have shifted to higher frequencies. This is especially apparent at the first resonance originally at 400 Hz. The second change is that the amplitude distribution of the power spectral density has been modified due to the introduction of the air-filled latex balloon. It could be observed that the power spectral level of the signals below 500 Hz was clearly lower than those of the original empty tube spectrum. The frequency shift and the amplitude reduction might indicate a significant dispersion and attenuation because the individual balloon resonance frequency resided within the data collection frequency range. This matter will be further discussed in the next section.

The measurements on the tube with an inflated balloon have demonstrated that this method is successful in estimating the resonance properties of lightly damped encapsulated bubbles. However, the fish soft tissue surrounding the gas-filled swim bladder was known to add significant damping to the swim bladder, resulting in a lower resonance amplitude and a broader peak width, which would make it harder to be detected in the spectra compared to lightly damped bubbles.

3.3.3 Recently Euthanised Fish

The next stage in the development of the method was experiments on recently euthanised fish which were conducted to ensure that this method could detect the highly damped resonance of real swim bladders contained in the fish body using the same experimental method. Moreover, it avoided unnecessary and unethical pilot trials to be performed on live fish. The performance of these trials would also contribute to the better design of future experimental arrangement and manufacture of the custom-made test tank.

The study species used in this experiment was the brown trout (*Salmo trutta*). In Spring 2022, 18 brown trout, previously used for another experiment at International Centre of Ecohydraulics

Research, were divided into three groups and euthanised before the measurement under the approval of the University of Southampton's Animal Welfare and Ethical Review Board. Considering the potential deflation of the swim bladders after death, all specimens were euthanised within 30 minutes before the measurement as the impedance tube method could only measure one fish at a time. The fork length of each fish was taken and noted, as is shown in Figure 3.6, and the mean body length L_{fish} *was* 22.1 ± 2.1 cm. The estimated body weight m_{fish} based on the empirical weight length conversion for brown trout was 117 ± 12 g.

Figure 3.6 Measurement of the fork length of a brown trout.

After each measurement, every fish was dissected to examine the intactness and inflation of swim bladders. The characteristic dimensions of the swim bladders were measured for the estimation of the volume of the air cavity, as shown in Figure 3.7.

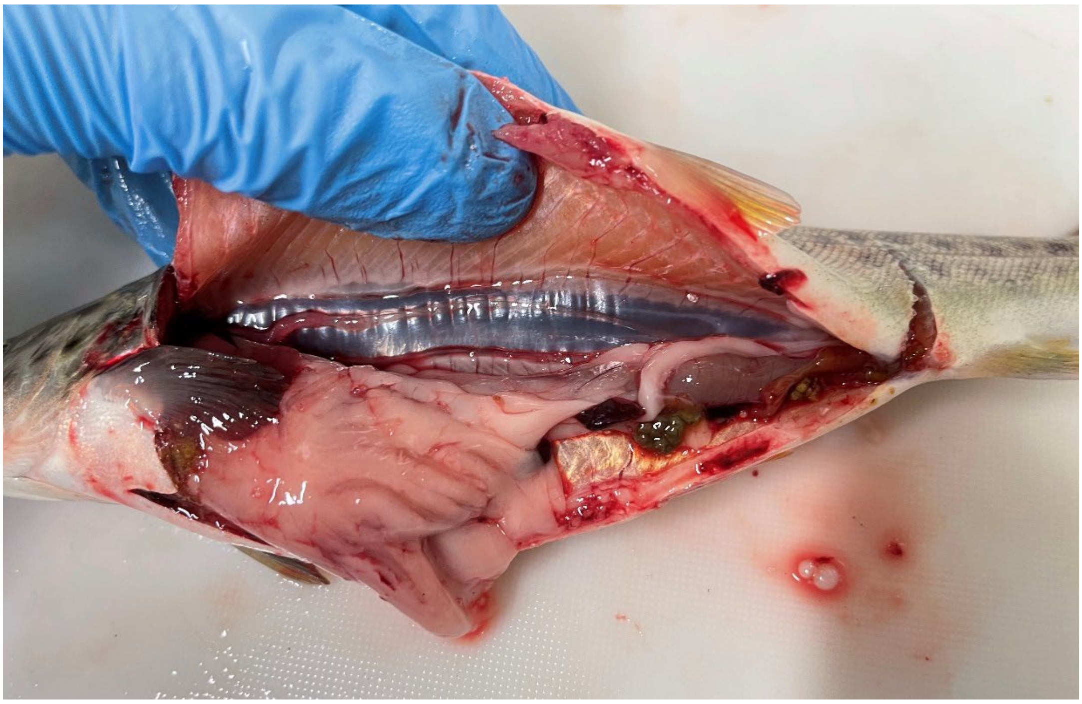

Figure 3.7 Examination of the intactness of the swim bladder.

Unlike some other species like the goldfish and the crucian carp that had their swim bladder divided into two chambers, the form of the brown trout's swim bladder is a single camber in a cigar shape, which would be expected to have a higher eccentricity value and a high overall resonance frequency, with a mean air cavity volume of V_{sb} = 8.7 mL and an equivalent spherical bubble radius of a_{sb} = 1.26 cm (Cox and Rogers, 1987).

Despite the shape and eccentricity value of the swim bladder of brown trout, the spherical scattering assumption was again used since the wavelength at the resonance frequency was much longer (50 to 100 times) than any one of the characteristic dimensions of the swim bladder, hence the prolate spheroid was expected to act as a viscously damped single degree of freedom spring-mass-damper system and scatter the incident sound energy into all directions equally.

The estimated resonance frequency calculated from Minnaert equation based on the equivalent spherical bubble radius of the fish swim bladder was 258.5 Hz. However, as mentioned above, fish swim bladders were usually elongated: the resonance frequency of an elongated air bubble can be approximately given by:

$$f_{elongated} = \frac{x(\varepsilon)}{2\pi a_{equivalent}} \sqrt{\frac{3\gamma_{eff} p_0}{\rho_w}} = x(\varepsilon) f_0 \qquad (13)$$

where $a_{\mathrm{equivalent}}$ is the equivalent equilibrium spherical bubble radius, $x(\varepsilon)$ is the resonance frequency correction factor due to bubble elongation, and $\varepsilon = a_b / a_a$ is the bubble eccentricity parameter to describe its geometry with a_b being the minor axis length of the ellipsoid and a_c

being the major axis length (Weston, 1967; Cox and Rogers, 1987). This formula carried the same approximations as Minnaert's result for ideal gas bubbles and neglects the effects of bladder wall tension as well as Y_{eff}, the frequency-dependent effective polytropic exponent of the bubble gas cyclically undergoing compression and rarefactions. However, for typical equivalent spherical bubbles, changes of state in the swim bladder gas will, except for a small thermal boundary layer, be adiabatic and the well-known value for diatomic gases $\gamma_{eff} \approx \gamma \approx 1.4$ was chosen.

Because of its elongated shape, the resonance frequency of the swim bladder would be higher than that of an equivalent spherical bubble. The resonance frequency correction factor due to the elongation could be calculated, by (Strassberg, 1953):

$$x(\varepsilon) = \varepsilon^{-1/3}(1-\varepsilon^2)^{1/4}\log^{-1/2}(\frac{1+\sqrt{1-\varepsilon^2}}{\varepsilon}). \qquad (14)$$

The resonance frequency of the swim bladder of a 22.3 cm long recently euthanised brown trout with an equivalent spherical bubble radius of 1.34 cm and an eccentricity parameter of 0.124 is estimated to be 302.3 Hz according to the elongated bubble model (Equation (13) and (14)).

The experimental procedure of the frequency response measurement of the tube with a recently euthanised fish inside was basically the same as that of the latex balloon. Data were taken under the excitation of the same 100-second band-limited white noise signal following the same protocol for previous measurements performed under the empty tube condition and the tube with a balloon condition. The power spectral density of the received signal from the measurement of the test fish in Figure 3.4 was computed and presented in Figure 3.8.

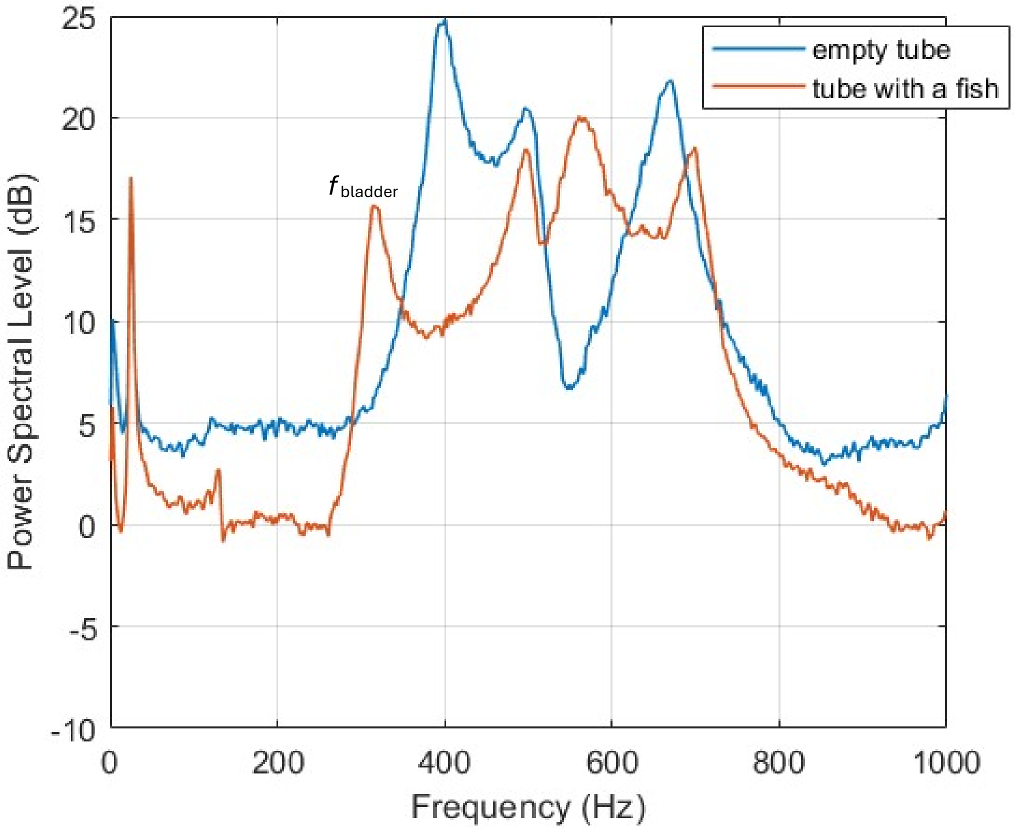

Figure 3.8 Power spectral density of the signal recorded with a 22.3 cm recently euthanised brown trout in the tube.

The measured resonance frequency of the swim bladder f_{bladder} was 316 Hz, and the quality factor Q_{bladder} of this resonance was 9.7. The difference between the measured and the estimated resonance frequency of the swim bladder is 4.3%. The speculation for such an error there could be that the swim bladder is not an ellipsoid, and that the measurements of swim bladder dimensions had errors. Moreover, in this experiment, the swim bladder had an isinglass bladder wall and was surrounded by fish soft tissue. The wall and the soft tissue had elasticity levels, which would consequently raise the pressure of the gas in the swim bladder and make the swim bladder stiffer so that the swim bladder resonant frequency might increase (Weston, 1967). Hence, the difference between the estimated and measured value was considered to be normal and as expected, similar differences have been reported in previous research (Weston, 1967; McCartney and Stubbs, 1971; Love, 1978; Cox and Rogers, 1987).

The quality value $Q_{\text{bladder}} = 9.7$ was lower than the quality value of the latex balloon $Q_{\text{bladder}} = 22.3$, indicating a much higher damping for the swim bladder resonance than the latex balloon resonance, which was again as we expected. However, the quality value of the swim bladder here $Q_{\text{bladder}} = 9.7$ was noticeably higher than the estimated or measured quality values in some previous research, which ranged between 3 to 6 (McCartney and Stubbs, 1971; Cox and Rogers, 1987). There were three possible factors that might cause the higher quality factor that was measured in this experiment. Firstly, the swim bladder resonated at 316 Hz, which was near the lowest original tube resonance. According to Leighton *et al.* (2002) and Lee *et al.* (2012), reverberation would reach the greatest level near the test tank resonances and could change the bubble resonance frequency and damping behaviour from their original values when in free-field due to the enhanced pressure loading on the bubble wall by the reverberant field (Leighton *et al.*, 2002; Lee *et al.*, 2012). Leighton *et al*. (2002) discovered an increase of up to 60% for the quality factor of free bubbles at frequencies close to the tank resonance frequency. Lee *et al.* (2012) found that the reverberation effect on the measured bubble resonance frequency was small and could be neglected (about 1% for encapsulated bubbles), while quantifying the reverberant loading effects on the bubble's damping was more difficult, and it was suggested that a reasonable solution was to have the individual bubble resonance frequency to be well below the first tank resonance to avoid reverberation loading (Lee *et al.*, 2012).

The second factor that might cause the increase in Q_{bladder} lay upon the close distance between the tube wall and the bubble, as a proper mass loading of the bubble by the immediately surrounding layer of fluid would require a separation distance of several bubble radii between the bubble and the tank wall, and the measured damping coefficient could be altered from the original value when the condition was violated. The effect of this factor would need further analysis by taking the limited internal diameter of the impedance tube into consideration, which was beyond the scope of the current work of this project. However, the proper mass loading could be achieved by making the test tank bigger, thus, the bubble within the test tank could stay further away from the tank wall, resulting in a more accurate measurement of Q_{bladder}.

The third possible factor was that the euthanasia of the test fish might relax the surrounding fish soft tissues and therefore decrease the surface tension of the swim bladder wall, resulting in a less damped resonance and a higher measured quality factor on the dead fish than the live fish. This factor could also be avoided by building a specially designed, fish-friendly test tank that was capable of holding a live and free-swimming test fish inside during the measurement.

A frequency shift and an amplitude decrease of the original tube resonances were also observed in Figure 3.8, which agreed with the measured frequency response of the tube with a balloon in Section 3.3.2. Figure 3.9 presented the power spectral density of all three conditions, showing a similar frequency shift and an attenuation of the original tube resonances, which could be caused by the presence of the swim bladder and the latex in the water body.

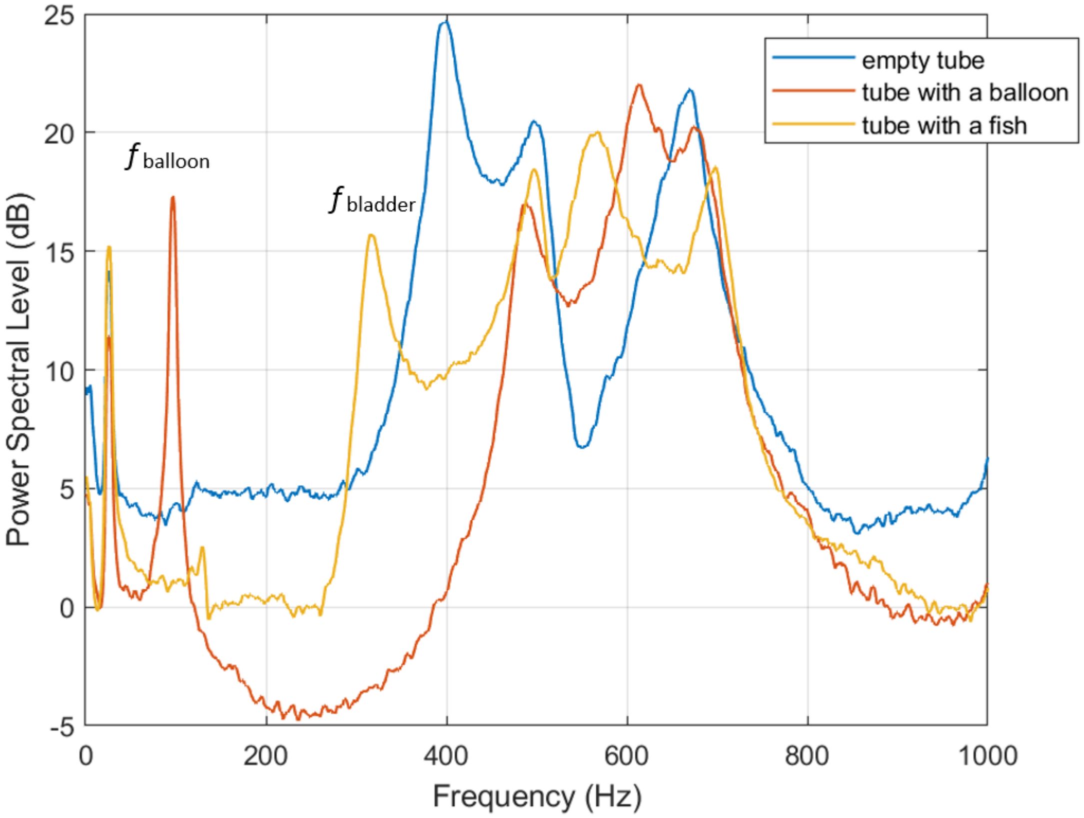

Figure 3.9 Power spectral density level of signals recorded in the impedance tube filled with only water (blue), water with a latex balloon (orange), and water with a recently euthanised fish inside the tube (yellow).

More results of power spectral density levels of measured signals from different test fishes with similar body lengths are presented in Figure 3.10 and Figure 3.11. Resonance peaks of their swim bladders appeared at around 300 Hz, but the amplitude of different swim bladder resonances varied slightly potentially because of their body conditions (*e.g.* muscle strength), and positions in the tube during measurement (*e.g.* mass loading). The displacement and attenuation of the original tube resonances due to the presence of swim bladders also differed slightly from each other but remained under the same tendency of shifting the lowest tube resonance to a higher frequency and decreasing the amplitude of the resonance peak for 5 to 10 dB. The first and second tube resonances were shifted closer and merged as they were close in the frequency domain.

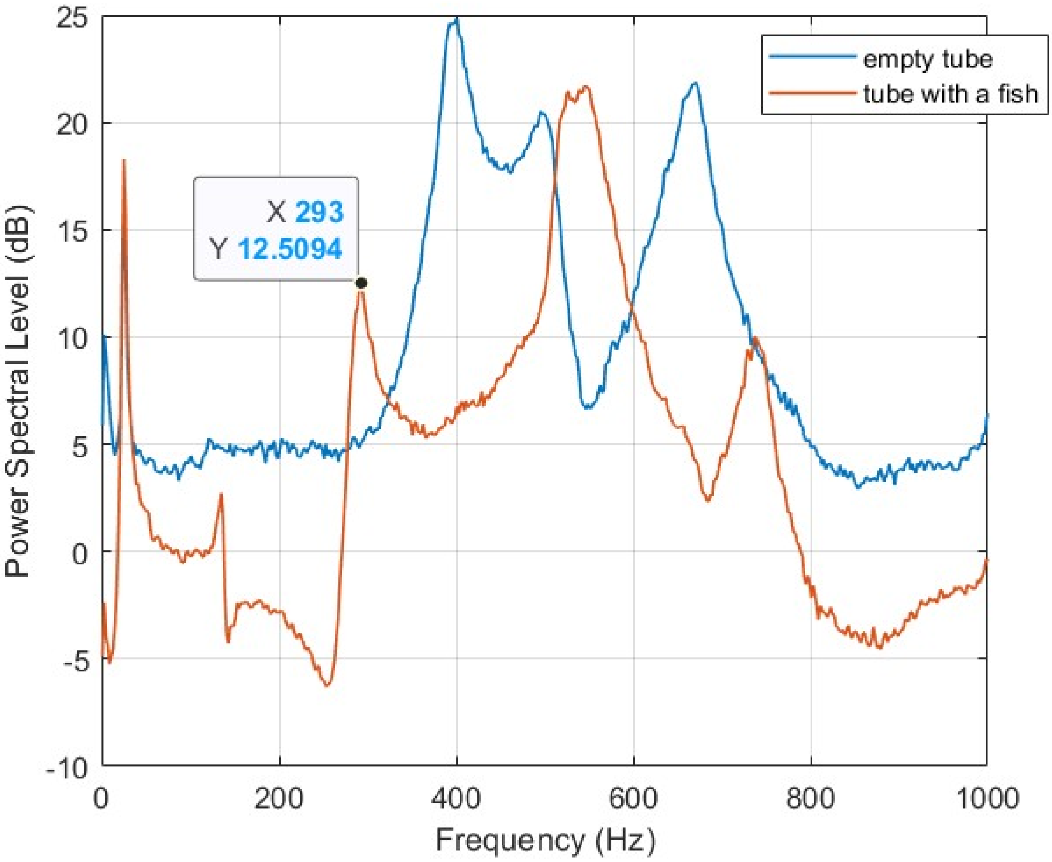

Figure 3.10 Power spectral density of the signal recorded with a 21 cm recently euthanised brown trout in the tube, $f_{bladder}$ = 294 Hz and $Q_{bladder}$ = 11.7.

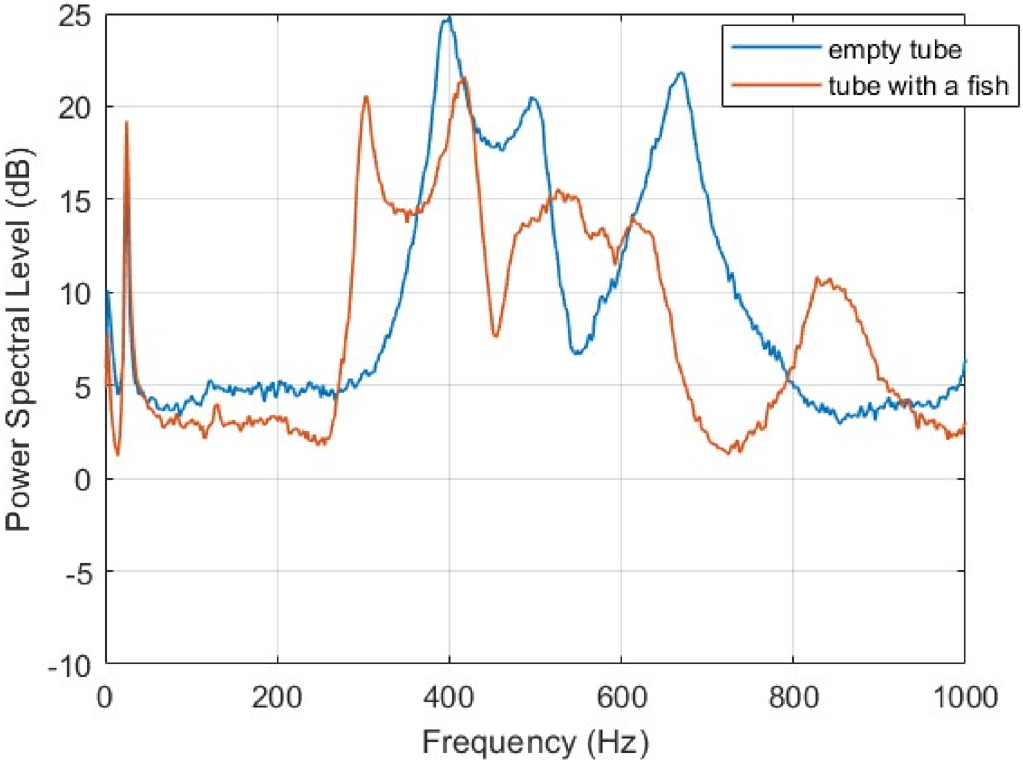

Figure 3.11 Power spectral density of the signal recorded with an 18.2 cm recently euthanised brown trout in the tube, $f_{bladder}$ = 305 Hz and $Q_{bladder}$ = 12.7.

The measured resonance frequencies and quality factors versus the body length of all 18 fish are plotted in Figure 3.12 and Figure 3.13. The original empirical model $f_0 = 7232 / L$ for estimating the resonance frequency of swim bladders of saltwater species by (Lovik and Hovem, 1979) has been modified for the freshwater species based on the difference of swim bladder to fish body volume ratio. It is because that freshwater species tend to have bigger swim bladders (8% of fish body volume) than saltwater species (5% of fish body volume), resulting in a lower swim bladder resonance frequency in freshwater species (Bone and Moore, 2008). In general, a bigger fish would have a bigger swim bladder and consequently a lower resonance frequency, while the quality factor does not change significantly with the body length. The modified empirical model for the estimation of swim bladder resonance frequency for freshwater species is $f_0 = 5983 / L$.

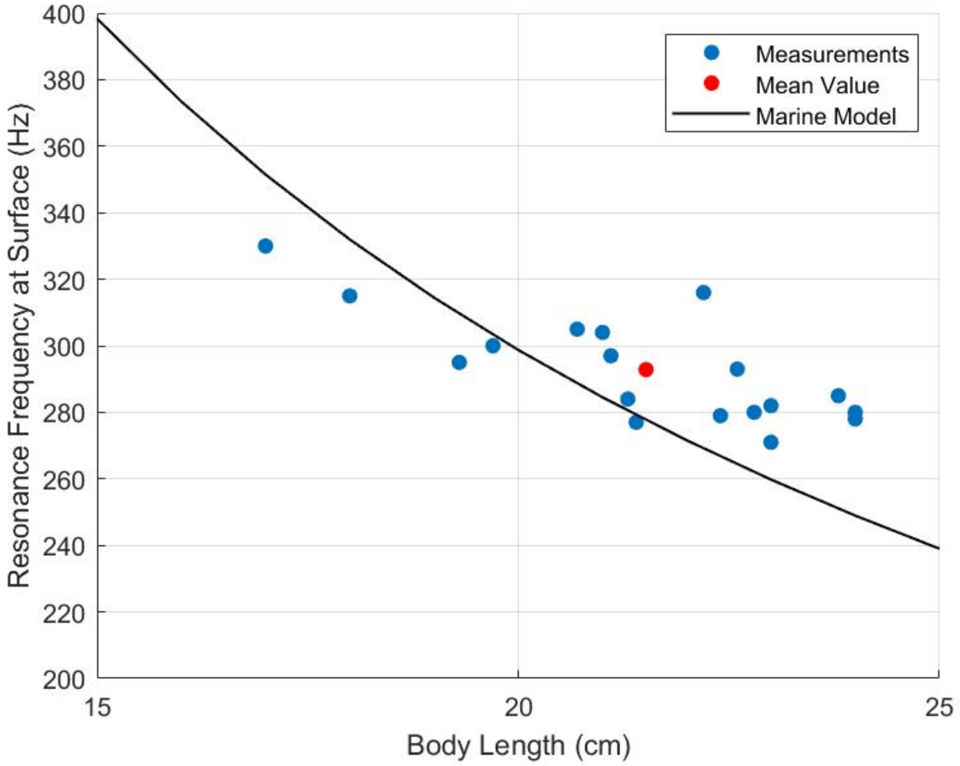

Figure 3.12 Measured swim bladder resonance frequency vs. fish body length in euthanised brown trout, the solid black curve represents the modified marine model for freshwater fish.

In Figure 3.13, there is no clear relationship between the fish body length and the quality factor of their swim bladder resonance, which is as expected based on results from previous studies (Cox and Rogers, 1987). The quality factor of live fish may be different than euthanised ones as factors like muscle tension can change due to the act of euthanasia, same for unhealthy ones with swim bladder diseases when compared to healthy fishes. Therefore, a truly non-invasive measuring method on live fish will be discussed in the next chapter.

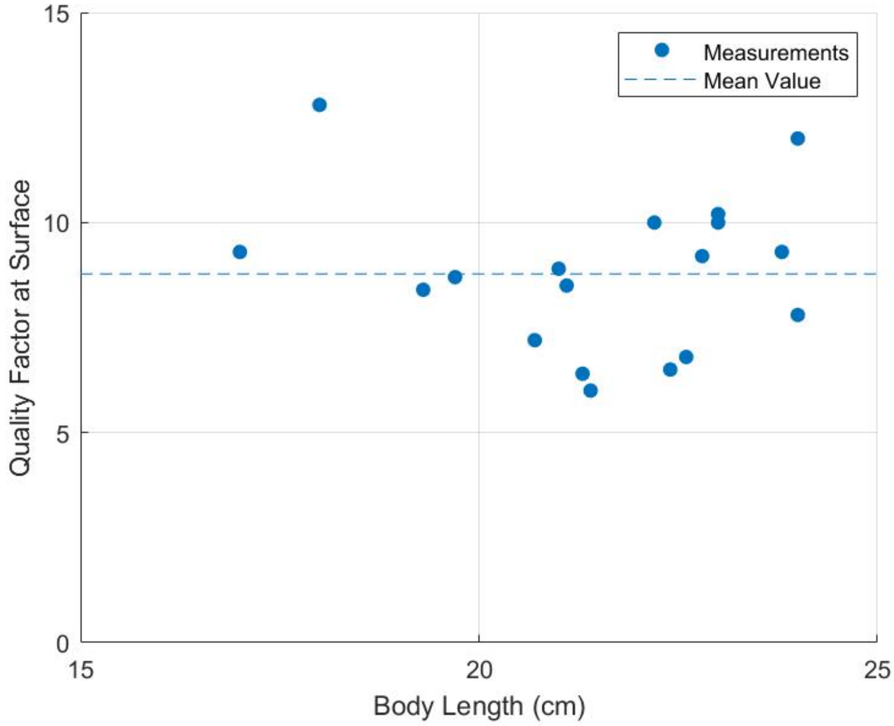

Figure 3.13 Measured quality factor vs. fish body length in euthanised brown trout, the dashed line represents the mean value of measured quality factors of fish swim bladders.

3.4 Validation of Measured Results Using Finite Element Modelling

FEM has become one of the most powerful and versatile numerical tools available for solving a broad range of physical problems, including structural mechanics, fluid dynamics, and, crucially, acoustics. The method is particularly suited to scenarios where analytic solutions are either impractical or impossible, due to complex geometries, multiple physical interactions, or intricate boundary conditions. By subdividing the domain of interest into smaller, simpler elements, FEM allows the governing partial differential equations to be discretised and solved numerically. Over the past few decades, rapidly increasing computational power, along with the continual refinement of modelling software, has facilitated the use of FEM for problems of growing sophistication, including the simulation of acoustic waves in fluids and solids or even complex multi-physics coupling problems under realistic conditions.

In acoustics, FEM is generally employed to model the propagation of sound waves through media with complex boundaries or material properties. Such applications might involve the characterisation of reverberation in an oddly shaped concert hall, the study of acoustic transducers, or even the propagation of seismic waves in the Earth's subsurface. Within underwater acoustics, FEM methods have proven particularly valuable, as they enable researchers and engineers to account for a variety of interactions that occur when sound travels through water, reflects off structures, or penetrates and reverberates within biological tissues and other complex bodies. Traditional analytical approaches to underwater acoustics often rely on far-field or plane-wave approximations that may lose accuracy whenever the geometry becomes complicated or when near-field phenomena and multiple scattering paths are significant. FEM, however, is well equipped to capture both local and global effects, even when physical details, such as curvilinear shapes or elastic boundaries, are essential to the solution.

Amongst the broad landscape of available simulation platforms, COMSOL Multiphysics has emerged as a widely adopted software environment for FEM-based studies in acoustics and vibration studies. The Acoustics Module in COMSOL Multiphysics supports numerous formulations suitable for both frequency-domain and time-domain analysis. Users can, for example, specify acoustic pressure as the primary variable within a domain representing water or air, while simultaneously coupling it to structural equations governing an elastic or viscoelastic object immersed in the same environment.

COMSOL's multiphysics coupling capabilities made it possible to incorporate additional complexities, such as the elasticity of fish swim bladder walls or the fluid-structure interface between water and the tank wall, all within a single unified framework. This is especially beneficial when studying encapsulated bubble resonance phenomena, where the mechanical properties of an object are intimately linked to its acoustic response. Traditional analytic models are quite efficient for simpler scenarios, like plane waves scattering from an ideal spherical target, yet the real world often presents significantly more intricate geometries and boundary conditions. Fish swim bladders, as was mentioned before, are rarely spherical but often in species-specific shapes. FEM provides a more direct route: the geometry of an object, like a swim bladder, can be discretised into a mesh of small elements and be assigned with specific material properties: density, speed of sound, Young's modulus, etc. By solving the set of equations that govern acoustic pressure in the fluid and structural displacements in the solid, FEM naturally captures wave reflections, refractions, mode conversions, structure-acoustic interactions, and even bubble resonance effects. Hence, FEM is capable of computing the exact patterns of pressure scattering and distribution when a bubble was excited at specific frequencies, enhancing our understanding of its resonance behaviour, acoustic scattering characteristics, and potential implications for fish hearing.

Bubble resonance can be highly sensitive to shape, boundary conditions, and interactions with surrounding structures—features which an idealised bubble-in-infinite-water model may neglect. FEM is uniquely suited to incorporating these complexities, whether the shape is derived from measurements, CT scans, or other advanced imaging techniques. By implementing a realistic 3D geometry of the swim bladder and surrounding tissues, the researcher can systematically evaluate changes in resonance characteristics under different assumptions of boundary interactions, elasticity, or external excitations.

3.4.1 Inflated Latex Balloon – FEM Simulation

All FEM numerical simulation projects in this thesis were performed on COMSOL Multiphysics (version 6.1, Stockholm, Sweden) in the 3D object interface. An FEM model of a latex balloon in free-field conditions was constructed as part of the validation of the model. Firstly, a 0.5 m radius sphere of water was constructed as the computing domain. Secondly, a 3.4 cm radius sphere of air (the same size as the latex rubber balloon measured in 3.3.2) was constructed and placed at the centre of the computing domain. For the purpose of simulating encapsulated gas bubble resonance in water, both *Pressure Acoustics, Frequency Domain* module, and *Structural Mechanics (Shell)* module were used for the simulation. *Pressure Acoustics, Frequency Domain* module was capable of solving pressure acoustics problems, like calculating the transfer function of bubble scattering field, within or across the acoustic wave propagation medium in the frequency domain. *Structural Mechanics (Shell)* module was used to define and represent the mechanical behaviour of the air-water boundary (balloon wall or swim bladder wall). *Structural Mechanics (Shell)* module could also be substituted by *Solid Mechanics* module under *Structural Mechanics* as both modules could define the property of the air-water boundary and contribute to the solution of structure-acoustic coupling problem (Salas *et al*., 2019; Su *et al*., 2024). However, *Structural Mechanics (Shell)* module was selected against *Solid Mechanics* for the calculation of encapsulated bubble wall characteristics at resonance because of the speed of computation. The way that *Solid Mechanics* solved bubble wall resonance behaviour required the user to build a geometric shell with a thickness of around 0.2 mm, which would later be meshed to a very fine resolution before the final computation of the transfer function. The high level of resolution in this case, however, significantly increased the burden of both the 3D model construction and finite element computation. *Structural Mechanics (Shell)*, did not necessarily require a thin, extremely finely meshed geometric shell as it was able to directly define the characteristics of the air-water boundary, like elastic material properties, damping factor, and layer thickness, speeding up the computation process of FEM. Simulations were performed in COMSOL to compare the simulated results under the same project set-up, no difference was observed other than the computational speed of *Solid Mechanics* being slower than *Structural Mechanics (Shell)*. *Therefore*, *Pressure Acoustics, Frequency Domain* was applied to the air domain of the balloon, and the water domain surrounding the latex balloon, whereas *Structural Mechanics (Shell)* was applied to the air-water boundary between the latex balloon domain and the surrounding water domain. Since the simulation needed to capture the coupling effect (*i.e.*, how the acoustic pressures drive structural deformations and vice versa), *Acoustic-Structure Boundary* module was added to the FEM project for the coupling of *Pressure Acoustics, Frequency Domain,* and *Structural Mechanics (Shell)*.

Apart from choosing multiphysics modules, material properties were also defined carefully. Three types of material were included in this simulation: water surrounding the balloon, air inside the balloon, and latex rubber making the wall of the balloon. For water, standard density (1000 kg/m^3) and speed of sound (1480 m/s) were assigned for further simulation; for air, the density was defined to be 1.204 kg/m^3, and the speed of sound was 343 m/s. For the latex rubber making the balloon wall, three properties were defined in *Structural Mechanics (Shell)* as a linear elastic material: density (950 kg/m^3), Young's modulus (2 MPa), and Poisson's ratio (0.49). The thickness of the latex rubber balloon wall was defined to be 0.2 mm as measured.

Following the assignment of modules, coupling boundary, and material properties, a monopole source in *Pressure Acoustics, Frequency Domain* was set as the excitation source, and placed 20 cm beneath the inflated latex ballon. The latex balloon wall was considered solid material, in which vibrations were solved using *Structural Mechanics (Shell)* and *Acoustic-Structure Boundary*. Wave propagation in an inhomogeneous fluid medium can be computed using the wave equation:

$$\frac{1}{\rho_0 c^2{}_S}\frac{\partial^2 p}{\partial t^2}+\nabla\cdot\left(-\frac{1}{\rho}\nabla p\right)=Q_m, \tag{15}$$

where ρ_0 and c_S represent the static density and sound speed of the medium, respectively. p represents the dynamic sound pressure after the source is induced to radiate sounds, and ρ is the resulting variable density in the medium. The initial sound source Q_m is given as a point source in the form of

$$Q_m=\frac{4\pi}{\rho_0}S\partial\left(x-x_0\right), \tag{16}$$

Where S has a form of

$$S=e^{j\phi}\frac{i\omega\rho_0 Q_S}{4\pi}, \tag{17}$$

and Q_S give the volume flow rate from the source at $x=x_0$, which was set to be 0.0001 m^3/s.

To couple the interaction between the fluid and solid media, the pressure continuity condition should satisfy $F_p=-\vec{n}\cdot p$, where F_p is the pressure load on the boundary, p is the pressure, and

$\vec{n}$ is the normal vector. To minimise boundary reflection, the radiation condition was set as spherical spreading allowing a further propagation of waves with minimal reflections. The outer boundary of the computation water domain was defined as perfectly matched layers (PMLs) to approximate an unbounded free domain with all incident acoustic waves absorbed at the outer boundary.

Meshing strategy was set as free tetrahedral with a sufficiently fine physics-controlled mesh resolution, which was much shorter than the acoustic wavelength at the highest frequency of interest in this simulation. The frequency was swept from 10 to 1000 Hz with a step of 10 Hz, all physics modules were solved for. Figure 3.14 showed the setting of the numerical model containing sound stimuli, water domain, and the latex air-filled balloon.

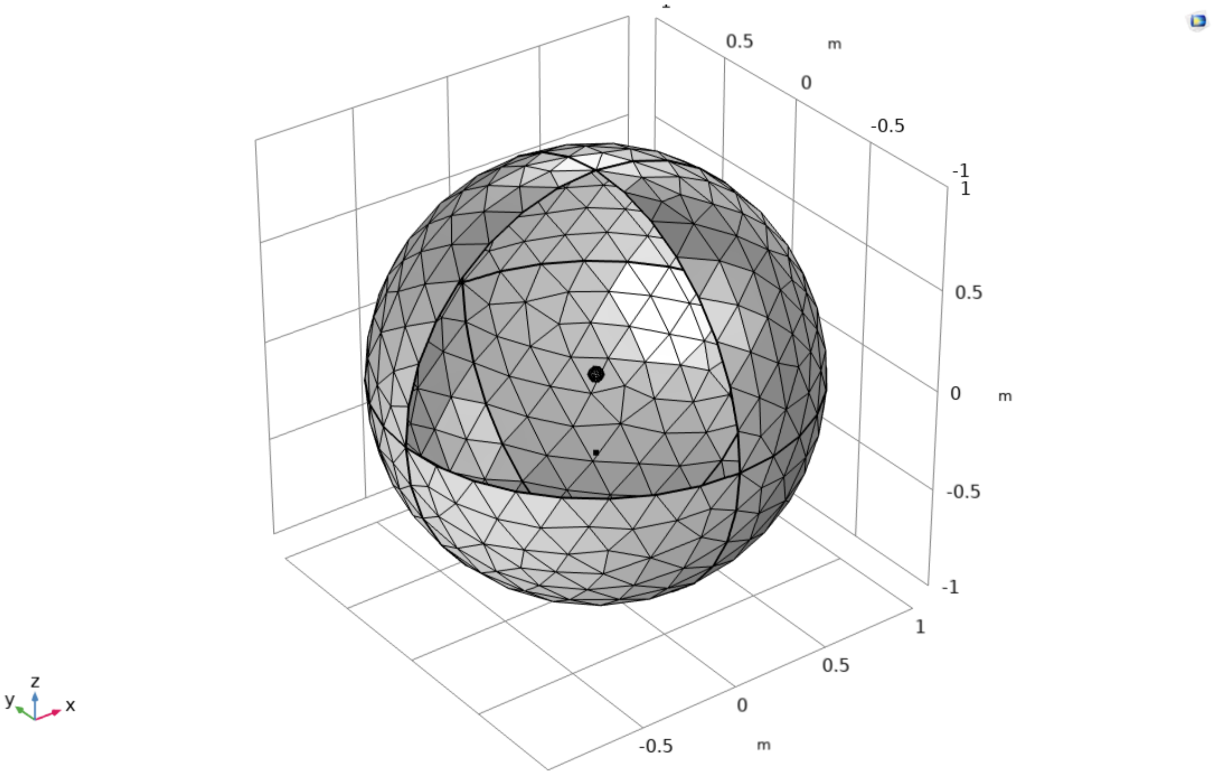

Figure 3.14 FEM model set-up containing the water domain (surrounding sphere), the latex air-filled balloon (small sphere at the centre), and the sound stimuli (black point under the balloon).

The SPLrms distribution on the latex balloon, and the transfer function of the balloon surface pressure were calculated by COMSOL and presented as follows:

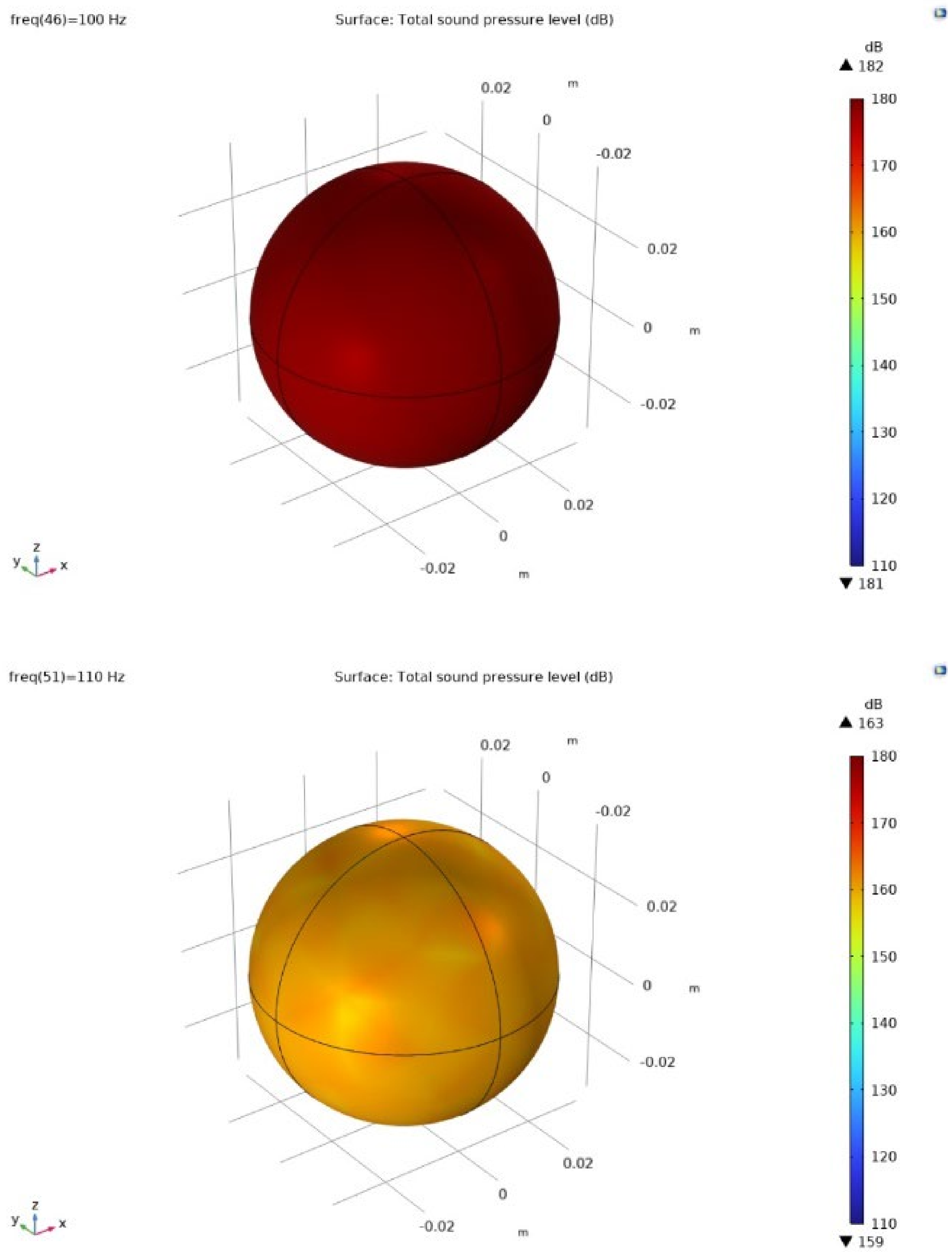

Figure 3.15 Comparison of simulated sound pressure field of the latex balloon at the test frequency of 100 Hz (resonance frequency) and 110 Hz.

Figure 3.15 shows the simulated sound pressure distribution of the latex balloon at 100 Hz (resonance frequency) and 110 Hz, and an ununiform near-resonance pressure distribution pattern on the balloon surface can be observed at 110 Hz whereas the overall pressure distribution for 100 Hz is uniform. The frequency response of latex balloon surface sound pressure was calculated as the transfer function from the excitation signal out of the monopole being the input signal, as in Figure 3.16. The resonance peak at 100 Hz was sharp and tall, representing the lightly damped (due to viscosity and radiation damping) resonance of the latex balloon when excited by pure tone sound stimuli, which was anticipated based on the result of our real-life measurements.

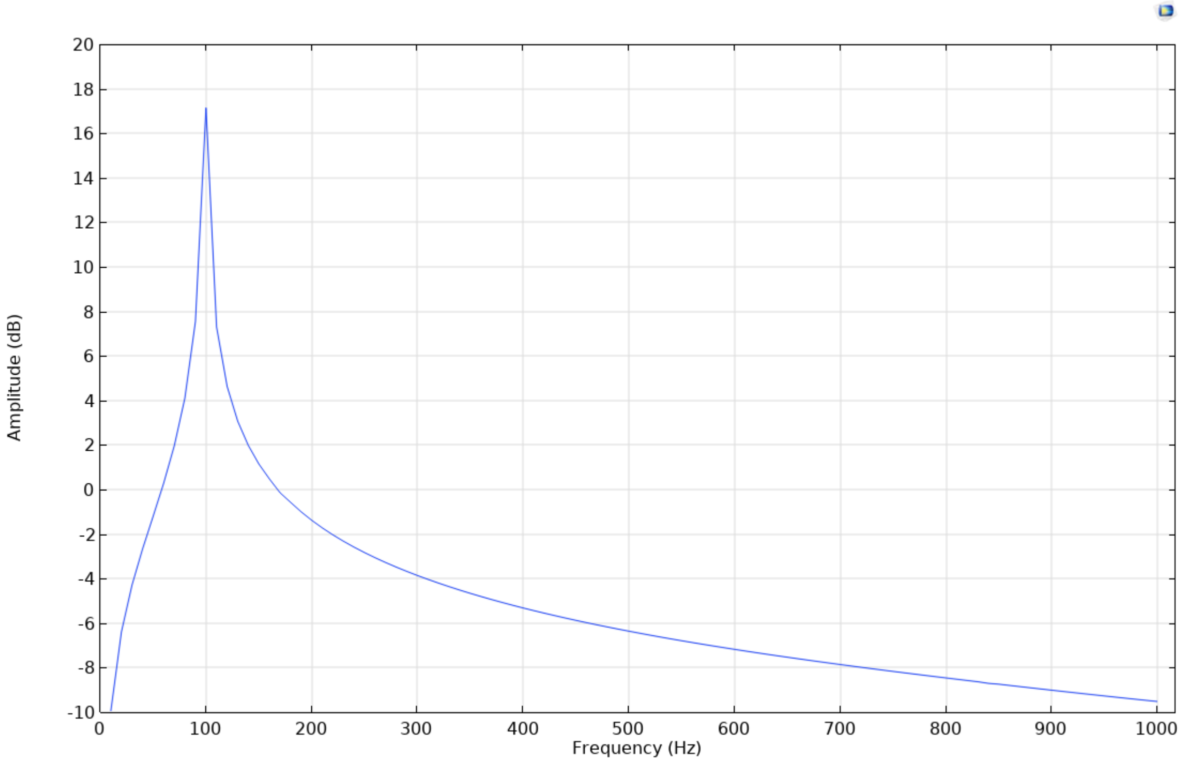

Figure 3.16 Frequency response (transfer function) of sound pressure in the latex balloon.

To better compare and validate the measured result and simulated result, the transfer function computed by FEM was plotted in the same figure with the measured transfer function of the impedance tube that was previously shown in Figure 3.5 of Subsection 3.3.2. Figure 3.17 compares the transfer function of the latex balloon measured experimentally (solid blue line) with the simulated FEM model (dashed orange line). Both curves exhibit a prominent resonance peak near 100 Hz, indicating strong agreement between the measured and modelled results in predicting the resonance frequency of the balloon.

One noticeable difference is the slight frequency shift observed in the FEM simulation (100 Hz), where the resonance frequency appears marginally higher than the measured peak (97 Hz). This discrepancy likely arises from the pre-defined frequency resolution (step length) of the FEM study being 10 Hz, in which condition the 3 Hz difference lies within the error tolerance. Simplifications in the model geometry or material properties might also contribute to the difference between them, but considering the key result being the resonance frequency, which is highly dependent on the volume of the air cavity, such tiny deviations from real-life properties were considered to be unavoidable but negligible. Additionally, the measured TF consists of other resonance peaks, which, as discussed before, were because of the mechanical resonance of the inertial shaker and the shifted first resonance of the impedance tube, whereas the result of FEM represented balloon resonance only as the surrounding PML created a free-field condition.

Despite these differences, the overall alignment of the bubble resonance peaks underscores the validity of the FEM approach in capturing the dominant acoustic characteristics of the air-filled latex balloon. This agreement reinforces the potential for using FEM to simulate, predict and validate the measured resonance properties of more complicated bubble structures like fish swim bladders.

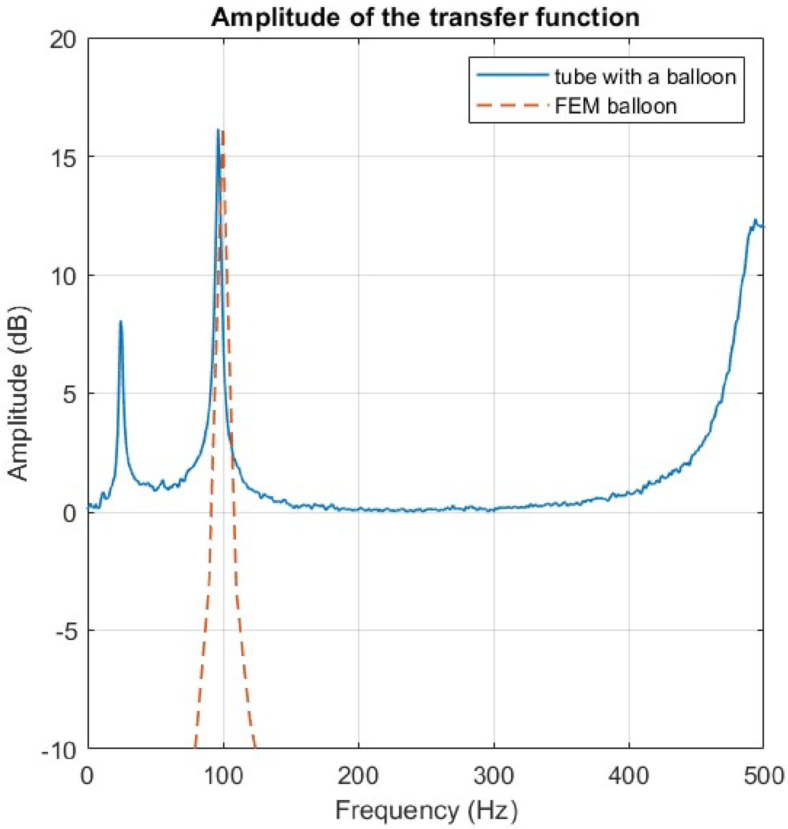

Figure 3.17 Transfer functions of the measured sound pressure (blue solid line) and the simulated sound pressure (dashed orange line) showing latex balloon resonance.

3.4.2 Recently Euthanised Fish – FEM Simulation

The FEM simulation of the air-filled latex balloon was extended to an ellipsoid encapsulated air-filled bubble to more closely resemble a trout's swim bladder. In accordance with the trout swim bladder in Figure 3.7, a semi-major axis length, a_a, was, according to the physical measurement of the dimensions of the 22.3 cm brown trout's swim bladder shown in Figure 3.7, set to be 5.4 cm and the semi-minor axis length, a_b, to be 0.7 cm, with an equivalent spherical radius a_{eq} = 1.34 cm and an eccentricity parameter $\varepsilon = a_b / a_a = 0.124$. The material properties of water and air remained the same, but the material of the swim bladder wall was not modelled as latex rubber. The swim bladder wall was assigned a density of 1050 kg/m^3, a Young's modulus of 2 MPa, and a Poisson's Ratio of 0.45 (Li *et al*, 2024). The thickness of the swim bladder wall was set to be 0.1 mm with an isotropic structural loss damping factor of 0.18. The air-filled ellipsoidal swim bladder was again placed at the centre of the computation water domain and excited by the monopole 20 cm beneath. The FEM study was later computed over a frequency range from 10 Hz to 1000 Hz with a step length of 10 Hz. Following the initial setup described above, the results of the FEM simulation for the ellipsoidal swim bladder are presented in Figures 3.18 to 3.20. These figures illustrate the transfer function amplitude and SPLrms across the simulated frequency range and provide insight into the acoustic resonance characteristics of the encapsulated air-filled bubble.

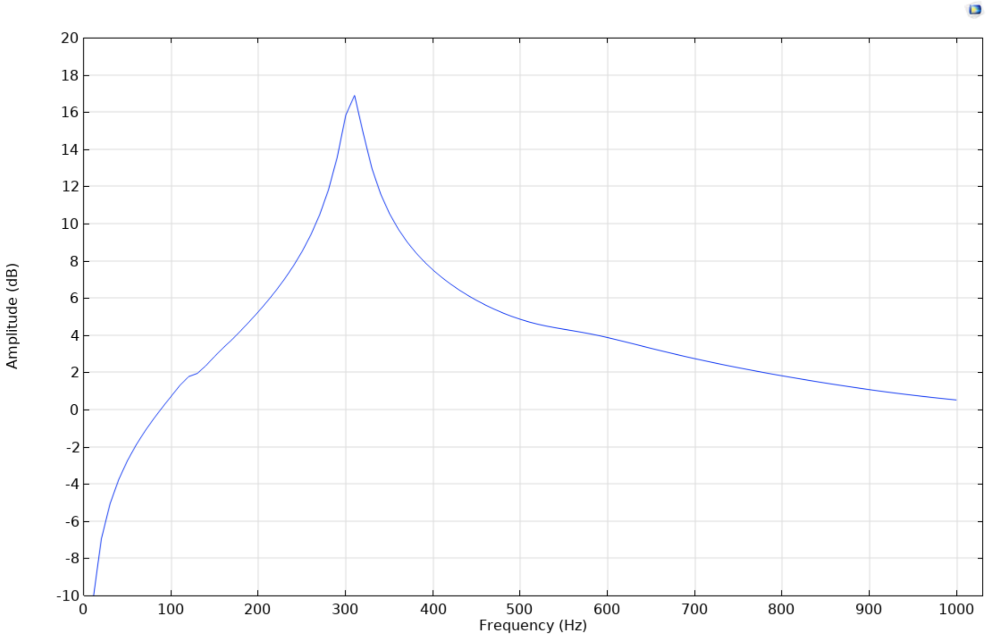

Figure 3.18 Transfer function of sound pressure in the modelled swim bladder.

Figure 3.18 shows the simulated transfer function of the swim bladder, highlighting a distinct resonance peak at 310 Hz. Comparing to the result of latex balloon resonance, the less sharpness and higher broadness of the peak indicate a more damped resonance, consistent with the material properties and wall thickness assigned to the swim bladder model, the higher frequency being primarily a result of the lower volume of gas.

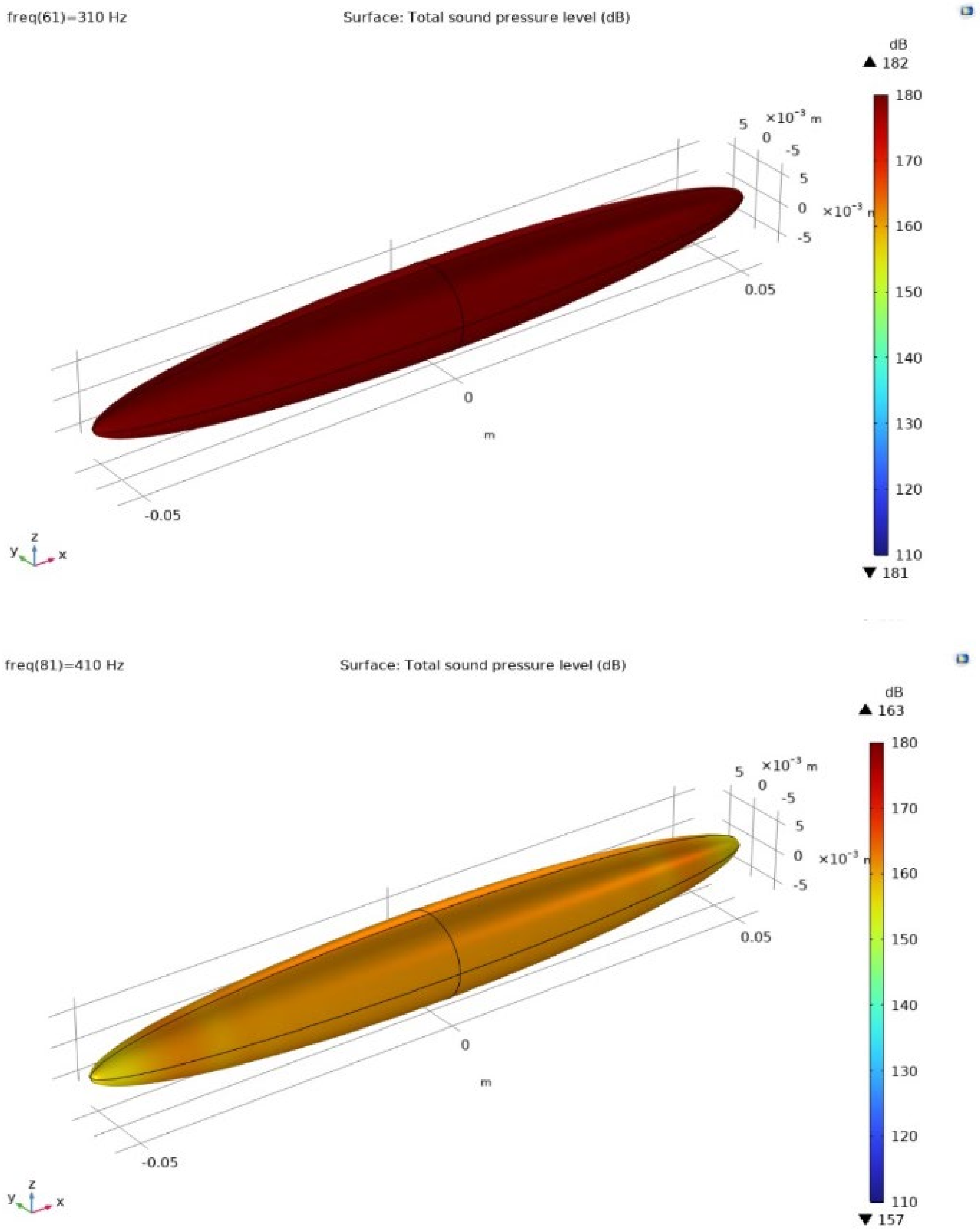

Figure 3.19 Comparison of simulated sound pressure field of the modelled swim bladder at the test frequency of 310 Hz (resonance frequency with uniform pressure distribution) and 410 Hz, which presented a special surface pressure distribution pattern with the tips of the modelled swim bladder showing lower sound pressure.

Figure 3.19 shows an example of the simulated sound pressure field on the surface of the modelled swim bladder at the test frequency of 310 Hz and 410 Hz. It shows a geometric pattern over the swim bladder surface at frequencies higher than the resonance frequency, *i.e.* the tips of the swim bladder at 410 Hz being yellow instead of orange, standing for a slightly lower sound pressure on the tips of the swim bladder, whereas the pressure distribution at the resonance frequency being uniform. This could be due to the bubble wall motion being in-phase with the driving sound pressure when excited below or at the resonance frequency, while the wall motion being out-of-phase under excitations above the resonance frequency reflecting the attenuation effect at higher frequencies, which will be further addressed in Subsection3.5.2 (Lee *et al.*, 2010).

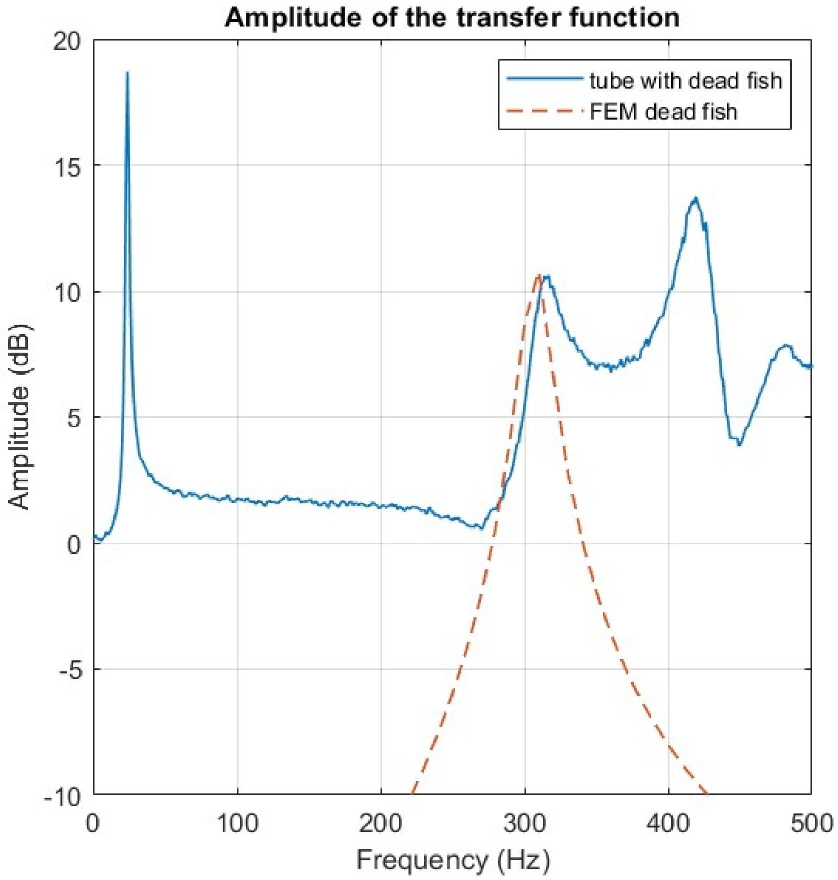

Figure 3.20 Transfer functions of the measured sound pressure (blue solid line) and the simulated sound pressure (dashed orange line) showing swim bladder resonance.

Figure 3.20 compares the transfer function of the simulated ellipsoidal modelled swim bladder with the experimentally measured result of the recently euthanised brown trout. The simulated resonance frequency is 310 Hz, which is 6 Hz lower than the measured result. However, this is less than the 10 Hz frequency resolution of the simulation. The similar sharpness and broadness suggest a similar damping between the simulation and measurement. The simulated swim bladder resonance has a quality factor of 15, and the measured resonance has a quality factor of 9.7, indicating a slightly less damped resonance was simulated in FEM, which was as our expectation because the swim bladder in the simulation was only constrained by the 0.1

mm thick swim bladder wall, whereas, in reality, the swim bladder of the euthanised fish suffered from more damping mechanisms like surround fish soft tissue and bones, resulting in a higher damping and a smaller quality factor.

More FEM simulations have been performed repeatedly and were validated against measured resonances of balloons and swim bladders of different sizes. The results clearly demonstrated the critical roles of the swim bladder's size, shape, and material properties in determining its acoustic response. In short, swim bladders with higher internal gas volume have low resonance frequencies. The elongation of the swim bladder would increase the resonance frequency whereas the hypothetical spherical swim bladder of the same gas volume would have the lowest, as expected from Eq. 13 and 14. Thicker swim bladder walls would slightly increase the resonance frequency due to higher surface tension, and it would also decrease the quality factor because of the introduction of more damping loss.

These findings support the hypothesis that swim bladders function as resonators, potentially enhancing auditory sensitivity in fish through their unique structural and material characteristics. The consistency between the numerical model and physical measurements underscores the mutual validity of the FEM approach in predicting bubble resonance behaviour of various bubble geometric characteristics, and the experimental method in successfully measuring swim bladder resonance properties in fishes. However, the FEM simulations described in sections above can only act as a simplified tool of validating FEM’s ability to estimate the bubble resonance frequency against measured results. The simplification has neglected factors that were assumed to be less relevant to the bubble resonance properties and only kept the essential ones like the internal gas volume and the overall shape of the encapsulated bubble. In order to achieve a more accurate simulation, high resolution CT scanning is recommended to be considered. Along with the accurate volumetric and mechanical information of the swim bladders and the otoliths, more detailed FEM simulations could be performed to better estimate the swim bladder resonance behaviour and study its contribution to fish hearing.

3.5 Further Analysis

After the previous analysis of measurements in three different experimental conditions and the numerical simulations, this section aims to further address some unsolved issues in the data and the results during the processing of collected signals. There are two major parts to be analysed separately: 1. The use of transfer function to explain the W-shaped feature at approximately 180 Hz; 2. The causes of the frequency shift and the amplitude decrease of original tube resonances due to bubble presence.

3.5.1 The W-shaped Feature: PSD and Transfer Function

When processing the data collected by the hydrophone, it was noticed that an unusual “W”-shaped feature was frequently observed at around 180 Hz along the power spectral curve, see Figure 3.21 for examples. This frequency lay in between the resonance frequency of the inertial shaker, 26 Hz, and the resonance frequency of the swim bladder, around 300 Hz, which was not shown on the power spectral density plot for the empty tube.

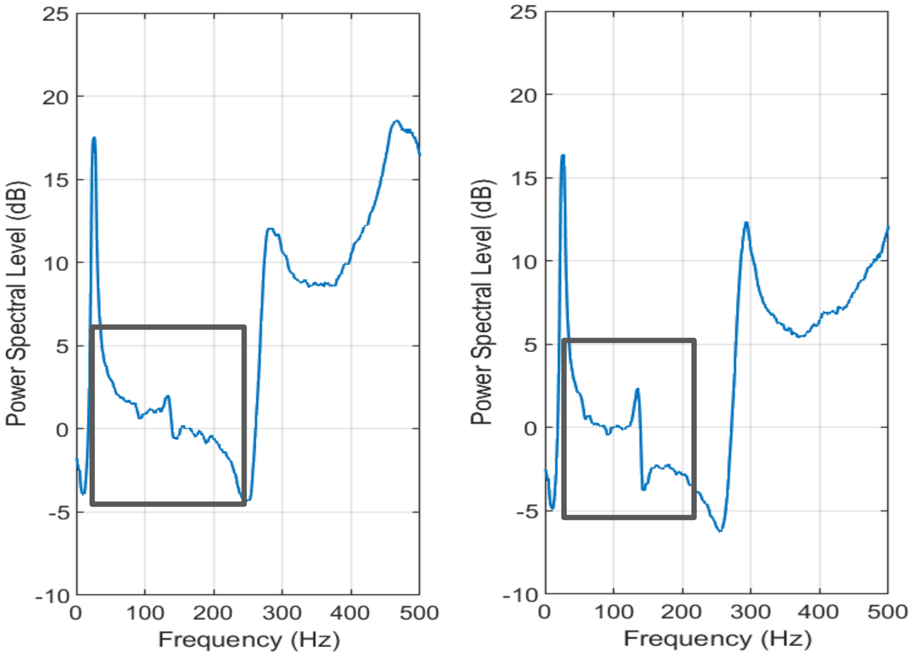

Figure 3.21 The zoomed-in power spectral densities for a 22.5 cm brown trout (left) and a 21 cm brown trout (right) for a closer observation of the “W”-shaped feature.

This feature seemed to consist of three parts: the small peak at around 130 Hz on the left, a broader dome-like shape in the middle, and the rising curve due to the swim bladder resonance, which was not seen in the data for the empty tube and the latex balloon. The key distinction between using the transfer function and the PSD to analyse a system’s frequency response lies in their ability to isolate the system’s true behaviour from external influences. The transfer function is derived using both the input and output signals, ensuring that only the components directly correlated with the input excitation are considered. This allows it to reveal finer details of the system’s frequency response, such as anti-resonance points, which may otherwise be obscured by noise in the PSD. In contrast, the PSD is computed solely from the output signal, meaning it reflects the total power distribution across all recorded frequencies, including contributions from background noise, reverberations, and external disturbances. Since the PSD does not distinguish between signal components originating from the input excitation and those from unrelated sources, important features of the system’s response may be masked by noise.

By filtering out uncorrelated components, the transfer function provides a clearer and more accurate representation of the system's dynamic behaviour, making it a more effective tool for identifying detailed frequency-dependent characteristics such as resonance and anti-resonance that might remain hidden in the PSD. Figure 3.22 presents the transfer function obtained from the 23.9 cm brown trout in Figure 3.10.

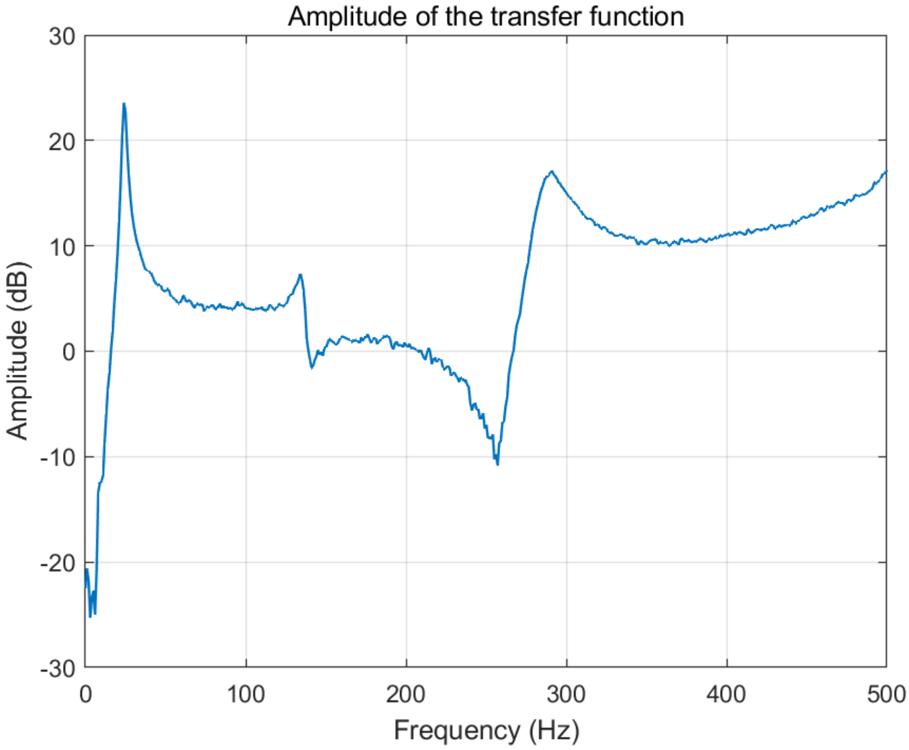

Figure 3.22 The transfer function of the system when a 23.9 cm brown trout was placed in the tube.

As the "W"-shaped feature still existed in the figure, the transfer function of the empty tube condition was also calculated and plotted together with the fish condition in Figure 3.23.

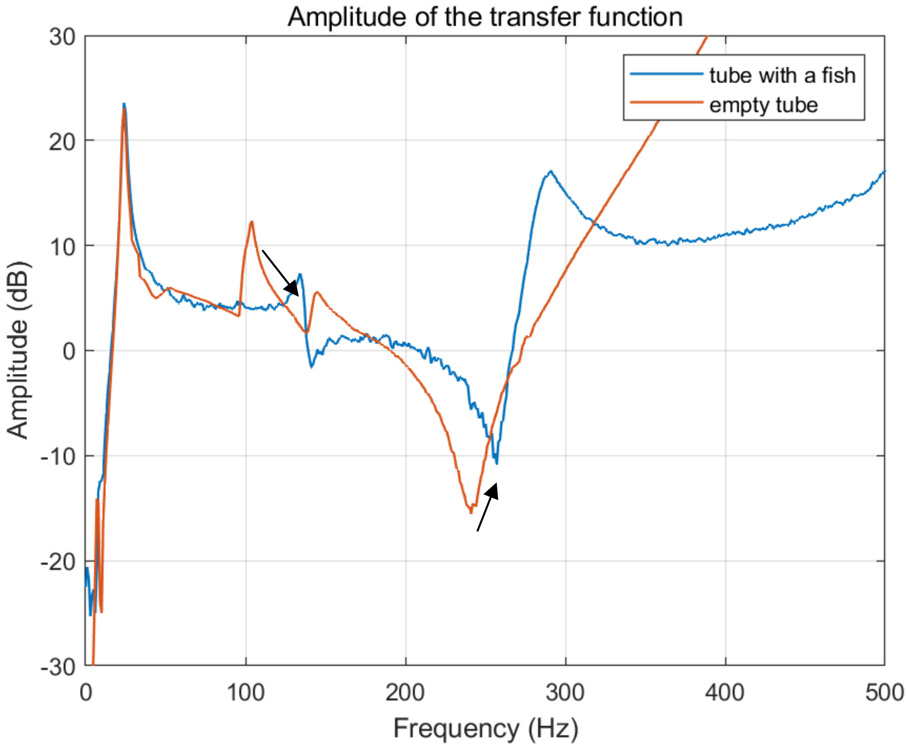

Figure 3.23 Transfer function of the system filled with only water (orange) and when a 23.9 cm brown trout was placed in the tube (blue).

In the case of the empty tube condition, the transfer function revealed important details that were hidden in the relatively flat PSD between 100 and 300 Hz. While the PSD suggested a lack of significant spectral features in this frequency range, the transfer function uncovered two small peaks at approximately 100 Hz and 140 Hz, as well as a notable anti-resonance around 245 Hz with a -20 dB drop. These features, which were masked in the PSD due to uncorrelated noise, became clearly visible when the transfer function was computed, demonstrating its ability to isolate the system’s true frequency response. The observed “W”-shaped feature in this frequency range was formed by the interaction of these peaks and the anti-resonance.

Additionally, changes in the frequency response were observed when a swim bladder was introduced into the tube. Unlike a latex balloon, which exhibited a resonance that overlapped with the small peak near 100 Hz of the empty tube response and effectively masked it, the swim bladder had a more damped resonance with a lower amplitude at a higher frequency than the small peaks. As a result, instead of obscuring the spectral feature, the swim bladder attenuated signals in that frequency band, reducing uncorrelated noise while making the correlated components more distinguishable in the PSD. The transfer function further confirmed the presence of the anti-resonance at 245 Hz, and it highlighted how the highly damped swim bladder resonance developed between the anti-resonance and the first tube resonance, making it less prominent in the spectrum due to its limited amplitude relative to the tube and balloon resonances.

Given that the transfer function provides a clearer representation of the system's true frequency response by filtering out noise that is irrelevant to the input excitation, it was decided as the preferred method for analysing all collected data in the rest of this thesis. Since certain spectral features, such as anti-resonances and weak resonances, may be masked in the PSD due to noise uncorrelated to the input signal, the transfer function will be used throughout the analysis to ensure a more accurate characterisation of the system's acoustic properties.

3.5.2 Frequency Shift and Attenuation due to Bubble Presence

The phenomena of the frequency shift and amplitude decrease of the tube resonances has been mentioned previously. By definition, the peaks can only shift if a bubble is present. If a bubble is not present, it is the original system. It clearly relates to the presence of a bubble of some form and this section will discuss a possible explanation.

Commander and Prosperetti (1988, 1989) proposed the theory that describes the propagation of linear plane acoustic waves in a bubble-liquid mixture. Commander and Prosperetti's model (CP model) treats the bubbly liquid as an effective medium (Commander and Prosperetti, 1989). The macroscopic properties of the medium are based on the physical properties and relative fractions of its constituent components (Lee *et al.*, 2010). In a similar study, Lee *et al.* (2010, 2011, 2012, 2014, 2017) considered the effect of the presence of a latex balloon in a rectangular tank and used CP model to predict the shifts in the tank resonance that arose by the balloon resonance. However, it should be noted that CP model assumes a large population of bubbles making a bubbly liquid, whereas Lee *et al.*, 2010 applied CP model to water with a single bubble and used it to predict the tank frequency shift based on parameters like the void fraction and bubble radius. We followed their approach to predict the impact of encapsulated bubbles (latex balloons and swim bladders) on the impedance tube resonance, like tube resonance frequency shifts and attenuation.

The void fraction, β, is an important parameter describing the air-water mixture, the ratio of the volume of air, V_{air},to the total volume of the mixture, $V_{air}+V_{liquid}$:

$$\beta=\frac{V_{air}}{V_{air}+V_{liquid}}. \tag{18}$$

The physical system that the model considers is a uniform distribution of spherical gas bubbles within a liquid host medium. The positions of the individual bubbles are not important, only their sizes and their relative number density compared to the host medium. Thus, the bubble distribution in the liquid can be specified completely by the void fraction and the bubble size probability distribution function, $\wp(a)$, which depends on spherical bubble radius a.

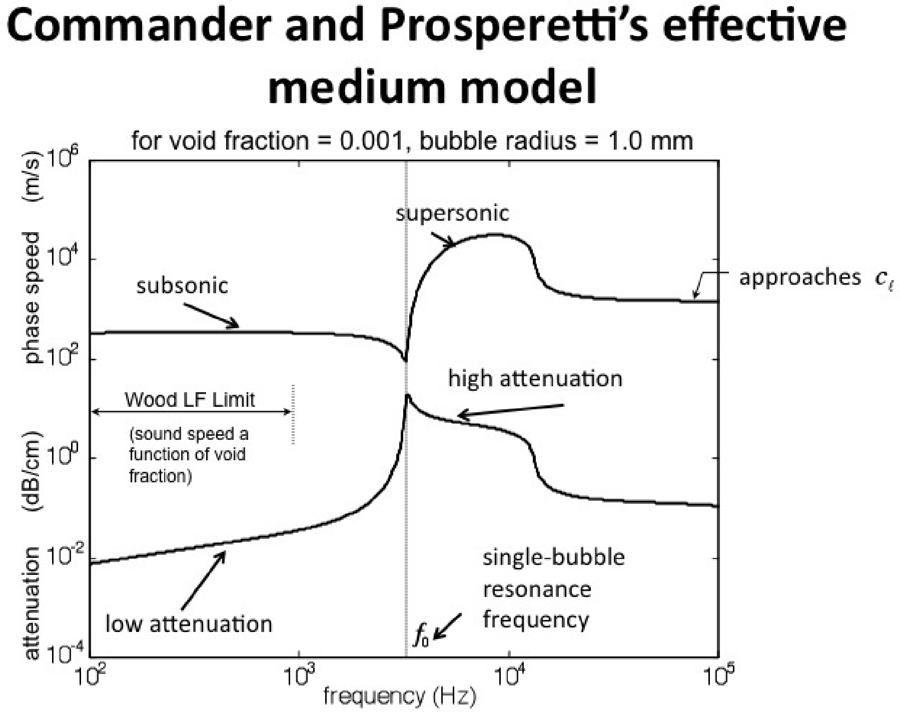

Figure 3.24 Predicted sound speed and attenuation from CP model for a monodisperse bubble size distribution with a = 1 mm and β = 0.001 (Lee *et al.*, 2010).

The basic nature of sound propagation in bubbly liquids is illustrated in Figure 3.24, showing the model output for a monodisperse distribution with a = 1 mm and a void fraction of 0.001. For frequencies below the natural bubble resonance frequency, the sound speed is nearly constant and is greatly reduced compared to that of bubble-free water, from about 1500 m/s to about 340 m/s below the single bubble resonance, and then sharply increased to supersonic above the resonance.

Below the resonance frequency, the bubble wall motion and driving sound pressure are in phase, and the compliance of the gas phase makes the medium appear acoustically soft, reducing the sound speed (Lee *et al.*, 2010). Above resonance, there is a sharp increase in sound speed, and for a range of frequencies, the sound speed is supersonic compared to that of bubble-free water. This supersonic regime occurs in this frequency range because the bubble wall motion is out of phase with the driving sound pressure such that the medium becomes acoustically stiffer than water or air (Lee *et al.*, 2010). At frequencies much higher than the bubble resonance, the sound speed approaches that of the host medium.

Figure 3.24 also shows the attenuation of sound in the bubbly liquid. Well below the single-bubble resonance frequency, the attenuation is very low. Approaching the resonance frequency, the attenuation increases to a maximum. At resonance, the bubble wall is at its maximum excursion, and the gas inside the bubble experiences its maximum compression. For the bubble size considered in Fig. 3.24 (a = 1 mm) as an example, the primary loss mechanism is from the thermal heating of the gas inside the bubble. The sound wave deposits its energy as heat inside the bubble. For smaller bubbles, viscous damping dominates, while for larger bubbles the acoustic re-radiation dominates. In the latter case, the acoustic energy is re-radiated by the resonating bubbles in a phase-incoherent manner such that the radiated waves cancel each other out. The attenuation remains high for a range of frequencies above resonance and falls to low values again well above resonance.

CP model predicts a complex-valued phase speed for the bubble-liquid mixture, which can be given for a time-independent bubble size distribution as

$$\frac{1}{c_m{}^2}=\frac{1}{c_0{}^2}+4\pi\int_0^\infty\frac{a\wp(a)da}{\omega_{CP}{}^2-\omega^2+2ib\omega}, \tag{19}$$

where c_m is the prediction of the phase speed of the bubble-liquid mixture, ω is the acoustic excitation angular frequency, and the integral is over the bubble radii a . The bubble resonance frequency, ω_{CP}, is given by:

$$\omega_{CP}=2\pi f_{CP}, \tag{20}$$

and

$$f_{CP}=f_0-\frac{1}{2\pi a}\sqrt{\frac{2\sigma}{\rho_w a}}=\frac{1}{2\pi a}\sqrt{\frac{3\gamma P_{b0}}{\rho_w}-\frac{2\sigma}{\rho_w a}}, \tag{21}$$

where f_0 is the Minnaert frequency, the additional term $-2\sigma/\rho_w a$ accounts for liquid surface tension σ , which is absent in Minnaert's model. Acoustic energy dissipation is described by the damping term:

$$b(\omega,a)=\frac{2\mu}{\rho_w a^2}+\frac{P_{b0}}{2\rho_w a^2\omega}\operatorname{Im}\phi+\frac{\omega a^2}{2c_w}, \tag{22}$$

which describes losses due to viscous, thermal, and acoustic re-radiation processes, respectively, and the term ϕ was previously given by Equation (3). (Commander and Prosperetti, 1989). In the previous expression, μ is the dynamic viscosity of the host liquid. It can be seen from calculating the relative importance of the various terms in Equation (18) that the re-radiation mechanism dominates for the large bubble sizes like latex balloons and fish swim bladders used in this study.

The simplest distribution of bubble sizes is the monodisperse distribution, for which all bubbles have the same size and are given by

$$\wp_{mono}(a)=n\delta(a-\bar{a}), \tag{23}$$

where n is the number of bubbles per unit volume, $\overline{a}$ is the bubble radius, and δ is a Dirac delta function.

Lee *et al.* (2010, 2011, 2012, 2014, 2017) carried out a series of experiments using water-filled tanks and large encapsulated bubbles ($a \approx 5$ cm) to study how the presence of encapsulated bubbles changes the frequency response of a water-filled container for the development of an underwater noise abatement system. Lee *et al.* (2012) measured the pressure spectra of a completely water-filled tank with and without an encapsulated bubble present, as is shown in Figure 3.25 in linear scale. The original tank resonance on the black solid curve was at 320 Hz, and the resonance frequency was shifted to around 355 Hz while the amplitude of the tank resonance peak was decreased by half, indicating the effect of dispersion and attenuation due to the presence of the resonant air bubble. The resonance frequency shifted about 10% from the original resonance frequency with the void fraction being $\beta \approx 0.02$. The phase speed of 355 Hz with the bubble present was 1703 m / second, and the corresponding wavelength became 4.80 m. The original wavelength of the empty tank resonance at 320 Hz was 4.69 m, which was very close to the estimated new wavelength of the first tank resonance at 355 Hz.

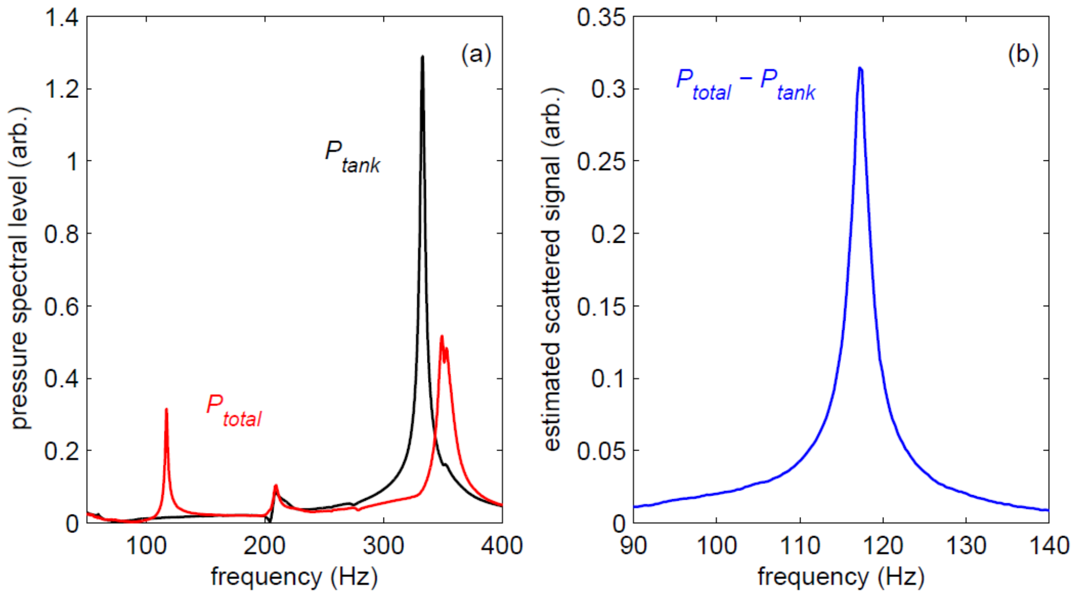

Figure 3.25 (a) The pressure spectral level of two measured signals when the tank was with and without the encapsulated bubble present. (b) The estimated scattered signal from the bubble by the subtraction of P_{total} and P_{tank} (Lee *et al.*, 2012).

Another experiment was performed by Lee *et al.* (2014) studied the effect of the presence of a large, encapsulated bubble array on the frequency response of a 6 m deep water tank with a higher void fraction: $\beta \approx 1.2\%$. The result is shown by Figure 3.26 in a linear scale.

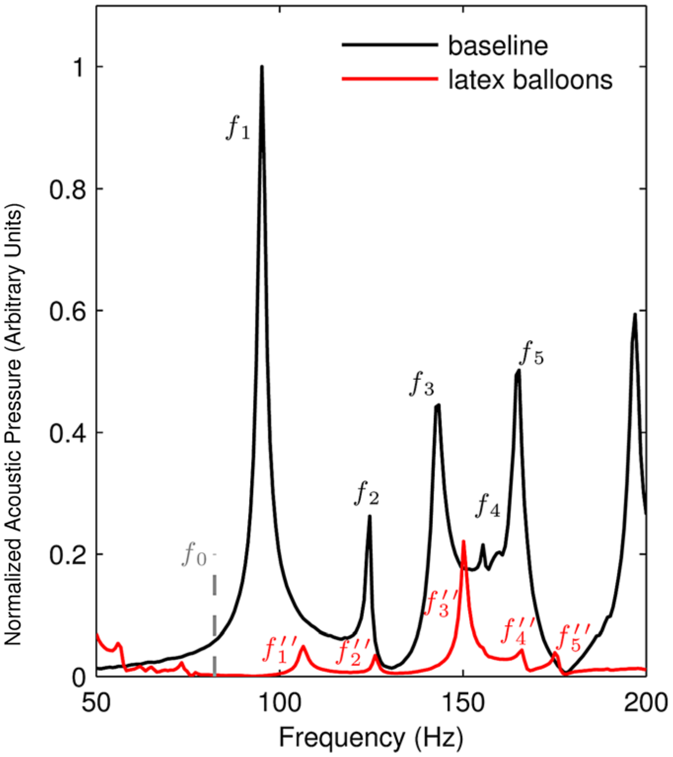

Figure 3.26 Normalised pressure spectra of the tank measured at 6 m depth showing frequency shift and attenuation effects due to bubble resonance f_0 (Lee *et al.*, 2014).

All resonance peaks of the first five tank modes in Figure 3.26 were shifted to higher frequencies (*e.g.*, f_1 = 95.2 Hz was shifted by 12% to f_1''=106.7 Hz) due to the air-water mixture. All the amplitudes of the five original resonance peaks decreased because of the bubble-induced sound attenuation above the bubble resonance frequency f_0 = 82.3 Hz.

Following the approach of Lee *et al.* (2014), it was hypothesised that similar effects would be observed in the frequency response functions of the impedance tube system when an encapsulated bubble or a fish swim bladder was present. The predicted phase speed and attenuation of the swim bladder-water mixture were calculated using Commander and Prosperetti's model. As was mentioned previously, the equivalent spherical bubble radius $a = \overline{a}$ = 1.27 cm as the swim bladder was the only bubble in the impedance tube. The volume of the equivalent spherical bubble and the water body in the impedance tube were calculated to be V_{bladder} = 8.7 mL and V_{tube} = 6170.7 mL, hence the void fraction was $\beta \approx$ 0.14%. The dynamic viscosity of the surrounding fish flesh was taken as $\mu = 60\text{Pa}\cdot\text{s}$ (Weston, 1967; Lewis,1994). Figure 3.27 presents the results of the phase speed and attenuation in the presence of the swim bladder and a free bubble of the same radius.

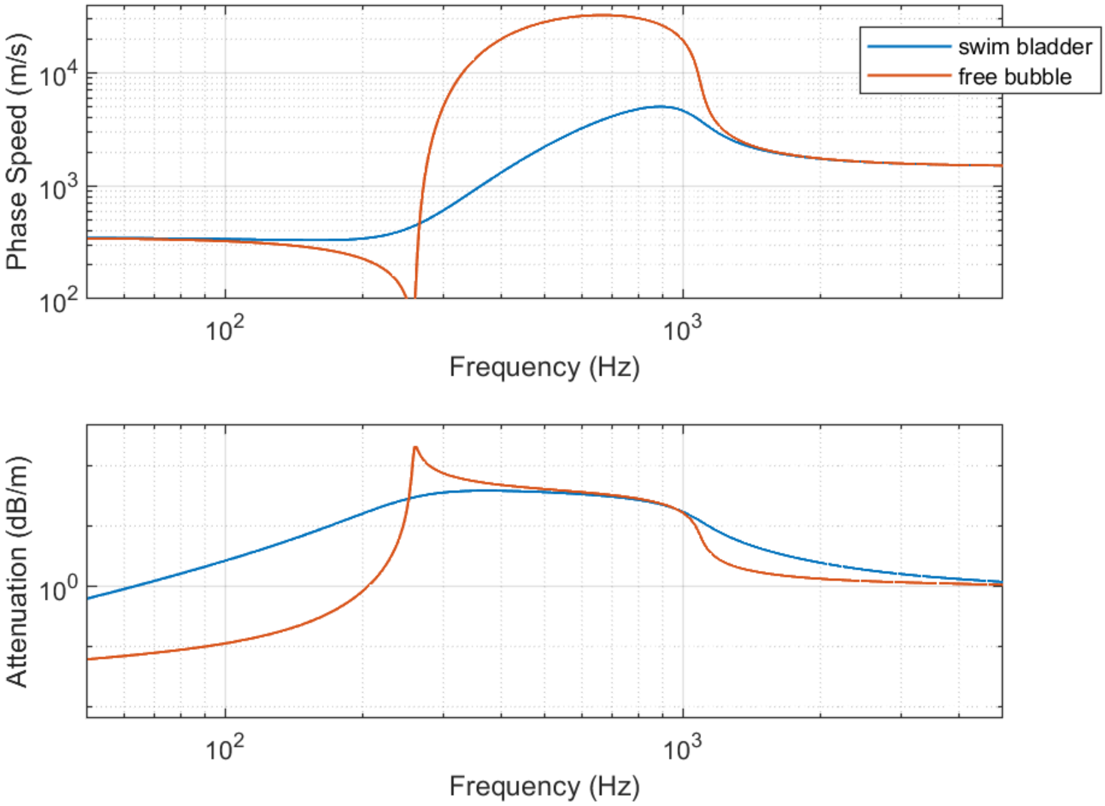

Figure 3.27 Predicted sound speed and attenuation from CP model with the swim bladder versus a free bubble in the impedance tube with a = 1.27 cm and β = 0.14%.

The original first tube resonance was at 397 Hz assuming sound speed of 1480 m/s, giving the wavelength of the resonance frequency λ_{tube} = 3.78 m. After the introduction of the swim bladder, the first tube resonance shifted to 497 Hz, and the predicted phase speed at 500 Hz was 1991 m/s according to the CP model, giving the wavelength of resonance frequency λ_{CPtube} = 3.98 m, 5.2% higher than the original wavelength. All 18 brown trout used in the experiment were from the same fish hatchery, of similar sizes, and stayed in the same husbandry facility before the euthanasia, so mechanical properties of the fish's bodies are unlikely to show excessive variation between individuals. To study the impact of the cause of dynamic viscosity, μ , of surrounding tissue, a range of 50 to 80 $\mathrm{Pa}\cdot\mathrm{s}$ was considered. The resulting phase speed at 500 Hz varied from 1719 m/s to 2241 m/s, corresponding to a first tube resonance frequency varying from 431 Hz to 624 Hz. The measured first tube resonance frequency, 497 Hz, occurred in that range.

A comparison of the normalised power level between the empty tube and the tube with a euthanised fish is plotted in Figure 3.28 on a linear power scale, and the corresponding tube resonances are indicated in the figure. The original tube resonances, f_1, f_2, f_3, have shifted to f_1', f_2', f_3' because of the effect of the bubble resonance, and the amplitude of acoustic power has also been decreased due to the attenuation at frequencies higher than the bubble resonance.

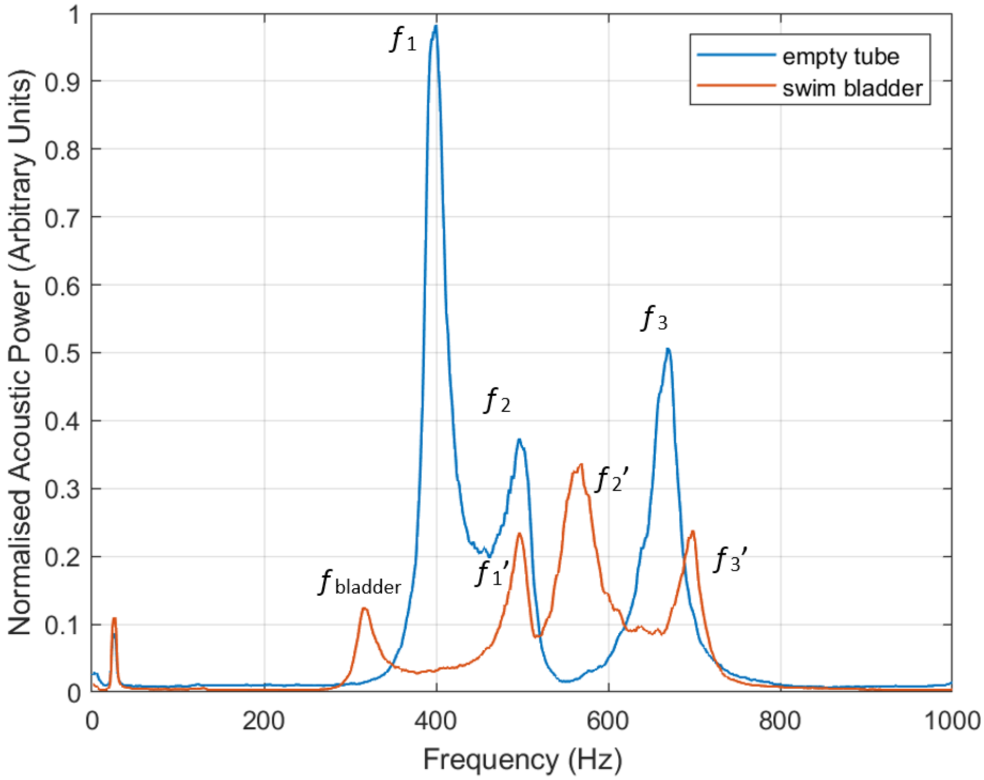

Figure 3.28 Normalised acoustic power spectra of the tube in two conditions showing frequency shift and attenuation effects due to the bubble resonance.

3.6 Chapter Conclusions

This chapter has detailed a multifaceted methodology, encompassing theoretical modelling, experimental measurements, and numerical simulations, aimed at characterising the resonance properties of encapsulated bubbles and fish swim bladders in an impedance tube. By comparing measured resonance data in the impedance tube against finite element simulations of encapsulated bubbles in free-field, it established a high degree of agreement between experimental observations and simulation predictions. This mutual validation not only enhances confidence in the measured resonance parameters but also underscores the rigour of the numerical modelling approach.

Importantly, the methods defined in this chapter provide a robust foundation for extending the study of swim bladder resonance to live fish in a controlled, non-invasive manner. The successful validation of the encapsulated bubble and euthanised fish models, combined with the insight gained from comparing numerical and experimental results, supports the feasibility of detecting and analysing resonance behaviour in free-swimming specimens.

The next chapter will build on these findings by introducing new protocols for live fish measurement and applying the CT-aided FEM simulation to advance our understanding of swim bladder resonance *in situ*. These subsequent investigations will further demonstrate the potential for this technique to deliver valuable insights into fish acoustics, thereby enriching our knowledge of bioacoustic systems in both laboratory and field contexts.

Chapter 4 Non-invasive Measurements of Swim Bladders Resonance Properties on Free-swimming Fish

4.1 Introduction

Previous chapters established theoretical foundations and demonstrated preliminary measurements and simulations on euthanised fish under controlled conditions, providing essential insight into resonance phenomena. These methods, while robust, introduced constraints by necessitating euthanasia or extensive handling of specimens, thereby introducing significant ethical issues and possible sources of error. Developing a non-invasive method for measuring the resonance properties of fish swim bladders in live, free-swimming specimens represents a crucial step forward, extending both the breadth and applicability of this research.

This chapter presents the design and execution of a non-invasive, tank-based measurement technique that enables the capture of swim bladder resonance data from live, free-swimming fish. The primary objectives are fourfold:

1. Design, optimise, and manufacture a closed, water-filled test tank such that it imposes minimal disturbance on the fish and allows for the measurement of acoustic responses of resonances.
2. Achieve non-invasive measurement of swim bladder resonance properties on live, free-swimming fish inside the test tank using low level white noise.
3. Validate experimentally measured resonance frequencies by comparing them with advanced FEM simulations that incorporate accurate three-dimensional swim bladder and otolith models derived from high resolution CT scans.
4. Establish correlations between fish morphological features, namely length and weight, and the resonance frequency of their swim bladders, providing new perspectives on how physical attributes influence resonance behaviour and fish hearing.

Section 4.2 details the tank design and rationale, outlining the engineering considerations and acoustic principles underlying its construction. Subsection 4.2.1 introduces a modal analysis of a lightly clamped steel circular plate, offering insight into how the tank’s base behaves mechanically and how its vibrational characteristics interact with water-borne acoustic fields as the sound source, and Subsection 4.2.2 elaborates on the tank's manufacture and assembly from the practical perspective.

Section 4.3 describes how the tank's acoustic response is experimentally evaluated. Subsection 4.3.1 focuses on the measurement of the empty tank's transfer function. Subsection 4.3.2 presents the corresponding FEM Simulation of the empty tank, leveraging COMSOL to predict the acoustic field within the tank, and compute the simulated empty tank transfer function.

Moving from tank-specific characterisation to biological measurement, Section 4.4, documents the protocols for fish husbandry, handling, and introduction into the measurement apparatus. Subsection 4.4.1 addresses fish maintenance and ethics, and Subsection 4.4.2 discusses the measurement protocol, detailing the acoustic signals used, data acquisition hardware, and experimental workflow.

Section 4.5 describes the analysis and interpretation of the measurement results. Subsection 4.5.1 highlights how swim bladders of fish in various size groups alter in resonance properties, and Subsection 4.5.2 reports the statistical results, including the relationship between body length, weight, swim bladder dimensions and resonance properties across multiple specimens and repeated trials.

In Section 4.6, the CT scanning of swim bladders is considered. Subsection 4.6.1 elaborates the associated imaging protocol, and Subsection 4.6.2 presents the procedures for 3D model extraction. These steps yield highly accurate three-dimensional representations of swim bladders and otoliths of the fish.

Section 4.7 then describes how these reconstructed 3D models are combined with FEM. Subsection 4.7.1 outlines the parameters employed for the modelling. Subsection 4.7.2 shows results for an isolated swim bladder, and the Subsection 4.7.3 extends the simulation to account for the presence of the tank.

Section 4.8 focuses on how closely the FEM results align with measured data. Subsection 4.8.1 explores the consistency and divergence between measured and simulated resonance peaks in transfer functions. Subsection 4.8.2 considers the potential sources of discrepancies.

Finally, Sections 4.9 and 4.10 present a discussion of these findings and draw conclusions from the chapter.

4.2 Tank Design and Rationale

Several limitations of performing experiments in the previous stainless-steel impedance tube motivated this transition. First, the weight and size of the steel tube made it cumbersome to manipulate. Frequent lifting and tilting of the impedance tube were necessary to expel unwanted air pockets—often trapped in the horizontal sections or near the tube lid—which, if unremoved, could significantly affect resonance measurements. Second, the opaque stainless-steel walls not only prevented real-time assessment of the presence of unwanted bubbles, but also obstructed the visual monitor of live fish behaviour and welfare. Third, the restricted interior dimensions allowed minimal space for larger fish or encapsulated bubbles, creating additional uncertainty regarding boundary effects that might influence bubble oscillations. Finally, the horizontal configuration of the impedance tube required complete draining with each removal of the side-mounted lids after every single measurement, making the testing process both time-consuming and less environmentally considerate.

Based on insights gained from the initial measurements performed with latex balloons and recently euthanised brown trout using the impedance tube in Chapter 3, it became evident that a more experimentally efficient and fish-friendly test tank would be essential for subsequent experiments, particularly those involving live fish. Acrylic was selected as the primary construction material for the wall and the lid of new tank. Acrylic not only offers a substantially lower mass compared to metals, thereby simplifying handling, but more importantly confers transparent walls that allow visual observation of fish behaviour and verification of the non-existence of any unwanted air pockets left within the tank.

By opting for an acrylic-based structure, the new test tank was to simplify handling, ensure reliable visibility of internal conditions, and could be tailored to optimal geometric dimensions for the experimental procedure. The primary objective of this specially designed facility was to enable reliable, non-invasive acoustic measurements of swim bladder resonance on live, free-swimming fish in a controlled environment.

4.2.1 Modal Analysis of a Lightly Clamped Steel Circular Plate

The test tank mainly consists of an acrylic cylindrical tank body, a customised acrylic tank lid, and a 2 mm thick circular stainless-steel plate with the inertial shaker attached as the sound source. To design the test tank for engineering efficiency and experimental feasibility, the key factor was to simulate and optimise the mechanical and acoustical response of the sound source, namely the stainless-steel plate at the bottom of the tank, so that its original mechanical resonances would not overlap with fish swim bladder resonances in the frequency domain during any future measurements. Figure 4.1 shows the initial design of the tank bottom's setting.

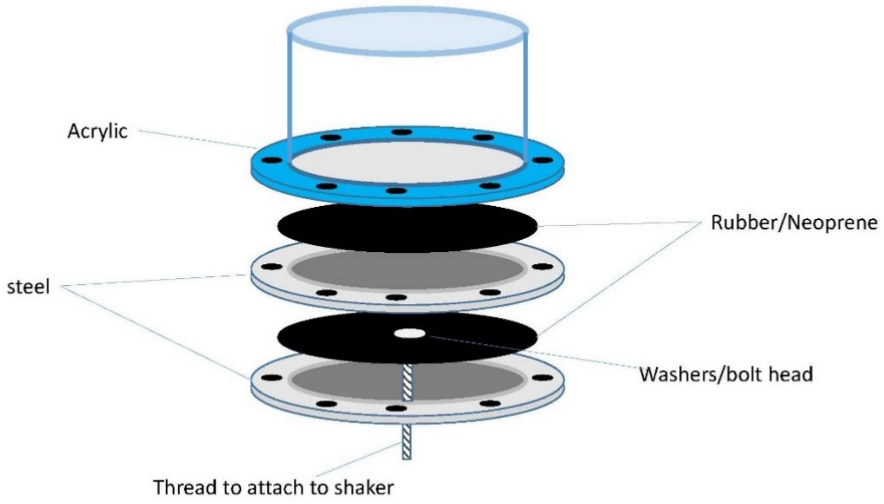

Figure 4.1 The initial design for the structure of the tank bottom.

For the purpose of designing and assessing the mechanical resonances of the sound source (thin steel plate), it was approximated as a clamped steel circular plate for further analysis. In many engineering assemblies, circular steel plates serve as closures or support elements, for instance at the ends of cylindrical containers or as partitions within fluid-filled test chambers. When the clamping force around the plate's circumference is kept low, which was strong enough to achieve a watertight seal for our test tank here but not so much as to crack the comparatively fragile acrylic tank flange. The boundary constraint differs from a fully fixed (rigidly clamped) edge since the plate's rim retains some freedom to rotate, approximating a simply supported (lightly clamped) boundary condition. Such a configuration holds significant implications for both structural resonance and acoustic interactions, especially if the steel plate is in contact with distinct media on either side, in this case, air on one face and water on the other.

From a theoretical point of view, we may use Kirchhoff–Love thin-plate theory to predict natural frequencies, provided the ratio h_P / R_P (plate thickness over effective radius) is suitably small. The ratio for our design is roughly 0.01, satisfying the assumption as a think-plate (below 0.05). Under these conditions, bending deformation dominates, and both shear deformation and rotational inertia are assumed to be negligible (Blevins, 2001). We treat the plate as quasi-simply supported, meaning that its circumference cannot undergo normal displacement but is free to rotate to a certain degree. Hence, the rigidity commonly associated with a fully clamped boundary is relaxed. For a circular plate of radius R_P, thickness h_P, material density ρ_P, Young's modulus E_P, and Poisson's ratio ν_P, its flexural rigidity is (Blevins, 2001):

$$D_P = \frac{E_P h_P^{\;3}}{12\left(1 - \nu_P^{\;2}\right)}. \tag{24}$$

Under free vibrations (no external forces or damping), the governing biharmonic equation in polar coordinates leads to modal solutions with an angular frequency ω_{mn} (radians per second) determined by:

$$\omega_{mn}^{\;2} = \lambda_{mn}^{\;4} \frac{D_P}{\rho_P h_P R_P^{\;4}}, \tag{25}$$

where λ_{mn} is a dimensionless constant dependent on the boundary conditions and the particular vibratory mode (m,n). Converting to linear frequency f_{mn} (Hz):

$$f_{mn} = \frac{\omega_{mn}}{2\pi} = \frac{\lambda_{mn}^{\;2}}{2\pi} \sqrt{\frac{D_P}{\rho_P h_P R_P^{\;4}}}. \tag{26}$$

For a simply supported circular plate, the first few dimensionless values are: $\lambda_{0,1} = 3.196$, $\lambda_{1,1} = 6.306$, and $\lambda_{0,2} = 7.197$ (Blevins, 2001). Typically, these results are in lower natural frequencies than predicted for a rigidly clamped boundary condition.

For a stainless-steel circular plate at the tank bottom and as the sound source of our test tank, an effective vibrating diameter of 470 mm (R_P=0.235 m), a thickness of 2mm (h_P = 2 mm), with a material density $\rho_P \approx 7850$ kg/m^3, a Young's modulus $E_P \approx$ 200 GPa, and a Poisson's ratio $\nu_P \approx$ 0.30, its flexural rigidity is $D_P \approx 146.5$ N m.

Using the above parameter, the first three modal frequencies are:

1. First fundamental mode (0,1): frequency around 90 Hz,
2. Second mode (1,1): frequency roughly 350 Hz,
3. Third mode (0,2): frequency about 450 Hz.

Considering the need for space in the test tank for fish of various sizes to be comfortably maintained during the measurement, the effective vibrating diameter of 470 mm was feasible to provide enough internal water volume for the fish while keeping an efficient working frequency range from 90 Hz to 350 Hz. Considering common carp of a size range from 4'' to 14'' with estimated swim bladder resonance frequencies between 150 Hz and 300 Hz, most of their swim bladder resonance peaks will lie between the first and second tank modes.

Preferably, it would be better to tune the plate characteristics so that its first mechanical resonance would lie above all possible fish swim bladder resonances, similar to what it was for the impedance tube in the last chapter. There are mainly three possible ways to tune the first mechanical resonance frequency higher: one is to clamp the thin steel plate very strongly so that it forms a fully fixed (rigidly clamped) edge but not too tight to prevent cracking the acrylic tank body; the other one is to make the circular steel plate smaller thus increasing the resonance frequency. This is limited since this project was aimed to build a fish-friendly system with enough space and oxygen for the fish to stay in for about half an hour. The third one is to increase the plate thickness, but this will in turn decrease the efficiency of energy transmission from the inertial shaker to the water body, possibly resulting in insufficient sound pressure for the test.

Notably, acoustic considerations become more nuanced if one face of the plate is exposed to air while the other is in contact with water, just as our experimental setting. On the air side, the plate’s vibration can radiate airborne sound. On the water side, fluid loading alters the plate’s dynamic response: water, being much denser than air, imposes an added mass that often increases the mechanical resonant frequencies and damping. The magnitude of this shift hinges on factors like the size of the plate, the extent of submerged surface, and the acoustic impedance mismatch between steel, water, and any intervening gaskets or sealant layers. Consequently, in such conditions, the actual modal frequencies may lie above the simple vacuum or air-based estimates given by the equations above. Furthermore, noise radiation into water tends to be more efficient for a flexible boundary, so the plate could become a significant acoustic radiator at or near its resonant modes. Therefore, further analysis will be performed to compare with and validate the preliminary calculations from Kirchhoff–Love thin-plate theory. Real-life measurements and FEM simulations of the new water-filled test tank will be carried out and discussed to incorporate the fluid-structure-acoustic coupling effect more explicitly.

Finally, it was noted that these formulas served as initial estimates the design of the test tank bottom. Real tank assemblies often feature gaskets, slight eccentricities, or partial contact regions that deviate from the ideal simply supported scenario. Nevertheless, the quasi-simply supported approach provided a predictive perspective for identifying possible tank resonance properties early on and contextualising how a steel plate—lightly clamped at its periphery, with air on one side and water on the other—may exhibit a heightened propensity for low-to-mid frequency vibrations and significant acoustic radiation or fluid interaction.

4.2.2 Tank Design, Manufacture and Assembly

Considering all factor above, the design of all parts of the new test tank was accomplished on SolidWorks with the help from Design Service, Engineering Design and Manufacturing Centre, School of Engineering, University of Southampton. Figure 4.2 shows the two-dimensional engineering drawing of the tank bottom plate sub-assembly mentioned in 4.2.1; Figure 4.3 shows the two-dimensional engineering drawing of the whole tank assembly.

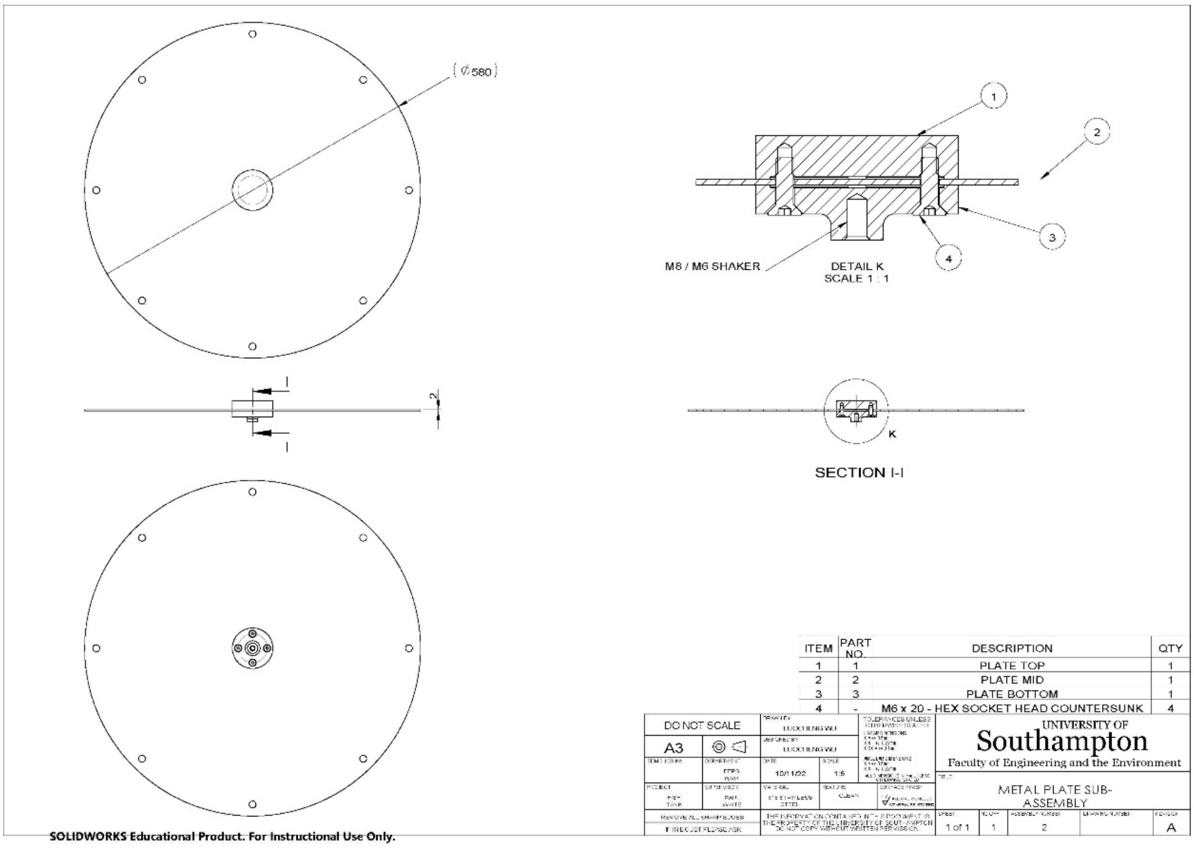

ITEM	PART NO.	DESCRIPTION	QTY
1	1	PLATE TOP	1
2	2	PLATE MID	1
3	3	PLATE BOTTOM	1
4	-	M6 x 20 - HEX SOCKET HEAD COUNTERSUNK	4

Figure 4.2 The 2-D engineering drawing of the tank bottom plate sub-assembly.

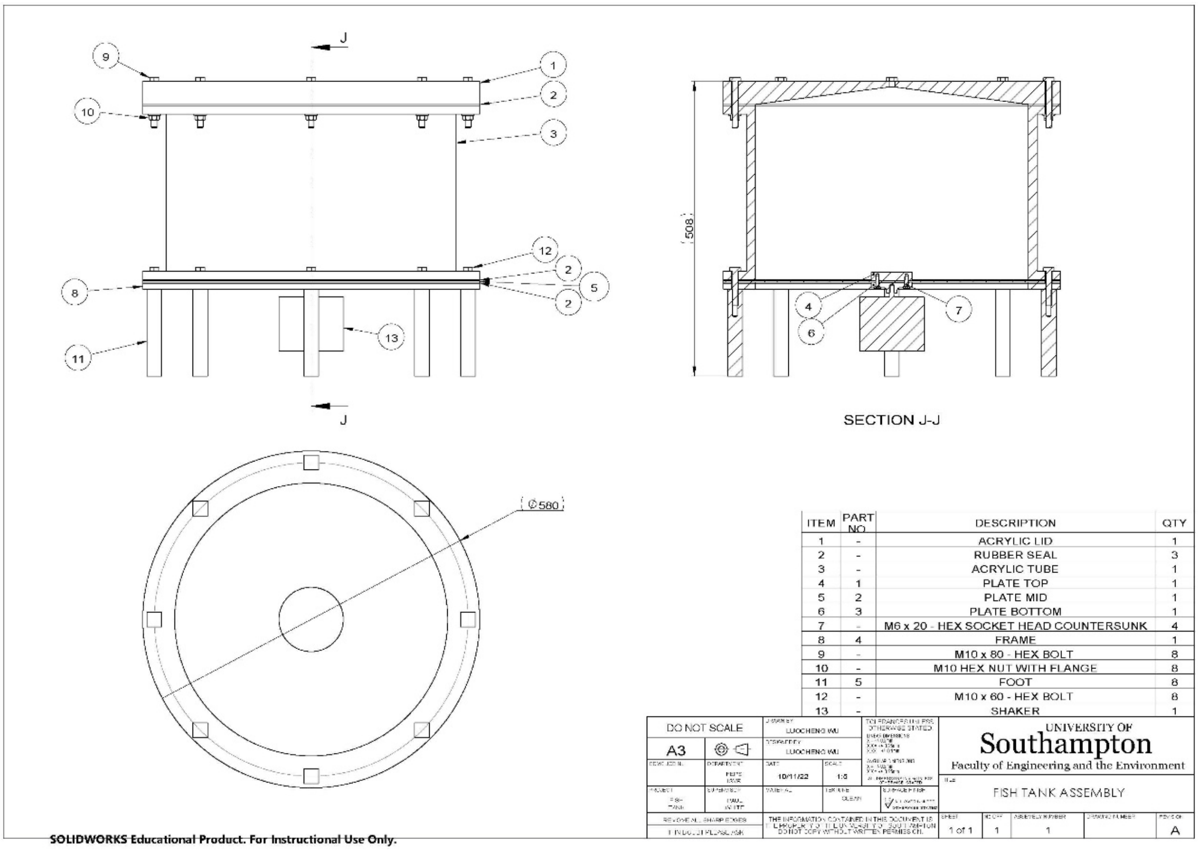

ITEM	PART NO	DESCRIPTION	QTY
1	-	ACRYLIC LID	1
2	-	RUBBER SEAL	3
3	-	ACRYLIC TUBE	1
4	1	PLATE TOP	1
5	2	PLATE MID	1
6	3	PLATE BOTTOM	1
7	-	M6 x 20 - HEX SOCKET HEAD COUNTERSUNK	4
8	4	FRAME	1
9	-	M10 x 80 - HEX BOLT	8
10	-	M10 HEX NUT WITH FLANGE	8
11	5	FOOT	8
12	-	M10 x 60 - HEX BOLT	8
13	-	SHAKER	1

Figure 4.3 The 2-D engineering drawing of the new test tank assembly.

Figure 4.4 is the 3-D model of the test tank assembly in SolidWorks, which was later used for further FEM simulations in following sections.

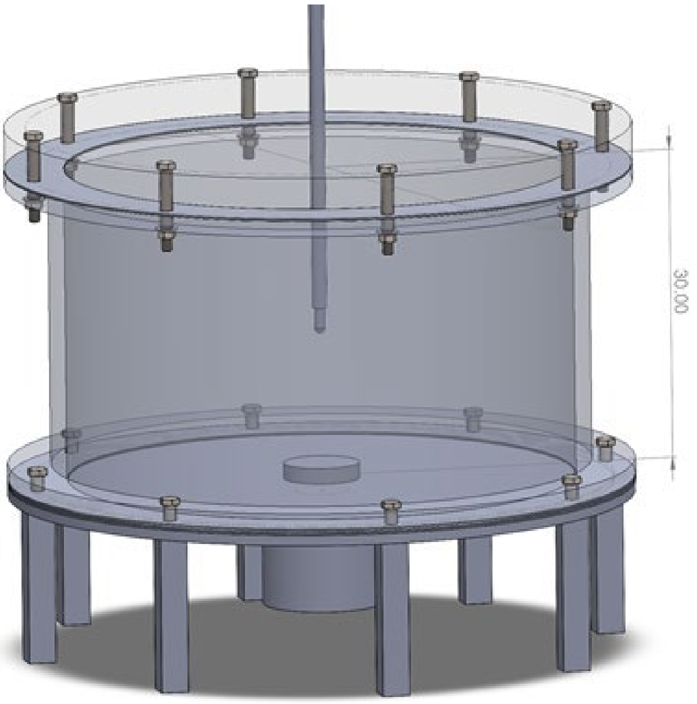

Figure 4.4 The 3-D model of the new test tank assembly rendered in SolidWorks.

Figure 4.5 is a photo of the manufactured and assembled test tank, which was assembled and machined for the water inlet and outlet by technicians of Optoelectronics Research Centre, University of Southampton. The valve controls the inlet water flow, as the water level rises above the top gasket, the internal conical shape of the acrylic lid will automatically expel air through the top vent, as is shown in cross-section J-J in Figure 4.3. The steel tube is then mounted into the tank with a hydrophone at its bottom after the tank was fully filled with water. As was shown in Figure 4.2, the inertial shaker was mounted onto the bottom of the steel plate sub-assembly by a M6 thread, providing the acoustic excitation.

The test tank has an outer (flange) diameter of 580 mm and an inner (water body) diameter of 470 mm with a 15 mm thick tank wall, an internal height of 300 mm, and an overall height of 508 mm, which is able to hold roughly 53 L water inside the tank when fully filled. The lid can be removed by unscrewing the bolts and nuts on the edge, and a live, free-swimming fish can be moved into the half-filled tank. Then, the lid is bolted back on the tank body and the water filling process continues until all air being expelled from the top vent. Lastly, the hydrophone will be inserted into the water body, sealing the top air vent, and the air vent's gap will be sealed by a tighten O-ring.

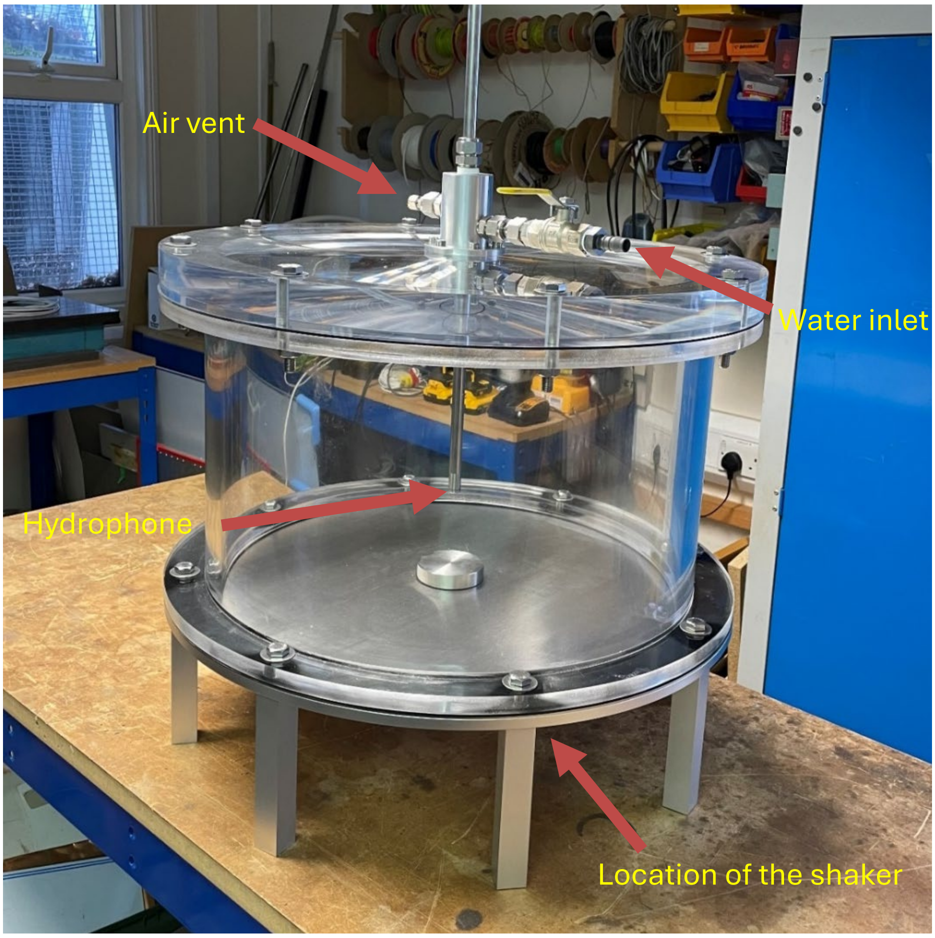

Figure 4.5 Photo of the assembled the acrylic test tank with the water inlet and a hydrophone feedthrough at the top of the lid.

4.3 Tank Characterisation

After the successful manufacture and assembly of the test tank, it was then transported to Engineering Centre, Chilworth Science Park, University of Southampton for further experiments.

4.3.1 Experimental Measurement of Tank Transfer Function

Following the same experimental method as the impedance tube trials, a 100-second pseudorandom white noise signal was generated by a DELL PRECISION 7550 running MATLAB R2020a and sent from a NI USB-6361 DAQ to a DataPhysics PA30E power amplifier, which provided the amplified driving signal to the inertial shaker, DataPhysics IV40. The performance response of IV40 is shown in Figure 4.6, in which it is observed that the shaker generates the highest force from around 30 Hz to 50 Hz (around its mechanical resonance), thereby the input white noise signal was applied with a high-pass filter with a cut-off frequency at 100 Hz to avoid shaker malfunctioning, which would not affect the ability of measuring swim bladder resonance since the largest fish to be held in the tank had a predicted resonance over 150 Hz.

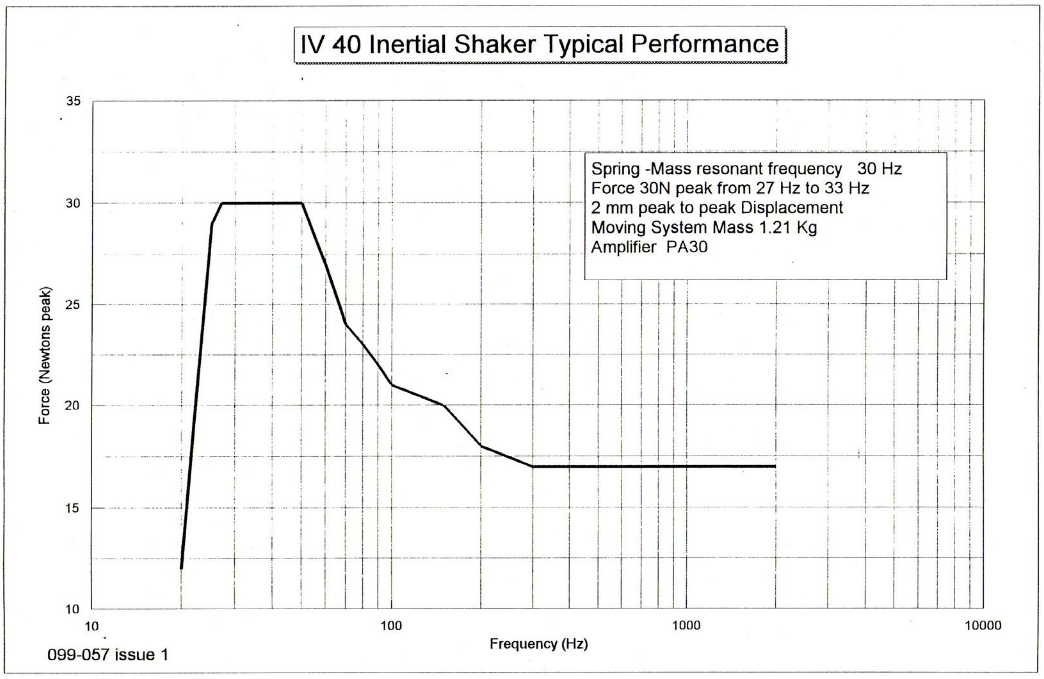

Figure 4.6 The typical performance frequency response of the inertial shaker IV40.

The Bruel & Kjaer 8103 hydrophone with a sensitivity of -211dB re 1V/μPa (signal conditioned by a RESON EC 6081 mk2 VP2000 preamplifier) was mounted through the acrylic tank lid and placed at the centre of the cylindrical water body and 25 cm above the bottom plate. The position was selected after trials of the hydrophone at different depths. If the hydrophone was positioned too close to the bottom plate (sound source), the hydrophone was mainly picking up the direct acoustic signal from the source and the scatter from a swim bladder was hard to detect. At the selected depth the hydrophone was able to perform stable measurements of the tank response whilst being capable of picking up the comparatively weak scattered acoustic signals from the swim bladder resonance. When placed too close to the acrylic tank lid, the signal was likely to suffer from complex boundary effects due to the mismatch of acoustic impedance between water and acrylic. Therefore, the position of 25 cm above the bottom plate was selected as the main hydrophone position for further experimental measurement and numerical simulation when analysing the tank frequency response and swim bladder resonances.

Magnitude of the empty *i.e.* tank filled by water but no fish, tank transfer function was calculated and plotted in Figure 4.7.

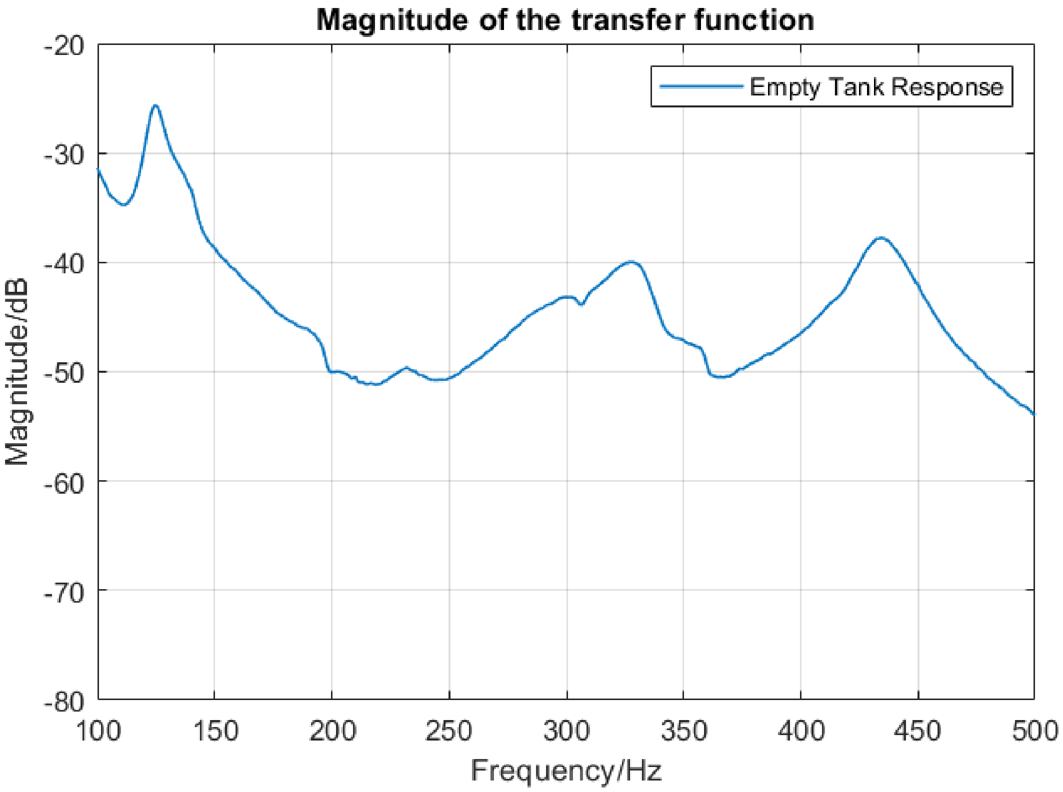

Figure 4.7 Measured transfer function of the empty test tank between 100 Hz and 500 Hz.

As is shown in Figure 4.7, three resonance peaks are believed to be observed in the measured frequency response: 125 Hz, 330 Hz, and 435 Hz, which correspond to the first three mechanical resonance modes of the lightly clamped circular steel plate calculated using Equation (24) and Equation (26): 90 Hz, 350 Hz, and 450 Hz.

The transfer function of the empty test tank had been re-measured multiple times at the same depth throughout the work (a period of roughly one year) and no significant deviations from Figure 4.7 were observed. Therefore, the transfer function curve in Figure 4.7 is used as the reference empty tank transfer function and later compared with simulated results and swim bladder measurement results.

4.3.2 FEM Simulation of Tank Transfer Function

Following the experimental measurement of the test tank's transfer function described in Subsection 4.3.1, a detailed FEM simulation was performed to corroborate both the analytically estimated plate modes (Subsection 4.2.1) and the experimentally detected resonance peaks in the water-filled tank. This simulation aimed to capture the vibrational behaviour of the lightly clamped steel bottom plate, focusing particularly on whether the three primary resonances indeed arose from the plate's first three bending modes. What follows is an account of the modelling approach, assumptions, meshing strategy, loading definition, and the results obtained.

3D Model Geometry and Material Properties

The three-dimensional model of the tank assembly built in SolidWorks, shown in Figure 4.4, was exported and transformed to a Parasolid .x_b file for FEM simulations in COMSOL Multiphysics (version 6.1) replicating the whole tank assembly, the cylindrical water domain inside it, and other ancillary mechanical parts. The bottom plate was imported and modelled as a circular steel disc of 2 mm thickness and 470 mm effective inner diameter, consistent with earlier dimensions. The bolted flange region around the plate's perimeter was also included to represent the transition zone where bolts apply pre-tension. The water domain fully occupied the inner cylindrical volume of the tank (with a hydrophone tube sealing the water outlet hole), created through a Boolean subtraction of the mechanical components from a larger water cylinder—thus capturing the fluid-filled space seamlessly touching the tank components.

The material properties used were as follows:

- Thin steel plate and bolts: density 7850 kg/m^3, Young's modulus 2.0 × 10^11 Pa, Poisson's ratio 0.30.
- Acrylic lid and tank body with flanges: density 1190 kg/m^3, Young's modulus 3.2 × 10^9 Pa, Poisson's ratio 0.35.
- Aluminium alloy supporting frame and feet: density 2700 kg/m^3, Young's modulus 7.0 × 10^{10} Pa, Poisson's ratio 0.33.
- Rubber gaskets: density 1100 kg/m^3, Young's modulus 2.0 × 10^6 Pa, Poisson's ratio 0.49, isotropic structural loss damping factor 0.05.
- Water: density 1000 kg/m^3, sound speed 1480 m/s.

The steel bottom plate was assigned a 20 kN bolt pre-tension condition where it joined with the tank flanges, mimicking the moderate torque reported during physical assembly for water tightness. This detail was crucial for approximating the "lightly clamped" boundary restraint in a realistic manner, rather than a purely theoretical simply supported condition.

Physics Interfaces and Coupling

Two primary physics interfaces were enabled in COMSOL:

Solid Mechanics, assigned to the steel plate, the flanges, and any other mechanical components of the whole tank assembly. This module solved for displacements, stresses, and strains in the solids under harmonic excitation. The bolt pre-tension was implemented within *Solid Mechanics* via a "Bolt Pretension" feature. Gravity was also included in this module to better simulate the effect on the tank transfer function due to the mass of the water.

Pressure Acoustics, Frequency Domain, assigned to the water domain. The acoustic wave equation was solved for acoustic pressures at each frequency, ensuring that the compressible fluid's density and speed of sound determined wave propagation characteristics. All fluid-solid interfaces (water–steel and water–acrylic boundaries) were coupled via the *Acoustic-Structure Boundary* module. This boundary guarantees that the normal velocity of the solid matches the fluid's particle velocity and that the pressure in the fluid imposes an appropriate load on the solid. By maintaining continuity of pressure and normal displacement, structural vibration can radiate acoustic waves into the fluid, while fluid pressure fluctuations can, conversely, excite structural motion. Since the water domain was fully surrounded by tank parts with acoustic-structure coupling, no PMLs was required as in FEM bubble resonance simulations in Chapter 3.

Loading Definition and Boundary Conditions

A harmonic sound source was simulated at the centre of the steel bottom plate, using a 10 N boundary load to represent the excitation of inertial shaker from the real experiment. Instead of distributing the force across an area, the load was set as a boundary condition in a small region approximating the shaker attachment (Figure 4.2), ensuring a consistent force amplitude across the frequency sweep (100–500 Hz). The bolt pre-tension setting guaranteed that the plate perimeter had no lateral or axial degrees of freedom, aside from potential micro-slip or rotation implied by the contact condition.

Meshing Strategy

A fine physics-controlled meshing strategy was applied to both the water volume and the structural components. In COMSOL's default setup, the solver automatically refines the mesh in regions where gradients of the physics variables are expected to be high—particularly near boundaries and potential resonant surfaces. For the acoustic domain, the mesh element size was selected to accurately resolve frequencies up to 500 Hz in water. This required the maximum element size (recommend to be at least six elements for the shortest wavelength) in the fluid domain should be smaller than 0.5 m if the maximum frequency was 500 Hz, but a substantially finer resolution (maximum 3 cm) was adopted for the simulation due to the limited physical dimensions of computation domains. Figure 4.8 shows the meshed test tank in COMSOL.

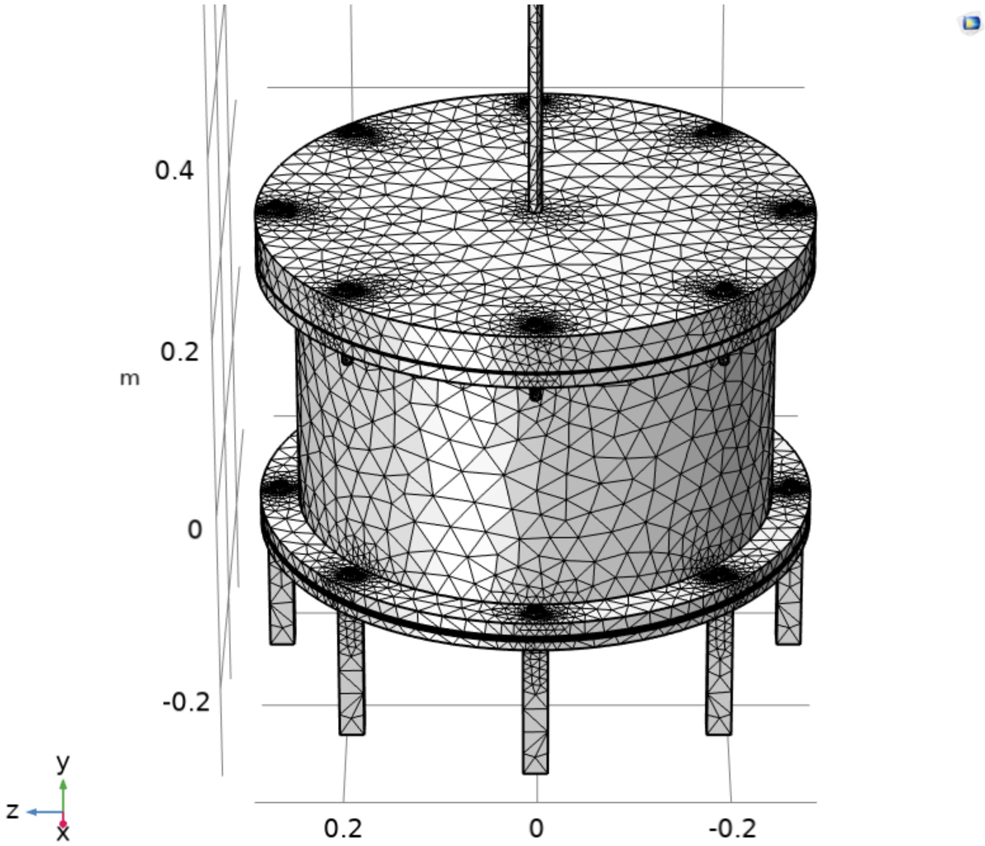

Figure 4.8 The meshed test tank in COMSOL awaiting further FEM simulations.

Simulation Results and Comparison

After assigning frequency analyses in the 100 Hz to 500 Hz range, the solver computed the steady-state response for each frequency step of 5 Hz. The frequency response was extracted at a location 25 cm above the bottom plate centre, which the hydrophone position in the physical tank during experiments. The resulting transfer function curve in Figure 4.9 shows three resonances at 155 Hz, 310 Hz, and 460 Hz. While these peaks do not perfectly match the measured values of 125 Hz, 330 Hz, and 435 Hz, they do lie reasonably close, especially given the complexities of real hardware assembly, fluid damping, and potential micro-gaps or O-rings that were not explicitly modelled.

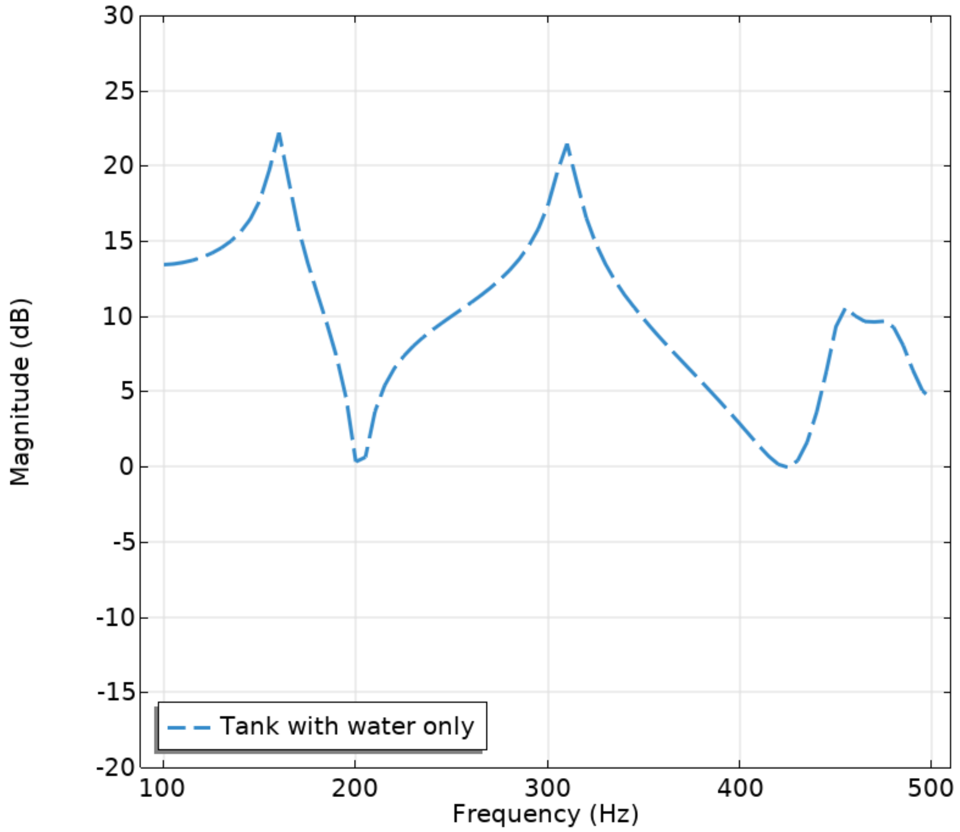

Figure 4.9 FEM simulated transfer function of the empty test tank between 100 Hz and 500 Hz.

Both experimentally measured and FEM simulated transfer functions have been plotted in Figure 4.10 with the absolute levels of the simulated result being adjusted to be similar the measured one.

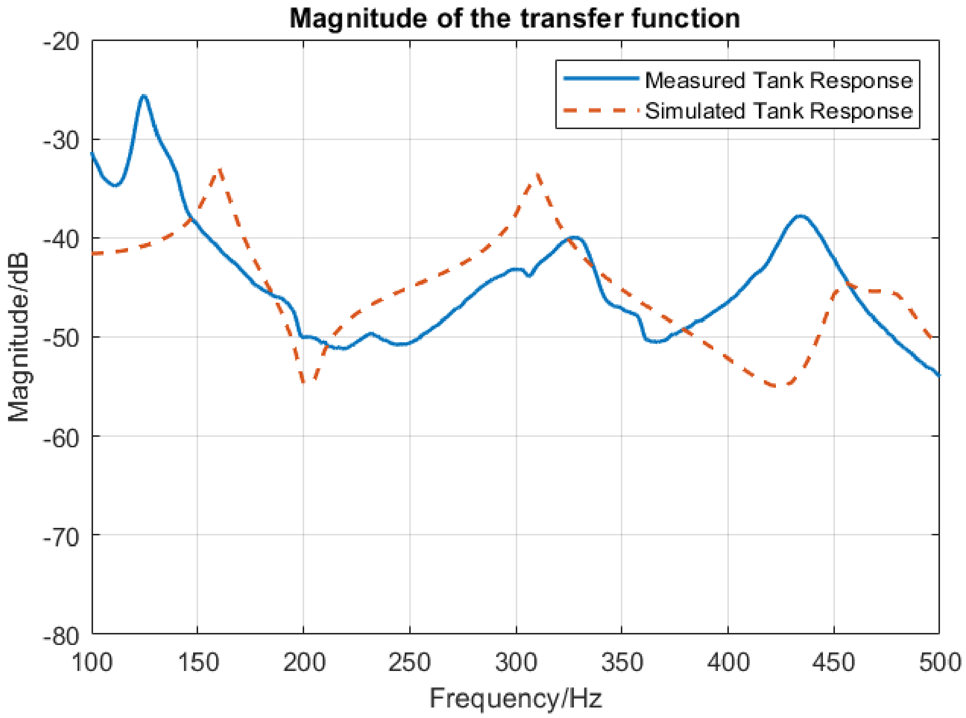

Figure 4.10 Comparison between experimentally measured transfer function and FEM simulated transfer function of the empty test tank between 100 Hz and 500 Hz.

The overall alignment of resonance frequencies between measured and simulated values verifies the ability of FEM simulations to predict and validate real-life measurements. However, the measured tank response does show a higher level below 200 Hz than the simulated result. It is within our expectation as the inertial shaker has a higher output force for driving signals below 200 Hz, as was shown in Figure 4.6. This alignment indicates that the first, second, and third bending modes of the steel plate are responsible for the primary acoustic resonance response in the test tank. To visualise the modes, the simulated stress distribution and deformation at the second resonance frequency (310 Hz) of the whole test tank is plotted in Figure 4.11. The colour on the tank represents the peak Von Mises stress, which reaches its highest at the centre of the bottom plate due to the excitation of boundary load from the inertial shaker. The rim of the bottom steel plate, however, was lightly clamped between the acrylic flange and the supporting frame by pretensioned bolts. Therefore, only the unclamped part (470 mm diameter) of the plate was clearly deformed under the stress, thus transmitting acoustic energy into the water body directly above it. To create Figure 4.11, the level of deformation was magnified by 3000 times to exaggerate the effect of stress. The stresses and deformations can be seen to be almost completely confined to the bottom plate. Figure 4.12 focuses on the deformed shapes of the plate at the tank resonance frequencies, and the plate's modal shapes can be observed.

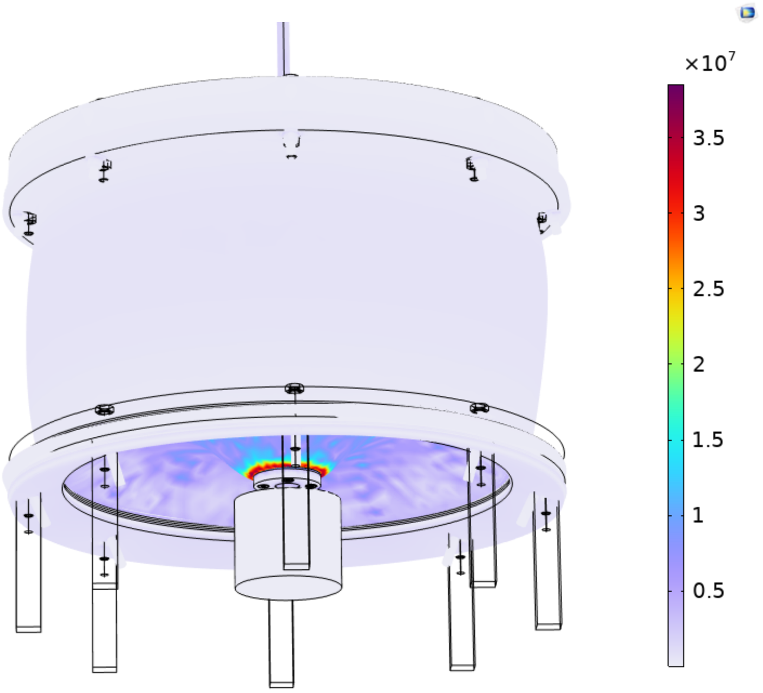

Figure 4.11 The simulated distribution of Von Mises stress and deformation of the test tank at its second resonance frequency (310 Hz).

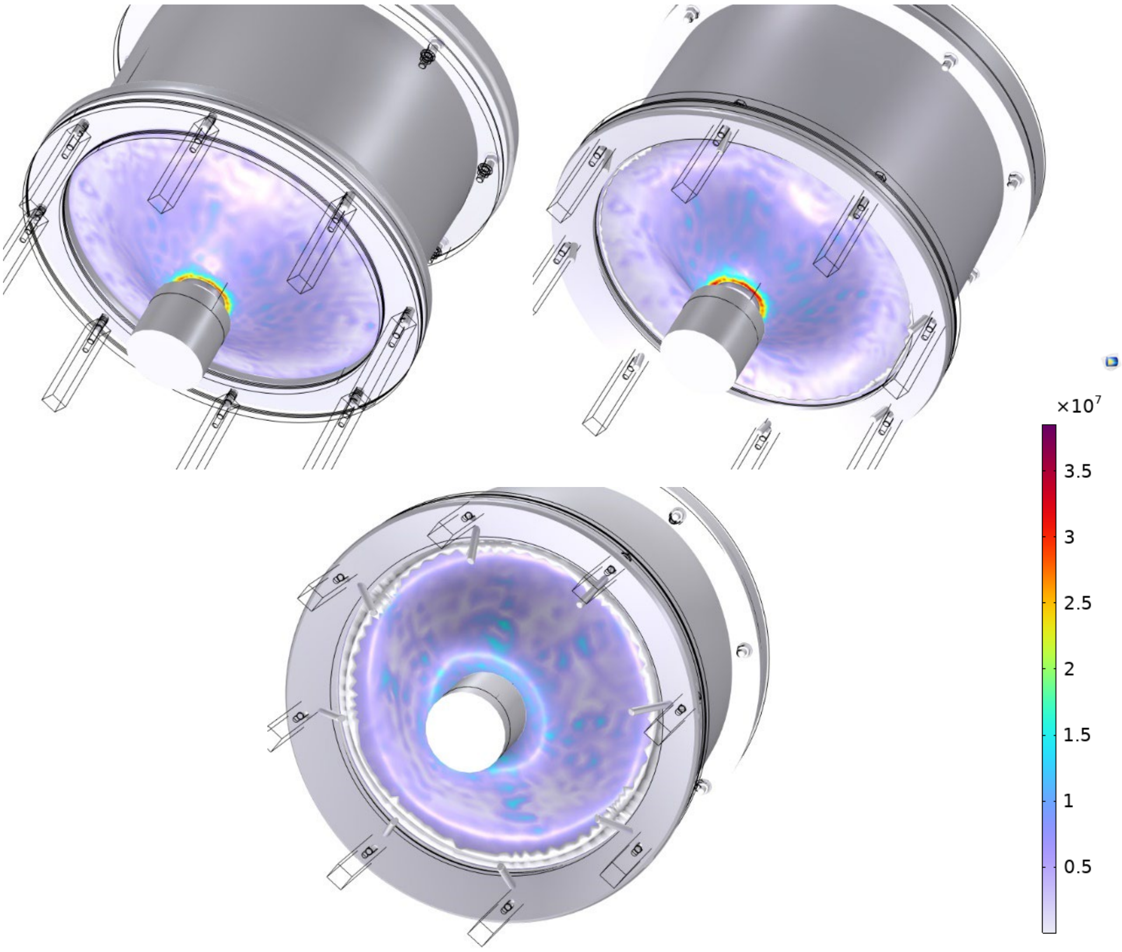

Figure 4.12 Stress distribution and deformed shapes of the bottom plate at simulated tank resonance frequencies: 155 Hz (top left), 310 Hz (top right), and 460 Hz (bottom).

The plate deformation reached the highest magnitude at the resonance frequencies in different modal patterns. Figure 4.13 shows the modal displacement shapes of a lightly clamped circular steel plot at the lowest three non-dimensional modal frequencies studied by Kermani *et al*., 2012, which presents similar modal patterns on the plate to our simulations in Figure 4.12.

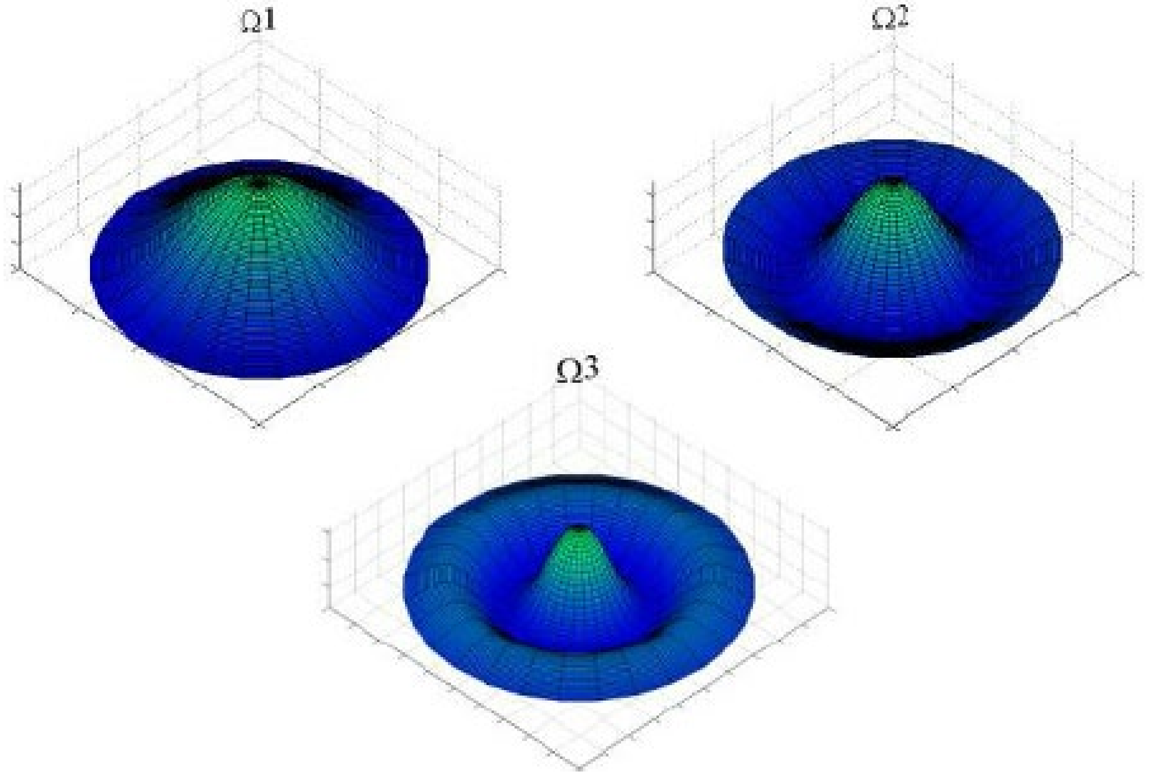

Figure 4.13 Thickness displacement mode shapes of a lightly clamped circular plate corresponding to the first three modal frequencies (Kermani *et al.*, 2012).

The first mode (155 Hz) features a broad curvature with no nodal circle, the second mode (310 Hz) has one nodal circle, and the third mode (460 Hz) has two nodal circles.

Following the analyses above, it is concluded that the three major tank resonances that appeared closely in both measurements and simulations are due to the first three mechanical modes of the lightly clamped circular plate under the excitations of the inertial shaker. The first three resonance frequencies from the Kirchhoff–Love thin-plate theory, experimental measurements, and FEM simulations are summarised in Table 4.1.

Table 4.1 Resonance frequencies of the test tank system using different methods.

Method	**1st Resonance**	**2nd Resonance**	**3rd Resonance**
Kirchhoff–Love thin-plate theory	90 Hz	350 Hz	450 Hz
Experimental measurements	125 Hz	330 Hz	435 Hz
FEM numerical simulations	155 Hz	310 Hz	460 Hz

From Table 4.1, one can see that the experimentally measured values for the first and the second resonance frequency lie between those of the thin-plate theory and the FEM simulation, while the measured third resonance frequency is somewhat lower than either predicted ones. The overall alignment between measured, estimated, and simulated values indicates that the fundamental, second, and third bending modes of the steel plate indeed drive the primary acoustic resonances of the test tank.

The differences between the FEM simulation and reality can be attributed to: a) material property uncertainties: the real Young's modulus, Poisson's ratio or densities may deviate slightly from values used in the simulations. b) bolt pre-tension variation: In practice, the actual clamp force may vary from the specified 20 kN. Inhomogeneous, or non-ideal contact conditions also introduce local stiffness variations. c) fluid damping and viscous losses: viscous and frictional effects in water were not comprehensively modelled but can shift resonance peaks. d) other damping mechanisms: small O-rings within the bottom plate sub-assembly and the hydrophone tube were neglected in the simulation. e) mesh refinement and convergence: while physics-controlled meshing is robust, extremely fine resolution might be required to capture subtle high-mode effects or contact nonlinearity at the boundary. f) boundary condition mismatch: the real clamping scenario and complicated acoustic boundary (*e.g.*, the acrylic tank wall being pressure-release) may deviate from the idealised implementation in COMSOL. g) the test tank and the floor it stood on might not be perfectly level, causing the overall modes to deviate from the perfect condition. Other factors like minor gaps, asymmetrical bolt tightening, local sealant behaviour, or slight misalignments can alter how the plate perimeter is constrained. These real-life boundary details may not be fully represented by the simplified or nominally uniform bolt pre-tension and contact assumptions in the FE model, resulting in shifts or splitting of actual resonances compared to their predicted counterparts.

In summary, this FEM simulation successfully reproduced the three primary resonance modes observed experimentally, which aligned satisfactorily with the measurement peaks and with prior theoretical estimates for a lightly clamped thin plate. The small discrepancies highlight typical challenges in capturing real-world hardware with finite element models, where additional damping, contact stiffness, or minor geometry variations may come into play, but also proved the ability of FEM simulations in the better designing and optimisation of experimental facilities. Overall, the good correspondence across theory, experiment, and simulation underscores the conclusion that the steel plate's first three bending modes govern the tank's low-to-mid frequency acoustic response—a crucial factor for any further investigations into fish swim bladder resonance, fish behavioural studies, or other advanced acoustic applications.

4.4 Experimental Methods for Live Fish Measurements

4.4.1 Fish Maintenance and Ethics

Common carp (*Cyprinus carpio*) (n = 30) in five size groups (4”- 6”, 6”- 8”, 8”- 10”, 10”- 12”, and 12”- 14”; with six fish in each group) were sourced from Fisher’s Pond Fishery, Eastleigh, and transported in oxygenated water to the Fish Husbandry Room at the Engineering Centre, Chilworth Science Park, University of Southampton, in April 2024. They were maintained in large holding tanks (1.5 m long, 1.0 m wide, and 0.8 m deep, filled to a water depth of 68.0 cm) containing approximately 1200 L of aerated, filtered, and dechlorinated water. The tanks were housed in a controlled environment with a photoperiod of 12:12 hours light:dark, replicating natural seasonal light conditions at the time of the year.

Figure 4.14 Photo of a 26-cm long common carp.

The fish were fed daily with a species-appropriate pellet feed (protein content: 42%), ensuring their nutritional requirements were met. Water quality parameters, including ammonia (0.1 (0.2) ppm), nitrites (0.0 (0.0) ppm), nitrates (40.0 (0.0) ppm), and pH (8.2 (0.0)) (measured using an API Freshwater Master Test Kit), were monitored daily to ensure optimal conditions. Temperature stability (12.3 (1.2)°C) was maintained throughout the holding period.

Partial water changes were performed weekly as necessary to maintain high water quality. To minimise stress, the tanks were positioned in a quiet, low-disturbance area, and the fish were monitored daily for signs of distress or illness. Any individuals displaying abnormal behaviour or signs of ill health were treated in accordance with established welfare protocols, which included consulting the Named Animal Care and Welfare Officer (NACWO).

The common carp were acclimated in the holding tanks for at least four days prior to the commencement of experimental trials. During this period, they were observed for any signs of stress or difficulty adapting to the tank environment. This husbandry protocol ensured that all fish were in optimal health and acclimatised to experimental conditions, providing a stable baseline for subsequent acoustic exposure studies.

All experiments were conducted in accordance with the guidelines set out by the UK Home Office under the Animal Welfare Act (2006) and adhered to all relevant international, national, and institutional protocols for the care and use of animals. The study received approval from the University of Southampton Ethics and Research Governance Committee (87876.A1) following review by the Animal Welfare and Ethics Review Body.

The principles of the Three Rs (replacement, refinement, and reduction; NC3Rs, 2014) were applied throughout the experimental design to minimise the number of common carp used, while ensuring robust and reliable data collection. Fish were handled with care, and the duration of handling was kept to the minimum necessary for safe transfer between holding and experimental tanks.

During the trials, there were no observed signs of stress, fatigue, or behavioural anomalies in response to the acoustic stimuli. All fish resumed normal activity patterns immediately following exposure, irrespective of the SPLrms or frequency applied. The experimental procedures were designed to mitigate any potential welfare concerns, ensuring that the health and wellbeing of the fish were maintained throughout the study.

4.4.2 Measurement Protocol

The measurement of swim bladder resonance properties was conducted in the specially designed acrylic test tank. The tank was filled completely with 53 L aerated and dechlorinated water sourced directly from the husbandry tanks to ensure consistency in water quality and temperature throughout the trials.

Common carp were individually transferred from the holding tanks to the experimental tank using a fine-meshed net, following a two-net method to minimise handling time and reduce stress and potential physical injury. Each fish underwent a 10-minute acclimation period in the experimental tank prior to acoustic exposure. This acclimation period was monitored via continuous video recording to ensure the fish settled and exhibited normal behaviour.

After the acclimation, six fish were tested in each of the five sizes. Non-invasive acoustic measurements were performed by exposing each fish to white Gaussian noise at 125 dB re 1 μPa for a duration of 100 seconds using the same method and experimental set-up as measurements of the empty tank transfer function in Subsection 4.3.1 with the same input signal. The 125 dB re 1 μPa noise was only 12 dB higher than the noise floor of 113 dB re 1 μPa in order to prevent excessive stress caused by the sound stimulus, and it was also later used as the masking noise during the behavioural studies.

Acoustic signals were recorded with the same Bruel & Kjaer 8103 hydrophone placed 25 cm above the bottom plate at the centre of the tank (same position for tank transfer function measurement and simulation). Transfer functions of the tank fully filled with water and holding a live, free-swimming common carp inside were calculated using MATLAB immediately after the signal recording to analyse swim bladder resonance properties. After the measurement of swim bladder resonance properties of each individual fish, a following behavioural study was conducted to determine fish startle responses to pure tone stimuli at the swim bladder resonance frequencies, which will be later discussed separately in Chapter 5. Figure 4.15 is the photo of a free-swimming common carp inside the test tank during a swim bladder resonance measurement.

Figure 4.15 Photo of a common carp inside the test tank.

Upon completion of each trial, fish were placed and humanely killed in a small tank with a fatal overdose of anaesthetic (2-phenoxyethanol), and then death was confirmed through the destruction of the brain in accordance with Schedule 1 of Animals Scientific Procedures Act 1986 (ASPA). This procedure was conducted by those trained and certified as competent to do so, and who were named on the “University Humane Killing Register”. After the confirmation of death, body fork length, height, and weight of each individual were measured and noted, along with the physical dimensions of every gas chamber of the swim bladder, as is shown in Figure 4.16. Humane killing and dimensional measuring took place immediately after each trial so that the swim bladder was unlikely to suffer significant volume change.

Figure 4.16 Photo of an intact, healthy and sufficiently inflated swim bladder of a common carp.

4 specimens coming separately from four size groups (6–8", 8–10", 10–12", and 12–14") were returned to a husbandry tank after the swim bladder resonance measurements and behavioural studies without being immediately euthanised and dissected because they were used for CT scanning at the end of the whole experiment. Common carp of the smallest size group (4”- 6”) showed early signs of behavioural stress within their husbandry tank before any measurements in the test tank. To prevent the potential outbreak of any health issues like fungal infection, all six fishes of this size group were used for swim bladder resonance measurements and behavioural studies before the rest of the fish and were euthanised after the trials. Therefore, there was no specimen from the smallest size group that available for CT scanning.

The water in the test tank was fully replaced after each trial to eliminate any residual cues from previous trials. The test tank was cleaned thoroughly to ensure no chemical or physiological markers left and interfered with subsequent experiments. No abnormal behaviour, stress, or fatigue was observed in the common carp during or after the trials. This protocol ensured the precise measurement of swim bladder resonance properties under controlled conditions, contributing to the study of swim bladder acoustic responses in freshwater fish species.

4.5 Analysis and Statistics of Resonance Frequencies

4.5.1 Representative Results and Observations

This subsection presents a detailed overview of the transfer functions acquired from each of the five size groups tested. As outlined in Subsection 4.4.2, each measurement involved fully immersing a live, free-swimming common carp in the fully water-filled acrylic test tank, exciting the system with a controlled acoustic signal (input signal of the system), and recording the resulting pressure field with a centrally located hydrophone (output signal of the system). Through these recordings, a measurement of the system transfer function was generated, allowing the identification of a resonance peak attributable to the oscillation of the fish swim bladder on top of the original transfer function of the empty test tank simulated and measured in Section 4.3.

In the figures that follow, one representative transfer function is showcased per size group. Notably, the presence of a live fish typically modifies the baseline tank response mainly by superpositioning an additional resonance peak within a certain frequency region depending on the size of the swim bladder. This peak corresponds to the fundamental resonance of the fish swim bladder, whose magnitude and bandwidth vary from fish to fish and primarily depending on the swim bladder size. For smaller individuals (4”- 6” group), the resonance peak tends to occur at relatively higher frequencies, aligning with the expectation that smaller swim bladders exhibit reduced volumes and therefore resonate at higher sound frequencies. Conversely, for larger fish (10”- 12” and 12”- 14” groups), the resonance peak tends to appear at lower frequencies, reflecting the greater gas volume in bigger swim bladders.

Although this general trend is consistent across specimens, certain variations are evident in both the resonance frequency and the overall amplitude of the peak. These discrepancies can be attributed to several factors, including inter-individual differences in bladder shape or mechanical properties of surrounding fish soft tissue. Additionally, because the fish were free to swim and could not be controlled to stay at the same position in every trial, minor positional adjustments inside the tank could alter the coupling between the swim bladder and the acoustic field, thus influencing the sharpness, or magnitude of the resonance peak.

The results shown in the subsequent figures underscore the repeatability and clarity of the measurement protocol: even amidst small inter-trial variations, the main swim bladder resonance is identifiable across individuals. This observation not only corroborates the viability of the non-invasive approach but also highlights the potential for further quantitative analyses. By examining trends in resonance frequency with respect to fish size and weight, we can begin to establish empirical relationships that may ultimately lead to improved modelling of fish acoustics and a deeper understanding of swim bladder function in living fish under naturalistic conditions.

Specimen A (*L* = 26.2 cm, *W* = 668 g) from fish size group 1 (12”- 14”):

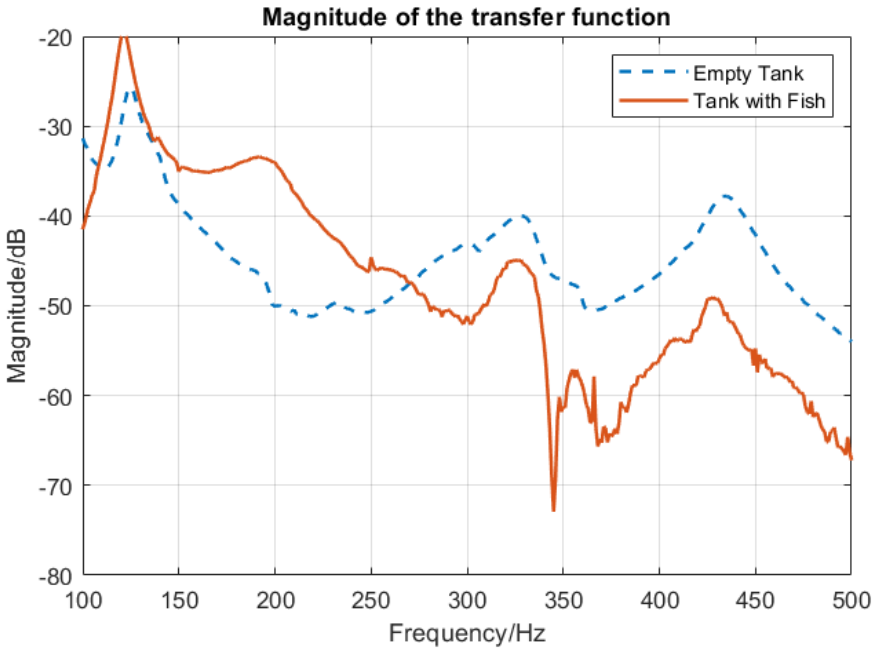

Figure 4.17 Measured transfer functions of the empty tank (blue dashed line) and the tank with a live, free-swimming common carp (solid orange line) showing the swim bladder resonance frequency f_R = 192 Hz and the quality factor Q_R = 5.4.

Specimen B (*L* = 23 cm, *W* = 380 g) from fish size group 2 (10”- 12”):

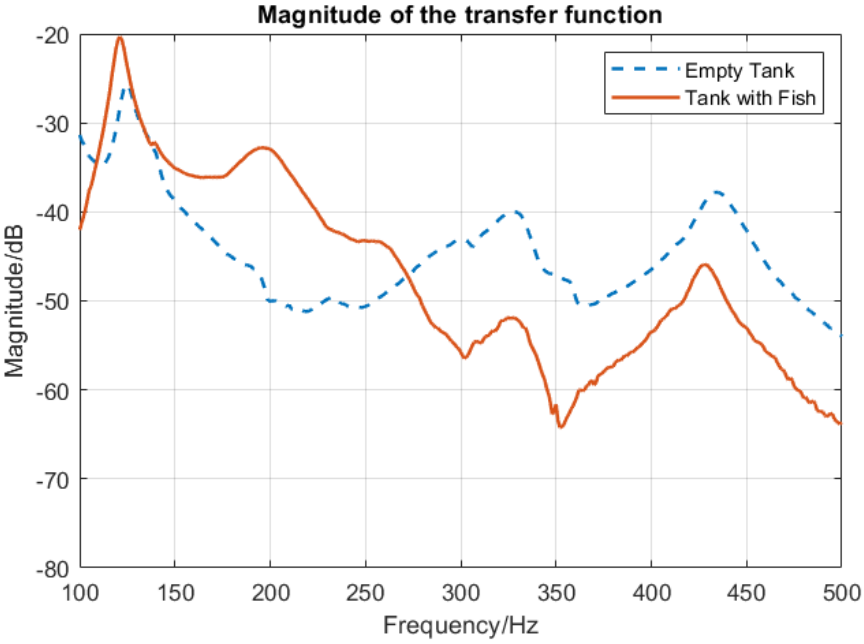

Figure 4.18 Measured transfer functions of the empty tank (blue dashed line) and the tank with a live, free-swimming common carp (solid orange line) showing the swim bladder resonance frequency f_R = 201 Hz and the quality factor Q_R = 6.5.

Specimen C (*L* = 21 cm, *W* = 290 g) from fish size group 3 (8”- 10”):

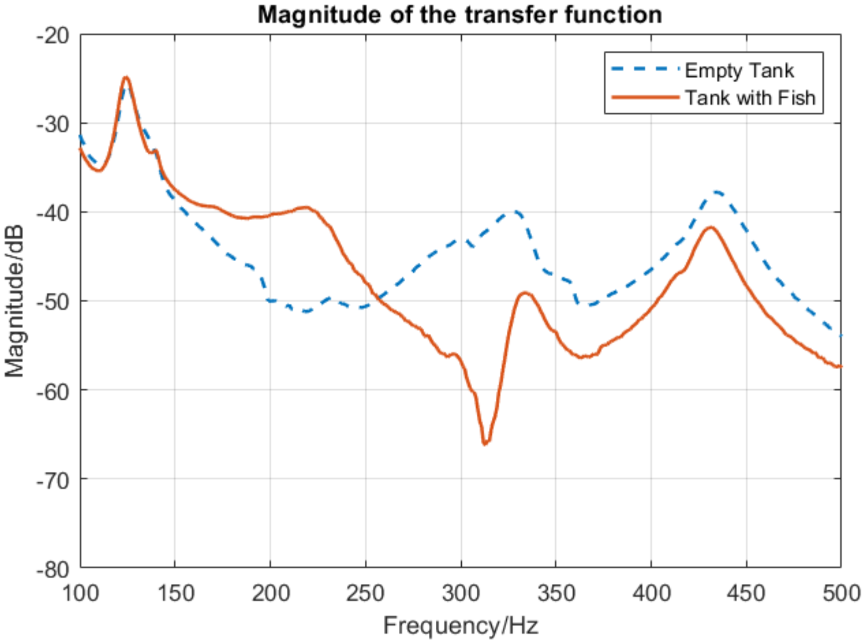

Figure 4.19 Measured transfer functions of the empty tank (blue dashed line) and the tank with a live, free-swimming common carp (solid orange line) showing the swim bladder resonance frequency f_R = 220 Hz and the quality factor Q_R = 7.5.

Specimen D (*L* = 16 cm, *W* = 144 g) from fish size group 4 (6”- 8”):

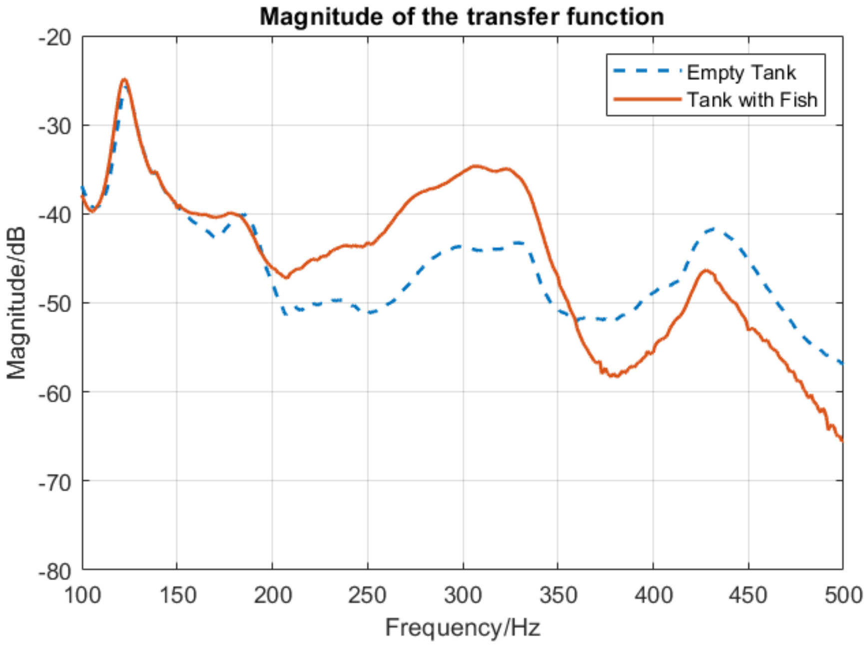

Figure 4.20 Measured transfer functions of the empty tank (blue dashed line) and the tank with a live, free-swimming common carp (solid orange line) showing the swim bladder resonance frequency f_R = 302 Hz and the quality factor Q_R = 6.3.

Specimen E (*L* = 12.5 cm, *W* = 42 g) from fish size group 5 (4”- 6”):

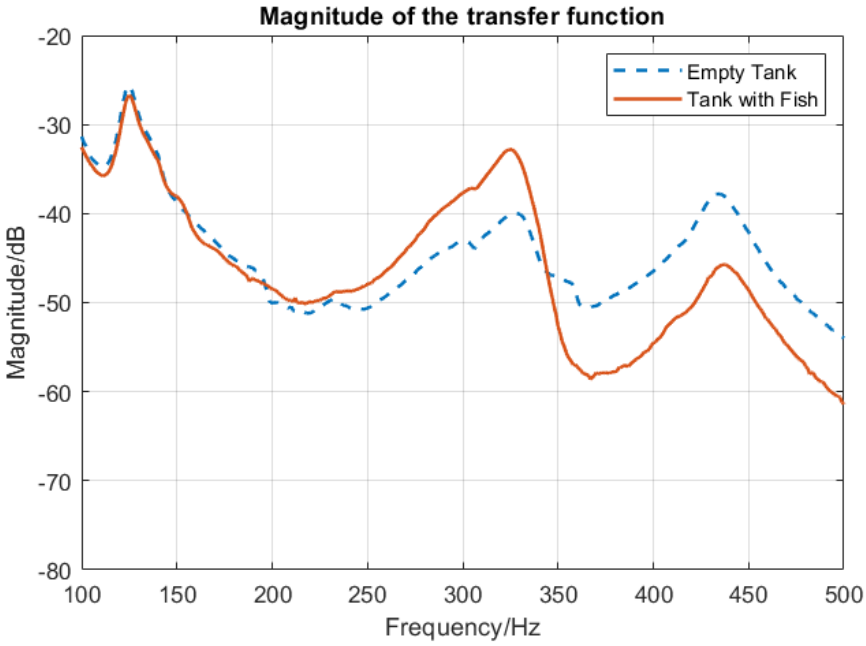

Figure 4.21 Measured transfer functions of the empty tank (blue dashed line) and the tank with a live, free-swimming common carp (solid orange line) showing the swim bladder resonance frequency f_R = 327 Hz and the quality factor Q_R = 7.2.

Figure 4.17 – 4.21 show five representative transfer functions of the tank fully with water and a common carp (specimen A - E) inside, in comparison with the measured empty tank transfer function. Measured fish body fork length, *L*, and body weight, *W*, are presented along with the measured resonance frequency, f_R , and quality factor, Q_R . As expected, bigger fish with bigger swim bladders have lower resonance frequencies, while smaller fish with smaller swim bladders have comparatively higher resonance frequencies. Quality factors, similar to our findings in Chapter 3, are not clearly related to the body length or weight but may vary due to the different physiological patterns of each individual like swim bladder shape, muscle tension, and other soft tissue near the swim bladder. The statistical relationship between body length, weight, and resonance properties will be further analysed in Subsection 4.5.2.

The shapes of the resonance peaks shown in the figures above are correlated to the shape of the empty tank transfer function at the frequency range where the swim bladder resonance lies. Therefore, some resonance peaks appear slightly skewed, broader on one side than the other side, or overlapped with the second tank resonance due to interferences from the empty tank transfer function. The swim bladder acts as a passive resonator whose radiated sound energy depends not only on the near-resonance properties of the swim bladder itself but is also highly correlated to the frequency pattern of the driving signal, in such cases, presented as the empty tank transfer function. Being driven by the signal with a perfectly flat frequency response would be ideal to present the natural shape of the swim bladder resonance, however, it is rather impossible to achieve such a driving condition in reality, but we can aim to optimise the experimental equipment to be flatter in a certain frequency range like the impedance tube under 400 Hz while maintaining the efficient and fish-friendly design.

For bigger fish like Specimen A, B, and C, their swim bladder resonances lie between the first tank mode and the second tank mode, so their resonance peaks are easy to be observed in Figure 4.17, 4.18, and 4.19. However, smaller specimens like Specimen D and E are much smaller than the bigger groups, therefore, their swim bladder resonance frequencies are expected to be higher and potentially overlap with the second tank mode at around 325 Hz, which makes it difficult to identify the resonance peaks and distinguish between a fish and a tank mode in the transfer functions. Even if the swim bladder resonance peak merged with the second tank mode, it is still obvious that the magnitude of the second tank mode has been increased due to the introduction of the swim bladder by about 8 dB in Figure 4.20 and 4.21, representing the presence of the swim bladder resonance. The magnitude of the original tank modes was very stable throughout the whole 6-month-long experiment and would not change unless specifically amplified by certain factors, which, in the experiments of this project, only happened when a fish swim bladder resonance overlapped with it. Besides, the presence swim bladder resonance would also bring in another effect: the attenuation of the tank response at frequencies higher than the swim bladder resonance frequency. Figure 4.17, 4.18, and 4.19 all showed the drop of magnitude in the transfer function for frequencies higher than the swim bladder resonance frequency when the swim bladder resonance was present. Similarly, the same effect also appeared in Figure 4.20 and 4.21 right above the second tank mode, again indicating the presence of swim bladder resonance even it overlapped with the second tank mode. The resonance frequency and quality factor were measured after subtracting the 'Tank with fish' curve with the 'Empty tank' curve, which made it easier to take measurements. The fact that swim bladder resonance of small fish overlapping with the second tank mode will be simulated, validated, and discussed in later sections when the 3D reconstruction model of CT-scanned Specimen D's swim bladder is used for FEM simulations.

Results above proved the method's ability to achieve non-invasive measurement of swim bladder resonance properties on live, free-swimming fish inside the test tank without touching the fish or applying anaesthesia, euthanasia, or the physical removal of swim bladder from the test fish. Moreover, this method presented the potential ability of non-invasively diagnosing swim bladder diseases on live and healthy-looking fish. Specimen F was a normal, healthy-looking common carp from fish size group 3 (8"- 10"), who showed no abnormality during fish maintenance, feeding, and the experimental measurement. However, unlike other trials on other test fish, recorded signal during the test on specimen F showed no resonance patterns in the measured transfer function, which was basically in the same shape as the empty tank transfer function. Figure 4.22 shows the measured transfer function of Specimen F. For other healthy specimens from its size group, the swim bladder resonance frequency is expected to be roughly around 225 Hz, and would not overlap with any of the tank modes. In Figure 4.22, there is no clear sign of magnitude amplification or attenuation throughout the transfer function like results in figures above that showed swim bladder resonance effects. Therefore, it is deemed that there is not any swim bladder resonance on Specimen F in Figure 4.22.

Specimen F (*L* = 20 cm, *W* = 247 g) from fish size group 3 (8”- 10”), **abnormal swim bladder**:

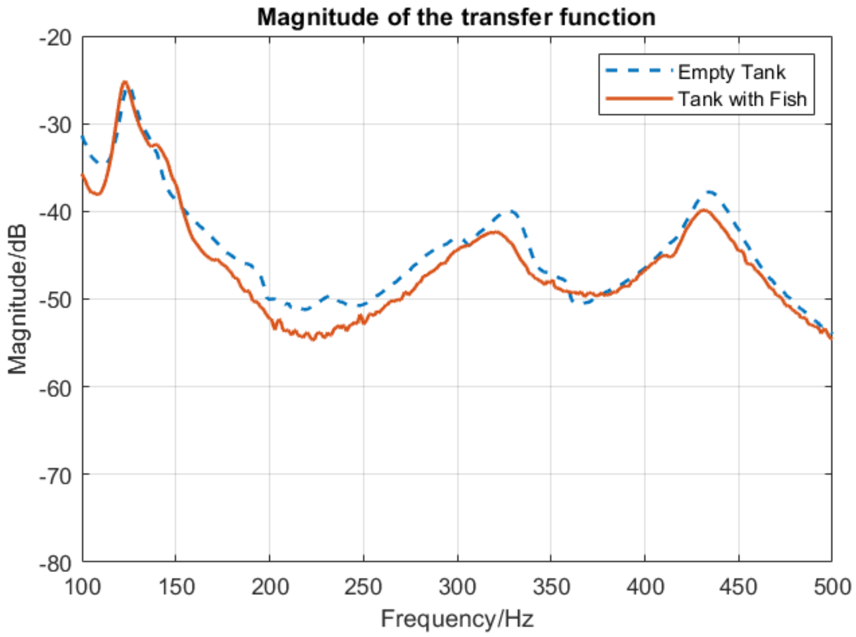

Figure 4.22 Measured transfer functions of the empty tank (blue dashed line) and the tank with a live, healthy-looking, free-swimming common carp with an abnormal swim bladder (solid orange line) showing no evidence of swim bladder resonance.

Immediately after the measurement, specimen F was euthanised and dissected to examine the swim bladder. Figure 4.23 shows the removed swim bladder of specimen F with clear abnormality. Apart from the tumour-like tissue growing on the swim bladder wall and the pneumatic duct, the posterior chamber of the swim bladder was dislocated, and bigger than normal and healthy swim bladder posterior chambers. The swim bladder wall of the posterior chamber was clearly thicker and had an irregular surface texture. Moreover, the abnormal swim bladder was also insufficiently inflated as seen in healthy specimens (Figure 4.16). Insufficient inflation of the swim bladder would result in low surface tension so the abnormal swim bladder will not act as an encapsulated bubble and not resonate. Sirri *et al*., 2020, also discovered similar symptoms in koi carp (*Cyprinus rubrofuscus "koi"*, previously named as *Cyprinus carpio*, the same as common carp), coloured varieties of common carp, that tumours can cause dislocation, enlargement, and other abnormalities on the swim bladder. Figure 4.24 shows the swim bladder with germ-cell tumour diagnosed by histology, which shares similar visual patterns as the abnormal swim bladder of specimen F in Figure 4.23.

This measurement-based diagnosis prior to dissection shows the potential of this method to non-invasively diagnose abnormalities in swim bladders, for instance to determine the level of parasitic infection in swim bladders of critically endangered European eel (*Anguilla anguilla*), which will be later discussed in Section 4.9.

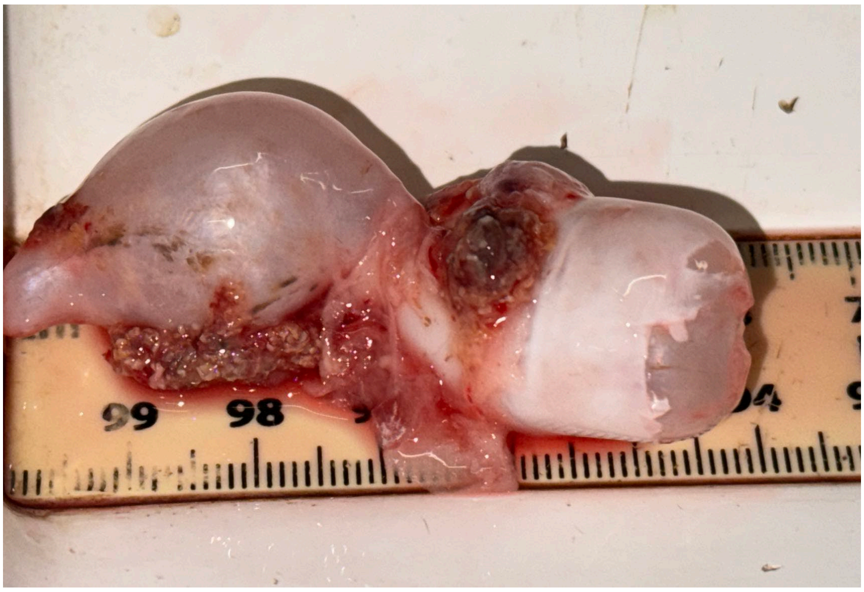

Figure 4.23 Photo of the abnormal, insufficiently inflated swim bladder of Specimen F with multiple tumours growing on and compressing the swim bladder wall and the pneumatic duct.

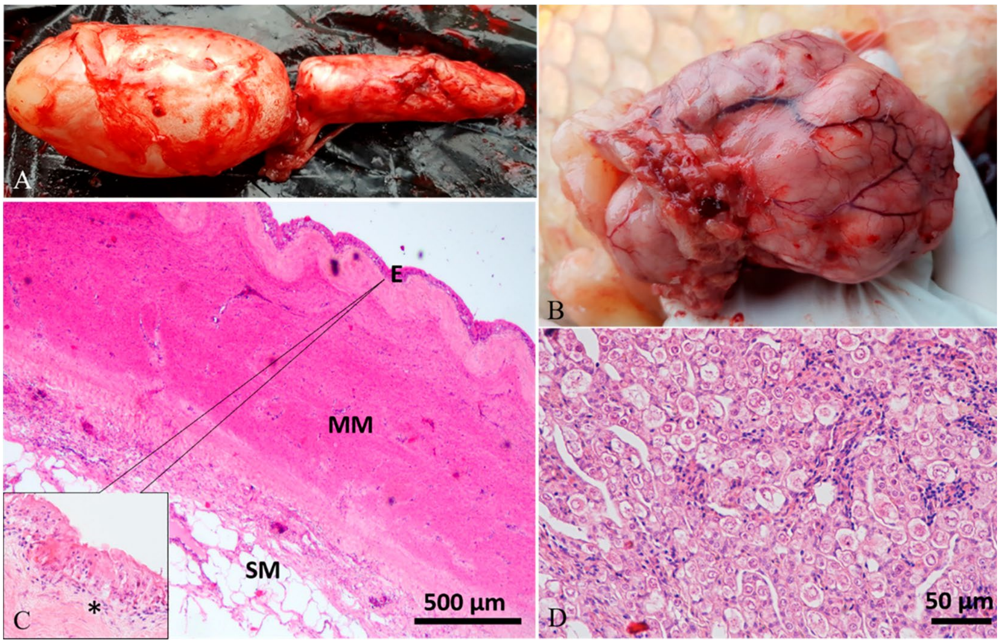

Figure 4.24 (**A**) Swim bladder showing a moderate enlargement of the posterior chamber. (**B**) The fish had a large intracoelomic tumour that is very similar to the tumour tissues we found in Figure 4.23, which caused the compression and deformation of the swim bladder. (**C**) Histological analysis of the swim bladder showed fibrous hyperplasia of the muscularis mucosae, submucosal multifocal inflammatory cell infiltration, edema of lamina propria, and mucosal (**E**) hyperplasia with squamous metaplasia. (**D**) Histology of the tumour revealed a gonadal germ-cell tumour (H&E stain) (Sirri *et al.*, 2020).

4.5.2 Statistical Analysis

In this section, we focus on exploring the statistical relationships among the key morphological and acoustic parameters measured in the 30 fish specimens. Our goal is to determine whether a specimen's fork length, body height, and body weight correlate with its measured resonance frequency and quality factor. Table 4.2 presents a summary of all the information of the specimens.

Table 4.2 Summary of fork length, body height, body weight, resonance frequency and quality factor for 30 Specimens.

Fish number	**Fork length (cm)**	**Body height (cm)**	**Body weight (g)**	**Measured f_R (Hz)**	**Measured *Q***	**Specimen ID**
1	11	4.5	20	332	6.6	
2	11.5	4	23	341	5.2	
3	12	4.5	27	343	6.1	
4	12	4.5	25	332	5.9	
5	12.5	5	40	327	7.2	E
6	13	5	52	296	7.1	
7	15	5.5	106	293	5.4	
8	15	6	110	296	6	
9	15	6.2	118	300	4.8	
10	15.5	5.7	122	297	7.7	
11	15.5	5.5	115	304	5.7	
12	16	6.4	144	302	6.3	D
13	16	6.2	140	286	5.8	
14	20	7.5	247	N/A	N/A	F
15	20.8	8	290	220	7.5	C
16	21	8	295	210	7.2	
17	21.3	7.5	293	215	6.7	
18	22	7.5	300	211	5.3	

19	22.5	8	307	221	7	
20	23	7.3	350	212	5.4	
21	23	8.5	374	220	6.9	
22	23.5	8.5	380	201	6.5	B
23	24	8.3	420	199	6	
24	25	9.5	504	197	6.3	
25	26.2	11	668	191	5.4	A
26	26.5	10.5	677	185	6.4	
27	27	10.7	672	180	5.6	
28	27.3	10	700	187	6.2	
29	27.7	10.5	741	178	4.9	
30	28	11.2	810	175	5.6	

One of the key factors in Table 4.2 is the body fork length of the fish, which was the initial controlled factor in the experimental design phase and was expected to be highly correlated with other factors like body weight, body height, and of particular interests here, swim bladder resonance frequency. Other parameters were also measured and considered, which included: total length, height, and width of the swim bladder; length, height, and width of the anterior chamber and the posterior chamber of the swim bladder. Internal gas volume within the two chambers could be calculated based on the measurement, and was also considered potentially as metrics to be analysed with factors like body length and resonance frequency. However, it was found that the shape of swim bladders on different specimens was rather random, resulting in uncontrollable errors in estimating the internal gas volume. For example, some fish had big and more spherical anterior chambers with tiny but conic posterior chambers (like Specimen D in the next section), while some other fish had more balanced two ellipsoidal chambers (like Specimen B in the next section). Therefore, only the relationships between body length and body weight, body height, measured swim bladder resonance frequency, and measured quality factor are illustrated in the figures below:

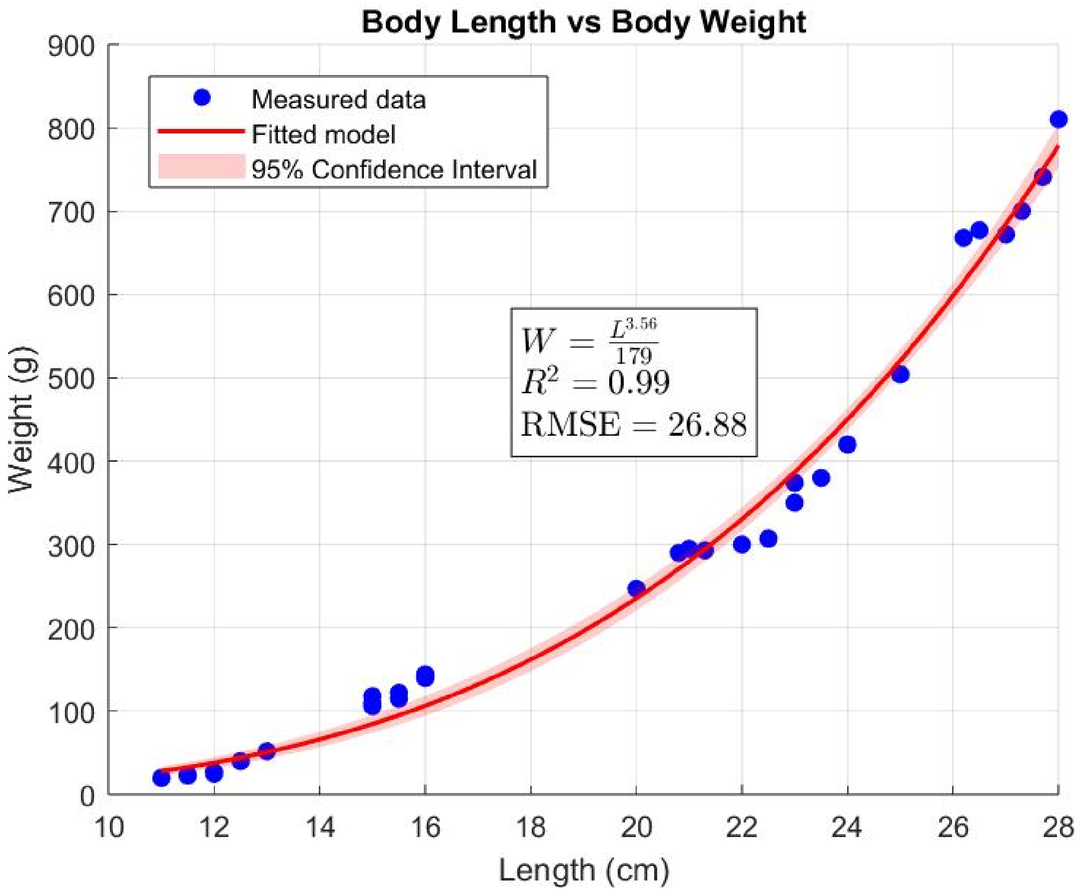

Figure 4.25 The fitted relationship between measured body length and body weight.

In Figure 4.25, the measured data (blue dots) and the fitted model (red curve) illustrate a clear power-law relationship between measured body length (*L*) and measured body weight (*W*). The curve shows that weight increases rapidly with length, as described by the fitted exponent factor of 3.56, which is within the range of common biological scaling factors in fish growth. The high coefficient of determination $R^2 = 0.99$ and relatively low Root Mean Square Error (RMSE) of 26.88 suggest an excellent fit. Biologically, this indicates that as the fish grow in length, their body mass rises in a manner slightly faster than cubic scaling. Moreover, the lack of measured data between 16 cm and 20 cm indicates an imperfectly controlled body length distribution in test fish.

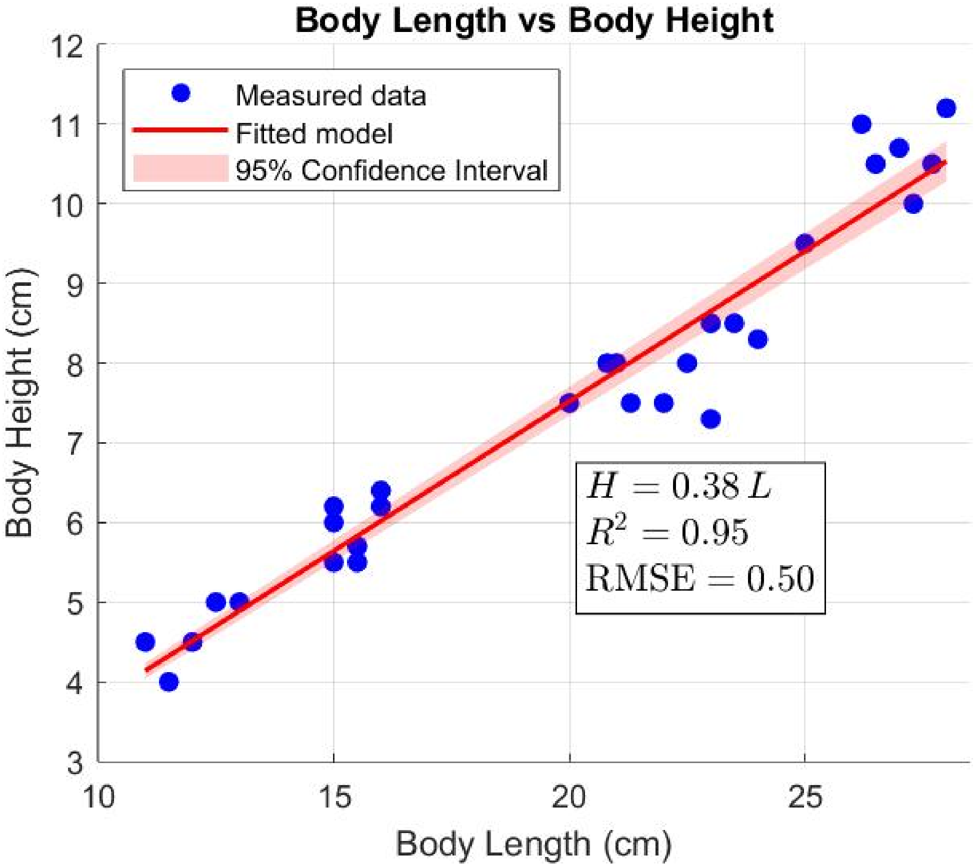

Figure 4.26 The fitted relationship between measured body length and body weight.

Figure 4.26 plots body height (*H*) against body length (*L*) and shows a strong linear trend. The linear fitting line ($H = 0.38L$) captures most of the variability, as reflected by the high $R^2 = 0.95$ and an RMSE of 0.5. This strong correlation implies that fish body height scales in near-linear proportion to length with a low level of variation due to differences in individual morphological characteristics, which indicates a relationship consistent with typical morphological growth patterns where overall body dimensions generally expand in unison. Moreover, the strong correlation between body length and body height also implies the swim bladder length and height are likely to be correlated with fish body length and height, since the swim bladder dimensions are roughly proportional to fish body dimensions.

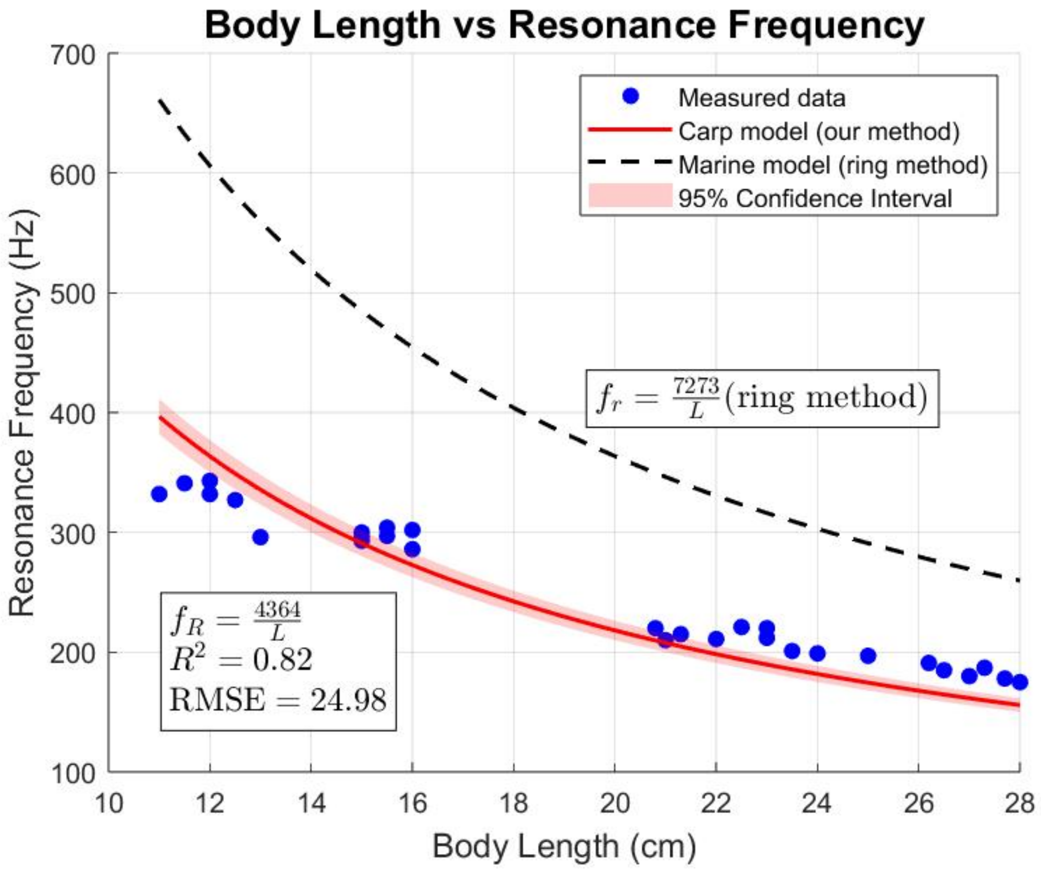

Figure 4.27 The fitted relationship between measured body length and measured swim bladder resonance frequency in comparison with the model proposed by McCartney and Stubbs, 1971.

In Figure 4.27, the measured resonance frequencies (blue dots) are plotted against body length, along with two comparative curves: a "Carp model" (based on the method of this thesis, solid red line) and a "Marine model" (based on the ring method proposed by McCartney and Stubbs, 1971, dashed black line). The measured points follow a downward trend, indicating that measured resonance frequency f_R decreases as the fish grows larger, which is in agreement with our previous findings on recently euthanised brown trout in Chapter 3. Our fitted model, $f_R = 4364 / L$, yields an $R^2 = 0.82$, and a RMSE of 24.98. However, the ring-method model, $f_r = 7273 / L$, derived from measurements on saltwater species by McCartney and Stubbs, 1971, overestimates resonance frequency for much of the length range in this particular group of fish. Overall, the negative correlation reflects that a larger swim bladder volume (associated with a bigger fish) typically resonates at a lower frequency. However, even if the body length was considered to be the main controlled independent variable both in this fitting and the ring-method based model, we noticed that the fitting in Figure 4.27 was not accurate enough. The prediction seemed to be higher than measurements for smaller fish while lower than measurements for bigger fish. It can be argued that a straight-line fitting may be better than the inverse curve. However, the inverse curve fitting was not only widely used in previous research (McCartney and Stubbs, 1971; Love, 1978; Cox and Rogers, 1987), but also based on the nature of the swim bladder resonance frequency inversely depending on the swim bladder spherical equivalent radius (Eq. 1), which is highly related to the fish body volume, fish body length, and fish body weight. Hence, the inverse relationship was chosen to fit between measured body length and measured swim bladder resonance frequency. Fish body weight was introduced as the second independent variable along with body length for a better fitting by taking morphological difference between individuals into account.

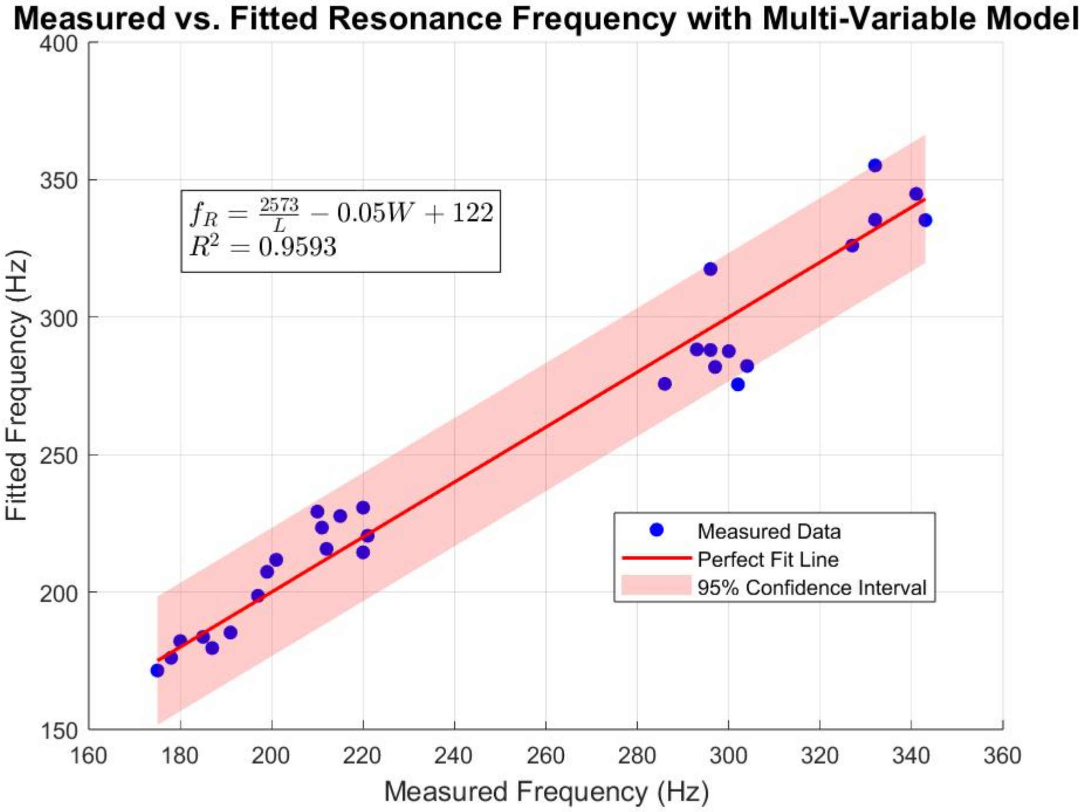

Figure 4.28 The relationship between measured swim bladder resonance frequency and fitted swim bladder resonance frequency based on a two-variable model.

Figure 4.28 compares the measured resonance frequencies (blue dots) against a fitted multi-variable model (red solid line), which incorporates both body length (*L*) and body weight (*W*). The new model, $f_R = 2573 / L - 0.05W + 122$, achieves a $R^2 \approx 0.96$, indicating that adding weight as a secondary predictor significantly refines the resonance frequency estimate relative to length-only formulas. The shaded region shows the 95% confidence interval, within which most data points lie. This improvement suggests that incorporating mass, not just length, provides a more realistic description of the swim bladder resonance properties, as fish of similar length but different bulk might display slightly different resonances. It also implies that a shorter fish may have a slightly higher swim bladder volume to fish body volume rate than a longer one (allometric growth pattern), agreeing with the finding in Figure 4.27 that body-length-based model predicted higher for shorter fish and lower for longer fish, which again supports the importance of using a multi-variable model in predicting swim bladder resonance frequencies.

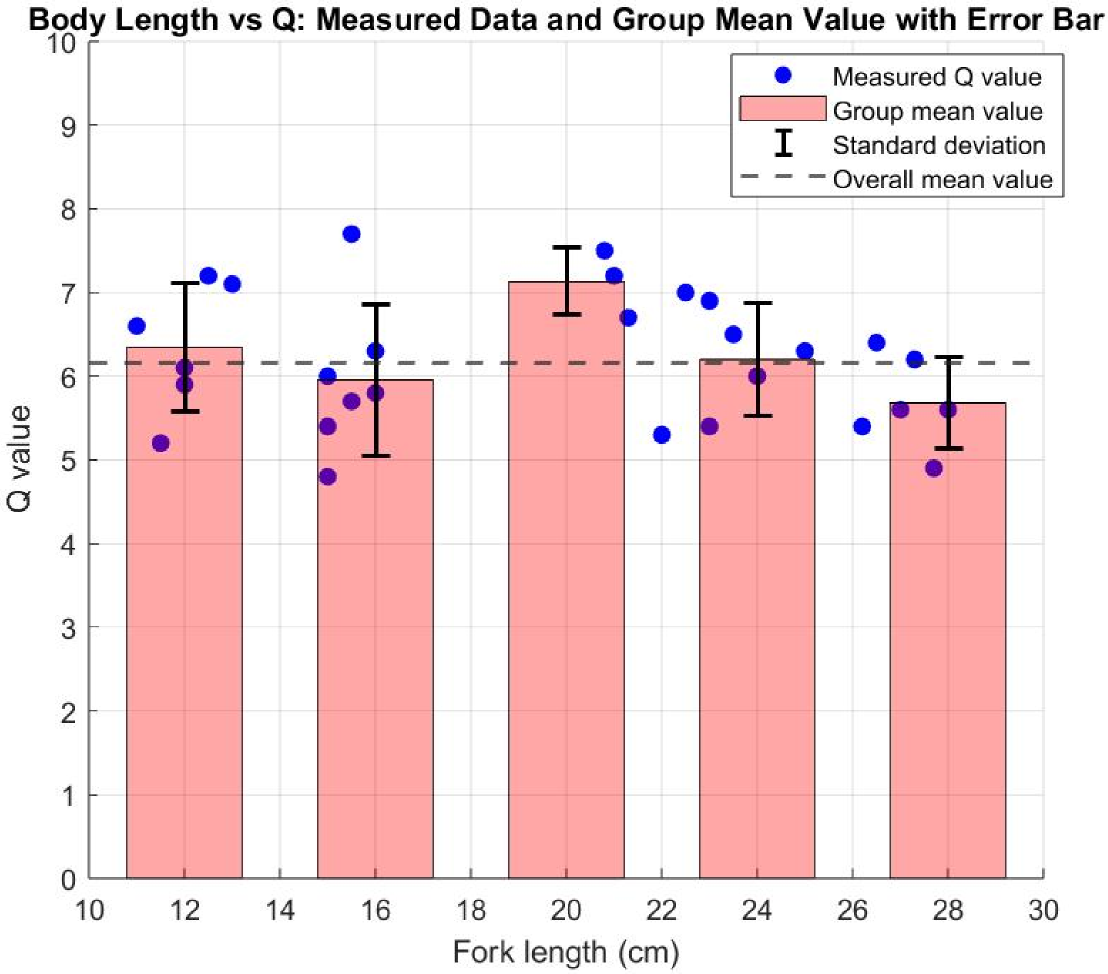

Figure 4.29 Statistical distribution of measured quality factor against fish body length with separate analysis within each size group shown with error bars.

In Figure 4.29, each bar represents a length group with individual measured quality factor, *Q*, overlaid as blue dots. The height of each bar denotes mean *Q* of the size group, and the error bar indicates one standard deviation of the group. A dashed horizontal line shows the overall mean *Q* across all groups. The result suggests moderate variability in quality factors within each length category, consistent with our findings with recently euthanised brown trout shown in Figure 3.11 and also with results from previous research (Cox and Rogers, 1987). While there appears to be a tendency for *Q* to decrease somewhat for the largest fish, the standard deviations overlap considerably, implying that there is not strong evidence of a significant relationship between quality factor and fish length. The interplay of shape, swim bladder volume, and surrounding tissue properties likely all contribute to a broader spread of *Q* values at each length. However, all data plotted in Figure 4.29 were based on healthy specimens. Due to the fact that no resonance could be observed in Specimen F with an unhealthy swim bladder, its quality factor could not be estimated or quantified. The quality factor of healthy swim bladders' independence on fish body length also suggested that the quality factor could be potentially used as a diagnostic indicator for specimens with swim bladder diseases that might change the mechanical properties and resonance characteristics of swim bladders.

Collectively, these figures reveal clear trends and strong correlations among body length, body weight, and body height, while implying allometric-like growth patterns of common carp swim bladders. The negative correlation between length and resonance frequency underscores how an increasingly voluminous swim bladder in larger fish resonates at lower frequencies, while including body weight in the predictive model further refines resonance estimates. In contrast, a relationship between body length and quality factor is not apparent. Overall, these findings provide new insights into how morphological features relate to the acoustic properties of fish, laying the groundwork for more refined models that could incorporate additional factors such as swim bladder interactions with surrounding soft tissue, or finer scale simulations that include Weberian structures and the inner ear.

4.6 CT Scanning for Geometric Reconstruction of Swim Bladders

4.6.1 Imaging Protocol

After the measurements of swim bladder resonance properties and behavioural studies, the carp were usually euthanised immediately after each trial. Four common carp (referred to as specimens A, B, C, and D, see Table 4.2) from four size groups (12”- 14”, 10”- 12”, 8”- 10”, and 6”- 8”) were kept alive and maintained well for further CT scans.

In order to generate high-resolution volumetric datasets of each specimen's internal structure, particularly the swim bladder and the otoliths, specimens A, B, C, and D were later euthanised and immediately scanned at the Biomedical Imaging Unit, University Hospital Southampton, with the support from 3D X-ray Histology team, μ-VIS X-RAY Imaging Centre, University of Southampton. Rapid scanning post-euthanasia minimised tissue degradation and preserved accurate swim bladder morphology. Special attention was paid to observing any volume change in swim bladders by calculating the standard deviation between the first and the last image at the same angle during the CT scan. No sign of swim bladder deflation or change in volume was observed, presumably because of the structure of the swim bladder in this species.

Following final measurements of fish dimensions and body weight, each fish was positioned on foam supports and taped securely to maintain a stable orientation. As shown in the Figure 4.30

and Figure 4.31, the scanner was carefully set up to image the full body in a single pass without repositioning mid-scan. The scanning parameters, summarized below, reflect a good balance between resolution, contrast, and scanning speed.

Figure 4.30 Photo of final body length measurement of specimen A before CT scanning.

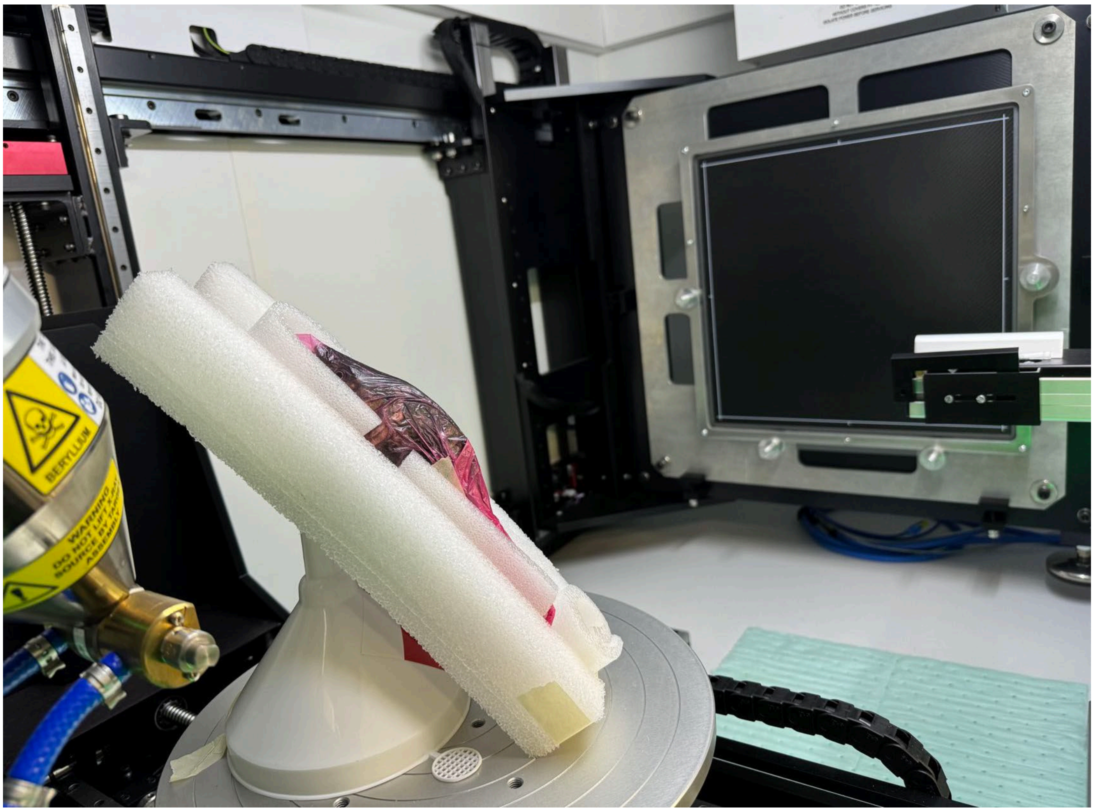

Figure 4.31 Photo of the experimental set-up showing the position and orientation of specimen D during CT scanning.

All scanning was conducted on a Nikon XT H 225 ST microCT, running at 120 kVp and 167 µA (20.04 W total power), acquiring 1501 angular projections over roughly nine minutes. Each projection included four frames at an 89 ms exposure time and an analog gain of 30 dB to enhance contrast, particularly around the swim bladder regions. The Reflection 225 multi-metal X-ray head was selected to achieve sufficient penetration through soft tissues and bone without requiring additional filtration. To minimize file size and reduce noise, 2× binning was used on the detector, resulting in a final voxel size of approximately 170 µm for specimen A, 97 µm for specimen B, 75 µm for specimen C, 49 µm for specimen D, showing that finer resolutions were used for smaller specimen in order to acquire accurate volumetric information of their smaller swim bladder and otoliths. For each fish, the specimen was wrapped in plastic to contain fluids and fixed on foam blocks at a predefined orientation, ensuring stable positioning and complete coverage in a single scan pass. Figure 4.32 shows the photo of specimen A inside the scanner during the scanning, and Figure 4.33 shows the raw output from the scanner with a clear presentation of the gas-filled swim bladder of specimen A.

Figure 4.32 Photo of specimen A inside the scanner during the scanning with the monitor showing the real-time raw output image.

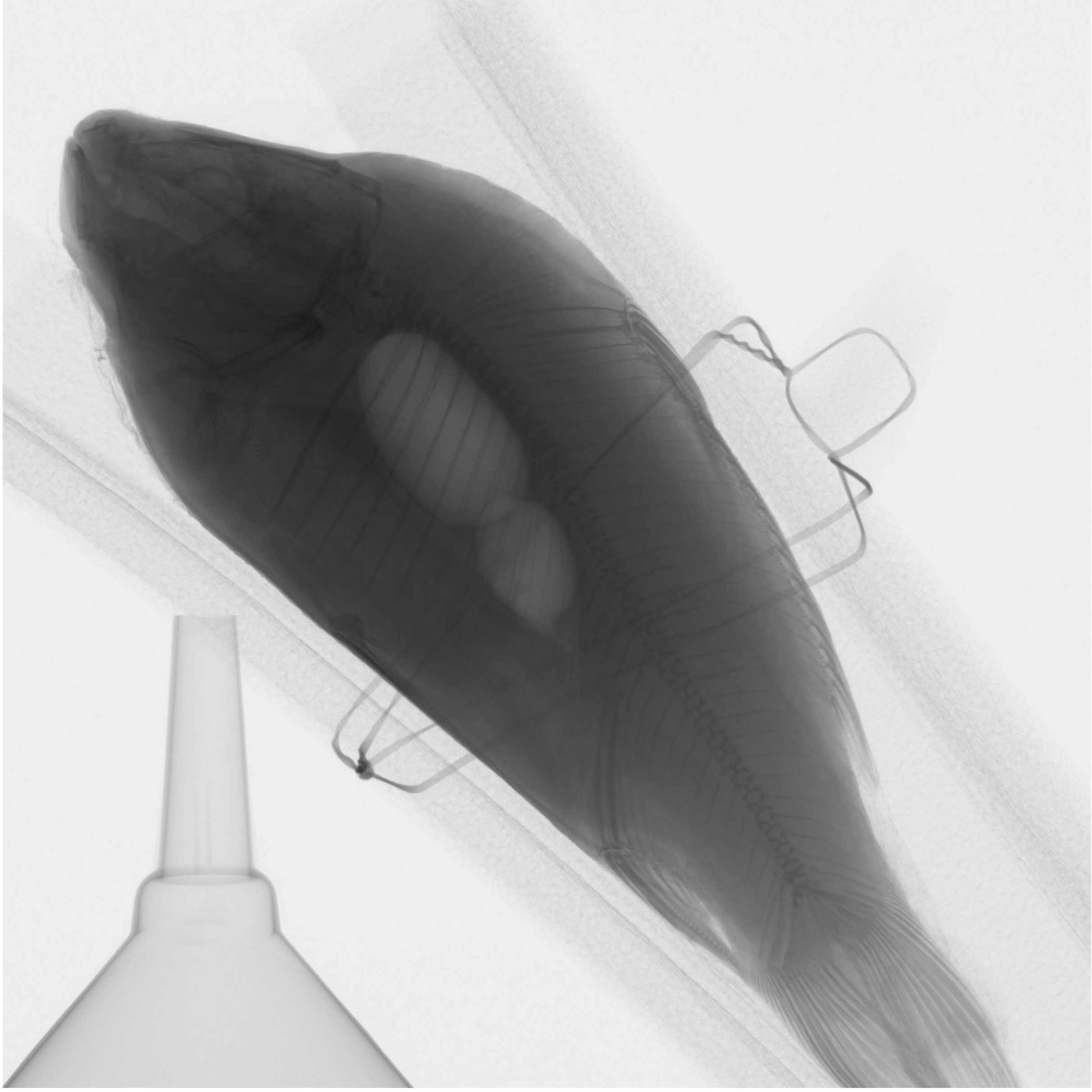

Figure 4.33 Raw radiograph of specimen A when rotated to 90 degrees, the brighter region within the fish's body corresponding to the swim bladder.

Finally, the raw radiograph data were reconstructed into a three-dimensional volume using cone-beam CT algorithms in Fiji (ImageJ) , providing high-resolution slices that clearly delineated both the skeletal and soft-tissue structures, including the swim bladder, for further data processing, segmentation, and tetrahedral meshing.

4.6.2 Model Extraction

Following each CT scan, 1501 raw radiograph images were processed and resliced in Fiji (ImageJ). Figure 4.34 shows the resliced side view of specimen A, revealing the internal anatomy with the skeleton, swim bladder, and otoliths highlighted by their notably higher or lower densities compared to surrounding soft tissues. This density contrast is especially pronounced for the calcified skeletal structure and otoliths, as well as for the air-filled swim bladder, making those regions appear significantly brighter or darker in the resliced volume.

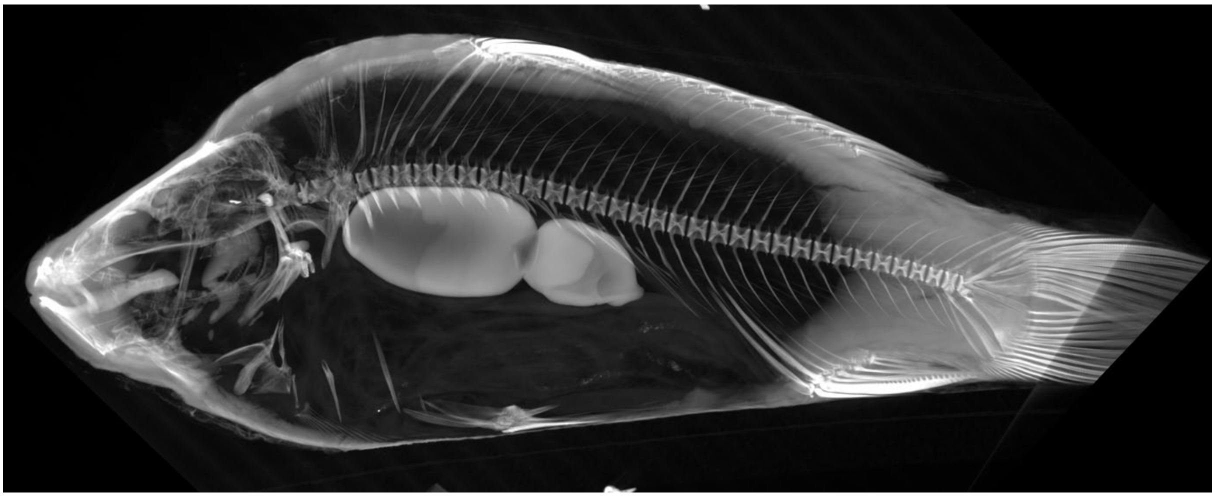

Figure 4.34 The resliced side view of specimen A showing its internal anatomy.

To generate accurate 3D models, the resliced volumetric data were then imported into Dragonfly software, Version 2024.1. Comet Technologies Canada Inc, for segmentation and tetrahedral meshing. The workflow is outlined below, it employed a combination of manual and automated tools:

Thresholding and manual segmentation

A density-based threshold was applied to isolate the bony skeleton and otoliths from the surrounding flesh, while an inverted threshold helped identify the swim bladder. Two regions of interest (ROIs) were created separately by applying thresholds that highlighted the gas-filled swim bladder and otoliths together with other high-density structures. The unique position and three-pair pattern helped with the segmentation of otoliths within the skull, while the distinctive shape and high-contrast of the gas-filled swim bladder were the key for manual segmentation using the 3D ROI segment tools.

Final refinement of ROIs

Dragonfly's built-in ROI refinement filters (Process Islands – Keep by Largest) were then applied to reduce unwanted volumetric noise and remove spurious isolated voxels. This step generated final and accurate ROIs of the swim bladder and three pairs of otoliths while preserving intricate anatomical details and their coordinate information.

Mesh generation

After segmentation, each ROI was converted into a 3D tetrahedral volumetric mesh, as standard contour mesh or thickness mesh did not contain the volumetric elements necessarily needed for further FEM analysis and would be recognised as thousands of individual points by COMSOL. The swim bladder was later measured in Dragonfly software for volume, physical dimensions, wall thickness, and its distance to the otoliths.

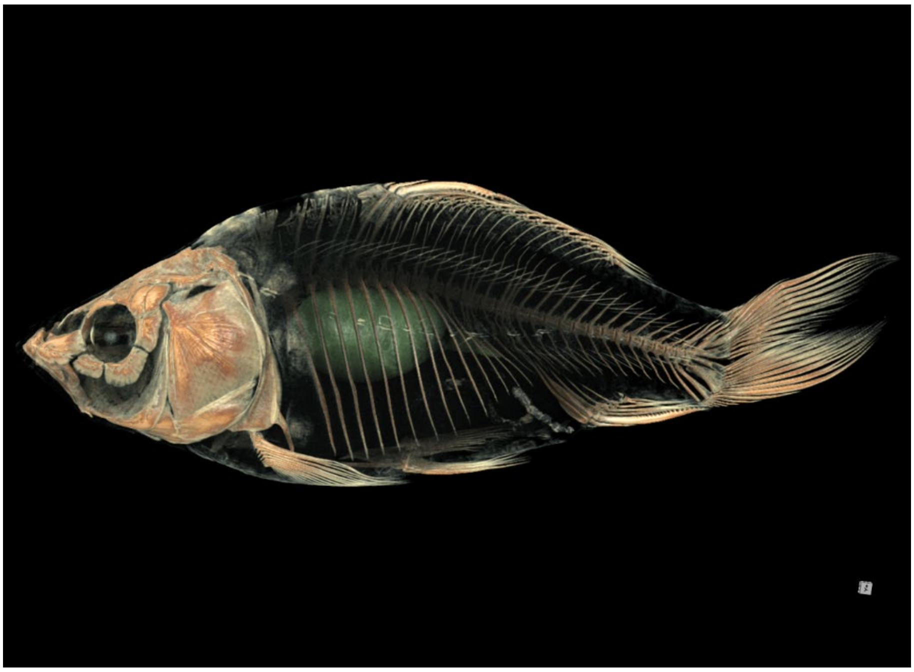

Figure 4.35 3D rendered specimen D after segmentation with swim bladder coloured in green.

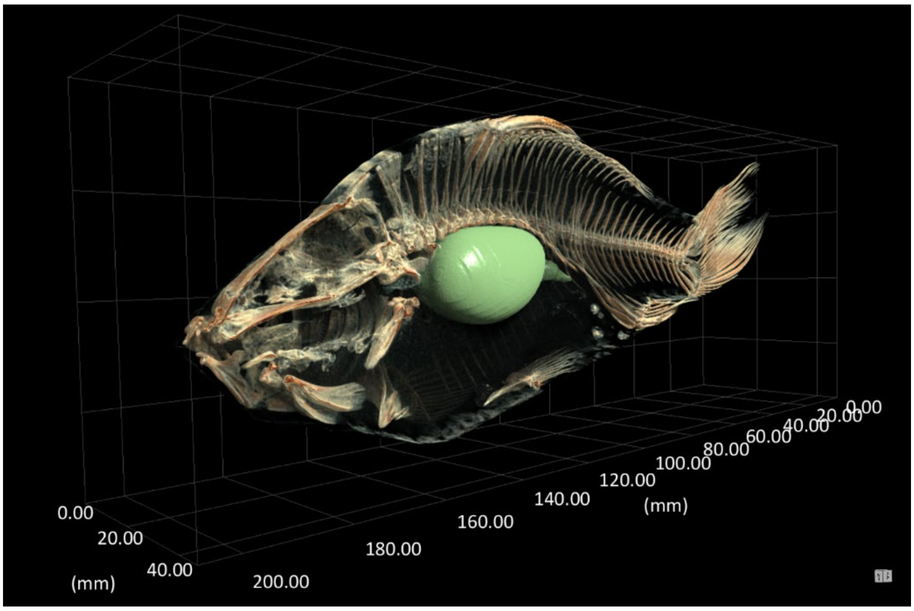

Figure 4.36 3D rendered specimen D with swim bladder coloured in green with grid on.

Figures 4.35, 4.36, and 4.37 illustrate the coloured renderings of the segmented fish, showing the relative positions of the skeleton, bladder, and otoliths in three-dimensional space. In Figure 4.35, the skeletal frame is rendered in neutral tones, and the swim bladder appears as a dark green volume surrounded by ribs near the centre of the body cavity. Figure 4.36 uses a 3D grid coordinate overlay to showcase the precise spatial dimensions of the fish's anatomy, while

Figure 4.37 highlights a close-up of the skull region with the otoliths and an isolated bladder mesh. As shown, these final 3D models capture both large-scale morphological features—such as the outline of the ribs and the broad shape of the swim bladder—and finer details like the position of otoliths within the fish body.

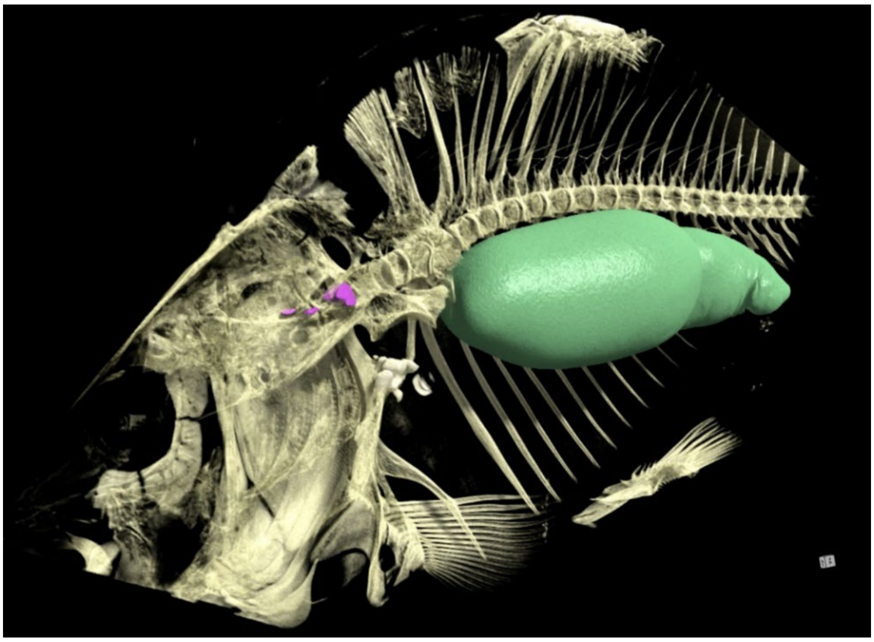

Figure 4.37 Specimen A with its swim bladder coloured in green and otoliths highlighted in purple 3D rendered in Dragonfly.

Figure 4.38 shows the interface of Dragonfly presenting isolated ROIs of the swim bladder and otoliths of specimen B with a swim bladder-otolith distance of 18.1 mm. Computed tetrahedral meshes of all CT scanned specimens were then imported into COMSOL for FEM simulations.

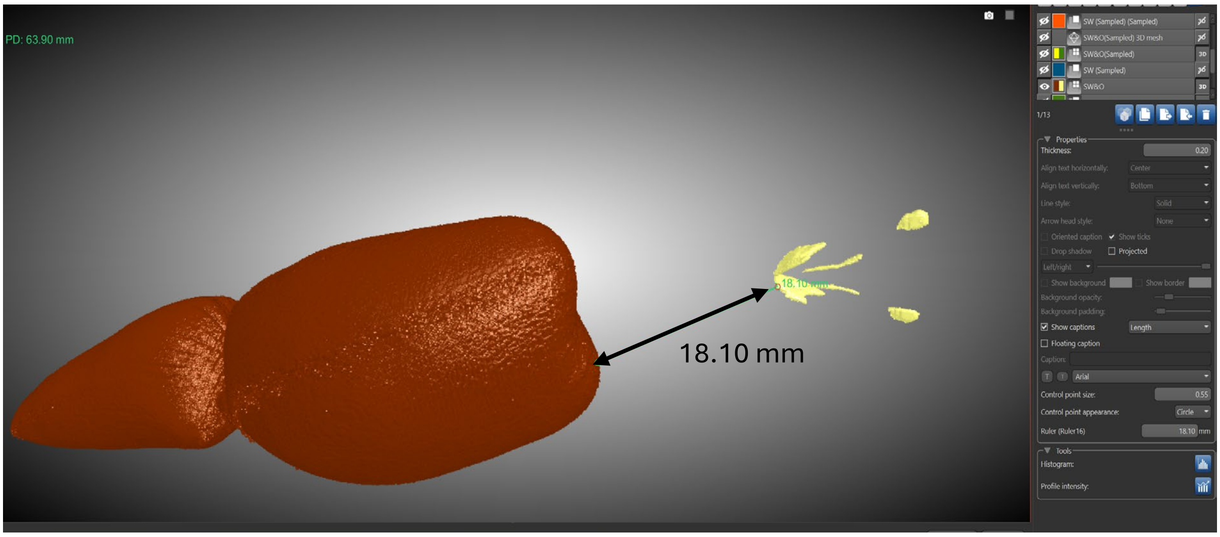

Thickness: 0.20

Align text horizontally: Center

Align text vertically: Bottom

Line style: Solid

Arrow head style: None

☐ Oriented caption ☑ Show ticks

☐ Drop shadow ☐ Projected

Left/right

☐ Show background ☐ Show border

Background opacity:

Background padding:

☑ Show captions Length

☐ Floating caption

Caption:

Arial

Control point size: 0.55

Control point appearance: Circle

Ruler (Ruler16) 18.10 mm

Figure 4.38 Screenshot of the interface of Dragonfly showing ROIs and the measured distance.

4.7 FEM simulation of Swim Bladder Resonance

CT data enabled the possibility of using accurate 3D models of swim bladders instead of ellipsoidal approximations for FEM simulations. The volumetric information of CT-scanned swim bladders, in the form of tetrahedral meshes, was used as the geometrical input to FEM simulations together with other supporting properties and assumptions.

4.7.1 Modelling Assumptions and Material Properties

In Chapter 3, FEM simulations of a spherical encapsulated bubble (air-filled latex balloon) and an ellipsoidal encapsulated bubble (air-filled swim bladder of a recently euthanised brown trout) were performed and verified against the experimentally measured resonance properties. This section focuses on the FEM simulation of four CT scanned specimens for the resonance properties of swim bladders in free-field conditions and the SPLrms values of their otoliths due to the radiated sound field of the swim bladders. To better study the swim bladder resonance properties and the received sound pressure of the otoliths under ideal conditions, the same simulation setting described in Subsection 3.4.1 and 3.4.2 was used for this FEM project. The swim bladder and otoliths were placed at the centre of the water-filled spherical computation domain, excited by a monopole sound source 20 cm directly beneath them (mimicking the experimental setting where the sound source was at the bottom of the test tank). PMLs with radial absorption pattern were assigned to the boundaries of the spherical computation domain in order to minimise influence from boundary reflections. Figure 4.39 shows the physics-controlled mesh of the swim bladder and otoliths of specimen B in COMSOL prepared for the final computation.

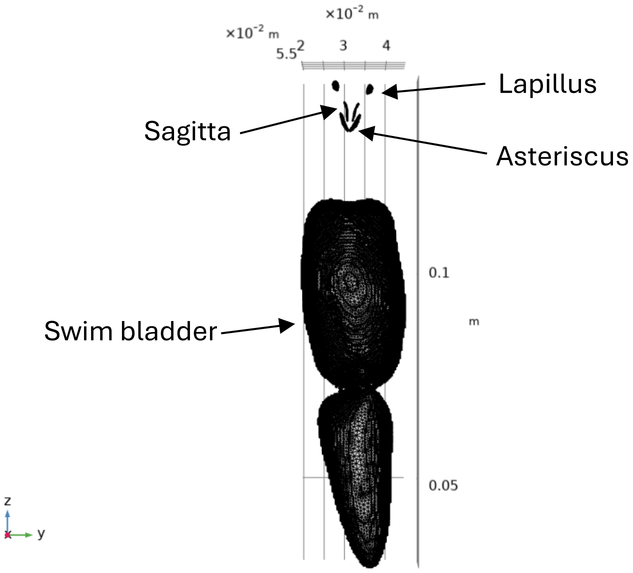

Figure 4.39 Imported tetrahedral CT mesh was re-meshed by COMSOL in a physics-controlled strategy, showing the swim bladder and otoliths with the coordinate grid on.

Material properties of swim bladder wall remained the same as it was in Subsection 3.4.2 according to previously measured mechanical characteristics, which had a density of 1050 kg/m^3, a Young's modulus of 2 MPa, a Poisson's Ratio of 0.45, and an isotropic structural loss damping factor of 0.18 (Salas *et al.*, 2019, Li *et al.*, 2024). Swim bladder wall thickness for specimen A, B, C, and D were measured from CT data in Dragonfly to be 0.33 mm, 0.30 mm, 0.25 mm, and 0.20 mm, showing a relationship that bigger fish tend to have thicker swim bladder walls. Distances between swim bladders and otoliths were also measured in Dragonfly to be 20 mm for specimen A, 18 mm for specimen B, 16 mm for specimen C, and 13 mm for specimen D, showing that the otoliths of a smaller fish were closer to and consequently more closely coupled with the swim bladder acoustically.

The material properties of otoliths are slightly different and more complicated than the swim bladder. There are three pairs of otoliths in total for each fish: (in the direction from fish head to tail) lapillus, sagitta, and asteriscus. The first two pairs of utricular and saccular otoliths (lapillus and sagitta) are relatively far away from the swim bladder and are made of aragonite (Salas *et al.*, 2019). The last pair of lagenar otolith (asteriscus) closest to the swim bladder is made of vaterite with a lower density than aragonite (Ren *et al.*, 2013). The compressional wave speed c_P and shear wave speed c_S of aragonite and vaterite otoliths were calculated using Equation (26) and Equation (27):

$$c_P = \sqrt{\frac{E(1-\sigma)}{\rho(1+\sigma)(1-2\sigma)}}, \tag{27}$$

$$c_S = \sqrt{\frac{E}{2\rho(1+\sigma)}}, \tag{28}$$

where ρ is the density of the otolith, E represents Young's modulus of otolithic property, and σ is Poisson's ratio (Salas *et al.*, 2019, Li *et al.*, 2024). The measured otolithic material properties and estimated compressional and shear wave speed are included in Table 4.3.

Table 4.3 Properties of lapillus (aragonite), sagitta (aragonite), and asteriscus (vaterite).

Material	**Density ρ (kg/m^3)**	**Young's modulus E**	**Poisson's ratio σ**	c_P **(m/s)**	c_S **(m/s)**
Aragonite	2930	64.9 GPa	0.31	5541	2908
Vaterite	2540	64.5GPa	0.31	5931	3114

FEM simulations were then run separately for each specimen from 10 Hz to 500 Hz with a step length of 5 Hz. Results are shown in the following subsection.

4.7.2 Simulated Frequency Response of Swim Bladder and Otoliths

To evaluate how the CT-derived swim bladder geometries and otoliths respond acoustically over the 10 - 500 Hz range, frequency-stepped finite element simulations were performed at 5 Hz intervals under the conditions and settings outlined in the previous subsection. Each simulation accounted for the monopole sound source placed 20 cm beneath the specimen within a spherical water domain equipped with perfectly matched layers. The resultant outputs include both the SPLrms of the swim bladder domains and the otolith domains (object with a volume are considered as a domain in COMSOL), thereby illustrating how the swim bladder and otoliths might interact under external acoustic excitation.

Figure 4.40 shows an example of a uniform distribution of simulated SPLrms on the swim bladder of specimen B when excited at 210 Hz (close to its measured resonance frequency, 203Hz, and the simulated resonance frequency, 220 Hz).

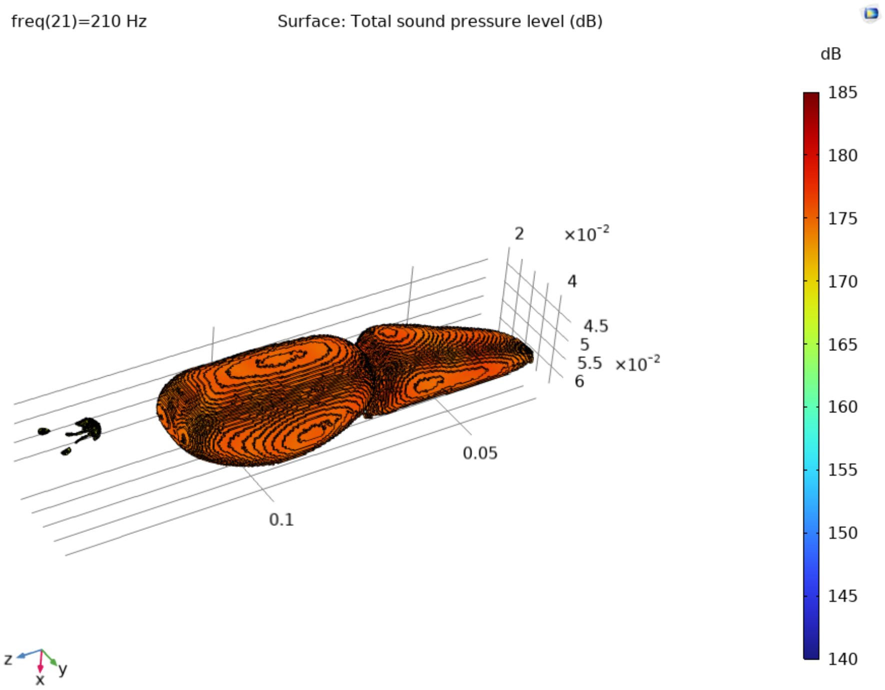

Figure 4.40 SPLrms distribution on the swim bladder of specimen B under the excitation of the monopole source at 210 Hz with a colour bar and a coordinate grid.

Figures 4.41, 4.43, 4.45, and 4.47 present the near resonance SPL distribution on the swim bladder and the otoliths of the specimens A, B, C, and D. Figure 4.42, 4.44, 4.46, and 4.48 show the corresponding transfer function of the swim bladder domain and three pairs of otoliths separately. In the transfer function figures, the magenta dashed line is the baseline transfer function of when no swim bladder or otoliths were present, and the red solid lines represent the transfer function of the swim bladder domain, showing a distinctive resonance peak. Solid lines in cyan, blue, and black are the transfer function of asteriscus, sagitta, and lapillus respectively.

Asteriscus, being the closest otolith to the swim bladder, shows a higher received SPLrms and resonance amplitude than sagitta and lapillus that are slightly further from the swim bladder, consistent with simulation results in Li *et al.*, 2024.

Specimen A (L = 26.2 cm, W = 668 g) from fish size group 1 (12”- 14”):

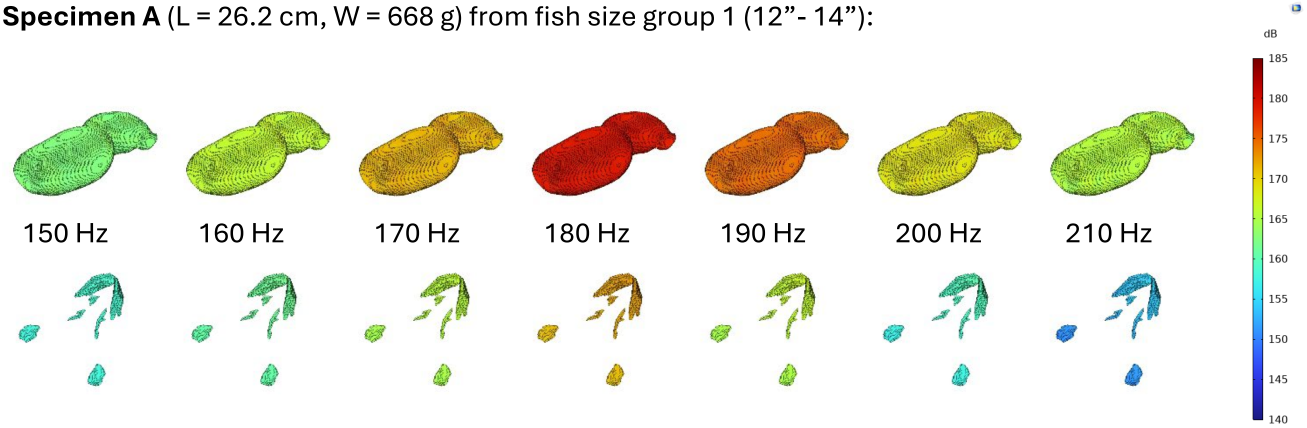

Figure 4.41 Simulated SPLrms of the swim bladder (top) and the otoliths (bottom) at the test frequency of 150, 160, 170, 180 (resonance frequency), 190, 200, and 210 Hz.

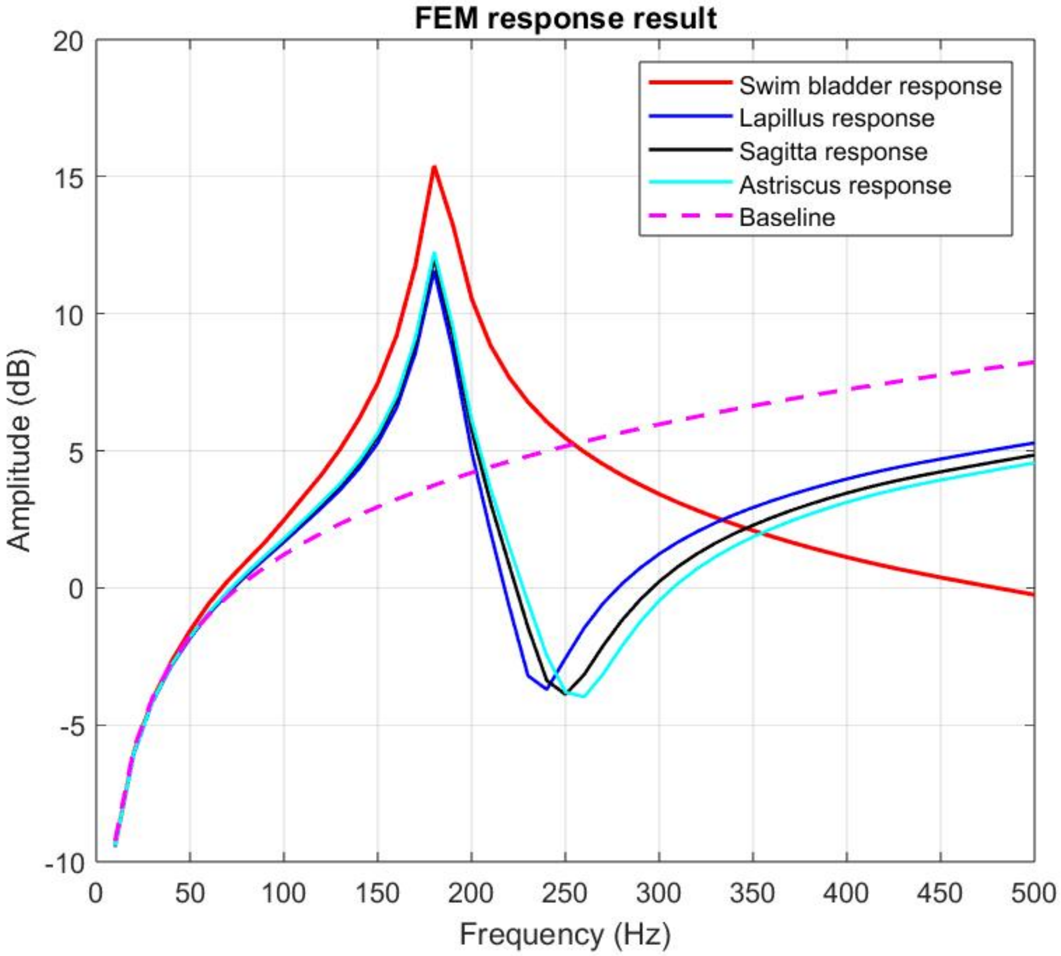

Figure 4.42 Simulated transfer functions of the swim bladder (red), lapillus (blue), sagitta (black), asteriscus (cyan), and the baseline (dashed magenta), showing the resonance peak at 180 Hz.

Specimen B (*L* = 23 cm, *W* = 380 g) from fish size group 2 (10”- 12”):

Figure 4.43 Simulated SPLrms of the swim bladder (top) and the otoliths (bottom) at the test frequency of 185, 195, 205, 215 (resonance frequency), 225, 235, and 245 Hz.

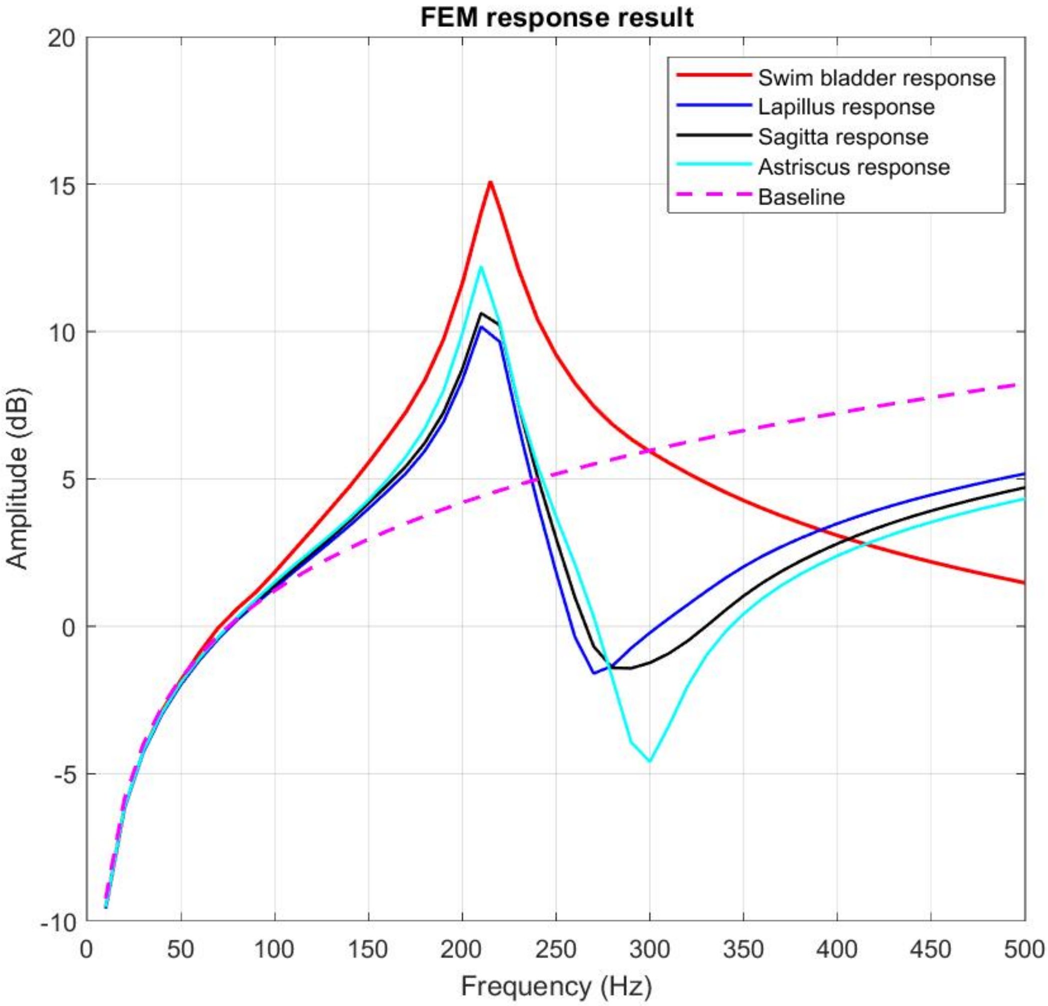

Figure 4.44 Simulated transfer functions of the swim bladder (red), lapillus (blue), sagitta (black), asteriscus (cyan), and the baseline (dashed magenta), showing the resonance peak at 215 Hz.

Specimen C (*L* = 21 cm, *W* = 290 g) from fish size group 3 (8”- 10”):

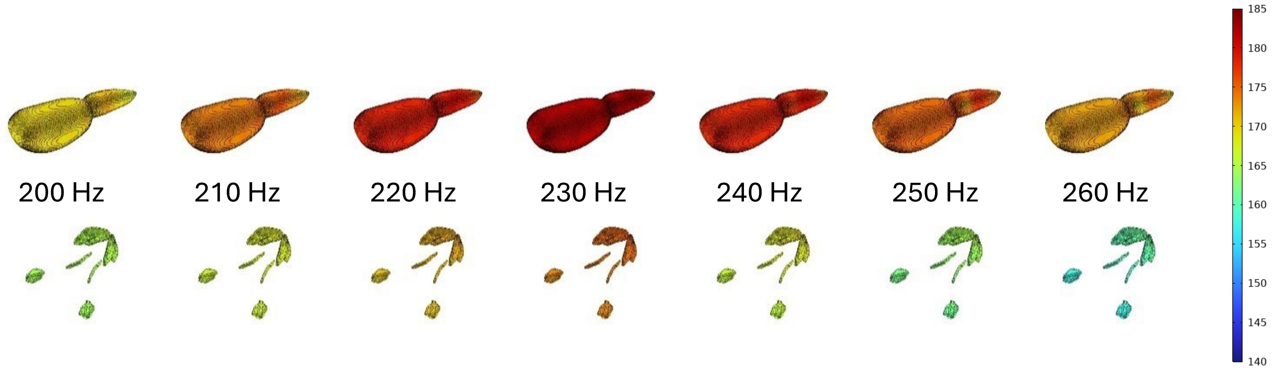

Figure 4.45 Simulated SPLrms of the swim bladder (top) and the otoliths (bottom) at the test frequency of 200, 210, 220, 230 (resonance frequency), 240, 250, and 260 Hz.

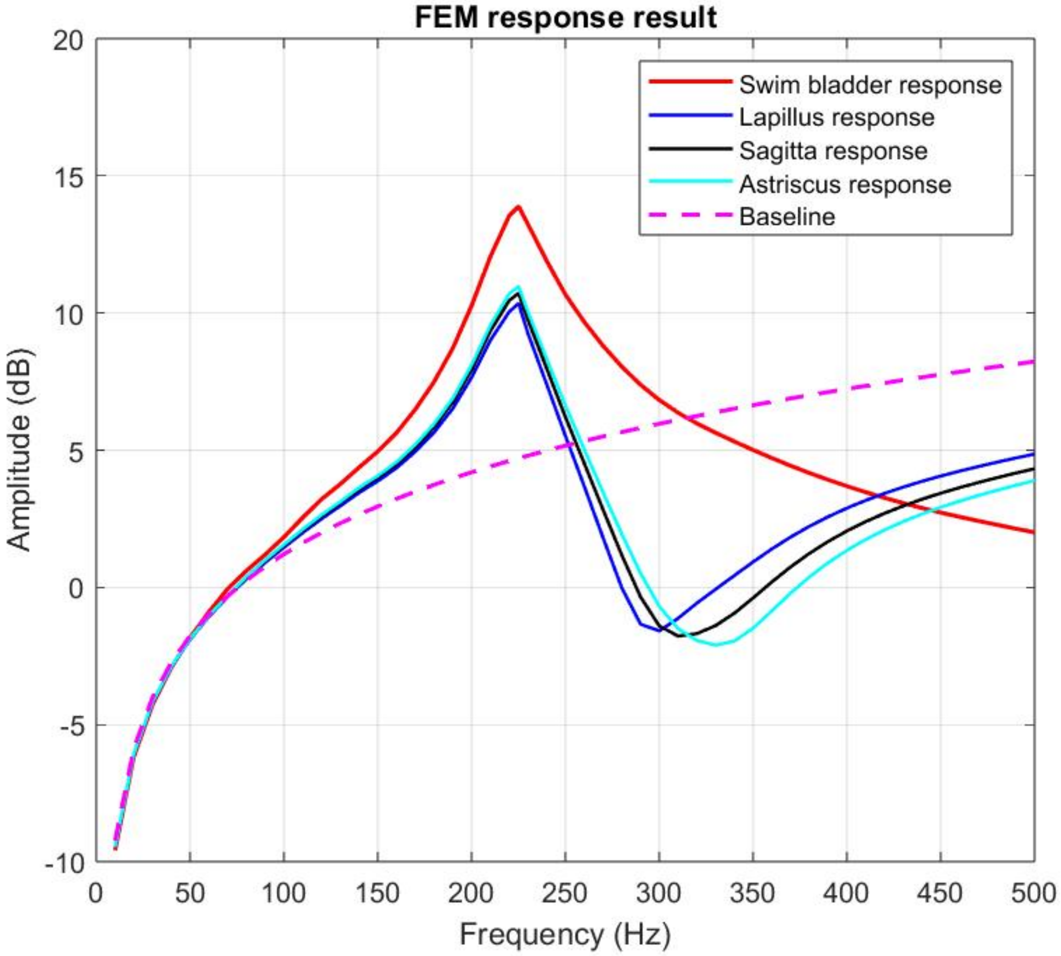

Figure 4.46 Simulated transfer functions of the swim bladder (red), lapillus (blue), sagitta (black), asteriscus (cyan), and the baseline (dashed magenta), showing the resonance peak at 230 Hz.

Specimen D (*L* = 16 cm, *W* = 144 g) from fish size group 4 (6”- 8”):

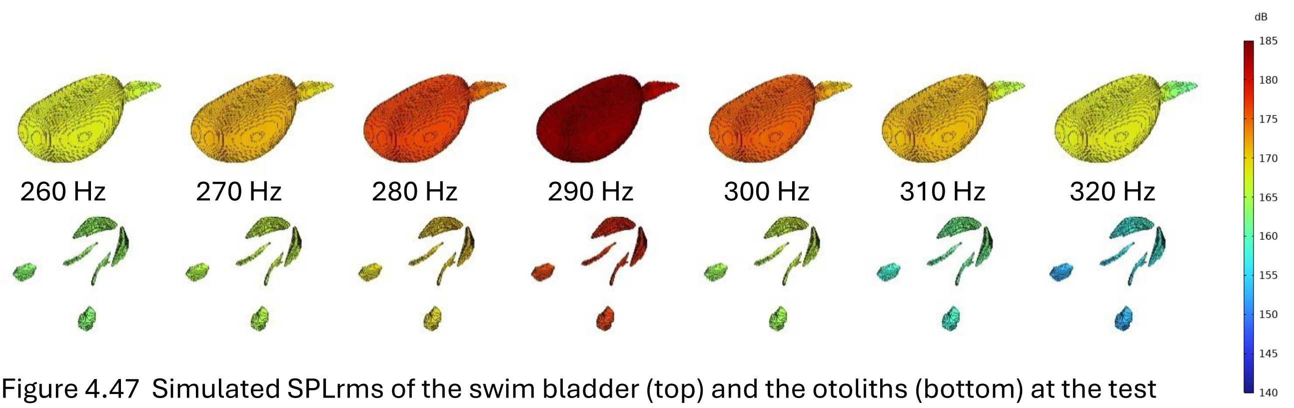

Figure 4.47 Simulated SPLrms of the swim bladder (top) and the otoliths (bottom) at the test frequency of 260, 270, 280, 290 (resonance frequency), 300, 310, and 320 Hz.

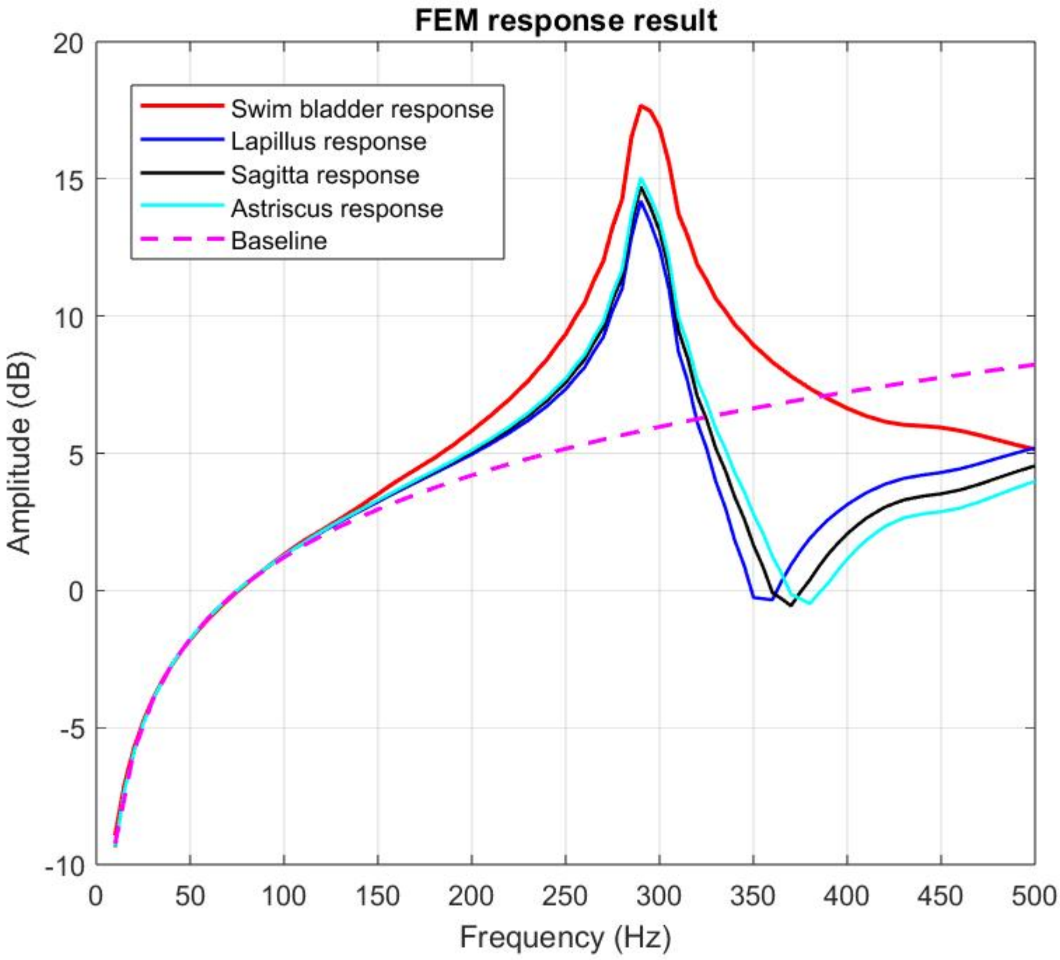

Figure 4.48 Simulated transfer functions of the swim bladder (red), lapillus (blue), sagitta (black), asteriscus (cyan), and the baseline (dashed magenta), showing the resonance peak at 290 Hz.

These figures indicate that fish otoliths will pick up the radiated sound field from the near-resonating swim bladder under acoustic excitations, thereby potentially increasing the fish’s hearing sensitivity at the frequency range around swim bladder resonance with the amplification more on the frequencies lower than the resonance frequency, whilst the amplification is lower for the frequencies higher than the resonance frequency due to the out-of-phase oscillation patterns discussed in the last chapter.

One can observe that the baseline (dashed magenta) increases with the frequency, this is because the monopole source in COMSOL simulations were defined with a constant volume flow rate, Q_S , which is regardless of the frequency. Equation (16) and (17) explained that the monopole source strength Q_m would increase with the increasing exciting frequency when the volume flow rate Q_S was set as a constant.

Figures above also show that a smaller fish normally has a smaller swim bladder, and has a higher resonance frequency in FEM simulations, which is consistent with the statistical findings based on previous measurements on live fish.

Another factor to consider is that the swim bladder-otolith coupling in the free-field simulation does not take the Weberian apparatus into account, and it was only water between the swim bladder and the otoliths. It is likely that the otoliths will have higher received sound pressure than the simulated results because of the close coupling between the swim bladder and the otoliths in real fish through the Weberian apparatus. The structure of the Weberian apparatus is complicated and consists of delicate structures made of both soft tissues and tiny bones, which will require a finer resolution in CT scanning. Marcé-Nogué and Liu, 2024 performed FEM simulations on the sound transmission in the Weberian apparatus of zebrafish (Danio rerio) and found that the resonance frequency of the zebrafish’s Weberian ossicular chain is approximately 900 Hz, matching their optimal hearing range. Therefore, it can be a further research project to combine the swim bladder resonance simulation with the sound transmission in the Weberian apparatus to better understand the hearing mechanisms and the hearing evolution of vertebrates.

4.7.3 Swim Bladder Coupling with the Tank Environment

After the modelling of the resonance properties of CT-scanned fish swim bladders in the free-field conditions, the final goal of this section was to integrate FEM simulations of swim bladder resonance with test tank response, creating a more comprehensive simulation environment that could better mimic the practical setting of the experimental measurements and achieve mutual validation between the measured transfer functions and the simulated ones. Therefore, a multi-module-coupled FEM simulation project was built in COMSOL containing the SolidWorks-based 3D model of the test tank assembly and the extremely fine scale CT-scanned swim bladder meshes of the specimens together within the same geometry set-up.

Figure 4.49 shows the meshed geometric setting of the simulation with *Solid Mechanics* (all test tank parts) coupling with *Pressure Acoustic, Frequency Domain* (water body and the air inside the swim bladder) that was also coupled with *Shell* (*Structural Mechanics*) applied on the swim bladder wall (air-water interface).

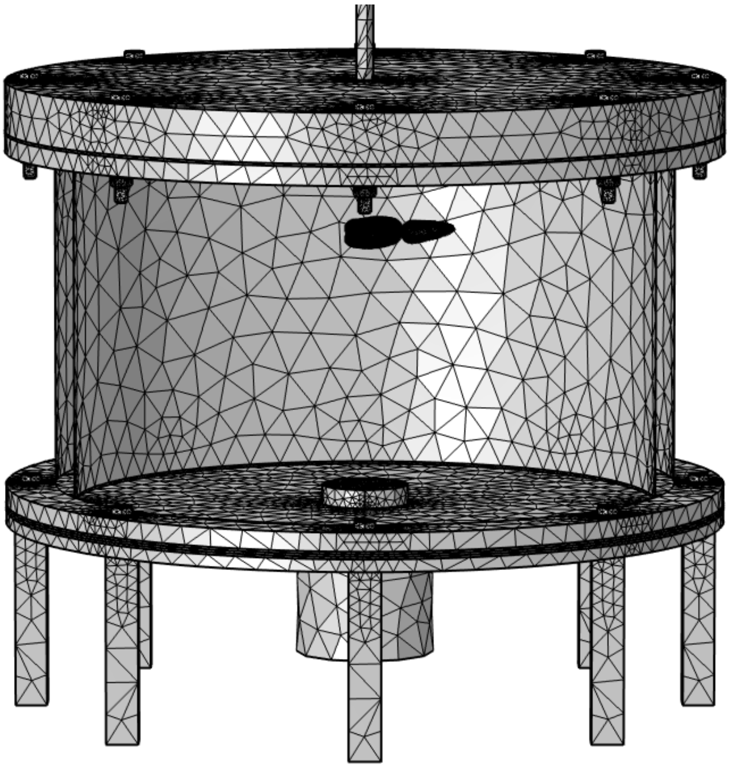

Figure 4.49 The meshed geometry showing the CT-scanned swim bladder within the fully water-filled test tank with boundary load excitation applied on the bottom steel plate.

Despite the drastic difference in mesh resolutions (computed elements per unit length) between the coarsely meshed test tank and the comparatively ultra-finely meshed swim bladder and the resulting computational load (12 hours per trial), the multi-module-coupled simulation was performed successfully and returned with detailed results. Figure 4.50 shows the near-resonance SPLrms distribution of the water body and the swim bladder within when excited at 180, 200, 220 (swim bladder resonance frequency), 240, and 260 Hz. It is observed that the swim bladder is scattering the highest sound energy (red – standing for 185 dB) at its resonance frequency (220 Hz), and it does not resonate when not excited at its resonance frequency. The presence of the swim bladder, as was discussed in Chapter 3, slightly changes the sound pressure distribution of the empty tank under the same excitation, *i.e.* 240 Hz and 260 Hz in Figure 4.50.

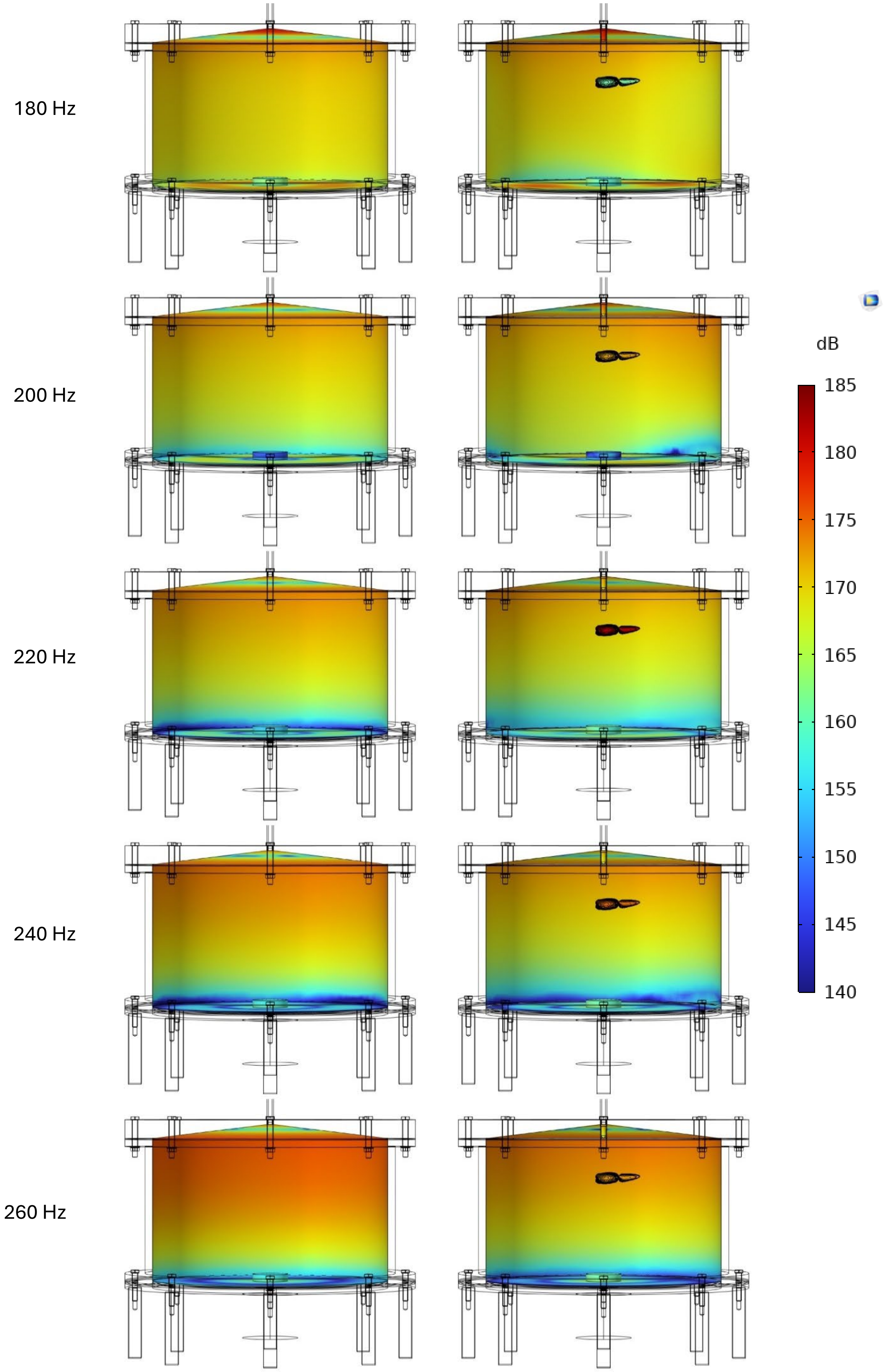

Figure 4.50 SPLrms distribution of the water and the swim bladder when excited in the tank.

Specimen A (L = 26.2 cm, W = 668 g) from fish size group 1 (12”- 14”):

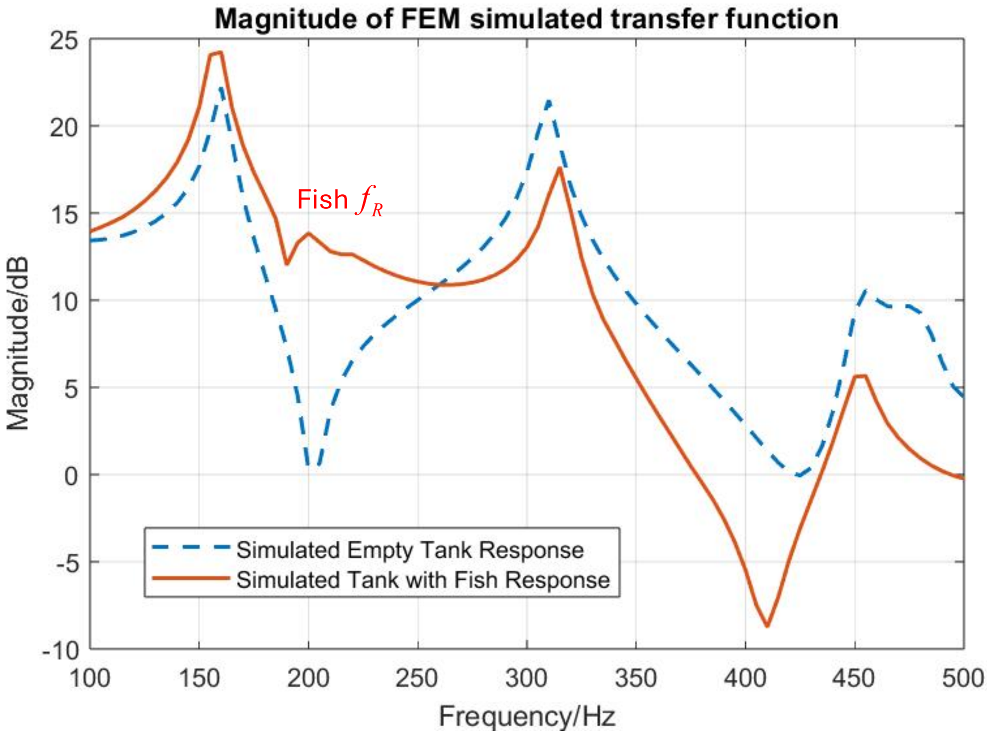

Figure 4.51 Simulated transfer functions of the empty tank (dashed blue line), and the tank with a swim bladder (solid orange line), showing the resonance frequency at 200 Hz.

Specimen B (*L* = 23 cm, *W* = 380 g) from fish size group 2 (10”- 12”):

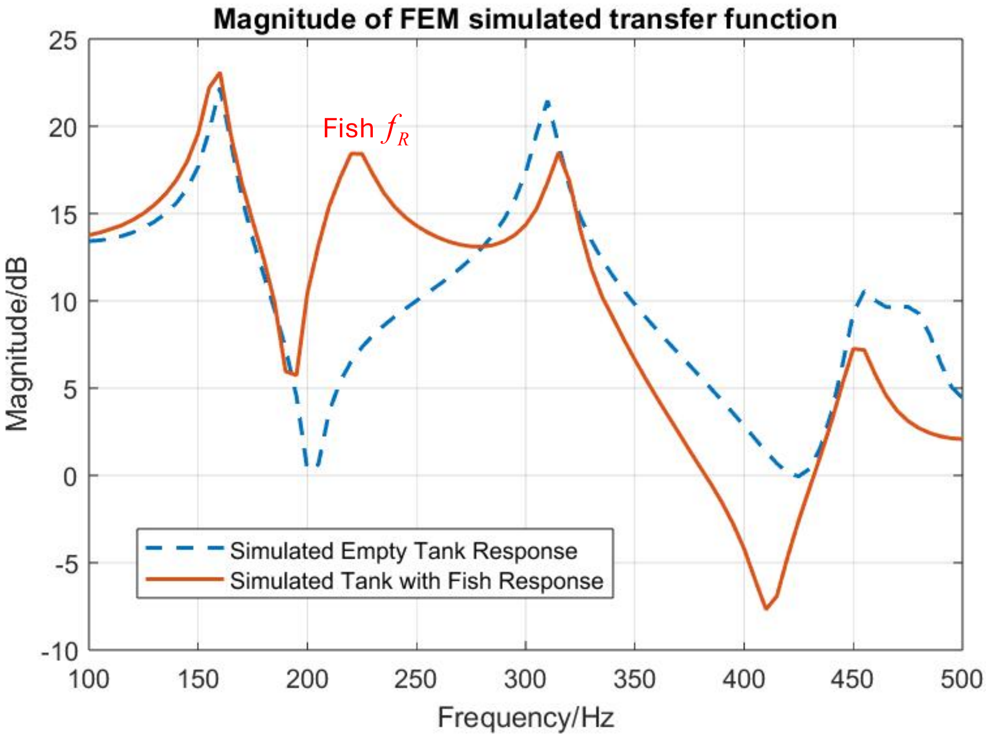

Figure 4.52 Simulated transfer functions of the empty tank (dashed blue line), and the tank with a swim bladder (solid orange line), showing the resonance frequency at 220 Hz.

Specimen C (L = 21 cm, W = 290 g) from fish size group 3 (8”- 10”):

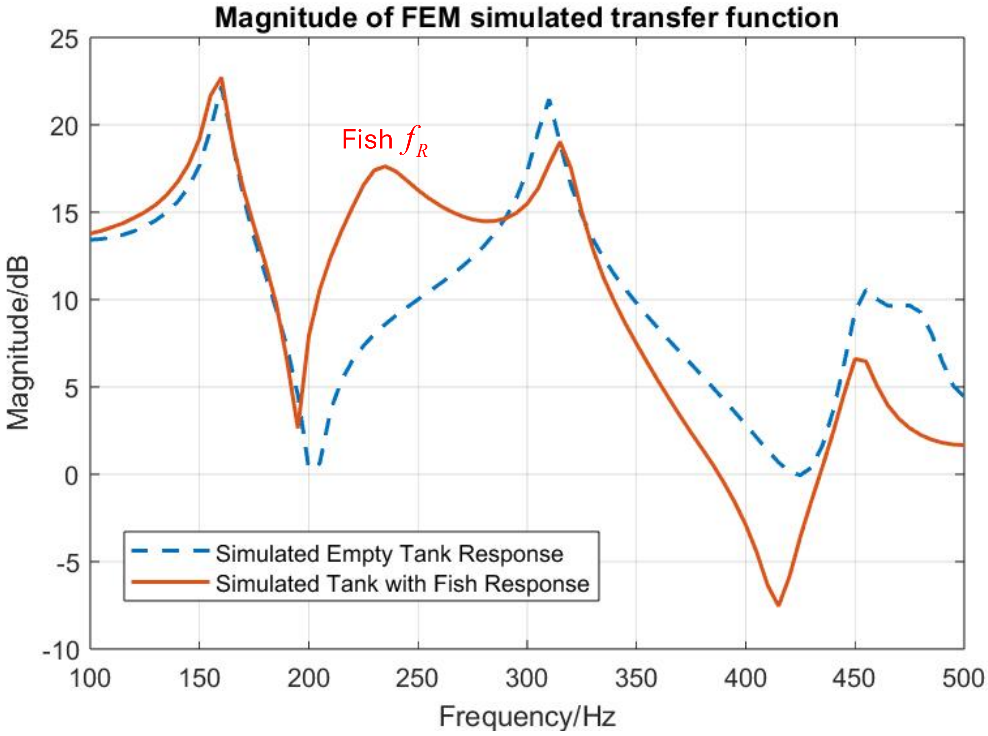

Figure 4.53 Simulated transfer functions of the empty tank (dashed blue line), and the tank with a swim bladder (solid orange line), showing the resonance frequency at 230 Hz.

Specimen D (L = 16 cm, W = 144 g) from fish size group 4 (6”- 8”):

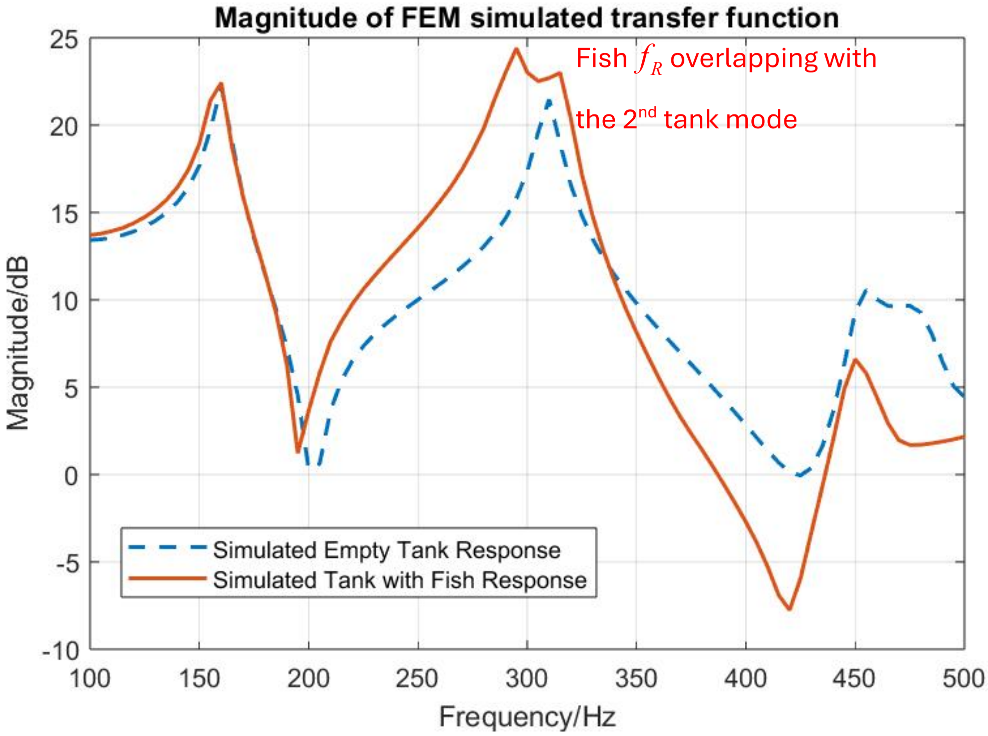

Figure 4.54 Simulated transfer functions of the empty tank (dashed blue line), and the tank with a swim bladder (solid orange line), showing the resonance frequency at 295 Hz.

Figure 4.51 – 4.54 show the simulated transfer functions of the empty tank (dashed blue line), and the tank with a swim bladder (solid orange line) under the same excitation applied as the 10 N boundary load at the centre of the bottom plate, mimicking the experimental set-up that employed an inertial shaker as the sound source. The comparison between the simulated and the experimentally measured transfer functions of the empty tank was previously presented and discussed in detail in subsection 4.3.2. The transfer function showing the swim bladder resonance, as was mentioned before, was highly corelated with the exciting sound field, whose frequency response would ideally be flat but practically possess a pattern. Therefore, the shape of the simulated transfer function of the test tank with a swim bladder was more complex than the transfer function in a free-field condition as in subsection 4.7.2. For example, specimen A's swim bladder resonance at 200 Hz shown in Figure 4.51 was not in the shape of a sharp and distinctive peak, because it overlapped with an anti-resonance at 200 Hz. The swim bladder resonance peak, however, which is about 13 dB higher than the anti-resonance (the exciting signal), indicating a normal and distinct swim bladder resonance. Similarly, the swim bladder resonance (295 Hz) of specimen D in Figure 4.54 also interacts with one of the simulated tank modes (310 Hz), specifically the second tank resonance. Similar effects (swim bladder resonance overlapping with the second tank mode) were observed in measured transfer functions on smaller fishes as well (Figure 4.21), which will be addressed in the next section.

The effects of a bubble on the tank response are also seen in the simulated results as well. Slight shifting of the second tank resonance from 310 Hz to 315 Hz can be seen in all four simulation results, together with the attenuation of around 4 dB on the original tank resonance amplitudes when the swim bladder was present. Further comparisons between measured and simulated transfer functions with or without the air-filled swim bladder were performed and discussed in Section 4.8.

4.8 Comparison Between Measurement and Simulation

4.8.1 Measured VS Simulated Swim Bladder Resonance Properties

Having achieved multi-module-coupled FEM simulation that combined the original tank response with swim bladder resonance, the simulated transfer functions were plotted in comparison with measured transfer functions in Figure 4.55 – 4.58 with the matching pairs of measured and simulated resonances (the 1st , 2nd , 3rd tank modes and the swim bladder resonance) indicated in the figures for better understanding.

Specimen A (L = 26.2 cm, W = 668 g) from fish size group 1 (12”- 14”):

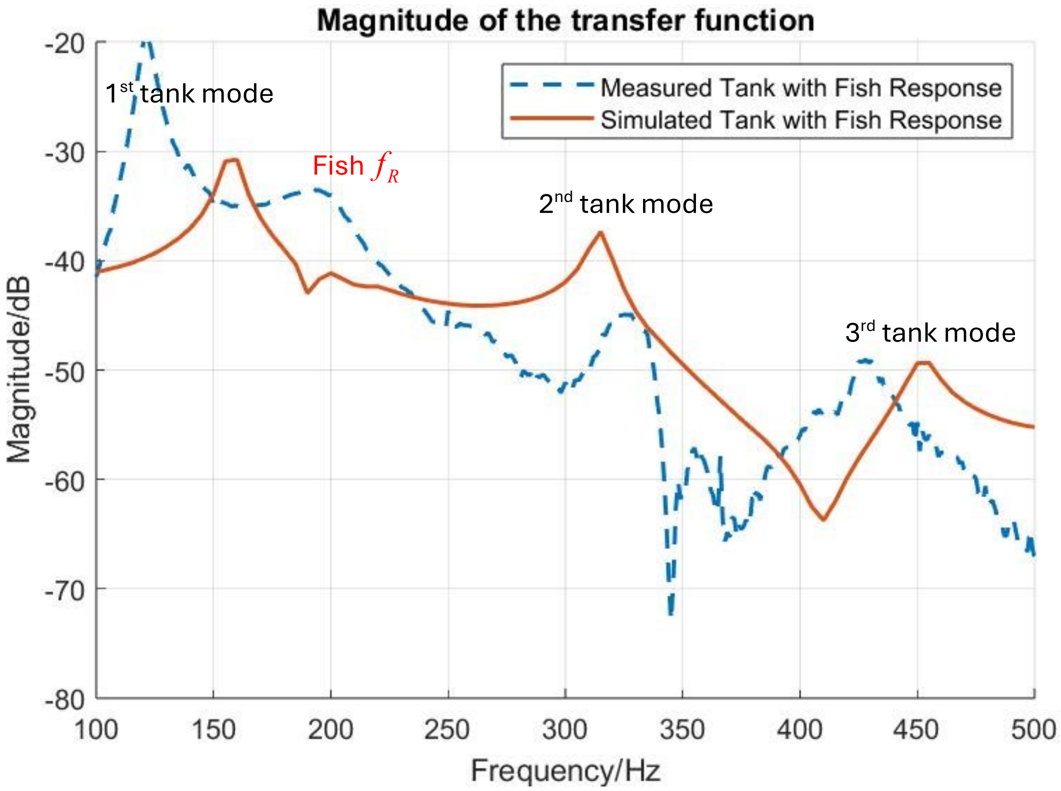

Figure 4.55 Comparison between measured and simulated transfer functions of specimen A.

Specimen B (*L* = 23 cm, *W* = 380 g) from fish size group 2 (10”- 12”):

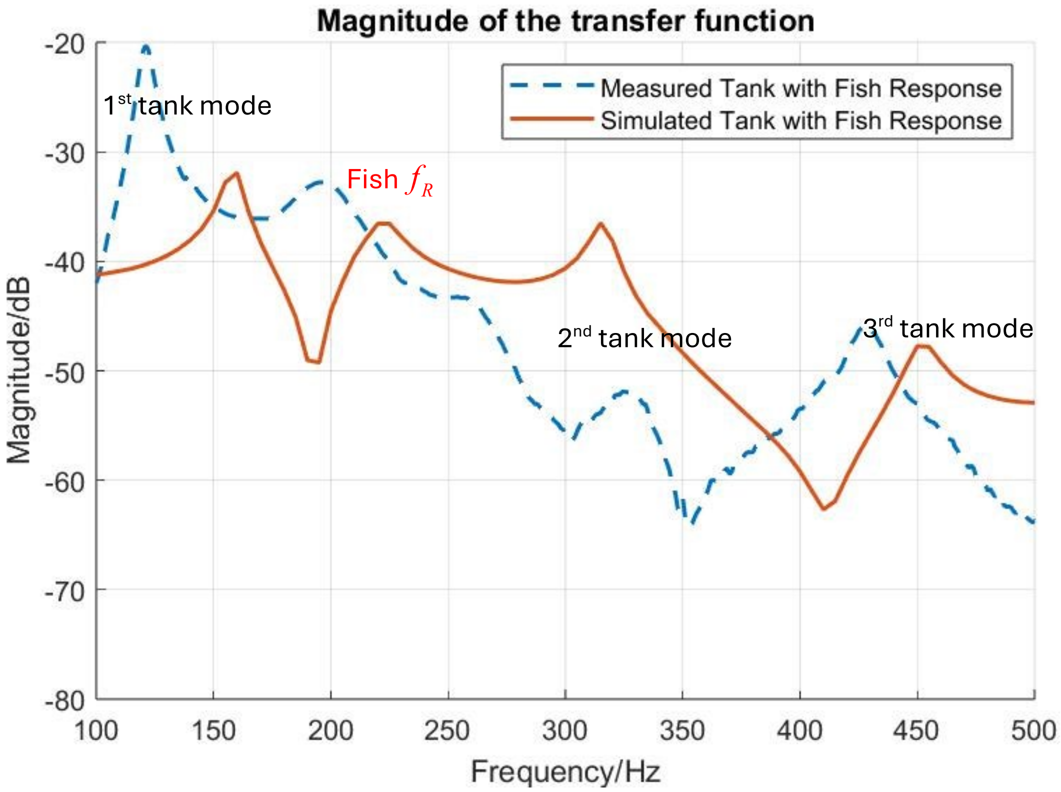

Figure 4.56 Comparison between measured and simulated transfer functions of specimen B.

Specimen C (*L* = 21 cm, *W* = 290 g) from fish size group 3 (8”- 10”):

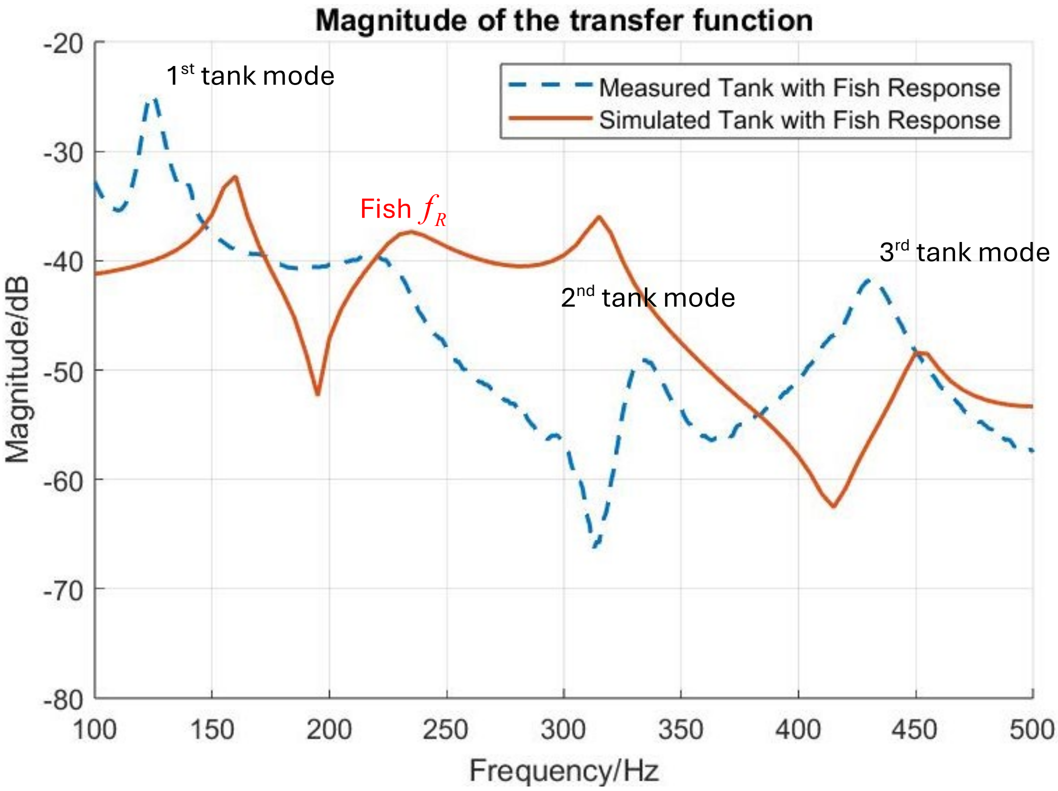

Figure 4.57 Comparison between measured and simulated transfer functions of specimen C.

Specimen D (*L* = 16 cm, *W* = 144 g) from fish size group 4 (6”- 8”):

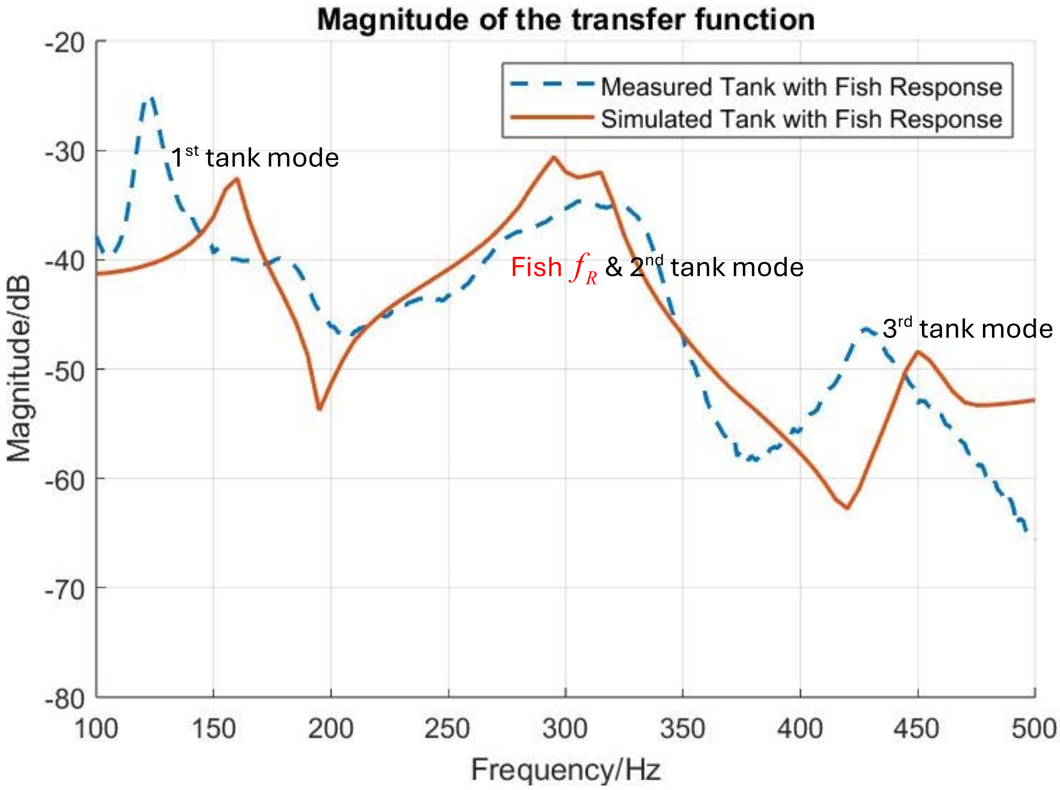

Figure 4.58 Comparison between measured and simulated transfer functions of specimen D.

The overall alignment of measured and simulated transfer functions indicates the ability of FEM simulation to predict and validate experimental results, despite minor discrepancies like differences in measured and simulated original tank resonance frequencies and slight deviations in the magnitude of resonance peaks. Possible sources of error will be further discussed in the next subsection. Similar effects in measured and simulated results like frequency shift and attenuation, and swim bladder resonance merging with original tank modes are also observed in the figures above, while the overall measured system responses show a tendency of being more damped than simulated results. Values of the measured and simulated swim bladder resonance frequency f_R and quality factor Q are shown in Table 4.4.

Table 4.4 Table of experimentally measured and FEM simulated resonance properties.

Test fish	**Measured** f_R	**Simulated** f_R	**Measured** Q	**Simulated** Q
Specimen A	192 Hz	200 Hz	5.4	6.1
Specimen B	201 Hz	220 Hz	6.5	6.3
Specimen C	220 Hz	230 Hz	7.5	5.3
Specimen D	302 Hz	295 Hz	6.3	7.4

As shown in Table 4.4, the simulated resonance frequencies for all four specimens lie within 10–20 Hz of the measured values, indicating generally good agreement between the FEM model and the experimental data. Specimen A (192 Hz vs 200 Hz) and specimen D (302 Hz vs 295 Hz) exhibit the smallest discrepancies, whereas Specimen B (201 Hz vs 220 Hz) shows a slightly larger deviation in resonance frequency. A similar level of consistency is evident for the quality factor: the FEM simulations capture the overall trend but sometimes over- or underestimate the measured. For instance, the simulated Q value for specimen C is notably below its measured value (5.3 vs 7.5), whereas for specimen A and specimen B the differences from the measured data are comparatively minor. Despite these variations, the results confirm that the CT-based FEM approach effectively predicts both the resonance frequency and damping behaviour of the fish swim bladder, capturing key aspects of swim bladder geometry, wall thickness, and material characteristics.

4.8.2 Possible Sources of Error

In interpreting the simulated results and comparing them to real-world measurements, two primary sources of discrepancy stand out: (1) differences between the idealised simulation environment and the actual test tank setup, and (2) variations between the CT-based swim bladder and otolith geometries and the anatomy of a living fish.

Discrepancies in the test tank simulation

Although the FEM model attempts to replicate the same water domain and acoustic excitation used in tank experiments, certain real-world factors are difficult to capture fully:

1. Differences in material properties, unevenness from eight tank feet standing on the lab floor, the imperfect connection between the inertial shaker and the bottom plate, and small air gaps or misalignments can introduce additional interferences that are not present in the idealised tank and water domains used in simulations.

2. The hydrophone mounted on the test tank lid, even damping mechanism applied, might still be mechanically coupled with the inertial shaker and directly pick up vibration signals alongside piezoelectrical acoustic signals, resulting in the overall more damped and lacked details (like antiresonances) transfer functions in measurements than in simulations.

3. The test fish was swimming freely inside the test tank throughout the measurement, so the position of swim bladder varied during the recording of the signals, whereas the swim bladder was kept at the same position in the simulation. Different fish position can cause up to 2 dB difference to the magnitude of the simulated swim bladder resonance peak.

These factors mean that the swim bladder’s excitation level in a real tank might be higher or lower than predicted by the FEM. This discrepancy can lead to frequency shifts and differences in the measured amplitude of resonance peaks compared to the simulation.

Variations between the FEM 3D model and live fish anatomy

A second major source of error lies in using CT-derived meshes of a euthanised specimen as surrogates for live fish:

1. Although each fish was scanned shortly after euthanasia, some changes in tissue elasticity, gas distribution, and ambient pressure occur once circulatory and metabolic processes stop. In a live fish, the swim bladder may actively regulate internal pressure in the water, and surrounding tissues (*e.g.*, musculature) remain perfused and slightly more elastic, which could alter resonance behaviour.

2. The simulation typically focuses on the swim bladder and otolith geometry with minimal attention to other tissues (*e.g.*, muscle, fat) other than the swim bladder wall thickness, which, in a real fish, is not uniform throughout the swim bladder surface. While bones and skeleton reportedly have limited direct effects on resonance properties (Salas *et al.*, 2019), subtle damping or loading from soft tissues might still shift or broaden the resonance peaks.

3. As was discussed in Subsection 4.7.2, some species equipped with Weberian ossicles (like common carp), these small bony structures connect the swim bladder to the inner ear and can enhance hearing sensitivity. In the present COMSOL models, only the swim bladder and otoliths (in the inner ear) were included with only water in between, with these ossicles and other tissues excluded. Real fish may thus experience even stronger hearing amplification than the model predicts, further complicating otoliths' transfer functions and their actual role in fish hearing.

Overall, these anatomic and physiological disparities underscore the challenge of directly translating CT-based simulations of euthanized fish into exact predictions for live, swimming animals. While the computed results provide invaluable insight into how a fish's bladder and otoliths may respond to sound in controlled conditions, however, practical discrepancies should be expected when compared to in-tank measurements of living specimens.

4.9 Discussion

This chapter has advanced the research on fish swim bladder resonance by blending the development of non-invasive experimental techniques with high-fidelity CT-aided numerical modelling. From the outset, the primary challenge lay in creating a tank environment that minimally disturbed free-swimming fish while still delivering repeatable and reliable acoustic data. Sections 4.2 and 4.3 addressed the design and characterisation of this test tank, detailing how engineering considerations, such as mitigating unwanted structural resonances, were balanced against practical constraints like maintaining fish welfare and ease of measurement. Crucially, the optimised test tank facilitated accurate *in situ* measurements of resonance frequencies without necessitating sedation or euthanasia, thereby preserving a closer reflection of real-world biological conditions. However, improvements can be made by improving the design of the test equipment, aiming for a flatter frequency response and a higher fundamental resonance frequency of the test container, which is possible as the test tank manufactured for this project was a prototype that was required to perform both swim bladder resonance measurements and fish behavioural studies at the same time. If possible to design two pieces of equipment specialised separately in measurements or behavioural studies, the efficacy and efficiency of the more specialised equipment would achieve better results.

Next, Section 4.4 described the experimental protocols under which the live fish were maintained and acoustically tested, with emphasis on ethical considerations and minimal interference. Section 4.5 then used these measured data to analyse resonance frequencies in various size groups, highlighting correlations between morphological features (body length and weight) and swim bladder resonance. Significantly, the introduction of CT scanning in

Section 4.6 offered precise three-dimensional representations of the swim bladder and otoliths, helping transition from simplified shapes (*e.g.*, spheres or ellipsoids) to accurate meshes for computational simulations. In Section 4.7, these meshes enabled advanced and complicated FEM simulations of swim bladder resonance and otolith responses, showing how actual anatomical details influence resonance behaviour and potential hearing sensitivity.

The comparison in Section 4.8 demonstrated a generally robust agreement between measured resonance peaks and simulated predictions, validating the modelling assumptions for both the tank environment and fish internal structures. Discrepancies such as small shifts in frequency or minor differences in quality factors can be attributed to realistic factors like structural damping in the test tank, variations in tissue elasticity for live fish, or unmodeled anatomical features (*e.g.*, Weberian ossicles or other soft tissue). By rigorously examining such sources of error, the chapter underscores both the promise and limitations of using CT-aided FEM simulations in tandem with non-invasive measurements.

Overall, the synergy between experimental measurements and numerical simulations builds confidence that the swim bladder significantly contributes to acoustic phenomena in fish, and that the morphological parameters (*e.g.*, wall thickness, swim bladder volume, otolith position) are essential determinants of resonance and fish hearing. These findings not only contribute to clarifying fundamental bioacoustic questions but also provide a stepping stone for advanced applications in fisheries management, underwater acoustics , and ecological monitoring.

4.9.1 Non-invasive Diagnosis of Parasitic Infections on Swim Bladders of Critically Endangered European Eels

The coincidental finding of specimen F (the seemingly healthy common carp discovered to have tumours on its swim bladder) and the prior indication of an abnormal swim bladder from its lack of resonance behaviour not only underscores the diagnostic potential of our non-invasive measurement method.. In particular, using this resonance-based approach to diagnose parasitic infections or other pathological lesions of the swim bladder would be especially valuable for species of critical conservation concern. The tumour-affected bladder in specimen F failed to exhibit the normal resonance response seen in the transfer function, thus confirming that altered bladder tissue properties—whether from tumours, infections, or thickened membranes—can directly disrupt or eliminate the characteristic resonance signal. By detecting a significant departure from baseline resonance behaviour, our method revealed an internal abnormality that might otherwise go unnoticed, reinforcing the possibility of a generalised screening tool for swim bladder pathologies.

Parasitic infections of the swim bladder in European eels, notably by *Anguillicola crassus*, represent a severe and compounding threat to a species already under critical endangerment. This nematode worm becomes lodged in the eel's swim bladder, feeding on host blood and markedly diminishing both buoyancy control and aerobic capacity (Frisch *et al*., 2016). By damaging bladder tissues and increasing the physiological workload, *Anguillicola crassus* infection leads to oxygen transport inefficiencies, depleted energy reserves, and reduced swimming performance. Such impairments are devastating for eels that undertake lengthy transoceanic migrations, relying on pristine swim bladder function and robust aerobic fitness to survive and reproduce. Heavily infected eels thus experience heightened risk of early fatigue and mortality, jeopardising the entire population's reproductive output. Given that these migrations are crucial to the eel's life cycle, any factor that undermines swim bladder performance becomes a major obstacle to species survival (Palstra *et al*., 2007).

Beyond these immediate physiological impacts, *Anguillicola crassus* infection can restructure the swim bladder's acoustic properties by degrading or thickening the swim bladder wall. Such changes reduce elasticity, are likely to shift the swim bladder's resonance frequency to higher values or, in more severe cases, eliminating resonance entirely. Evidence from this study's specimen F suggests that advanced tumours or comparable pathological thickening can suppress the resonance behaviour to the point that no peak is measurable in the transfer function. Similar mechanisms plausibly apply to heavily infected eels, where serious tissue deterioration from the parasite results in negligible or absent resonant signals (Currie *et al*., 2020). In moderate infections, some resonance may persist but becomes noticeably damped, with elevated frequencies and heightened energy losses indicative of the swim bladder's compromised compliance. Figure 4.59 illustrates varying degrees of *Anguillicola crassus* infection in European eels, using both X-ray imaging (a) to visualise internal structural changes and dissection (b, c) to confirm the nematode load. By detecting these alterations in resonance behaviour at early or intermediate stages, a non-invasive acoustic approach could offer a practical way to screen for infection severity and help prioritise conservation interventions for critically endangered eels.

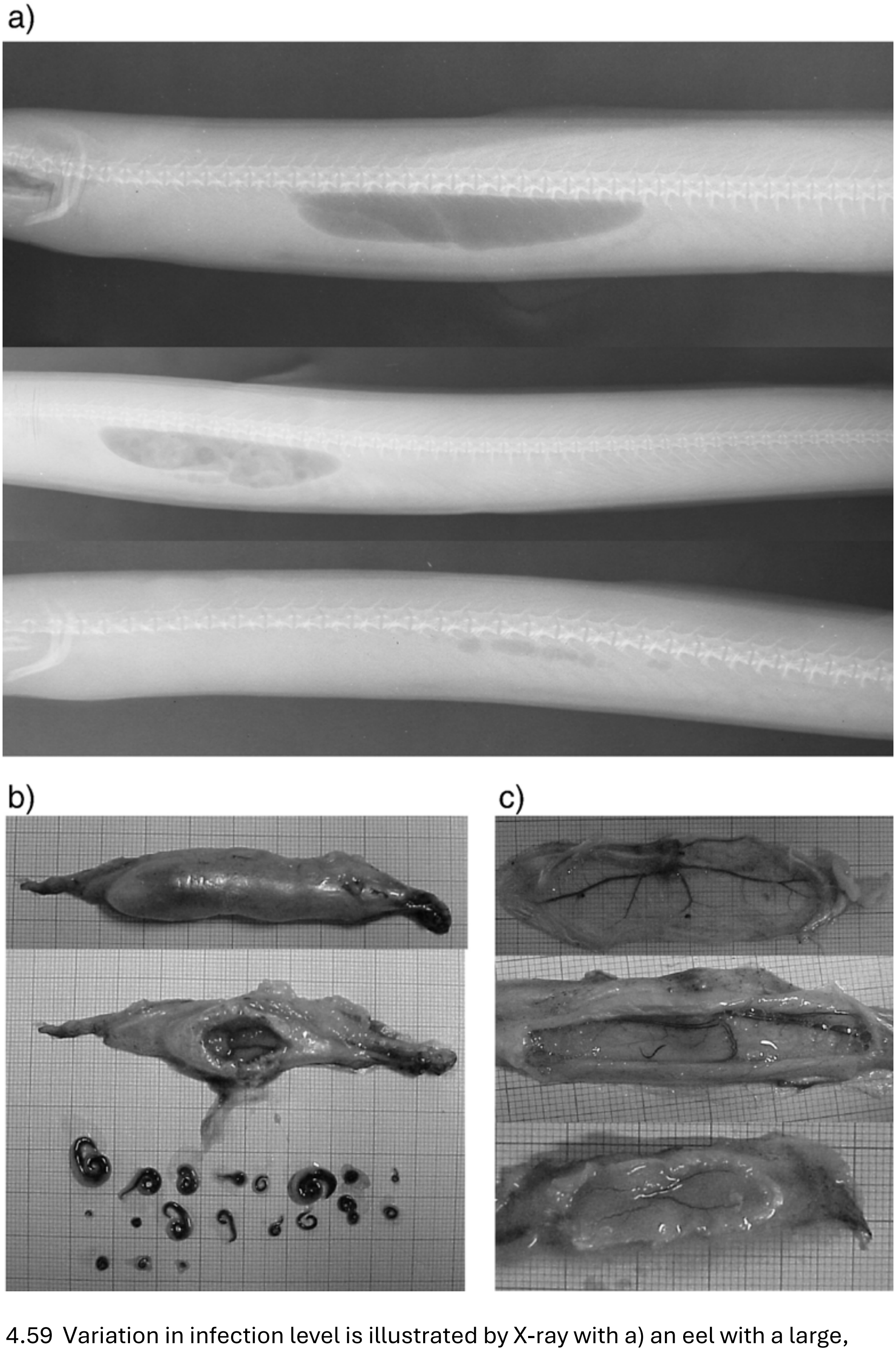

Figure 4.59 Variation in infection level is illustrated by X-ray with a) an eel with a large, uninfected bladder (top), an eel with a medium-sized bladder with visible parasites (middle) and an eel with a small bladder with minimal volume (bottom), b) Dissection of the swim bladder, whole (top) and cut open (bottom) showing 19 parasites of various sizes, and c) three levels of swim-bladder wall transparency, - thickness and length showing a large, thin-walled transparent swim-bladder (top), a medium-sized swim bladder with a thicker wall (middle) and a small thick-walled non-transparent swim bladder (bottom), (Palstra *et al.*, 2007).

In light of these dual concerns, direct physiological harm and potential disruption of vital acoustic functions, there is an urgent need to detect and quantify parasite loads without subjecting an already endangered species to further stress or lethal sampling. Non-invasive resonance-based diagnostic methods offer a promising alternative, allowing researchers to monitor changes in swim bladder properties while the eel remains alive and unharmed after a short period of measurement within a portable test container. By leveraging differences in resonance properties between healthy and infected swim bladders, scientists could assess the severity of infection and guide conservation actions more effectively. This approach not only advances our understanding of *Anguillicola crassus* induced swim bladder infection but also supports more sustainable management strategies for European eels, helping preserve a species of profound ecological, economic, and cultural importance.

4.10 Chapter Conclusions

This chapter presented a comprehensive methodology for non-invasive capturing and interpreting the resonance behaviour of fish swim bladders under near-natural conditions. By designing a custom test tank (Sections 4.2–4.3), refining measurement protocols to keep fish alive and swimming freely (Section 4.4) and applying statistical and computational analyses (Sections 4.5–4.8), it was possible to achieve a high level of biological realism alongside robust validation of results. Key accomplishments include:

Non-Invasive Tank System: Developed and characterised to sustain free-swimming fish, enabling accurate resonance measurements without anaesthesia or euthanasia.

CT-Based Meshing: Employed to reconstruct the detailed internal geometry of swim bladders and otoliths, moving beyond simplified shapes to capture morphological nuances critical for reliable FEM simulations.

FEM Validation: Demonstrated strong concordance between simulated and measured resonance frequencies, reinforcing the viability of these computational models for future predictive tasks.

Morphological Insights: Correlated fish size, swim bladder volume, and wall thickness with resonance characteristics, illuminating how natural variations in anatomy can shift or amplify acoustic behaviours and fish hearing.

Collectively, these findings substantiate that integrating non-invasive measurements with accurate numerical modelling offers a powerful framework for studying underwater bioacoustics. The outcomes point toward further potential improvements, such as optimising the tank’s frequency response and measurement efficiency or including additional anatomical details (*e.g.*, Weberian ossicles) in FEM simulation, but already establish a robust baseline for subsequent research. This work thus marks a step of advance in the field of fish bioacoustics, suggesting broad utility in ecologically oriented investigations, endangered species conservation, and other applications where understanding or leveraging fish hearing and swim bladder resonance is of great significance and potentials.

Chapter 5 Behavioural Response of Common Carp (*Cyprinus carpio*) to Acoustic Stimulus at the Swim Bladder Resonance Frequency

Following the results and discussion in Chapter 4, it is hypothesised that the test fish might exhibit a stronger behavioural response to acoustic excitations that are tuned into the resonance frequency of its swim bladder, which will resonate under the acoustic excitations and the otoliths in the inner ear of the test fish will pick up the radiated resonance-induced sound field, resulting in lower hearing thresholds (Li *et al.*, 2024) and potentially higher behavioural sensitivity. To test this hypothesis, behavioural experiments will be described, analysed, and discussed in this chapter.

5.1 Introduction

Previous chapters have established the theoretical foundations and experimental infrastructure for investigating fish responses to acoustic stimuli under controlled conditions. By focusing on swim bladder resonance, we have gained a deeper understanding of how a fish's morphological characteristics relate to the frequencies at which its bladder naturally resonates. Chapter 4 documented how common carp were briefly handled to measure individual swim bladder resonance frequencies f_R in a specially designed cylindrical tank. Having verified the tank's ability to create a suitably homogeneous sound field and having identified each fish's unique resonance frequency, we now build on those findings by examining how carp respond behaviourally to short-duration tonal stimuli centred around each individual's f_R.

Traditional acoustic deterrent studies often rely on fixed absolute frequencies (*e.g.*, 200 Hz, 400 Hz, 600 Hz) within the hearing range of the target species. However, researchers found fish hearing may be related to the swim bladder's capacity to resonate and amplify particular frequencies, a phenomenon potentially heightened for species with robust swim bladders and Weberian ossicles like the common carp (Li *et al.*, 2024). Apart from amplified fish hearing near swim bladder resonance frequency, another possible effect of resonance could be fish directly sensing the displacement and deformation of the swim bladder wall when it is resonating.

This chapter addresses how common carp respond to tonal stimuli specifically aligned with their individual swim bladder resonance frequencies, rather than relying solely on population-level hearing thresholds. The experiment considered three signal-to-noise ratio (SNR) levels, allowing us to gauge whether changes in SNR alter the likelihood of a startle response. The principal aims here are to:

1. Examine whether a fish's startle response occurs most reliably at or near its recently measured swim bladder resonance frequency, and

2. Assess how varying SNRs (0 dB, 10 dB, and 20 dB above the masking noise) influence that response threshold at different exciting frequencies.

By integrating individual resonance measurements, frequency steps spaced around f_R (± 1/3 octave increments), and different SNR settings, this experiment seeks to refine our understanding of how acoustic signals can be tuned to maximise fish avoidance behaviour. If shown to be effective, this approach may have further implications for the design and efficacy of non-invasive acoustic deterrent systems, offering a more scientifically grounded rationale for selecting stimulus parameters that induce reliable startle responses in free-swimming carp.

5.2 Experimental design

Building on the methodologies introduced in Chapter 4, this experiment was conceived to examine how common carp react to specific acoustic stimuli aligned with their individual swim bladder resonance frequencies. Each fish's swim bladder resonance was measured under controlled conditions immediately before behavioural experiments, providing a personalised reference point for selecting the stimulus tones. This approach diverges from the more conventional use of fixed frequencies by instead anchoring every test tone around each fish's unique f_R, thus offering a more nuanced investigation into the resonance-driven aspects of fish hearing and startle responses.

Following the resonance measurement, the test tank with transparent walls were in a black plastic to avoid any unexpected visual cues which might affect the behavioural study. Each fish (*N*=30) was subjected to five tonal stimuli at different SNRs and spaced in 1/3 octave increments around its own swim bladder f_R measured 10 minutes before the behavioural response studies, where the 10-minute interval acted as an acclimation period. Specifically, the frequencies tested included two lower frequencies $2^{-2/3} \cdot f_R$ and $2^{-1/3} \cdot f_R$, the resonance frequency f_R, and two higher frequencies $2^{1/3} \cdot f_R$ and $2^{2/3} \cdot f_R$. By covering a spread around the resonance frequency, we aimed to assess whether the likelihood of a startle response would peak near f_R, or if it would have a lower startle response threshold.

To incorporate realistic environmental noise conditions and avoid interference from unexpected behavioural stimuli (door of another lab closing), a constant masking white noise of 125 dB re 1 µPa was introduced into the experimental tank from the start of the 10-minute acclimation period until the end of the whole behavioural study. Three distinct SNRs, 0 dB, 10 dB, and 20 dB above the masking level, were established. The 125 dB masking noise level was the same level used to measure the swim bladder resonance. The study consisted of 10 replicates of 15 treatments based on a combination of five frequencies (to simplify, $2^{-2/3} \cdot f_R$, $2^{-1/3} \cdot f_R$, f_R, $2^{1/3} \cdot f_R$, and $2^{2/3} \cdot f_R$ are referred to $f_R(-2), f_R(-1), f_R(0), f_R(1), f_R(2)$ respectively) and three SPLrms values (125, 135, 145 dB re 1µPa). Each tonal stimulus was 120 ms in duration and ramped with a 20 ms Hanning taper, and a five-minute interval was maintained between successive exposures to reduce potential habituation. The order of frequency presentation and SNR level was randomised to minimise any bias that might arise from sequential effects. Although latencies of Mauthner cell activation in cyprinids is 5 - 10 ms, the tone was played at 120 ms so that it was sufficiently short to elicit a startle response but long enough to enable the frequency spectrum to be well defined at this lower signal duration (Eaton, 1977; Zeddies and Fay, 2005). Each fish was only exposed to 5 stimuli. Fish behaviour was continuously video recorded during the trial, and each fish was used in one trial only.

Table 5.1 An example of the selection of the treatments experienced by an individual fish. Treatment is each of the 15 combinations of SPLrms and frequency. Exposure represents the nth treatment (1-5) experienced by an individual fish in one trial.

Order of Exposure	**Frequency (Hz)**	**SPLrms (dB re 1 µPa)**	**SNR (dB)**
1	$f_R(-2)$	125	0
2	$f_R(2)$	145	20
3	$f_R(1)$	125	0
4	$f_R(-1)$	135	10
5	$f_R(0)$	135	10

5.3 Behavioural and data analysis

All trials were recorded on video (NIKON Z7 and Z 24-200 mm f4-6.3 lens) with the excitation acoustic signal directly recorded into the camera from DAQ, and each exposure was evaluated offline to identify whether a startle response occurred. The startle event (Figure 5.1) was defined as a rapid shift in body orientation or swimming trajectory within approximately one second of the tone's onset, a criterion that was consistently applied across all fish and conditions (Holgate *et al.*, 2023). Review of the recordings was carried out under a "blind" protocol in a random order, meaning that the observer did not know which frequency-SNR combination was being played at the time of video inspection.

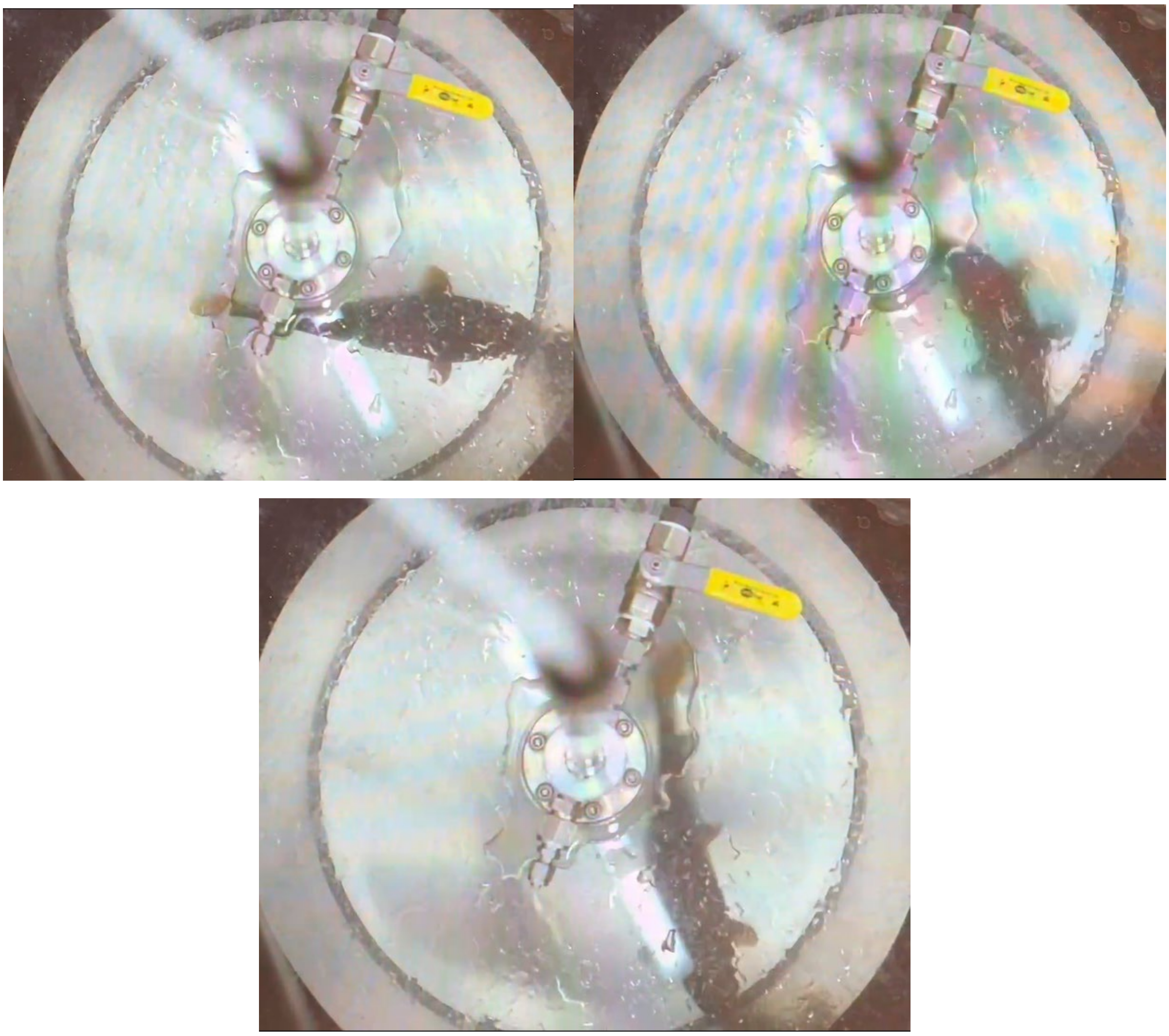

Figure 5.1 Still images from the video footage of a common carp startling to a tone: before the startle (top left), during the startle (top right), and after the startle (bottom).

To ensure that the probability of startle was consistently comparable across the five frequencies and three SNR levels, only a binary outcome, presence or absence of startle, was noted and considered for further analysis. No additional qualitative behavioural metrics (*e.g.*, half-turn, freezing, or changes in speed) were applied, which simplified the subsequent statistical modelling and reduced potential ambiguity in classifying subtler responses.

For each fish, the exposures were administered in a randomised sequence, thus minimising any bias from repeated tones of a certain frequency or loudness being presented consecutively.

Between each exposure, a five-minute interval was allowed to mitigate potential habituation. If a startle occurred multiple times within the same exposure window (for instance, a short burst of erratic movement followed by a second rapid turn), it was recorded as a single startle response presence. Conversely, if the fish maintained steady motion or exhibited only minor orientation changes, the outcome was classified as a no-startle event.

After data collection, a logistic regression analysis was used to relate the probability of a startle response to the exciting frequency and to the SNR. In practice, the model evaluated each stimulus presentation, taking into account whether it was at $f_R(-2), f_R(-1), f_R(0), f_R(1), f_R(2)$, and whether the tone level exceeded the background noise by 0 dB, 10 dB, or 20 dB. This regression framework made it possible to estimate how strongly each factor contributed to the likelihood of a startle, as well as to determine any interaction effects (*e.g.*, whether high SNR tones near f_R) produced a notably stronger response than high SNR tones at frequencies far from resonance).

Quality checks on the data included verifying that all exposures were clearly audible above background (for the respective SNR level), and that randomisation was preserved throughout. Additionally, any videos with poor visibility were flagged and reviewed a second time to confirm classification accuracy. The final logistic model outputs are presented in the subsequent section, illuminating trends in startle probability as a function of both individual resonance alignment and incremental changes in signal-to-noise ratio.

5.4 Results

5.4.1 Results of Logistic Regressions

Figure 5.1 presents the binary logistic regressions of startle probability for each frequency offset, $f_R(-2), f_R(-1), f_R(0), f_R(1), f_R(2)$, as a function of SNR. Each subplot displays:

1. Raw data points (grey and black dots) indicating startle (1) or no-startle (0) at each tested SNR, with a small vertical jitter for clarity.

2. Fitted logistic curves (blue line) for the probability of startle with 95 % confidence intervals (shaded regions).

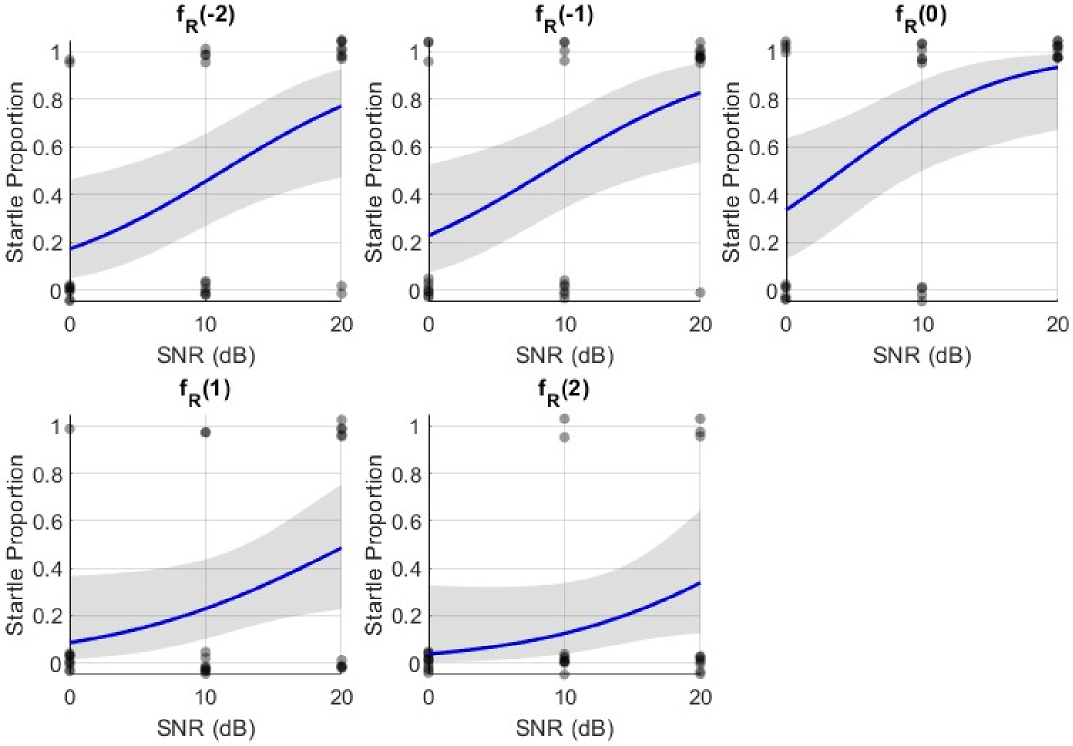

Figure 5.2 Logistic regression curves illustrating the proportion of common carp that startled in response to a 120 ms pure tone at SNRs of 0; 10; 20 dB. Results were plotted for each frequency offset: $f_R(-2), f_R(-1), f_R(0), f_R(1), f_R(2)$. The grey regions indicate 95.0% confidence intervals.

It is observed in Figure 5.2 that for frequencies at or below the swim bladder resonance frequency, common carp presented higher startle proportions then those higher than the resonance frequency, which agrees with experimental findings of Holgate *et al.*, 2023 on goldfish. As SNR and SPLrms increased, common carp exhibited more startle responses in all frequency offsets. Stimuli at swim bladder resonance frequencies of all SNRs showed highest startle response rates, indicating that common carp are behaviourally more sensitive to tonal stimuli at their resonance frequencies than other frequencies.

5.4.2 Influence of SNR within Each Frequency Offset

To better quantify how the probability of a startle changed with increasing SNR for each frequency offset, separate logistic regressions were performed, resulting in five models (one per offset). Table 5.2 shows the estimated z-values and p-values for the SNR coefficient in each model:

Table 5.2 Estimated z-values and p-values for the increasing SNR in each frequency offset.

Frequency Offset	z-value for SNR	p-value	Interpretation
$f_R(-2) =$	3.78	0.0002	Highly significant increase in startle with SNR
$f_R(-1)$	4.31	<0.0001	Highly significant increase in startle with SNR
$f_R(0)$	5.02	<0.0001	Strongest dependence of startle on SNR
$f_R(1)$	3.15	0.0016	Significant increase in startle with SNR
$f_R(2)$	2.68	0.0073	Moderate increase in startle with SNR

Although all frequency offsets show significant positive slopes suggesting the positive role of SNR in startle response, the highest z-value occurs at $f_R(0) = f_R$ (z = 5.02, p < 0.0001), indicating the steepest rise in the probability of startle as SNR increases at the exact resonance frequency of the fish swim bladder. Visually, this is reflected in the subplot for $f_R(0) = f_R$ (top-right of Figure 5.1), where only low SNR gains (~5 dB) were needed to produce a marked ($\geqslant$ 50 %) startle response in individuals whereas moderate SNR gains (~10 dB) were needed for $f_R(-2)$ and $f_R(-1)$ while higher SNR gains ($\geqslant$20 dB) were required for $f_R(1)$ and $f_R(2)$ to achieve a marked startle response under the same experimental set-up.

5.4.3 Comparison Across Frequency Offsets

Apart from the significance of SNR in startle response proportions, single logistic regression that included the frequency offset as a categorical factor and SNR as a numeric predictor was also tested. Below is an updated analysis where Frequency Offset = $f_R(2)$ at SNR = 0 dB is treated as the regression baseline, reflecting the condition with the lowest overall startle response rate in our data. We re-fit a single logistic regression that simultaneously models both the effects of SNR (numeric) and Frequency Offset (categorical) on the probability of a startle.

Rationale for the New Baseline

In logistic regression with categorical predictors, one category must be chosen as the baseline against which all other categories are compared. Since $f_R(2)$ at SNR = 0 dB showed the lowest startle rate in all treatments, we now define: $f_R(2)$ as the reference offset, and SNR = 0 dB as the intercept reference point (this occurs naturally if we keep SNR numeric and do not centre it).

Hence, the intercept in our new model will represent the log-odds of startle at $f_R(2)$ with SNR = 0 dB. Additional Offset coefficients indicate how log-odds shift when moving $f_R(-2), f_R(-1), f_R(0),$ and $f_R(1)$, while the coefficient of SNR describes how log-odds change per decibel of SNR.

Model Specification and Example Results

We fit the following logistic regression:

$$\text{logit}(\textit{Startle}) = \beta_0 + \beta_{SNR} \cdot SNR + \sum_{i \neq 2} \beta_{f_R(i)}, \tag{29}$$

where: *Startle* is 0 or 1, SNR is numeric (0, 10, or 20 dB above background noise level), $f_R(i)$ is the categorical factor standing for $f_R(-2), f_R(-1), f_R(0), f_R(1), f_R(2)$, with $f_R(2)$ set as the regression baseline. Table 5.3 below shows the illustrative coefficients calculated using fitglm function in MATLAB.

Table 5.3 Example logistic regression coefficients using $f_R(2)$ at $SNR = 0$ as baseline.

Term	**Coefficient *β***	**SE**	**z-value**	**p-value**	**Interpretation**
Intercept (β_0)	-2.85	0.51	-5.59	< 0.0001	At $f_R(2)$ with $SNR = 0$, the log-odds of startle is -2.85.
SNR	0.087	0.016	5.51	< 0.0001	For each 1 dB increase in SNR from 0 dB to 20 dB, log-odds of startle multiply by $e^{0.087} \approx 1.09.$
$f_R(-2)$	0.28	0.32	0.88	0.378	$f_R(-2)$ has slightly higher log-odds than baseline $f_R(2)$ but not statistically significant.
$f_R(-1)$	0.81	0.30	2.73	0.0063	A significant increase in startle log-odds vs $f_R(2)$
$f_R(0)$	1.92	0.33	5.82	< 0.0001	The largest jump in log-odds, indicating peak responsiveness at $f_R(0)$ vs $f_R(2)$.
$f_R(1)$	0.53	0.31	1.70	0.089	Trend toward higher log-odds than $f_R(2)$ with borderline significance.

Table Interpretation

1. Intercept ($\beta_0 = -2.85$) is the log-odds of startle at the baseline treatment: $f_R(2)$ at $SNR = 0$. In practical terms, $odds_{(Startle)} = e^{-2.85} \approx 0.058$. The corresponding probability of startle is $p_{(Startle)} = \frac{0.058}{1+0.058} \approx 5.5\%$. This low baseline probability reflects the empirical observation that, at the farthest offset above resonance $f_R(2)$ and no additional amplitude above background (SNR =0 dB), fish seldomly startled.

2. SNR Coefficient ($\beta_{SNR} = 0.087$, p < 0.0001) means each +1 dB increment in SNR multiplies the odds of startle by about $e^{0.087} \approx 1.09$. SNR moving from 0 dB to 20 dB means the odds can increase roughly $e^{0.087\times 20} \approx 5.7$ times with other factors held constant. This aligns with the earlier conclusion that raising the stimulus amplitude strongly influences startle response rates.

3. $f_R(-2)$ with $\beta_{f_R(-2)} = 0.28$ and p = 0.378 shows that it is not statistically significantly different from $f_R(2)$ at SNR=0 dB even its startle response ratio is slight higher, suggesting these two frequency extremes produce similarly low response at baseline amplitude. Both conditions deviate from the swim bladder resonance by frequency 2 steps, effectively placing them far from the fish's best behavioural sensitivity range.

4. $f_R(-1)$ with $\beta_{f_R(-1)} = 0.81$ and p = 0.0063 shows significantly higher log-odds (z = 2.73) than $f_R(2)$. Even one step closer to resonance results in a marked jump from baseline probability, which is visible in the raw data as well.

5. $f_R(0)$ with $\beta_{f_R(0)} = 1.92$ and p< 0.0001 presents z = 5.82, meaning this is the most statistically robust frequency treatment. $\beta_{f_R(0)} = 1.92$ means an $e^{1.92} \approx 6.8$ times jump in the odds of startle at SNR=0 dB, relative to $f_R(2)$. When combined with the positive slope for SNR, stimuli at swim bladder resonance frequencies can achieve significantly higher startle probabilities even at moderate amplitude levels.

6. $f_R(1)$ ($\beta_{f_R(1)} = 0.53$, p = 0.089) shows a borderline significant increase over $f_R(2)$. The direction is still positive, implying a partial gain in sensitivity from being closer to the resonance frequency, but with greater variability among replicates.

Table Conclusion: Clear Peak at Resonance

By choosing $f_R(2)$ at SNR = 0 dB as the baseline, we highlight the contrast between a condition with minimal startle response among all treatments and those who are nearer to the swim bladder resonance frequency. The highly significant coefficient for $f_R(0)$ with $p<0.0001$ confirms that using acoustic stimulus at the swim bladder resonance frequency significantly elevates startle odds relative to the farthest offset. Coupled with the strongly positive influence of SNR, these results reinforce the notion that:

1. Acoustic amplitude (SPLrms and SNR) positively affects the probability of startle response.

2. Alignment with the swim bladder resonance frequency magnifies that effect, requiring less SNR to achieve high startle response rates.

Thus, the fish's greatest startle response rate to acoustic stimuli occurs when the stimulus frequency most closely matches its swim bladder resonance, with near-resonance frequency offsets also increasing startle probability but to a lesser degree.

5.5 Discussion and Conclusions

The results from this chapter provide a clearer understanding of how common carp respond to tonal stimuli when those tones are centred on, or offset from, the fish's individual swim bladder resonance frequency. By applying both separate and combined logistic regression models, we have shown that two primary factors shape the probability of startle: (1) the amplitude of the acoustic stimulus (SPLrms), and (2) the proximity of the stimulus frequency to the measured swim bladder resonance frequency of each test fish. In particular, tones presented at f_R consistently achieved a higher probability of evoking a startle at lower acoustic energy levels than did tones one or two 1/3 octaves away from resonance. Below, we summarise how these findings situate within both the immediate context of fish deterrent system design and broader behavioural research.

5.5.1 Resonance-Driven Behavioural Sensitivity

One key outcome of this experiment is the strong evidence that even a moderate increase in SPLrms can prompt a substantial increase in startle responses, provided the frequency is at, or near, the fish's swim bladder resonance. This aligns with prior research on goldfish and other otophysine fish (*e.g.*, Zeddies and Fay, 2005; Mensinger *et al.*, 2021), which indicated that their enhanced auditory structures, bolstered by the swim bladder, enable acute detection near species-specific frequency bands. While the earlier chapters had highlighted the morphological impact of the swim bladder resonance (Chapter 4), the present behavioural study underlines the practical outcome: fish do not require as high an amplitude to elicit a startle when the tone is tuned to their f_R.

Comparisons with other fish deterrent studies further underscore the importance of this resonance matching. For instance, Putland and Mensinger (2019) demonstrated how a misalignment between peak hearing sensitivity and the deployed acoustic signal can severely reduce deterrent efficacy. Likewise, the variable success rates reported in acoustic deterrent fields (Maes *et al.*, 2004; Vetter *et al.*, 2015) might reflect the lack of tailored frequencies that exploit resonance. Our results imply that targeting f_R rather than simply selecting a "general hearing threshold" frequency—might yield a more consistent avoidance or startle response, especially under moderate noise conditions.

5.5.2 The Role of SNR and Implications for Real Environments

Across all tested offsets, higher SNR correlated strongly with an increased likelihood of startle, consistent with the fundamental principle that fish must detect the stimulus above the ambient noise floor. Nonetheless, the steepness of the logistic curves at resonance confirms that lower amplitudes are needed at f_R to surpass the response threshold there. From a fish deterrent or management perspective, this suggests that operating near f_R not only boosts avoidance rates but could also reduce the overall acoustic power required, potentially minimising energetic costs or noise pollution concerns at a site or even size-selectively deterring fish species from water inlets of human structures or local-species-protecting ecosystems.

In more turbulent or variable field conditions, background noise can fluctuate, and fish may move through acoustic "hotspots" or "quiet zones" within a water column (Short *et al.*, 2020). Our results hint that maintaining a stable margin of the level of the stimulus above local ambient levels is crucial for consistent deterrent performance. Future studies might investigate whether the presence of band-passed noise or alternative frequency components modulates the effectiveness of these resonance-based stimuli in free-swimming conditions.

5.5.3 Limitations and Avenues for Future Work

Controlled Tank Environment: Although we introduced a masking noise and the varied stimulus level, real aquatic habitats may exhibit more complex acoustic conditions (*e.g.*, varying turbulence, bubble-induced background noise, and complicated particle motions). Confirming these patterns in larger, semi-natural environments or *in situ* field tests would strengthen ecological validity.

Complex acoustic field: Although carefully designed, the nature of the experiment being performed within a small tank with different physical boundaries (like the pressure-release acrylic tank wall and thin steel plate not forming thick rigid boundaries) would still introduce complex acoustic pressure field and mismatched particle motion field. It is known that fish can directly sense the particle motion element of acoustic field; and for small tank experiments at frequencies above the lowest tank mode, the particle velocity and pressure fields, and their ratio, vary rapidly both spatially and with changes in frequency (Duncan *et al.*, 2016). Therefore, better acoustically designed experiments are recommended for further studies to take particle motion into serious account along with pressure fields (Rogers *et al.*, 2016; Jones *et al.*, 2019).

Other behavioural cues: Besides the pressure field and particle motion field, other cues that were not considered and studied in the experiment could also cause multi-modal behavioural response. In real aquatic habitats, fish is unlikely to experience the same environment as in the small test tank. Lighting conditions, turbulence, lack of visual cues, limited space, near-field sound waves in the experiment were far from natural environments where fish lives in.

SNR-aimed Studies: The masking noise level used for this experiment was 125 dB re 1μPa, with three stimulus levels. However, it is recommended that future trial can use several masking noise levels and corresponding stimulus levels to better study the effect of SNR, and if the effect of SNR on fish behaviour is consistent at different masking noise levels.

Species and Morphological Variations: Our findings specifically concern common carp. While the results are likely generalisable to other species with similar auditory mechanisms, fish that lack specialised hearing adaptations (*e.g.*, Weberian ossicles) may show different resonance effects. Parallel studies in hearing generalists or in marine teleosts may help clarify the universal or species-specific aspects of this resonance-driven phenomenon.

Potential for Habituation: This study employed discrete exposures separated by a consistent cooldown period. In longer-term applications, fish might adapt or habituate to repeated stimuli. Investigating whether resonance-based stimuli remain effective over prolonged usage, or require adaptive frequency tuning, is an important next step for designing robust deterrent systems. More test fish for behavioural studies with fewer exposure repetitions can be beneficial to achieving a more comprehensive understanding of resonance-based effects.

5.5.4 Chapter Conclusions

By systematically testing five offset frequencies around each fish's individual swim bladder resonance frequency and applying incremental SNR steps, this chapter demonstrates that resonance alignment significantly lowers the acoustic energy needed to elicit startle behaviour in common carp. The logistic regression analyses show SNR consistently increases the odds of startling across all frequency offsets, but the largest and most statistically robust shift arises at f_R, highlighting a peak for acoustic sensitivity.

These results confirm a resonance-centric view of fish behavioural responses, underscoring the potential benefits of tuned or band-passed deterrent signals in fisheries management and ecological conservation. Grounded in the morphological evidence from earlier chapters, we propose that fish are most susceptible to resonance-matched stimuli, which is an insight that can inform ongoing research into more humane and effective acoustic guidance systems, as well as broader ecological investigations into how fish perceive and prioritise sounds in their natural habitats.

Chapter 6 Conclusions

This chapter brings together the key outcomes of the research, referencing how each of the objectives stated in Chapter 1 has been fulfilled, and outlines potential avenues for continued investigation and practical application. It concludes by highlighting the original contributions that this thesis offers to the fields of fish bioacoustics and underwater acoustical engineering.

6.1 Conclusions

The overarching aim of this thesis was to develop and validate a non-invasive experimental methodology for measuring swim bladder resonance in live, free-swimming fish, then to assess how acoustic excitation at or near the swim bladder resonance frequency might influence fish behaviour. The study was motivated by ecological imperatives, particularly the drive to reduce fish mortality at hydropower or irrigation structures, and grounded in the theoretical understanding that resonantly driven swim bladders can generate strong responses in fish. Below is a summary of how each research objective from Chapter 1 has been addressed, drawing on the methods and findings in Chapters 2 to Chapter 5.

Objective 1: *Examine and consolidate existing knowledge on fish auditory mechanisms, underwater bubble acoustics, and swim bladder resonance.*

Literature Review (Chapters 1–2): A thorough survey established that many bony fish rely on their swim bladder to enhance hearing sensitivity, especially in species with morphological linkages (*e.g.*, Weberian ossicles) between the swim bladder and the inner ear. The review also explored how the swim bladder can be conceptualised as an encapsulated bubble, emphasising theories of bubble resonance and previous efforts on resonance measurement.

Contextual Gap (Chapter 2): While prior studies had examined fish hearing and bubble resonance separately, combining them into a practical deterrent approach that swim bladder resonance could be exploited to repel fish remained a major challenge due to difficulties in measuring swim bladder resonance *in vivo* on freshwater fish.

From this basis, the thesis identified a possible opportunity: to apply bubble resonance theory in a real-world fish context, thereby bridging engineering models with ecological and physiological insights.

Objective 2: *Develop experimental protocols to measure encapsulated bubble resonance using surrogate objects and recently euthanised fish, validating the approach with theoretical and numerical models.*

Surrogate Targets (Chapter 3): Initial protocols were established and refined using latex balloons as dummy swim bladders, enabling a direct test of resonant frequency measurements under controlled lab conditions. These trials demonstrated that the method could capture stable resonance peaks and quality factors of encapsulated bubbles.

Application to Recently Euthanised Fish (Chapter 3): The protocols were then extended to recently euthanised specimens, carefully considering factors such as swim bladder volume, shape, and tissue damping. Measurements of resonance in these fish aligned well with predicted values from scattering theory, confirming the viability of the approach.

FEM Validation (Chapter 3): In parallel, FEM simulations were conducted to compare theoretical resonance predictions with empirical data. The agreement between measured and simulated results lent credence to the experimental setup and supported further refinement toward live-fish studies.

This stage affirmed that bubble resonance measurements could be accurately taken in a laboratory environment and that the transition from simpler surrogates to actual fish tissue did not compromise the reliability of the approach, so long as appropriate damping and morphological parameters were considered.

Objective 3: ***Design and construct a specialised tank setup that enables non-invasive testing of resonance frequencies and quality factors in free-swimming fish*****.**

Tank Design (Chapter 4): Recognising the acoustic complexities inherent in standard rectangular tanks—specifically standing waves and geometric reflections—a cylindrical tank was conceived. This design underwent extensive FEM-based evaluations to predict and minimise unwanted modes, ensuring that fish could be exposed to a relatively uniform sound field over the relevant frequency range.

Manufacture and FEM simulation (Chapter 4): Acoustic characterisation tests and supporting FEM simulations confirmed that the cylindrical geometry and carefully selected boundary conditions yielded a more controlled environment, enabling stable tone generation at or near the fish's prospective swim bladder resonance.

Ethical and Welfare Considerations (Chapter 4): This new tank setup allowed fish to remain awake and free-swimming, fulfilling the desire to non-invasively measure resonance *in vivo* while avoiding the confounding influences of anaesthetics or euthanasia.

Thus, a previously unmet need was addressed: a specialised, non-invasive laboratory facility that supports free-swimming fish experiments without compromising data quality or animal welfare.

Objective 4: ***Measure and analyse in vivo swim bladder resonance for free-swimming fish without anaesthesia or euthanasia, correlating morphological attributes to measured swim bladder resonance properties.***

In vivo Non-invasive Resonance Measurements (Chapter 4): The completed tank design made it possible to identify the resonant peaks of each fish's swim bladder under free-swimming conditions. Subtle inter-individual differences in frequency and damping were noted, influenced by body size, swim bladder volume, and internal gas distribution.

Morphological Correlations (Chapter 4): Rough scaling analyses indicated that larger fish or those with proportionally greater swim bladder volumes, generally exhibited lower resonant frequencies, consistent with encapsulated-bubble physics. Meanwhile, variations in tissue elasticity or fish positions sometimes introduced minor shifts in the measured peaks, reflecting the dynamic nature of *in vivo* biology.

CT-aided FEM Simulations (Chapter 4): The high-resolution CT scanning of specimens in different body sizes brough the accuracy of FEM swim bladder resonance simulations to a higher level. By combining the 3D reconstruction of scanned swim bladders and the engineering 3D model of the test tank, the results from *in vivo* non-invasive resonance measurements were validated by comprehensive FEM simulations, confirming the alignment of real-life measurements and desk-based simulations.

Objective 5: ***Evaluate how fish behaviour changes under acoustic stimuli at their swim bladder resonance frequencies, especially relative to off-resonance noise conditions.***

Behavioural Trials (Chapter 5): By systematically shifting the acoustic stimulus around each fish's known resonance frequency, researchers could compare reactions under near-resonant versus off-resonant conditions. Observations utilised quantifying startle responses, with logistic regression identifying whether resonance alignment significantly heightened these reactions.

Statistical Findings (Chapter 5): Data showed that fish typically exhibited more pronounced startle or evasion when the stimulus frequency matched or closely approximated their measured bladder resonance. Off-resonance stimuli generated milder responses, supporting the hypothesis that resonant excitation can substantially enhance the fish's perceptual salience or discomfort.

Implication for Deterrents (Chapter 5): These results suggest that swim bladder resonance-based acoustic stimuli could be leveraged to reduce the need for high-intensity broadband noise, thereby offering a more targeted and potentially less intrusive deterrent for guiding fish away from hazards.

Taken together, Objectives 4 and 5 exemplify how direct swim bladder resonance measurement and subsequent resonance-focused stimuli can meaningfully influence fish behaviour, resulting in a conclusion that could underpin new, ecologically sensitive management strategies in hydropower and fisheries operations.

6.2 Further Research

Building on these accomplishments, several promising directions remain open for extension and refinement:

1. Species Diversity and Scaling Up

While experiments so far focused on specific species (*e.g.*, common carp) within moderate body size ranges, future work should explore fish of varying morphologies and families. Large-bodied or highly elongated species might present distinct resonance characteristics. The method may also require scaling for smaller species with higher resonance frequencies, possibly adjusting the tank geometry or acoustic hardware.

2. Weberian Ossicles, Enhanced Acoustic Pressure, and PA Detection

Extending the method to otophysan fish with more complex inner ear-swim bladder linkages may yield deeper insights into how swim bladder resonance influences hearing thresholds (both acoustic pressure and particle motion) and behavioural responses. Fine-grained soft tissue imaging (*e.g.*, Magnetic Resonance Imaging) combined with highly detailed FEM simulations could generate subject-specific mechanical models of the inner ear-swim bladder hearing structure, better explaining the role of swim bladder resonance in fish hearing.

3. Improvement of the Tank Design

As the prototype of the test tank, it was aimed to verify the ability of this method to non-invasively measure the swim bladder resonance and perform behavioural studies. As discussed in Chapter 4, there are many improvements to be done, *i.e.* making the plate stiffer so that swim bladder resonance is lower than the first tank resonance.

4. Swim Bladder Pathology and Conservation Monitoring

Beyond acoustic deterrence, the measurement technique could help diagnose issues in fish aquaculture or conservation programmes: parasitic infections, morphological deformities, or incomplete bladder inflation might shift resonance frequencies in a detectable way. Non-invasive measurements can thus offer a rapid health indicator, supporting endangered fish management or aquaculture management decisions.

6.3 Contributions to Existing Knowledge

This thesis delivers important advancements at the interface of fish ecology, bioacoustics, and underwater acoustical engineering:

1. A Non-Invasive Swim Bladder Resonance Measurement Framework

By conceiving and validating a cylindrical test tank-based method with carefully modelled acoustic fields, it overcomes many of the experimental and ethical obstacles that previously hampered *in vivo* resonance measurement. The synergy of experimental calibrations with FEM-based predictions sets a robust standard for replicability and reliability.

2. Empirical Support for Resonance-Based Behavioural Responses

While theoretical supports for resonance-induced fish hearing amplification and behavioural reactions have existed for decades, direct empirical confirmation using free-swimming fish remained elusive. This thesis's findings indicate that fish do manifest enhanced startle or avoidance behaviours near swim bladder their resonance frequencies, underscoring the potential practicality of resonance-based acoustic deterrents.

3. Integration of Morphological and Acoustic Parameters

The approach explicitly correlates fish size, swim bladder volume, and ear–bladder coupling to measured resonance frequencies. Incorporating morphological observations with advanced modelling tools (FEM and CT scanning) refines the understanding of how encapsulated-bubble acoustics translates into living organisms.

4. Practical Pathway Toward Selective Deterrents

By pinpointing frequencies that yield greater fish responsiveness while avoiding wideband, high-intensity noise, this research provides a conceptual and technical stepping stone for designing targeted acoustic deterrents. These systems could reduce overall acoustic pollution, lower energetic costs, and more carefully discriminate between fish species or sizes, fulfilling ecological mandates for minimal environmental disturbance.

In sum, the completed work not only meets the research objectives outlined in Chapter 1 but also brings more insights for harnessing fish swim bladder resonance in real-world ecological contexts. Its combination of engineering rigour, numerical validation, and ecological awareness stands to bolster fish protection strategies and deepen scientific understanding of bioacoustic phenomena in aquatic habitats.

List of References

Ainslie, M. A. (2010). Principles of sonar performance modelling, Springer.

Andreeva, I. (1974). "Scattering of sound by air bladders of fish in deep sound-scattering ocean layers." Sov. Phys. Acoust. 10: 17-20.

Argo IV, T. F., *et al.* (2008). "Measurement of the resonance frequency of single bubbles using a laser Doppler vibrometer." The Journal of the Acoustical Society of America 123(6): EL121-EL125.

Baik, K., *et al.* (2010). "Acoustic attenuation, phase and group velocities in liquid-filled pipes: Theory, experiment, and examples of water and mercury." J Acoust Soc Am 128(5): 2610-2624.

Baras, E. and M. C. Lucas (2001). "Impacts of man's modifications of river hydrology on the migration of freshwater fishes: a mechanistic perspective." International Journal of Ecohydrology & Hydrobiology 1(3): 291-304.

Bassett, C., *et al.* (2018). "Broadband echosounder measurements of the frequency response of fishes and euphausiids in the Gulf of Alaska." ICES Journal of Marine Science 75(3): 1131-1142.

Brinza, G. (2016). "*Structure and function of the trout and lamprey*, *Gretchen Brinza*." Available at: https://brinzaengineering.weebly.com/where-have-all-the-creatures-gone1/structure-and-function-of-the-trout-and-lamprey (Accessed: 24 April 2025).

Cheyne, S. A., *et al.* (1995). "Phase velocity measurements in bubbly liquids using a fiber optic laser interferometer." The Journal of the Acoustical Society of America 97(3): 1621-1624.

Church, C. C. (1995). "The effects of an elastic solid surface layer on the radial pulsations of gas bubbles." The Journal of the Acoustical Society of America 97(3): 1510-1521.

Church, C. C. (1995). "The effects of an elastic solid surface layer on the radial pulsations of gas bubbles." The Journal of the Acoustical Society of America 97(3): 1510-1521.

Coffin, A. B., *et al.* (2014). "Use of the swim bladder and lateral line in near-field sound source localization by fish." Journal of Experimental Biology 217(12): 2078-2088.

Commander, K. W. and A. Prosperetti (1989). "Linear pressure waves in bubbly liquids: Comparison between theory and experiments." The Journal of the Acoustical Society of America 85(2): 732-746.

Currie, H. A. L., *et al*. (2020). "A mechanical approach to understanding the impact of the nematode Anguillicoloides crassus on the European eel swimbladder." Journal of Experimental Biology 223(17).

Deleau, M. J., *et al*. (2020). "The response of anguilliform fish to underwater sound under an experimental setting." River Research and Applications 36(3): 441-451.

Deleau, M. J., *et al*. (2020). "Use of acoustics to enhance the efficiency of physical screens designed to protect downstream moving European eel (Anguilla anguilla)." Fisheries Management and Ecology 27(1): 1-9.

Dudgeon, D. (1992). "Endangered ecosystems: a review of the conservation status of tropical Asian rivers." Hydrobiologia 248(3): 167-191.

Duncan, A. J., Lucke, K., Erbe, C., & McCauley, R. D. (2016, July). “Issues associated with sound exposure experiments in tanks.” In *Proceedings of Meetings on Acoustics* (Vol. 27, No. 1). AIP Publishing.

Enders, E. C., *et al*. (2009). "Development of successful fish passage structures for downstream migrants requires knowledge of their behavioural response to accelerating flow." Canadian Journal of Fisheries and Aquatic Sciences 66(12): 2109-2117.

Fay, R. R. (1974). "Auditory frequency discrimination in vertebrates." The Journal of the Acoustical Society of America 56(1): 206-209.

Fay, R. R. and A. N. Popper (1974). "Acoustic stimulation of the ear of the goldfish (Carassius auratus)." Journal of Experimental Biology 61(1): 243-260.

Fay, R. R. and A. N. Popper (1975). "Modes of stimulation of the teleost ear." Journal of Experimental Biology 62(2): 379-387.

Fay, R. R. and A. N. Popper (2012). "Fish hearing: new perspectives from two'senior'bioacousticians." Brain, behavior and evolution 79(4): 215.

Feuillade, C. and R. W. Nero (1998). "A viscous-elastic swimbladder model for describing enhanced-frequency resonance scattering from fish." The Journal of the Acoustical Society of America 103(6): 3245-3255.

Fine, M. L. and E. Parmentier (2015). Mechanisms of fish sound production. Sound communication in fishes, Springer: 77-126.Foote, K. G. (1980). "Importance of the swimbladder in acoustic scattering by fish: A comparison of gadoid and mackerel target strengths." The Journal of the Acoustical Society of America 67(6): 2084-2089.

Frisch, K., *et al*. (2016). "Comparative imaging of European eels (Anguilla anguilla) for the evaluation of swimbladder nematode (Anguillicoloides crassus) infestation." Journal of Fish Diseases 39(6): 635-647.

Godø, O. R., *et al*. (2009). "Diel migration and swimbladder resonance of small fish: some implications for analyses of multifrequency echo data." ICES Journal of Marine Science 66(6): 1143-1148.

Gorska, N., *et al*. (2005). "Acoustic backscattering by Atlantic mackerel as being representative of fish that lack a swimbladder. Backscattering by individual fish." ICES Journal of Marine Science 62(5): 984-995.

Hahn, T. R. (2007). "Low frequency sound scattering from spherical assemblages of bubbles using effective medium theory." The Journal of the Acoustical Society of America 122(6): 3252-3267.

Halvorsen, M. B., *et al*. (2012). "Effects of exposure to pile-driving sounds on the lake sturgeon, Nile tilapia and hogchoker." Proceedings of the Royal Society B: Biological Sciences 279(1748): 4705-4714.

Halvorsen, M. B., *et al*. (2012). "Threshold for onset of injury in Chinook salmon from exposure to impulsive pile driving sounds." PloS one 7(6): e38968.

Hawkins, A. and C. Chapman (2020). "Studying the behaviour of fishes in the sea at Loch Torridon, Scotland." ICES Journal of Marine Science 77(7-8): 2423-2431.

Hawkins, A. D. and A. N. Popper (2018). "Directional hearing and sound source localization by fishes." J Acoust Soc Am 144(6): 3329.

Hocutt, C. H., *et al*. (1982). "Observations of behavioural responses of fish to environmental stress *in situ*." Journal of Applied Ecology: 443-451.

Jones, I. T., Stanley, J. A., Bonnel, J., & Mooney, T. A. (2019). “Complexities of tank acoustics warrant direct, careful measurement of particle motion and pressure for bioacoustic studies.” In *Proceedings of Meetings on Acoustics* (Vol. 37, No. 1). AIP Publishing.

K., S., *et al*. (2012). "Resonance classification of mixed assemblages of fish with swimbladders using a modified commercial broadband acoustic echosounder at 1–6 kHz." Canadian Journal of Fisheries and Aquatic Sciences 69(5): 854-868.

Katopodis, C., *et al*. (1994). Sea lamprey barriers: new concepts and research needs, Great Lakes Fishery Commission Ann Arbor, Michigan.

Kermani, I. D., Ghayour, M., & Mirdamadi, H. R. (2012). “Free vibration analysis of multi-directional functionally graded circular and annular plates.” *Journal of Mechanical science and Technology*, *26*, 3399-3410.

Ladich, F. (2019). "Ecology of sound communication in fishes." Fish and fisheries 20(3): 552-563.

Ladich, F. and R. R. Fay (2013). "Auditory evoked potential audiometry in fish." Reviews in Fish Biology and Fisheries 23(3): 317-364.

Lee, K. M., *et al*. (2011). "Sound propagation in water containing large tethered spherical encapsulated gas bubbles with resonance frequencies in the 50 Hz to 100 Hz range." The Journal of the Acoustical Society of America 130(5): 3325-3332.

Lee, K. M., *et al*. (2012). Measurements of resonance frequencies and damping of large encapsulated bubbles in a closed, water-filled tank. Proceedings of Meetings on Acoustics 164ASA, Acoustical Society of America.

Lee, K. M., *et al*. (2014). "Attenuation of standing waves in a large water tank using arrays of large tethered encapsulated bubbles." The Journal of the Acoustical Society of America 135(4): 1700-1708.

Lee, K. M., *et al*. (2017). "Attenuation of low-frequency underwater sound using an array of air-filled balloons and comparison to effective medium theory." The Journal of the Acoustical Society of America 142(6): 3443-3449.

Leighton, T. (1994). “*The acoustic bubble*.” Academic press.

Leighton, T., *et al*. (2007). "An acoustical hypothesis for the spiral bubble nets of humpback whales and the implications for whale feeding." Acoustics Bulletin 22(1): 17-21.

Leighton, T. G., *et al*. (2002). "The effect of reverberation on the damping of bubbles." The Journal of the Acoustical Society of America 112(4): 1366-1376.

Lovik, A. and J. M. Hovem (1979). "An experimental investigation of swimbladder resonance in fishes." The Journal of the Acoustical Society of America 66(3): 850-854.

Love, R. H. (1978). "Resonant acoustic scattering by swimbladder‐bearing fisha)." The Journal of the Acoustical Society of America 64(2): 571-580.

McCartney, B. S. and A. Stubbs (1971). "Measurements of the acoustic target strengths of fish in dorsal aspect, including swimbladder resonance." Journal of Sound and Vibration 15(3): 397-420.

Minnaert, M. (1933). "XVI. On musical air-bubbles and the sounds of running water." The London, Edinburgh, and Dublin Philosophical Magazine and Journal of Science 16(104): 235-248.

Munck, J. C. d. and N. A. M. Schellart (1987). "A model for the nearfield acoustics of the fish swimbladder and its relevance for directional hearing." The Journal of the Acoustical Society of America 81(2): 556-560.

Nero, R. W., *et al*. (2007). "Near-resonance scattering from arrays of artificial fish swimbladders." The Journal of the Acoustical Society of America 121(1): 132-143.

Noatch, M. R. and C. D. Suski (2012). "Non-physical barriers to deter fish movements." Environmental Reviews 20(1): 71-82.

Odeh, M. and G. Sommers (2000). "New design concepts for fish friendly turbines." International Journal on Hydropower and Dams 7.

Patrick, P. H., *et al*. (1985). "Responses of fish to a strobe light/air-bubble barrier." Fisheries Research 3: 157-172.

Piper, A. T., *et al*. (2019). "Response of seaward-migrating European eel (Anguilla anguilla) to an infrasound deterrent." Ecological Engineering 127: 480-486.

Poole, W. R. and J. Reynolds (1996). "Growth rate and age at migration of Anguilla anguilla." Journal of fish biology 48(4): 633-642.

Popper, A. N. (1974). "The response of the swim bladder of the goldfish (Carassius auratus) to acoustic stimuli." Journal of Experimental Biology 60(2): 295-304.

Popper, A. N. and R. R. Fay (2011). "Rethinking sound detection by fishes." Hearing research 273(1-2): 25-36.

Popper, A. N., *et al*. (2003). Sound detection mechanisms and capabilities of teleost fishes. Sensory processing in aquatic environments, Springer: 3-38.

Popper, A. N. and A. D. Hawkins (2018). "The importance of particle motion to fishes and invertebrates." The Journal of the Acoustical Society of America 143(1): 470-488.

Popper, A. N. and A. D. Hawkins (2019). "An overview of fish bioacoustics and the impacts of anthropogenic sounds on fishes." Journal of fish biology 94(5): 692-713.

Popper, A. N. and A. D. Hawkins (2021). "Fish hearing and how it is best determined." ICES Journal of Marine Science.

Popper, A. N., *et al*. (2020). "Use of sound to guide the movement of eels and other fishes within rivers: A critical review." Reviews in Fish Biology and Fisheries: 1-18.

Prosperetti, A., *et al*. (1988). "Nonlinear bubble dynamics." The Journal of the Acoustical Society of America 83(2): 502-514.

Putland, R. and A. Mensinger (2019). "Acoustic deterrents to manage fish populations." Reviews in Fish Biology and Fisheries 29(4): 789-807.

Radinger, J., *et al*. (2022). "Evident but context-dependent mortality of fish passing hydroelectric turbines." Conserv Biol 36(3): e13870.

Raveau, M. and C. Feuillade (2016). "Resonance scattering by fish schools: A comparison of two models." The Journal of the Acoustical Society of America 139(1): 163-175.

Rogers, P. H., Hawkins, A. D., Popper, A. N., Fay, R. R., & Gray, M. D. (2016). "Parvulescu revisited: small tank acoustics for bioacousticians." In *The effects of noise on aquatic life II* (pp. 933-941). Springer New York.

Rulifson, R. and M. Dadswell (1987). Mortality of Fish Passing through Tidal, Low-head Hydropower Turbines and Possible Mitigation Strategies. OCEANS'87, IEEE.

SAND, O. and P. S. ENGER (1973). "Evidence for an auditory function of the swimbladder in the cod." Journal of Experimental Biology 59(2): 405-414.

SAND, O. and A. Hawkins (1973). "Acoustic properties of the cod swimbladder." Journal of Experimental Biology 58(3): 797-820.

Stanton, T. K., *et al*. (2010). "New broadband methods for resonance classification and high-resolution imagery of fish with swimbladders using a modified commercial broadband echosounder." ICES Journal of Marine Science 67(2): 365-378.

Székely, C., *et al*. (2009). Impact of the swim-bladder parasite on the health and performance of European eels. Spawning migration of the European eel, Springer: 201-226.

Taft, E. (2000). "Fish protection technologies: a status report." Environmental Science & Policy 3: 349-359.

Taylor, R., *et al*. (2005). "Response of bighead carp to a bioacoustic behavioural fish guidance system." Fisheries Management and Ecology 12(4): 283-286.

Turnpenny, A. and N. O'Keeffe (2005). "Screening for intake and outfalls: a best practice guide." Environment Agency Science Report SC030231.

Turnpenny, A. W., *et al*. (1998). "A UK guide to intake fish-screening regulations, policy and best practice with particular reference to hydroelectric power schemes."

Vetter, B. J., *et al*. (2017). "Acoustic deterrence of bighead carp (Hypophthalmichthys nobilis) to a broadband sound stimulus." Journal of Great Lakes Research 43(1): 163-171.

Vetter, B. J. and J. A. Sisneros (2020). "Swim bladder enhances lagenar sensitivity to sound pressure and higher frequencies in female plainfin midshipman (Porichthys notatus)." Journal of Experimental Biology 223(14).

Vowles, A. S. and P. S. Kemp (2012). "Effects of light on the behaviour of brown trout (Salmo trutta) encountering accelerating flow: Application to downstream fish passage." Ecological Engineering 47: 247-253.

Wamboldt, J. J., *et al*. (2019). "Evaluation of an acoustic fish deterrent system in shallow water application at the Emiquon Preserve, Lewistown, IL." Management of Biological Invasions 10(3): 536.

Wiernicki, C. J., *et al*. (2020). "The Effect of Swim Bladder Presence and Morphology on Sound Frequency Detection for Fishes." Reviews in Fisheries Science & Aquaculture 28(4): 459-477.

Wilson, P. S., *et al*. (2003). "An improved water-filled impedance tube." The Journal of the Acoustical Society of America 113(6): 3245-3252.

Wilson, P. S., *et al*. (2005). "Phase speed and attenuation in bubbly liquids inferred from impedance measurements near the individual bubble resonance frequency." The Journal of the Acoustical Society of America 117(4): 1895-1910.

Wochner, M. S., *et al*. (2010). "Acoustic behavior of large encapsulated gas bubbles with resonance frequencies in the 50 to 100 Hz range." Proceedings of Meetings on Acoustics 9(1): 045003.

Ye, Z. (1997). "Low-frequency acoustic scattering by gas-filled prolate spheroids in liquids." The Journal of the Acoustical Society of America 101(4): 1945-1952.

Ye, Z. and E. Hoskinson (1998). "Low-frequency acoustic scattering by gas-filled prolate spheroids in liquids. II. Comparison with the exact solution." The Journal of the Acoustical Society of America 103(2): 822-826.

Zielinski, D. and P. Sorensen (2016). "Bubble curtain deflection screen diverts the movement of both Asian and common carp." North American Journal of Fisheries Management 36(2): 267-276.

Zielinski, D. P. and P. W. Sorensen (2016). "Bubble Curtain Deflection Screen Diverts the Movement of both Asian and Common Carp." North American Journal of Fisheries Management 36(2): 267-276.

Zielinski, D. P. and P. W. Sorensen (2017). "Silver, bighead, and common carp orient to acoustic particle motion when avoiding a complex sound." PloS one 12(6): e0180110.